

**LASER-INDUCED BREAKDOWN SPECTROSCOPY APPLICATIONS
FOR METAL-LABELED BIOMOLECULE DETECTION IN PAPER
ASSAYS**

by

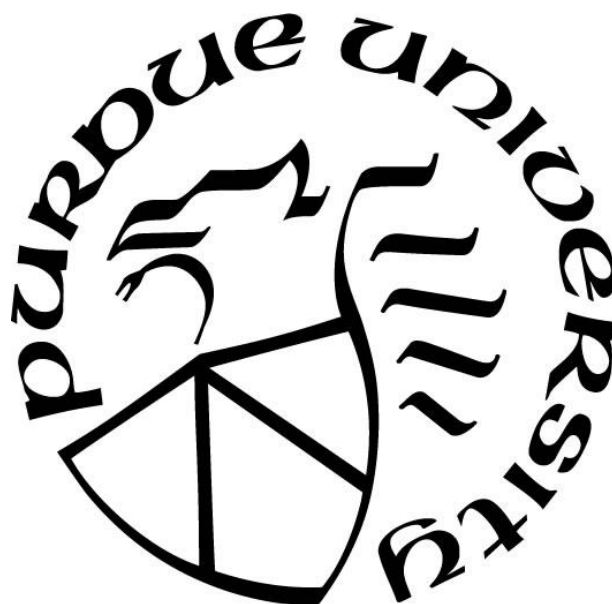
Carmen Gondhalekar

A Dissertation

Submitted to the Faculty of Purdue University

In Partial Fulfillment of the Requirements for the degree of

Doctor of Philosophy



Weldon School of Biomedical Engineering

West Lafayette, Indiana

August 2020

THE PURDUE UNIVERSITY GRADUATE SCHOOL
STATEMENT OF COMMITTEE APPROVAL

Dr. J. Paul Robinson, Chair

Basic Medical Sciences and Biomedical Engineering

Dr. Bartek Rajwa

Bindley Bioscience Center

Dr. Euiwon Bae

School of Aeronautics and Astronautics

Dr. Jaqueline Linnes

Biomedical Engineering

Approved by:

Dr. Harm Hogenesch and Dr. Andrew O. Brightman

Dedicated to those who adventure in the pursuit of knowledge.

ACKNOWLEDGMENTS

This work could not have been accomplished without the support of individuals, industry, and organizations. Deep gratitude is expressed towards Dr. Richard Russo's group at Lawrence Berkeley National Laboratories, Cytodiagnostics, Dr. Larry Stanker at the U.S. Department of Agriculture, and Dr. Gary Nolan's group at Stanford University for hosting me at their facilities and teaching me their respective specializations. Likewise, Dr. Prasoon Diwakar provided crucial guidance, especially in the early and mid-stages of the project when our group was learning laser-induced breakdown spectroscopy (LIBS) fundamentals. Partnership with industry, specifically Miftek Inc., Hübner Photonics, Chengdu Xinwujieopto Technology Co., SciAps, Avantes, and the United States Department of Agriculture, provided not only instrumentation, but also knowledge in LIBS system principles and operation. Among the team at Hübner photonics, Milan Zeman and Mikael Ek were instrumental in providing our group with a laser and recommendations for optics. Special thanks to Dr. Peng Xi at Peking University, who facilitated the collaboration with Chengdu Xinwujieopto Technology Co. Heartfelt appreciation is also extended to Dr. James Lindsay at the United States Department of Agriculture, whose support was the basis for the construction of the LIBS system at Purdue University. Miftek Inc. played a unique role in the project, providing me with not only their expertise in optics, software, and electrical engineering, but also the space in which to freely build instrumentation and experiment. Many of these collaborations were catalyzed by the SciX and CYTO annual conferences, where phenomenal leadership infallibly provided a space for students and professionals to learn and network. Grant funding was provided by the U.S. Department of Energy, Office of Defense Nuclear Nonproliferation Research and Development (contract number DE-AC02-05CH11231), the National Science Foundation (DGE-1333468), and the U.S. Department of Agriculture (project 1935-42000-072-02G, Center for Food Safety Engineering at Purdue University).

Greatest of all is my immense gratitude towards the team at Purdue University who founded the idea for the project and provided technical expertise, mentorship, encouragement, and discipline. Among these individuals were my committee members Drs. J. Paul Robinson, Euiwon Bae, Bartek Rajwa, and Jaqueline Linnes. Their mentorship and patience taught me more than I imagined when I first came to Purdue. My lab mates Iyll-Joon Doh, Huisung Kim, Jennifer Sturgis, Kathy Ragheb, Gretchen Lawler, Valery Patsekin, and Aleksandr Patsekin, were guides in times

of uncertainty, a helping hand, and a source of inspiration throughout this five-year journey. Last but not least are my past interns Pablo Martinez, Amanda Maples, Aadarsh Patel, and Cole Reynolds, who were a joy to work with and greatly contributed to this project. Many thanks to all these individuals.

TABLE OF CONTENTS

LIST OF TABLES	10
LIST OF FIGURES	11
LIST OF ABBREVIATIONS	19
ABSTRACT.....	20
1. REVIEW OF HAZARDOUS ORGANISM/BIOMOLECULE DETECTION, LASER- INDUCED BREAKDOWN SPECTROSCOPY, AND COMBINATIONS OF THE TWO.....	21
1.1 Dissertation Overview	21
1.2 Motivation: brief history of bioterrorism, food biocontamination, and food fraud	23
1.3 Field-deployable Biosensor Overview	25
1.3.1 Conventional Microbial Cultures	25
1.3.2 Biochemical Detection	25
1.3.3 Nucleic-Acid Detection.....	26
1.3.4 Immunologic Detection.....	27
1.4 Laser-induced Breakdown Spectroscopy as a Biosensor	28
1.4.1 LIBS and Immunogenic Analysis	28
1.4.2 Major Challenges in LIBS Analysis of Biological Samples	30
1.5 Laser-induced Breakdown Spectroscopy	31
1.5.1 LIBS Plasmas: formation and influential parameters	32
1.5.2 Mechanisms of LIBS Plasma Formation	33
1.5.3 Effects of LIBS Laser Characteristics on Plasma Formation: pulse width, wavelength, repetition rate	35
1.5.4 Effects of Environmental Conditions and Substrate Composition on LIBS Plasma Formation	37
1.5.5 LIBS Plasma Morphology	39
1.5.6 SIBS Plasma Formation and Emission	41
1.5.7 Section Summary	47
2. LIBS SYSTEM DESIGNS FOR DETECTION OF DISSOLVED/SUSPENDED METALS DRIED ON NITROCELLULOSE PAPER	48
2.1 Introduction	48

2.2 LIBS System 1	49
2.2.1 Laser	49
2.2.2 Spectrometer	50
2.2.3 Electronics and Software	53
2.2.4 Optics	53
2.3 Sample Chamber	55
2.3.1 Results	56
2.4 LIBS System 2	60
2.4.1 Spectrometer	60
2.4.2 Electronics and Software	61
2.4.3 Optics	62
2.4.4 Sample Chamber	63
2.4.5 Results	64
2.5 LIBS System 3	65
2.5.1 Results	66
2.6 LIBS System 4	68
2.6.1 Laser, Spectrometer, Software and Electronics, Optics, Sample Holder.....	68
2.6.2 Inductively-coupled Plasma Optical Emission Spectroscopy.....	68
2.6.3 Methods for Sample Preparation.....	69
2.6.4 Results	73
2.6.5 Summary of LIBS System 4	79
2.7 LIBS System 5	82
2.7.1 Laser, Spectrometer, Optics	83
2.7.2 Sample Preparation and Sample Holder	84
2.7.3 Results	85
2.8 LIBS System 6	88
2.8.1 Laser	88
2.8.2 Spectrometer	90
2.8.3 Sample Chamber	92
2.8.4 Electronics and Software	93
2.8.5 Optics	95

2.8.6 Results	95
2.9 Summary LIBS Systems 1-6	97
3. LIBS SYSTEM CHARACTERIZATION AND OPTIMIZATION FOR QUANTITATIVE LANTHANIDE DETECTION	99
3.1 Sample Preparation	99
3.2 Laser, Spectrometer, and Optics Quality Control	104
3.2.1 Laser Warm-up Time	106
3.3 Spot Size and Laser Energy	107
3.3.1 Imaging LIBS Ablation Zone	107
3.3.2 Spot size, Power, and Irradiance	110
3.4 LIBS Signal Processing	112
3.5 Emission Line Selection	117
3.5.1 NIST Atomic Spectral Database	117
3.5.2 LIBS System 6 Atomic Spectral Database	119
3.5.3 Limit of Detection	129
3.6 Multiplexed Heavy-Metal Data-Analysis Techniques	131
3.6.1 Sample Preparation	132
3.6.2 Data Analysis	133
3.6.3 Results: univariate analysis	135
3.6.4 Results: multivariate analysis	138
3.6.5 Discussion	140
3.7 Promising Biomolecular Labels Eu, Lu, and Yb: self-absorption, matrix effects, and recommendations for multiplexed detection	141
3.8 Summary of Chapter 3	146
4. APPLICATIONS OF LIBS TO BIOLOGICAL SCIENCES AND FOOD ANALYSIS	148
4.1 Introduction	148
4.2 Characterizing the Efficiency of Fluidigm MaxPar X8 Using LIBS	150
4.2.1 Background	150
4.2.2 Materials and Methods	151
4.2.3 Results and Discussion	154

4.2.4 Section Summary	160
4.3 LIBS Detection of Metal-labeled Antibodies Applied to a LFIA	160
4.3.1 Background	160
4.3.2 Materials and Methods	161
4.3.3 Results and Discussion.....	163
4.3.4 Section Summary	165
4.4 LIBS Detection of Gram-negative Bacteria Applied to a LFIA	166
4.4.1 Background	166
4.4.2 Materials and Methods	167
4.4.3 Results and Discussion.....	168
4.4.4 Section Summary	171
4.5 Hand-held LIBS Detection of Metal-labeled Antibodies Applied to a LFIA	171
4.5.1 Background	171
4.5.2 Materials and Methods	172
4.5.3 Results and Discussion.....	172
4.5.4 Section Summary	174
4.6 Investigation of Standard ELISA and Vertical Flow Assays for Toxin Detection	174
4.6.1 Lanthanide-labeled Antibody Conjugation to Gold Nanoparticles.....	174
4.6.2 Vertical Flow Assay Cartridge Design: single and multi-layer detection	177
4.6.3 Antibody Conjugation to Carboxylated Silica Beads and Polystyrene Beads	180
4.6.4 Antibody Conjugation to Gold Nanoparticles	185
4.6.5 Section Summary	190
4.7 Chapter Summary.....	190
5. CONCLUSION	192
APPENDIX A. OVERVIEW OF LIBS SYSTEMS 1-6: PERSPECTIVES ON LIBS DESIGN	196
APPENDIX B. R CODE FOR LIBS DATA ANALYSIS	202
REFERENCES	209

LIST OF TABLES

Table 2.1 Signal-to-noise ratio was measured for gold emissions lines 267.6 and 274.8 nm among three types of samples: gold foil, dry pregnancy test strips, and wet pregnancy test strips. The gold-foil positive control showed the highest S/N (at 267.6 and 274.8 nm), followed by the pink line, and then the area adjacent to the pink line (negative control).	79
Table 2.2 Signal-to-noise ratio was measured for lanthanide emissions among three types of samples: ICP standards on paper, lanthanide-conjugated antibodies on paper, and untreated paper. Each value represents S/N calculated from the aggregate of 15 ablations. Both the ICP standards and lanthanide-conjugated antibodies had higher S/N compared to untreated paper.	81
Table 3.1 Comparison of two methods for calculating emission line SNR for five elements. Method 1 (left) defined noise as the standard deviation of the 50-pixel region near the emission line. Method 2 (right) defined noise as the standard deviation of a median filter applied to 868 pixels of data (the full spectral window). Method 2 yielded much higher SNR for experimental treatments and slightly higher SNR among the negative controls.	117
Table 3.2 Emission lines for 17 elements and the delay time at which they were found to have the highest SNR. Limits of detection are listed for 7 elements, Lu having the lowest. *Identifies an element emission line with high standard deviation at the specified delay time.	127
Table 4.1 Percent efficiency of MaxPar X8 conjugation kit for antibody (Ab) and metal retention. Overall Ab and metal retention values represent the percent of each material retained from the beginning of the protocol to the final product. Metal retention for chelation represents the percent of each material retained in the reaction solution between the beginning of the protocol to post wash 2. Metal retention for Ab conjugation represents the percent of each material retained in the reaction solution between post wash 2 to the final product.	158
Table 4.2 Quantity of metal and antibody in the final product of MaxPar X8 conjugation. Based on these values, mg of metal, mol of metal, and atoms of metal per antibody were determined.	158
Table 4.3 Gold-nanoparticle conjugation treatments were described by the quantity of antibody used and pH of the conjugation buffer. Conjugation success was determined using peak absorbance measurements. A right shift in absorption wavelength indicated conjugation. Compared to unconjugated nanoparticles, all other treatments except the negative control displayed a right shift in absorbance.	166

LIST OF FIGURES

Figure 2.1 Design of LIBS System 1. A 70 mJ pulsed 1064 nm beam was directed to a sample chamber using a series of optics. Plasma emissions were collected by a collimating lens and fiber optics which interfaced with the sample chamber via a SMA connector. Laser water cooler and external power supply not shown.	49
Figure 2.2 Top image: picture of the timing circuit for LIBS System 1. Middle image: Function of each port in the timing circuit. Bottom image: timing diagram. The timing sequence starts with an external trigger pulse sent to the laser from a PC. 96.6 μ s after the trigger pulse, the laser is fired. The internal delay of the spectrometer once it is triggered (3.25 μ s) is considered such that data acquisition begins 1 μ s after the laser pulse. Values in red can be modified by the user, values in green cannot.	51
Figure 2.3 Schematic of the timing circuit of LIBS System 1.....	52
Figure 2.4 Photopaper placed along the path of the laser beam after passing through a 400 mm focal-length lens. The further the beam from the lens, the smaller the ablation marks on the photopaper, indicating beam focusing.	53
Figure 2.5 Left image, acquired with an electron microscope, represents ablation marks by LIBS System 1 on a silicon wafer. The images on the right (starting clockwise from top left) are stereomicroscope images of ablation marks on a silicon wafer, and foils of copper, aluminum, and nickel respectively.	54
Figure 2.6 A chamber facilitated sample placement in the path of the laser beam while obstructing most external light. Two fiber optics fitted with collimating lenses and a camera were interfaced with the chamber to permit sample viewing and signal acquisition.	55
Figure 2.7 Each plot represents the average of spectra produced from eight ablations on the surface of a silicon wafer, aluminum foil, and copper foil. A spectrum of the detector when the entrance was covered is represented as “dark spectrum.” Each plot represents the signal detected by two spectrometers that together cover the wavelength range from 220 to 600 nm.	57
Figure 2.8 Si (I) 288.158 nm emission line varies significantly between laser ablations of a silicon wafer	57
Figure 2.9 Top left: spectrum of Eu-labeled antibodies on a silicon-wafer surface. Bottom left: spectrum of silicon wafer. Top right: Focusing on the region indicated by the red box brings attention to the Eu (I) emission lines at 459.403, 462.722 and 466.188 nm and how they contrast with the silicon wafer background.	58
Figure 2.10 Design of LIBS System 2. A 50 μ J pulsed 1064 nm beam was directed to a sample chamber using a series of optics. The beam was expanded using a $f = -50$ mm lens, focused using a $f = 100$ mm lens, and re-directed to the sample chamber using a mirror. Plasma emissions were collected by a fiber optics which interfaced with the sample chamber via an SMA connector. ..	60

Figure 2.11 Timing circuit of LIBS System 2 shows data acquisition starting at the first of 1000 laser pulses. The laser pulses at 1 kHz for 1000 milliseconds. Data were acquired from the first pulse to the last pulse. Values in red can be modified by the user, values in green cannot.....	61
Figure 2.12 Top left is an image taken with stereomicroscopy. All other images were taken with electron microscopy (25.5 mm, 15 kV acceleration voltage, 200x magnification). As the number of the pulses increased, the amount of debris surrounding the crater, the size of the crater, and the apparent depth of the crater increased. Debris is deposited in a ring around the crater.	62
Figure 2.13 Spectra of aluminum foil, copper foil, gadolinium foil, and silicon wafer acquired with LIBS System 2.	63
Figure 2.14 The LIBS system designed by Applied Spectra Inc. consisted of a 213 nm, 4 mJ, nanosecond pulsed laser and a 6-channel spectrometer. The laser beam was directed to an enclosed sample chamber. This system allowed environmental gas control (Ar, He or air) and was interfaced with an inductively coupled plasma optical emission spectrometer. Data was displayed on monitors during and after data acquisition, allowing the user real-time data visualization.....	65
Figure 2.15 Acquisition of plasma emissions on the surface of Au foil using the IsoPLane SCT spectrograph fitted with the PI-MAX ICCD (top left) and the Aurora LIBS spectrometer (bottom left) showed a strong gold peak at 583.737 nm. The same peak was not observed during ablation of Au nanoparticles on nitrocellulose paper (top and bottom right).	67
Figure 2.16 Diagram of LIBS System 4. An 18 mJ beam produced by a NewWave Research Tempest 1064 nm Q-switched laser was directed to a sample using a series of optics. Sample position was adjusted using an x-y stage. Plasma emissions were directed to a fiber optic connected to a spectrometer and an ICCD detector. A camera was used for basic sample observation. Diagram not to scale.	69
Figure 2.17 Illustration of LIBS sampling approach for pregnancy test strips. Diagram not to scale.	71
Figure 2.18 Spectrum of gold foil. Gold emission lines, as indicated by NIST [159], were identified at 267.6 nm and 274.8 nm.....	75
Figure 2.19 Degradation of gold emission lines 267.6 and 274.8 nm as the pink line of a pregnancy test strip was sampled 10 times in the same location. Each data point represents the average of 3 measurements. Standard deviation ranged from 7.7-38.8%.	76
Figure 2.20 Water was added to eight pregnancy test strips. Four were immediately tested with LIBS (left) and the remaining were dried prior to sampling (right). For both wet and dry pregnancy test strips, gold emissions were observed where the pink line was sampled, and not in the area adjacent to the pink line (control). Each data point represents an aggregate of 27 measurements. Experimental and control spectra are offset to facilitate peak comparison.	77
Figure 2.21 LA-ICP-OES was performed on dry pregnancy test strips. The pink line on the strip produced stronger gold emissions at 208.2, 242.7, and 267.6 nm compared to the area adjacent to the pink.....	78
Figure 2.22 Water was added to pregnancy test strips. Three were immediately sampled with LIBS (left plot) and the three were dried prior to sampling (right plot). Two sections (the pink line and	

area adjacent to the pink line) of each pregnancy test strip were ablated 9 times each. Data on gold emission lines from the same sections of each pregnancy test were aggregated (27 measurements), converted to log of S/N, and plotted. Plot shows that the pink line produced a stronger gold emission line than did the area adjacent to the pink line. 78

Figure 2.23 LIBS performed on paper samples bearing Pr (a), Eu (b), Dy (c), Nd (d), and Yb (e). For each lanthanide, 3 treatments were tested: ICP standard on paper, lanthanide-conjugated antibody on paper, and untreated paper. All samples were ablated 15 times in different locations. The 15 sampling events were aggregated, converted to S/N in log scale, and plotted. The plots show that for each lanthanide (except the 404.6 nm line of Dy (c)), the ICP standard produced the strongest signal, followed by the lanthanide-conjugated antibody, and then the untreated nitrocellulose. 80

Figure 2.24 LA-ICP-OES was performed on Eu ICP standards on paper in a He carrier-gas environment. The Eu signal in the positive control was observed to spike following each ablation series. Signal was also observed to degrade as the paper was sampled from the edge towards the center. Lines are offset to facilitate peak comparison. 82

Figure 2.25 LIBS System 5 is a hand-held device sold by SciAps Inc. The LIBS system conveniently fits in a briefcase that can also store spare batteries, argon gas canisters, and supplemental equipment that allows the instrument to be interfaced with a PC or alternative power supplies. 82

Figure 2.26 Simplified diagram of LIBS System 5 design acquired from SciAps Website. 83

Figure 2.27 Samples of nitrocellulose paper containing Yb, Lu, or Eu CRM solution produced emissions lines that are not observed in the negative control (nitrocellulose treated with nitric acid). 85

Figure 2.28 As concentration of metal increases, so does the intensity of emission lines indicative of the element. For right-hand graph, data for Eu (I) 462.723 nm is hidden under data for Eu (I) 262.723 nm. 86

Figure 2.29 The diagram of LIBS System 6 shows the 1064 nm, 150 mJ (maximum), nanosecond laser in line with the optics system. A $f = -50$ mm lens (not clearly visible in the diagram) expands the laser beam, followed by beam-redirection using a mirror. The beam is then focused using a $f = 100$ mm lens into a sample chamber connected to a vacuum pump (not visible in the diagram). Alignment lasers aid with sample positioning. A series of lenses direct emissions to a fiber optic which is connected to a spectrometer and ICCD. 88

Figure 2.30 Laser synchronization pulses and photodiode readout. Purple line: A voltage rise in the Q-switch synchronization pulse indicated that the laser was about to fire. Pink line: A drop in the photodiode readout indicated that the laser had fired. Yellow line: lamp synchronization pulse rose 141 μ s before the Q-switch pulse (not visible in the displayed scale). 90

Figure 2.31 Oscilloscope readings of the Q-switch sync pulse from the laser, and ARM and Fire pulse from the spectrometer. Pink Line: laser Q-switch sync pulse – indicated that the laser was about to fire. This pulse goes to the Andor camera external trigger port. Green line: ARM signal – a high voltage indicated that the camera was ready to acquire data. Yellow line: Fire signal – a voltage increase indicated beginning of CCD exposure. 91

Figure 2.32 LIBS System 6 timing circuit for laser and Andor USB iStar ICCD camera. Values in red indicate internal delays that could not be modified by the user. Values in green could be modified by the user.....	94
Figure 2.33 LIBS System 6 timing circuit for laser and AvaSpec Mini spectrometers. Values in red indicate internal delays that could not be modified by the user. Values in green could be modified by the user.....	94
Figure 2.34 Copper emissions from early to late plasma. Over time, continuum radiation decreased, and emission lines appeared. Copper emissions increased in intensity until approximately 1000 ns after the laser pulse, after which emission line intensity decreased.	96
Figure 2.35 Emissions for Dy, Pr, Eu, Gd, and Nd CRM standards on nitrocellulose. Emission lines for each element are indicated by the arrows. Each treatment had a unique spectrum.	97
Figure 3.1 Laser-cut nitrocellulose squares, each 6×6 mm. The grooves made by the laser cutter prevented liquid added to a square from seeping beyond the boundaries.	102
Figure 3.2 Nitrocellulose squares were ablated 25 times in a grid-like pattern composed of five rows and five columns. The average of each row of the grid for two Gd emission lines are demonstrated in a bar chart. The edges of the nitrocellulose produced higher signal intensities than the middle regions.	103
Figure 3.3 Uneven drying of red food coloring on nitrocellulose in air at atmospheric pressure suggested that material gathered at the edges of the nitrocellulose. When nitrocellulose was dried under vacuum, the distribution of red food coloring was more even.	104
Figure 3.4 Day-to-day measurements of a 635 nm laser reflected on the surface of nitrocellulose were performed as a measurement of optics alignment and spectrometer performance. Variations in signal intensity were observed across months of measurements for two gratings with a 300 nm and 500 nm 1200 l/mm blaze.....	105
Figure 3.5 The flashlamp of the Litron SG-150 laser was pumped at 10 Hz for 75 min. Over the course of the 75 min, the Q-switch was activated 20 times at 10 Hz every 5 min. When the Q-switch was activated, laser energy and temperature were recorded. Over the course of 75 min, laser energy decreased and stabilized, whereas temperature increased and stabilized.	107
Figure 3.6 White-light interferometry image of a crater produced by LIBS System 4 on the surface of a silicon wafer. The laser beam formed a Gaussian-shaped crater, whose deepest point was approximately $5 \mu\text{m}$ from the surface. Circling the crater were two rings of material taller than the sample surface, potentially indicating material ablated from and deposited onto the wafer surface.	108
Figure 3.7 White-light interferometry image of a crater produced by LIBS System 4 on the surface of nitrocellulose paper. Maximum crater depth was approximately $88 \mu\text{m}$ from the sample surface. Circling the crater was an uneven ring of material taller than the sample surface, potentially indicating material ablated from and deposited onto the sample surface.	109
Figure 3.8 A microscope slide colored with a marker provided a convenient substrate on which to measure laser spot size. As laser energy increased, spot size remained the same regardless of	

sample position relative to the focal plane. As the sample was moved out of the focal plane, spot diameter increased.	110
Figure 3.9 As a microscope slide coated in black ink was moved into and out of the focal plane of the laser, spot size decreased, plateaued, and then increased. The plateau indicated the size of the beam waist.	111
Figure 3.10 Variation in irradiance on a nitrocellulose sample treated with Gd CRM solution yielded changes in signal intensity at 405.364 nm (Gd emission line location). The irradiance level at which the signal peaked was dependent on laser energy.	112
Figure 3.11 Europium peak intensities decreased as laser power increased while maintaining irradiance constant (by increasing spot size).	113
Figure 3.12 The signal-processing approach applied to Dy CRM solution (Dy ICP standard), Dy-conjugated antibody, and a negative control: row 1 displays the raw signal; the red line in row 2 represents a median filter applied to the data; row 3 shows subtraction of the median filter from the data.	114
Figure 3.13 Top right: raw spectrum of Dy CRM solution on nitrocellulose. The red areas labeled as “a,” “b,” and “c” indicate regions adjacent to Dy peaks considered noise and used to calculate SNR. A closer view of these regions shows that other unidentified peaks may be present in these regions, indicating that this method of calculating SNR is subject to error.	116
Figure 3.14 Spectrum of nitrocellulose paper at delay times of 0.5, 1, 2, 3, and 4 μ s. C (I), Na (II), N (I), and H(I) were observed to produce some of the strongest emission lines from nitrocellulose. An average of the spectra across all delay times was used as the negative control for treatments consisting of CRM solutions on nitrocellulose.	120
Figure 3.15 Spectra of Ho, Tm, Zn, and Ag on nitrocellulose paper at delay times of 0.5, 1, 2, 3, and 4 μ s.	122
Figure 3.16 Spectra of Cd, Fe, Tb, and Sm on nitrocellulose paper at delay times of 0.5, 1, 2, 3, and 4 μ s.	123
Figure 3.17 Spectra of Gd, Eu, Yb, and Lu on nitrocellulose paper at delay times of 0.5, 1, 2, 3 and 4 μ s.	124
Figure 3.18 Spectra of Au, Er, Dy, and Pr on nitrocellulose paper at delay times of 0.5, 1, 2, 3, and 4 μ s.	125
Figure 3.19 Spectra of Nd on nitrocellulose paper at delay times of 0.5, 1, 2, 3, and 4 μ s.	126
Figure 3.20 Dilution curves for Eu, Lu, Yb, Ag, Au, Nd, and Pr were used to determine the detection limit of LIBS System 6 for each element.	128
Figure 3.21 Raw spectra of pure metal solutions (Eu, Gd, Pr, Dy, and Nd) dried on nitrocellulose paper. HNO ₃ dried on nitrocellulose paper serves as a negative control.	135
Figure 3.22 Intensity of emission lines for Eu, Pr, Nd Gd, and Dy across treatments. Treatments consist of pure lanthanides and mixtures of four or five in which each lanthanide is at a	

concentration of 0.2 mg/l. Metals on nitrocellulose at 0.2 mg/ml generate a stronger signal in pure samples vs. mixed samples.	136
Figure 3.23 Signal intensity at 412.97 nm across a dilution series of Eu. Signal positively correlates to Eu concentration, and plateaus at a concentration of 0.2 mg/ml.	137
Figure 3.24 NNLS unmixing across mixed metal treatments for case 2. The mixing matrix M consists of data from pure-metal treatments, where each metal is present at a concentration of 0.2mg/ml, with the exception of Eu, which is at a concentration of 0.02 mg/ml. r is a vector representing a mixture of four or five metals, with each metal present at a concentration of 0.2 mg/l. False negatives result from each treatment, except for the mixture lacking Eu.	137
Figure 3.25 NNLS unmixing across mixed metal treatments for case 3. The mixing matrix M consists of data from pure-metal treatments, where each metal is present at a concentration of 0.2 mg/ml, with the exception of Eu, which is at a concentration of 0.02 mg/ml. r is a vector representing a mixture of four or five metals, with each metal present at a concentration of 0.2 mg/ml, with the exception of Eu which is at a concentration of 0.02mg/ml. False negatives were not observed.	138
Figure 3.26 NNLS unmixing across mixed metal treatments for case 1. The mixing matrix M consists of data from pure-metal treatments, with each metal present at a concentration of 0.2 mg/ml. r is a vector representing a mixture of four or five metals, with each metal present at a concentration of 0.2 mg/l. False negatives result from each treatment, except for mixtures lacking Gd or Eu.	139
Figure 3.27 Top graph: A positive relationship was observed between concentration (mg/L) and SNR until concentrations reached 100-200 mg/L, after which the signal peaks and plateaus or decreases. Left graph: relationship between signal-to-noise ratio and the log-transformed concentration (mg/L) for better representation of data at lower concentrations. Each emission line was observed to follow a log-logarithmic distribution.	142
Figure 3.28 Eu (II) 520.504-nm SNR in response to concentration of gold nanoparticles on nitrocellulose. Eu concentration remained constant across treatments. As gold nanoparticle concentration increased, Eu signal decreased, indicating that the matrix composition had an effect on Eu signal intensity.	144
Figure 3.29 Each graph represents the spectrum of Lu, Eu, and Yb on nitrocellulose at their optimum delay time. To more clearly distinguish Lu, Eu, and Yb peaks, the nitrocellulose background was subtracted from each spectrum. The nitrocellulose background is also represented on each plot. All three plots represent the same data, but on different wavelength scales to allow more clear visualization of peaks.	145
Figure 4.1 Standard curve of Eu, Lu, and Yb CRM solutions.	155
Figure 4.2 Dilution curve of MaxPar X8 metal stock solutions containing Eu, Lu, and Yb. Curves show a log-logistic trends. Negative controls for each treatment overlap.	156
Figure 4.3 SNR of Yb, Eu, and Lu in the metal stock and conjugated antibody (Ab) solution were measured by drying the solutions on nitrocellulose paper followed by LIBS analysis. SNR was converted to milligrams of metal using a standard curve. Milligrams of metal in post washes 1-6 was measured by drying the waste from each wash step on nitrocellulose, followed by LIBS	

analysis, unit conversion, and subtracting the amount of metal found in the waste solution from the amount of metal in the reaction solution. Post washes 1-6 represent an estimate of the amount of metal in the reaction solution..... 157

Figure 4.4 3 kDa and 50 kDa centrifugal filter units were used to remove unconjugated reagent from the reaction solution. To determine if metal remained embedded in the membranes of the filter units, the membrane surface was tested with LIBS. The material remaining in the filter could be metal-complexed polymer or metal-labeled antibody, indicating that reaction efficiency may have been impacted by product loss to the filters. 159

Figure 4.5 20 nm gold nanoparticles after 30 minutes of incubation with antibody and buffer. Numbers indicate the treatment. Coloration of the nanoparticles was used as an indicator of conjugation success. A red hue (absorbance = 516 nm) indicated little aggregation, whereas a purple hue (absorbance > 516 nm) or clumps indicated nanoparticle aggregates and precipitation. 163

Figure 4.6 WaterSafe® assay for detection of Gram-negative bacteria. The plastic covering of this strip was removed to expose the sample absorption pad (right). Anti-mouse antibodies conjugated to gold nanoparticles were added to the sample absorption pad and were observed to wick along the strip. After 10 minutes of incubation, test and control lines were observed on the strip, indicating that the reagents immobilized to these areas by the manufacturer were either antibodies raised in mice or reagents that cross-reacted with the anti-mouse antibody..... 164

Figure 4.7 Lu-labeled antibodies (left) and Eu-labeled antibodies (right) applied to WaterSafe® detection strips. The goal of the assay was to determine if the anti-mouse antibodies would bind to the test and positive control lines as did gold nanoparticles (GNPs) conjugated to the same antibodies. The strongest Eu and Lu emissions were found at the test line, followed by the control line and the negative control line. For the study with Lu-labeled antibodies, signal intensity was lower in the presence of gold nanoparticles. Signal intensity was minimal in the treatment where Lu-labeled antibodies were absent..... 165

Figure 4.8 Eu-labeled anti-Gram negative antibodies were applied to WaterSafe® Gram-negative bacteria detection strips in the presence of *E. coli* and buffers at different pH levels. In each case, the signal was strongest at the positive control line and equivalent at the test and negative-control lines. 170

Figure 4.9 Eu-labeled anti-*E. coli* antibodies were applied to WaterSafe® Gram-negative bacteria detection strips in the presence of *E. coli*. As a positive control, Eu-labeled anti-mouse antibodies were similarly applied to the strip. As a negative control, neither Eu-labeled antibody nor *E. coli* was added to the strip. In the experimental treatments, the signal was equivalent at the test and negative-control lines. In the positive-control treatment, signal was strongest at the test line. In the negative-control treatment, signal was equivalent at the test and negative-control lines. 170

Figure 4.10 (Right) Ablation marks on the test (pink line surrounded by pencil marks) and negative-control lines (white region) of the WaterSafe test strip were visible. (Left) Hand-held LIBS analysis of three detection strips treated with Eu-labeled anti-mouse antibodies showed a strong Eu signal at the test line compared to the negative-control line. Each strip was also treated with a different bacterial species, but it is believed that the bacteria had minimal impact on the

outcome of the assay. The LIBS spectrum was not analyzed for detection of graphite from the pencil marks.	173
Figure 4.11 Immuno-dot-blot tests for lanthanide-labeled antibodies conjugated to nanoparticles. An illustration of the bioassay is displayed to the right, the results are displayed to the left.	177
Figure 4.12 Design concept of a multi-layer vertical flow assay cartridge that utilizes nanoparticles conjugated to lanthanide-labeled antibodies	179
Figure 4.13 Proof-of-concept for multi-layer vertical flow assay cartridge. Pink spots indicate successful immobilization of nanoparticles on nitrocellulose paper.	179
Figure 4.14 Assay design to test binding of botulinum toxin to anti-botulinum antibodies. Two types of toxin were tested – one from Purdue (stored for extended time in a diluted state) and one from the USDA (frozen and freshly diluted). Results indicate that the freshly diluted toxin outperformed toxin stored in a diluted state.....	183
Figure 4.15 Bead-based ELISA assay designed to test binding of Shiga and botulinum toxin to anti-Shiga and botulinum toxin antibodies. Results indicate successful binding between beads, antibodies and toxin (Shiga toxin left plot, botulinum toxin right plot).	185
Figure 4.16 Top two images - Differences between treatments can be observed during the process of conjugation. Solution with a more blueish tint imply particle aggregation. Bottom image – immuno-dot-blot tests. Top row of cartridges show successful conjugation of rabbit anti- <i>E. coli</i> antibodies to nanoparticles. Bottom two rows indicate less successful conjugation of stx 2-1 and stx 2-2 to nanoparticles.	188
Figure 4.17 Illustration of 10 treatments conditions and results. Rows and columns correspond to the amount of antibody and BSA added to a 1ml solution of 20nm gold nanoparticles (OD1). The total volume of the BSA-Antibody mixture was 22µl for each treatment.	189

LIST OF ABBREVIATIONS

Ab:	antibody
CRM:	certified reference material
CyTOF:	time of flight mass spectrometry
GNP:	gold nanoparticle
ICP:	inductively coupled plasma
ICP-OES:	inductively coupled plasma optical emission spectroscopy
LOD:	limit of detection
LIBS:	laser-induced breakdown spectroscopy
LFIA:	lateral flow immunoassay
MS:	mass spectrometry
NIST:	National Institute for Standards and Technology
NIST ASD:	National Institute for Standards and Technology atomic spectra database
PBB:	paper-based bioassay
PC:	personal computer
PCR:	polymerase chain reaction
S/N:	signal-to-noise ratio
SNR:	signal-to-noise ratio
SIBS:	spark-induced breakdown spectroscopy

ABSTRACT

This doctoral thesis investigates the application of laser-induced breakdown spectroscopy (LIBS) for detection of labeled biomolecules on nitrocellulose paper. Nitrocellulose paper is a material often used for assays involving the concentration and labeling of a target analyte, followed by label detection. Among paper-based diagnostics are lateral-flow immuno-assays (LFIAs). Research efforts have made LFIAs into accessible, portable, and low-cost tools for detecting targets such as allergens, toxins, and microbes in food and water. Gold (Au) nanoparticles are standard biomolecular labels among LFIAs, typically detected via colorimetric means. Other labels, such as quantum dots, are also often metallic, and research is ongoing to expand the number of portable instrumentations applied to their detection. A wide diversity of lanthanide-complexed polymers (LCPs) are used as immunoassay labels but have been inapt for portable paper-based assays owing to lab-bound detection instrumentation, until now. LIBS is a multi-element characterization technique which has recently developed from a bench-top to a portable/hand-held analytical tool. This is among the first studies to show that LCPs can be considered as options for biomolecule labels in paper-based assays using bench-based and hand-held LIBS as label detection modalities.

Chapter one reviews the importance of rapid, multiplexed detection of chemical and biological contaminants, the application of current biosensors, and the role of LIBS as an emerging biosensor. Paper-based bioassays were identified as a promising approach for contaminant detection whose capabilities could be enhanced by LIBS. The next chapter dives into LIBS system designs to address which LIBS parameters were appropriate for label detection on paper assay material. A balance of LIBS parameters was found to be important for successful analyte detection. Chapter three optimizes a LIBS design for sensitive detection of 17 metals and establishes limit of detection values for 7 metals. Optimal detection parameters depended on the metal being detected and were applied to the objective of the final chapter: LIBS detection of labeled antigen immobilized on a paper-based assay. Both antibody and bacteria detection assays were successfully performed and analyzed using benchtop and portable LIBS, suggesting an exciting future for the use of LIBS as a biosensor. The prospect of using LIBS for multiplexed, rapid and sensitive detection of biomolecules in assays is explored, laying grounds for future work in the ever-relevant field of biological and chemical hazard detection.

1. REVIEW OF HAZARDOUS ORGANISM/BIOMOLECULE DETECTION, LASER-INDUCED BREAKDOWN SPECTROSCOPY, AND COMBINATIONS OF THE TWO

1.1 Dissertation Overview

This doctoral dissertation explores the application of laser-induced breakdown spectroscopy (LIBS) for analysis of commercial lateral-flow immunoassay (LFIA) platforms, and LFIA platforms modified with lanthanide biomolecular labels. The combination of these technologies primarily offers advantages for rapid, portable, and multiplexed biomolecular detection. Such a detection modality is particularly useful in food inspection and forensics, where rapid in-field identification of food contaminants such as *E. coli* has wide-spread public health impacts.

LFIAAs have become popular field-deployable diagnostic tools because they are simple, portable, low cost [1-3], and well described in the scientific literature [3, 4]. A common example is the pregnancy test strip, which utilizes gold nanoparticles (GNPs) coated in antibodies for colorimetric detection of human chorionic gonadotropin hormone. Configurations of LFIAAs vary greatly, but a common approach is to use a two-step lateral-flow assay design [5]. In this design, an antigen-containing suspension is mixed in a tube with an antigen label. The solution is introduced to one end of a nitrocellulose strip, and capillary forces wick the labeled antigen along the strip. A defined area downstream of the sample introduction zone displays antibodies that immobilize the labeled antigen, but not the background material, which is removed as it continues to travel downstream. Label that is not bound to a target is captured downstream at the control line. The concentrated label at the test and control lines is then detectable, typically through colorimetric means. Similar designs are common in commercial products, many of which have applications in food science, such as bacterial, allergen, and toxin detection [4]. While commercial LFIAAs are not stand-alone assessments of analyte presence, ongoing advancements and the advantages of LFIAAs in portability and cost suggest a promising future, especially for in-the-field detection.

Increasing the sensitivity and quantitative multiplexing (detection of more than one analyte in a single experiment) capability of LFIAAs is a key aspect of improving LFIA performance [4, 2]. Multiplexed LFIAAs for food-contamination detection are uncommon because of sample complexity, limited number of antigen labels, reagent chemistry on the paper substrate, and spatial

design [2]. Labels typically used among commercial LFIA are gold, silver, and latex beads, which visually contrast the background of the assay substrate and biological matrix by localized surface plasmon resonance [2]. In immunochemistry, fluorochromes are widely used labels because of their specificity and excellent signal-to-noise capacity [6] [7, 8]. However, multiplexing either fluorochromes or gold, silver, or latex particles is challenging for most detection modalities owing to overlapping emission or color profiles, short lifetimes, and background effects [9-11, 8]. These features make it challenging to develop detection modalities that are portable and highly multiplexed.

This study proposes a method to overcome the challenges of multiplexed LFIA by introducing a new detection modality, LIBS – a multi-analyte detection tool [12, 13]. The large number of metal labels potentially be applicable to LFIA creates opportunities for highly multiplexed assays that can be used as field-deployable or bench-based diagnostic tools. Existing labels that lend themselves to LIBS analysis are polymer-complexed metals, mostly lanthanides (e.g., europium, ytterbium, praseodymium, and neodymium), which have been developed in the last several years for use in immunoassays analyzed by mass cytometry for discoveries primarily in the field of hematology [11, 14]. The diversity of metal labels and the bandwidth of mass cytometry permits highly multiplexed immunoassays [9, 15, 16]. To date, metal-complexed polymers have not been applied to LFIA, possibly because the size, cost, and sample preparation requirements of mass spectrometry precludes their transition into the field of low-cost or portable diagnostics [17]. With the rapid advancements being made in laser and optical-sensor technologies, LIBS is becoming increasingly portable [13]. It has potential to become a portable analytical tool for highly multiplexed LFIA that use polymer-complexed metals for antigen labeling.

LIBS is a technique for simultaneous multi-element identification that relies on the generation and spectral analysis of a laser-induced plasma [12]. While it originated as a bench-top instrument, it has recently been developed into a hand-held commercial product, predominantly applied to characterization of soils, rocks, and scrap metal [13, 18]. Significant effort has been undertaken to apply LIBS to biological applications such as microbial identification and toxin detection [19, 20, 13, 21-23]. In a few instances, portable LIBS systems were designed for bio-contaminant detection [24, 19]. Some studies apply LIBS to analysis of clinical or biological samples, where analytes are labeled with metal tags [25-27, 23]. These studies primarily

apply gold, iron, titanium, and silicon micro- and nanoparticles as bio-labels detected with LIBS on a porous membrane-like paper.

This dissertation examines LIBS and LFIAs, with emphasis on the former. Chapter 1 provides the motivation behind this research as well as a literature review of LIBS, biosensors, and the application of LIBS as a biosensor. A counterpart of LIBS, spark-induced breakdown spectroscopy (SIBS), is also briefly explored. Chapter 2 goes into detail regarding the design of a LIBS system. The chapter is in part intended as a guide for those building their own LIBS systems by addressing design aspects of a LIBS system deemed most important. This chapter is also a demonstration of a trial-and-error process for finding a LIBS system appropriate for detection of metal bio-labels in paper substrates commonly used among LFIAs. Chapter 2 concludes with a final LIBS design applied to most studies in the following chapters. Chapter 3 investigates parameters important for LIBS system optimization for a specific application. In this case, the LIBS system was optimized for detection of lanthanides and other metals used as biomolecular labels. Several elements were identified as promising candidates for biomolecular labeling in LFIAs. Chapter 3 also investigates the potential of multi-label detection, which future studies would translate to multiplexed detection of antigens in a LFIA. Chapter 4 goes a step further by applying optimized LIBS parameters to label detection in LFIAs. Though Chapter 4 emphasizes LIBS analysis of LFIAs, other applications of LIBS in contaminant detection are also explored, since they represent future areas of research relevant to food safety. Chapter 5 expands on the future of LIBS applications in food safety considering the information gained through the work presented in the dissertation.

1.2 Motivation: brief history of bioterrorism, food biocontamination, and food fraud

Outbreaks of harmful biological material, whether accidental or as an act of bioterrorism, are significant concerns for groups trying to protect public health. Bioterrorism has been used to cause individual or mass harm since early human history. In the 14th century, Moguls invading the city of Kaffa on the Crimean Peninsula launched plague victims into the city, spreading the disease as a weapon [28, 29]. Likewise, bioweapons in the form of blankets infected with small pox and arrows dipped in blood and manure caused immense damage to entire civilizations [29, 28]. Use of bioweapons continued into the 20th century when governments around the world assembled programs specifically for their development. The history of bioweapons consists of agents that

affect human, livestock, and crop health [30]. To curb the use of bioweapons in warfare, the 1925 Geneva Protocol was signed by 108 nations. However, a number of those nations used bioweapons even after the treaty came into effect. On a more local scale, individuals or organized groups have also been responsible for the development and use of bioweapons. In 1984, followers of Bhagwan Shree Rajneesh were responsible for the intentional contamination of salad bars with *Salmonella* spp. in local restaurants in The Dalles, Oregon [31]. The attack resulted in 751 cases of *Salmonella*. In 2001, an attack was made by an individual on media and political officials through the delivery of anthrax spores contained within apparently innocuous letters. Five victims died and 22 were infected [32]. Early and recent history in bioterrorism makes defense against bio-warfare a top concern among United States agencies such as the Department of Agriculture and the Department of Defense [30, 33].

Accidental contamination of food, water, and/or soil with harmful biological agents results in millions of illness cases around the world every year. Contamination of food is of high interest to health and safety departments because it can be particularly hard to detect and track [30]. Detection is a challenge because foods vary widely in composition, material properties, and origin. Now that food products are shipped world-wide, it can be difficult to track the source of a given contamination, which can originate from the raw material, processing, handler, packaging, or the destination where it is unpacked [33]. Between the years 2000 and 2017, *Salmonella*, *Escherichia*, *Clostridium*, and *Listeria* have together caused more than 100,000 food-borne illnesses and 250 deaths. These contaminants were found in products such as peanut butter, spinach, fruits, fast food, packaged chicken, and ground turkey [34].

Between cases of bioterrorism and accidental contamination, there is a very wide variety of contaminants and occurrences of resulting illness. The vectors for illness come in all forms: food, water, soil, and air. Often, the identity of the contaminant is not known until laboratory tests can be performed. The classic gold standards for contaminant identification are often time consuming and lab bound [30]. Therefore, significant effort is being made to make detection tests that are both field-deployable and capable of detecting a large diversity of analytes (multiplexed) in a short amount of time.

1.3 Field-deployable Biosensor Overview

To address the concern of bioterrorism and food contamination, many technologies have been developed for detection of bio-contaminants. The diversity of technologies tackles the many challenges of bio-contaminant detection, but no single technology has yet addressed all challenges. A few of the challenges are complex sample matrices, low concentrations of analyte, and very large or small sample sizes. Challenges in biosensor design are high sensitivity, specificity, reproducibility, portability, speed, multiplexing capability, and user friendliness. Biodetection systems can be divided into four major categories: conventional cultures, nucleic-acid based, immunologic, and biochemical.

1.3.1 Conventional Microbial Cultures

Conventional cultures have been used for many years for bacterial or fungal identification, and in many cases represent the gold standard [30]. In the process of culturing bacteria, one can isolate the bacterial strain, and evaluate colony and cell morphology and metabolic processes. Based on the results, an experienced individual can identify the bacterium. However, culture and enrichment of bacteria takes multiple days and is based on the pathogen's being a viable, culturable organism. In addition, the microbiologist would need to test various growth conditions to account for the wide diversity of bacterial or fungal contaminants. For identification of food contaminants, culture has been a reliable and cost-effective method of detecting the contaminant. The primary draw-backs to these techniques are that they are mainly lab-based, rely on viable organisms, and are time consuming [30].

1.3.2 Biochemical Detection

Some forms of biochemical detection involve the analysis of metabolic products of bacterial cultures, or a chemical analysis of components within the cell (materials that are not amino acids or nucleic acids). Often, these techniques involve gas chromatography or gas chromatography mass spectrometry as a standard lab-based measurement [35]. Several automated systems have been developed for biochemical analysis in biodefense applications since bacterial and fungal cultures often produce aromatic substances [30]. Electronic noses that utilize sensors

such as acoustic waves, cantilevers, or conducting polymers detect the volatile compounds and identify the bacterium or fungus based on the chemical fingerprint [36, 35]. An advantage of these systems is that they can be multiplexed and applied to a variety of sample types: urine [37], food (milk [38] and bread [39]), wound bandages [40], swabs [41], and culture plates [42]. While electronic noses are still only potentials for commercialization, biochemical testing strips and plates sold by BioMerieux and BiOLOG are currently on the market. These techniques can be rapid and sensitive, but results may be unspecific and/or difficult to interpret, with limitations based on the database to which results are being compared [30].

1.3.3 Nucleic-Acid Detection

Nucleic-acid detection is the basis for widely used and successful biohazard detection technologies. It is sensitive, specific, rapid, and field deployable [30, 43]. Based on the success of nucleic-acid detection and sequencing technology, the Defense Threat Reduction Agency (DTRA) of the U.S. Department of Defense launched a bioinformatics platform that facilitates biothreat identification and communication among field-deployed polymerase chain reaction (PCR) systems and users [44]. qPCR systems can be used to detect several targets at once using combinations of fluorescent probes [43]. Disposable cartridges, such as the one used for the automated GeneXpert Q-PCR DNA detection system (Cepheid, California), makes handling and detection of biohazards safer for the user. Roche (Switzerland) developed the LightCycler system, which is similar to GeneXpert but requires DNA extraction. Field-deployable versions include the Ruggedized Advanced Pathogen Identification Device (RAPID) (Idaho Technologies, now BioFire Diagnostics, Utah), and BioSeeq by Smiths Detection (United Kingdom) [43, 30, 45]. Freeze-dried reagents contribute to the portability of these systems [46, 30, 47].

Drawbacks to portable and bench-top nucleic acid detection systems include the need for sample preparation, the potential for samples to be contaminated with interferants (not all of which are known), cost, inability to detect non-nucleic acid contaminants such as toxins, and inability to determine whether the target is a living or dead cell. Despite the drawbacks, nucleic-acid detection remains a highly sensitive, rapid, and field-deployable technology for biohazard detection [30].

1.3.4 Immunologic Detection

Like nucleic-acid detection, immunoassays have also been widely used in clinical and laboratory settings for detection of contaminants, and come in a wide diversity [48]. Whereas nucleic-acid detection is typically performed with fluorescent probes, immunoassays use fluorescence, luminescence, colorimetry, or electrochemistry to detect the presence of an analyte. Substrates on which detection is performed also vary widely and include electrodes, plastics, semi-conductors, and paper. The most common immunoassays are immunochromatographic paper-based assays, enzyme-linked immunosorbent assays (ELISA), time-resolved fluorescence (TRF) assays, and immunomagnetic separation-electrochemiluminescence (IMS-ECL) assays [48]. Among each of these assays, sensitivity is primarily determined by the quality of the reagents used, but is overall less than that of PCR detection technologies [48, 30].

Commercial immuno-assay technologies that have had particular success for detection of biohazards include Luminex xMAP, BV Technology, and DELFIA (dissociation-enhanced lanthanide fluorescence immunoassay). The list of available technologies is far more expansive, as is described in this emergency biotechnology selection guide [49]. Luminex xMAP relies on flow cytometry and is capable of a large degree of multiplexing for both immuno and nucleic-acid targets [50, 51]. xMAP has been applied to biohazard detection in environmental, food, and human samples by U.S. health agencies [50, 52]. So far, reports have not been made on a field-deployable xMAP system. BioVeris Technology (acquired by Roche in 2007) is also based on the use of beads and flow cytometry. In contrast to the Luminex system, this technology uses immunomagnetic electrochemiluminescence to detect the target. Unlike Luminex xMAP, only one analyte can be detected in a sampling event. Sensitivity of the BioVeris system is 10 pg/ml for toxins; the system is also capable of detecting viruses, bacteria, and DNA [53]. DELFIA systems by PerkinElmer rely on time-resolved fluorescence/luminescence to detect antigens. The system is based on a standard ELISA assay, but the detection probes are lanthanides (Eu^{3+} , Sm^{3+} , Tb^{3+} , or Dy^{3+}) that emit a long-lasting and strong signal with a large Stokes shift [54]. These assays are also single-plex, but have been shown to outperform standard ELISAs [54].

Paper-based bioassays (PBBs) have been used for a wide variety of applications, including detection of harmful chemicals and bioweapons [55, 56]. Their success is largely attributed to their low-cost, portability, ease of use, and speed of analysis. Their versatility is also notable – for example, PBBs can be used for DNA amplification and detection [57]. In addition, PBBs are

applicable to a broad diversity of sample types, including blood [58], saliva [59], urine [60], sweat [61], and other fluids. The detection probes include colorimetric (gold and silver nanoparticles), fluorophores (FITC), and luminescent materials [62]. Though current methods for PBB analysis are generally not as sensitive as the gold standard for immunoassays [30, 63], their ease of use, versatility, field deployability, and low cost make them practical for public health and military field applications. PBBs have been applied to the detection of contaminants such as Shiga toxin [55], ricin [64], and botulinum [65], as well as many other antigens – highlighting their many capabilities [4, 56]. The major drawbacks of PBBs are their limited sensitivity, quantitative and multiplexing capability[66], and misleading results (false negatives and positives)[67]. This study tries to determine if a new detection modality, laser-induced breakdown spectroscopy (LIBS), can be used to address the drawbacks of PBBs. The next section introduces LIBS applications in biomolecule detection/ biological material analysis, primarily in conjunction with immunoassays.

1.4 Laser-induced Breakdown Spectroscopy as a Biosensor

1.4.1 LIBS and Immunogenic Analysis

Before proceeding into the topic of LIBS applications in biology, a brief introduction of LIBS is warranted (Section 1.5 explores LIBS principles in more depth). Drs. David Cremers and Leon Radziemski provide an excellent description of LIBS in their highly cited *Handbook of Laser-Induced Breakdown Spectroscopy* [12]. Laser-induced breakdown spectroscopy (LIBS) is a technique for characterizing materials based on their elemental composition. The process of LIBS involves directing a focused high-energy laser pulse to a sample. Excitation of the sample by the laser is influenced by the laser power, pulse duration, wavelength, repetition rate, and environment. Sample excitation is also dependent on the material properties of the sample – whether the material is solid, liquid, gaseous, porous, or conductive. In the appropriate conditions, an ionic plasma will form from the material. The ionic plasma emanates optical radiation. A portion of the optical radiation is derived from excited atoms as they return to their resting state. These atomic emissions can be measured by a spectrometer. Based on the intensity of atomic emissions at certain wavelengths, elements comprising the material can be identified and quantitatively measured based on the atomic emission intensity [12]. Typical/commercial applications of LIBS are metal

identification and quantification in soils, rocks, and scrap metal [13, 18]. Interestingly, many of the biomolecule labels in immunoassays are also metals. Since LIBS can be designed for sensitive, quantitative and multiplexed detection of metals in rock, soil or scrap, a reasonable inquiry is whether LIBS can be applied to detection of biomolecule labels in immunoassays/immunoassay analysis.

LIBS is a material characterization technique and has been applied to the study of biology in a variety of ways. A promising venue of study is the application of LIBS to bioassay analysis, particularly bioassays that use biomolecular tags/labels with elemental compositions unique to a biological matrix. Interesting studies in this respect were performed by Yuri Markushin and Nouredine Melikechi [25, 27]. As discussed earlier, metals can be used to tag bio-molecules. Markushin and Melikechi took advantage of bio-conjugation with metal particles to detect cancer biomarkers using LIBS. The authors term this system Tag-LIBS. In a study published in 2015 [25], the authors used titanium and iron particles functionalized with antibodies targeting cancer-related antigen protein CA-125. Antibodies conjugated to titanium particles targeted one area of the protein, while those on the iron particles targeted another. If the antigen and both particles were present, the three components formed an antigen-titanium-iron complex. The complex was isolated and rinsed using magnetic separation to remove unbound titanium particles. The particles were applied to the surface of a filter, using vacuum suction to promote even distribution of the sample. The surface of the filter was then analyzed using LIBS. If the LIBS signal reported only iron particles, the antigen was absent from the sample. If both iron and titanium signals were reported, the antigen was present. The sensitivity of this method proved to be greater than that of conventional ELISAs for detection of CA-125 (estimated Tag-LIBS sensitivity: 0.01 U/ml; ELISA: 5 U/ml). LIBS detection was performed with a 150 fs pulsed 775 nm laser with a pulse energy of 1.6 mJ in an air environment [25]. In 2009 and 2012, similar studies by the same authors were performed using 3 μm silicon and 1.5 μm iron particles targeting different regions of CA-125 as well as other cancer-related biomarkers [27, 26]. Detection limits of 1 U/ml (for CA-125) in a blood matrix were achieved using 50 nm antibody-functionalized gold nanoparticles and 1.5 μm antibody-functionalized iron microparticles [27, 26]. The research on Tag-LIBS was accompanied by two patents released in 2011 and 2018 for LIBS analysis of bio-conjugates and membrane-isolated particulates [68, 69]. The studies discussed above were among, if not the first, published

materials describing LIBS analysis of tag-based bioassays. Since then, several additional studies were published using similar techniques [23, 70, 71].

In a review article Markushin and Melikechi mentioned biotag options other than gold, iron, titanium, and silicon (platinum, aluminum, copper, nickel, zinc, tin, and copper) [27], but studies have not yet been reported indicating their use, or the ability of LIBS to perform multiplexed detection using a broad panel of metal bio-tags.

The use of LIBS for analysis of portable paper-based bioassays, like lateral flow immunoassays (LFIAs) or vertical flow immunoassays (VFIAs), is a relatively unexplored niche. This application space is particularly interesting since a wide variety of paper-based bioassays already use metals (lanthanides, gold, iron, silver, silicon, zinc, and cadmium) for antigen detection, and LIBS is a tool for quantitative, and multiplexed detection. Metal tags that are not applied to paper-bioassays, but could be used with LIBS analysis, are those already used for mass cytometry. Metal tags applied to mass cytometry include the lanthanide series (La, Pr, Nd, Sm, Eu, Gd, Tb, Dy, Ho, Er, Tm, Yb, and Lu), gold, silicon, iron, silver, titanium, indium, bismuth, and quantum dots (Zn, Cd, and Si). If LIBS sensitivity of analytes on paper-like material could achieve 0.01 U/ml as identified in the Markushin and Melikechi 2015 study, then the use of LIBS for detection of biohazards in paper-based immunoassays would be promising – especially considering opportunities for multiplexed detection.

1.4.2 Major Challenges in LIBS Analysis of Biological Samples

In the biological realm, LIBS has not just been applied to the analysis of immunoassays. The literature demonstrates applications of LIBS as an analytical tool for studies in environmental health, food quality, forensics, clinical sample analysis, bacterial identification, and more [12]. Although these areas fit under the umbrella of LIBS applications in biology, the challenges faced by analysis of biological samples and the nature of the LIBS field result in a large diversity of methods for sample preparation, instrumentation, sampling methodology, and data analysis techniques [72]. Understanding the challenges and advances made in LIBS detection of biological contaminants in food, water, and soil can lead to further innovation [73-75].

In the field of LIBS, sample physical properties play a significant role in the performance of the system. Some LIBS analyses of food products utilize unprocessed/minimally processed

material – for example, the surface of fruits [76], meats [77], and bacterial cultures [78, 75]. While sample analysis is ideally performed without any modification to the sample, the diversity and complexity of biological material makes sample preparation a necessity in many cases [75]. The presence of water in most biological samples poses an additional challenge [79]. There is an advantage in drying and pelletizing samples, as demonstrated in many studies. This process removes water and compacts the material, which is favorable for laser ablation [80]. Alternatively, particulate samples are sometimes loaded onto a thin layer of glue or double-sided tape to hold the sample in place during ablation [81]. Owing to the small sampling areas of LIBS, inhomogeneities in the sample can result in large variation in results. Therefore, milling is often applied to homogenize samples before they are compressed and analyzed. Liquids like milk and wine are a challenge for LIBS because emissions are typically less intense and have short life-spans [18, 79, 81]. In addition, ablation causes splashing, formation of aerosols, and bubbles that negatively influence emissions [18, 79, 81]. To analyze liquids, many studies dry the liquid onto a solid or semi-solid matrix or membrane, removing the difficulties caused by splashing [81]. Examples of matrices are collagen gels [82] or paper-like material [83, 84]. Filter and nitrocellulose papers are often used for paper-based assays; however, limited research has been published regarding LIBS analysis of paper-based bioassays.

To properly apply LIBS to analysis of biological material, it is useful to understand the principles guiding LIBS. In this dissertation, the objective was to apply LIBS specifically to the analysis of biomolecules labeled with metals on an immunoassay platform. The following section reviews LIBS fundamentals.

1.5 Laser-induced Breakdown Spectroscopy

The production of electromagnetic radiation by atoms in strong electric or electromagnetic fields has fascinated scientists since the early 1800s. It was soon noted that the optical emissions produced when electrons are energized to $>10\text{eV}$ [85] are characteristic to the elemental composition of the material [86-89]. This observation led to a field of science that utilized atomic spectral analysis for qualitative and quantitative material characterization. The principle of spectral emission spectrochemistry has been applied to determining the chemical composition of stars, environmental health monitoring, forensic science, and many other fields [86-91].

The utility of atomic-emission generation, detection, and characterization tools prompted a continuing evolution of instruments that utilize various combinations of lasers, spark-generators, spectrometers, CCD cameras, and a slew of other instrumentation. A method that demonstrates promise as a low-cost field-deployable analytical tool is laser-induced breakdown spectroscopy (LIBS)[86, 92, 93]. LIBS is a sample characterization technique based on the production and analysis of the fourth state of matter – ionic plasma. Plasmas produced during LIBS emit complex optical emissions consisting of a continuous background spectrum and discrete line emissions representative of the elemental components of the sample.

Although LIBS instruments are not yet widely commercialized, they are a fascinating area of research based on their unique commercial potential as low-cost, fast, multiplexed, field-deployable instruments with a wide range of applications [94, 95]. The application most relevant to this review is detection of heavy metal–labeled biomolecules with the broad scope of biohazard detection. Owing to the wide variety of parameters that influence plasma formation, the literature presents a wide array of LIBS designs that try to optimize the technique for the intended application. Hence, an “optimal” design does not exist unless in reference to a specific application. Few designs have been proposed in the literature for the detection of metal labels on a paper-immunoassay platform. Designing such an instrument requires an understanding of the mechanisms of plasma formation and optical emissions. This review aims to describe the major parameters influencing plasma formation and emission, and explores designs used throughout the literature to create a theoretical model of a LIBS instrument capable of sensitive detection of heavy metal–labeled antibodies.

1.5.1 LIBS Plasmas: formation and influential parameters

When a high-energy laser pulse is applied to a solid substrate, the atoms in or near the path of the energy pulse are heated. If the heating is sufficient, the pulse is followed by a visible flash and popping sound generated by the rapid expansion of hot material and air. The expanding ionized gas is plasma, the fourth state of matter. The fraction of material that reaches the plasma-electron temperature threshold ($\sim 10\text{eV}$) forms a plume along the energy pulse path [96, 86]. Based on the spectral emission properties of the plume, one can characterize the composition of the source material. The nature of plasma formation and emission detection is highly dependent on certain parameters: (i) mode of induction, (ii) pulse duration, (iii) repetition rate, (iv) laser wavelength, (v)

time of analysis, (vi) environmental temperature, pressure, and atomic composition, (vii) physical properties of the substrate, and (viii) spatial distribution of the plasma [90, 97-99, 94, 100, 96]. The effects of these parameters on plasmas can be explained by the physical principles of thermal and non-thermal energy absorption and dissipation over time [101]. This section will address each parameter and the temporal process of energy absorption and radiation.

1.5.2 Mechanisms of LIBS Plasma Formation

During a single LIBS laser pulse, the material being ablated undergoes a complete transformation from solid, to liquid, to gas, and finally to plasma. Since nanosecond (ns) pulses are most commonly used for LIBS, the following describes the complete process of plasma formation for this type of pulse.

During a ns laser pulse, non-thermal and thermal effects guide the ionization process, but the latter dominates [102, 103]. In the first 100 femtoseconds (fs) of the laser pulse, non-thermal processes guide electron excitation: photon energy is first absorbed by electrons in the outer atomic orbitals through photon absorption [99]. If sufficient energy is absorbed, loosely bound electrons dissociate from the atom, forming free electrons and ions. Multi-photon ionization and avalanche ionization promote further excitation of electrons, increasing electron temperature [102]. This process occurs more easily in conductive materials, such as metals, which have loosely bound electrons [104]. The free electrons collide with surrounding particles, providing energy to the lattice through conductive heat transfer after 10 picosecond (ps) of laser irradiation. This generates more ions and free electrons [85]. Collisions between atoms, ions, and free electrons create randomized electron motion resulting in an increase in electron temperature. By 100 ps, thermal effects predominate and melting occurs, accompanied by a continuing increase in electron temperature, ablation, and plasma formation [99]. Plasmas produced by LIBS are weakly ionized, meaning that the ratio of free electrons to other species is less than 10% [105]. Applying more energy to the system yields more highly ionized plasma; however, the plasmas discussed in this paper are only weakly ionized. Whereas some electrons in the plasma become free electrons through radiative heat transfer, others remain associated with the atom and are elevated to a higher energy state. As they return to the ground state, they emit a photon with energy proportional to the discrete jump between states. Although the system during laser ablation is dominated by energy absorption, energy is constantly released as thermal and optical radiation [85].

In the system described above, electron and photon energy gain and release can be described by several terms that are important for understanding the literature. *Bremsstrahlung radiation* describes the process of radiative energy release by electrons during deceleration after collision with another particle [85]. Bremsstrahlung radiation persists as long as free electrons are present in the system and consists of a continuous emission spectrum. This continuum is considered background during LIBS spectral analysis [104]. *Inverse bremsstrahlung* describes the process of electrons absorbing photon energy, accelerating, and increasing in electron temperature as their motion is randomized through collisions with surrounding atoms [106]. Inverse bremsstrahlung persists for the duration of laser excitation.

From the perspective of photon interaction, energy exchange can be described by absorption, self-absorption, and quenching. When a photon collides with an electron bound to an atom, the photon is *absorbed*, meaning that the electron moves to a higher energy orbital, creating an excited atomic state. Absorbed energy can be released as kinetic energy when the excited atom collides with another particle [85]. In this *quenching* process, the electron returns to its ground state without emitting radiation, while the other particle gains kinetic energy. Absorbed energy can also be released as a photon by an excited electron returning to the ground state [107]. Photons emitted in this process are identified as having a specific frequency, termed *line emission*, and a longer lifetime than background emissions. When a plasma emission spectrum is analyzed, line emissions are critical for determining the atomic composition of the plasma [107]. If the path of the photon to the detector is obstructed by other particles, line emission is not detected because of self-absorption. During *self-absorption*, the photon is absorbed by the atom and re-emitted at a different frequency. If this process continues to repeat, a continuous spectrum is detected [108]. As a result, the density of particles in a plasma has an effect on the degree self-absorption. Because the type of emission produced during self-absorption is considered background, *optically thin* (low-density) plasmas are preferred over those which are *optically opaque* (high density) [108, 109]. Optically thin plasmas can be created by increasing plasma volume by decreasing environmental pressure while maintaining the amount of ablated mass constant[12].

1.5.3 Effects of LIBS Laser Characteristics on Plasma Formation: pulse width, wavelength, repetition rate

Laser Pulse Width

Typically, lasers used for LIBS provide irradiance levels from 10^9 to 10^{13} W/cm²[94]. Two- to 10 ns pulse widths with Nd:YAG (neodymium-doped yttrium aluminum garnet; Nd:Y₃Al₅O₁₂) 1064 nm lasers are common throughout LIBS literature, each pulse delivering 20-200 mJ depending on the LIBS system [102, 100]. Femtosecond (fs) and picosecond (ps) pulsed lasers are becoming more common in the LIBS literature owing to their decreasing cost and unique effects on the resulting plasmas – some studies indicating higher signal-to-noise ratios. However, complications of utilizing femto- and pico-second lasers include complexity, power demands, and operational skill [110, 99, 88, 85]. Significant differences exist between the nanosecond (ns) laser ablation process described above and ablation by fs and ps lasers. Fs and ps energy dissipation is primarily non-thermal [99, 102, 85], and ablation is mostly the result of Coulomb explosion [111, 112]. Coulomb explosion during fs and ps pulses occurs when a high density of electrons above the area of irradiation pulls ions out from the sample, leaving behind a uniform, circular crater. The ability of fs and ps pulses to yield precise craters improves repeatability between experiments [113, 114]. Although line-emission intensity is greater for ns pulses, they also yield irregular craters, compromising repeatability[115]. Accuracy in representing the stoichiometric composition of the matrix material is also improved for fs and ps pulses because ablation is not as dependent on the matrix properties for thermal diffusivity [116, 117]. This aspect of sample composition will be discussed in more depth later. Improved accuracy is also attributed to minimized ionization of the gas surrounding the material. Unlike fs or ps lasers, ns lasers continue to ablate the sample after plasma formation (100 ps). Therefore, a fraction of energy during an ns pulse is absorbed by the sample, while another fraction is absorbed by the emerging plasma through inverse bremsstrahlung (IB) [94]. IB slows the cooling of plasma and can enhance the plasma emission intensity and longevity by providing excited electrons with more energy. However, IB also increases the background emission continuum, obscuring line emissions [116, 118]. The role of IB in ns plasma formation introduces an important consideration: since the plasma lifetime for fs and ps LIBS is shorter than for ns LIBS owing to minimal or no IB, the delay time between the laser pulse and optimal line-emission signal collection is shorter (<1μs) for ps

and fs pulses than for ns pulses ($\sim 1\mu\text{s}$) [99]. Since ns lasers are most common for LIBS applications, the following sections refer to ns lasers unless otherwise stated.

Laser Pulse Repetition Rate

For experiments utilizing multiple laser pulses on a single area, there exists an optimal timing between material ablation with the first pulse and re-heating with subsequent pulses. The timing depends strongly on the nature of the substrate, since some substrates, such as powders, ablate more easily than others, such as metallic foils [100]. When a powder is ablated, the aerosolized debris blocks the second pulse until the debris re-deposits or is removed. This feature may also be the case with delicate porous substrates like nitrocellulose. Though a 10-Hz repetition rate is common in the literature, some studies use lower pulse repetition rates (1 Hz) to allow for debris deposition-[100, 94]. To remove debris, a continuous flow of gas positioned parallel to the sample surface can also be used [12].

Laser Wavelength

Wavelength is a critical parameter that influences plasma emissions. This section describes the effect of wavelength primarily for ns pulses. When comparing long (1064-nm/IR) and short (355 nm to 532 nm/UV) wavelengths, significant differences can be observed in ablation volume, plasma stoichiometry, signal intensity, standard deviation, and background signal [85, 89, 119]. Generally, short-wavelength lasers contain more energy per pulse than long-wavelength lasers. Whereas IR lasers excite electrons primarily through avalanche ionization, UV lasers do so primarily via multi-photon excitation [85]. As a result of the higher-energy photons, samples irradiated by UV lasers heat and ablate more quickly than those irradiated by IR lasers [119]. Differences in ablation rate in response to laser wavelengths are also dependent on material properties, as will be discussed in one of the following sections. Though IR wavelengths ablate a smaller mass, limiting plasma emission intensity, they are also preferentially absorbed by plasma via IB. The IB process during an IR pulse re-excites electrons and promotes the persistence and expansion of the plasma as compared to UV laser pulses. Even so, it has been found that there is equivalent electron density when comparing plasmas produced by IR and UV wavelengths[120,

89]. Owing to the effects of IB, IR lasers induce emissions that display higher signal intensity, background, and standard deviation compared to those from UV lasers[89].

Plasma stoichiometry also varies significantly between laser wavelengths [89, 119]. Over the course of multiple laser pulses, both IR and UV lasers create craters in the substrate. Even when substrate composition is uniform, the stoichiometry of the plasma created by IR lasers changes with depth. This effect is also observed with UV lasers, although the correlation between depth and plasma stoichiometry is significantly weaker [119]. Though a concrete explanation for this effect was not given in the cited study, the results suggest that IR wavelengths may not be best for depth profiling or repeated sampling of the same area.

1.5.4 Effects of Environmental Conditions and Substrate Composition on LIBS Plasma Formation

The environmental conditions surrounding the plasma plume as well as the substrate type have a significant effect on optical emissions. Variations in sample temperature, environmental pressure, and air composition impact signal intensity, limits of detection, and signal-to-noise ratio [102, 121, 122, 97].

Pressure

Studies have explored the option of utilizing a pressure chamber around the substrate to control plasma expansion and persistence. As pressure increases from vacuum to atmospheric, plasmas become smaller (~10 mm to ~2 mm diameter for ns pulses) and denser [122, 102]. These effects lead to an interesting trend in plasma line-emission intensity, which is observed to peak around 100 Torr in air [94]. On the high end of the pressure spectrum, low line-emission intensity can be explained by the increasing plasma opacity and susceptibility to IB. The collision rate between free electrons, atoms, and ions increases with denser plasmas, increasing opportunities for self-absorption [122]. Heat also dissipates faster in higher-pressure environments [122], leading to more rapid emission decay and reducing the window during which meaningful line emissions can be obtained [121]. The higher density of particles in the system also increases background by promoting IB in the plasma. The resulting increase in background is also produced by the gas surrounding the sample, which creates its own emission separate from those originating from the sample plasma. At low pressures, an opposite effect is seen that also yields lower emission

intensities. Lower pressures yield diffuse plasmas. If particle density is too low, the decrease in collision rate reduces the number of excited particles. In addition, the number of recombination events between electrons and ions is reduced. In sum, these effects lead to dim line emissions [121, 102]. As with most other parameters, there is an optimum pressure at which to conduct LIBS. Studies have determined that in air, approximately 100 Torr yields the best line emissions for metallic-foil samples [121, 94]. It is important to note that the phenomena described apply primarily to ns lasers, since ps and fs laser pulses are too short to significantly affect environmental gas, plasma heating, and heat dissipation in the substrate [121].

Gas Composition Around Sample

The effects of pressure on a plasma plume are correlated with environmental gas composition. Changes in the gas atomic mass and ionization energy can affect the plasma volume, persistence, and intensity [121]. Three common gases used in LIBS are helium, argon, and air. He is characterized by a relatively low ionization energy, low atomic weight, and high thermal conductivity; Ar has a higher ionization energy and atomic mass than He, but is a poor conductor; air has higher ionization energy than He and Ar, and atomic-mass and thermal-conductivity values are between those of He and Ar. A study by Yasuo Iida (1990) examined the influence of different gases on line emission at various pressures. At atmospheric pressure (760 Torr), He environments yielded a higher line-emission intensity than Ar or air environments. At pressures below atmospheric, Ar environments yielded consistently higher line-emission intensities. Overall highest line emission was observed at 100 Torr in the Ar gas environment. This phenomenon can be explained by Ar's ability to sustain the plasma by insulating the plume and creating higher electron densities [122]. A disadvantage of insulating environments is that they contribute to broader emission lines, and therefore lower spectral resolution [123]. At higher pressures, He environments may be more beneficial for producing strong line emission than are Ar environments because Ar's high atomic mass prevents plume expansion and formation of optically thin plasmas [122, 91].

Substrate Type

The material that composes the sample plays a strong role in plasma dynamics. This is attributed to differences in conductive properties and compactness of the sample. As previously discussed, the association between atoms and their electrons has a strong influence on plasma formation. Metal atoms have loosely associated electrons and form plasmas more easily than insulators or semi-conductors [104]. Most LIBS studies applied to soil sciences use soil pellets as the sample. Pellets are made by adding a certain amount of adhesive (for example mixing 5 g lime with 0.8 ml of 2% wt polyvinyl alcohol) and compressing the material in a mold using 24-MPa [124]. The purpose of compressing samples into pellets is to prevent the material from scattering during an ablation pulse and becoming an aerosol that blocks further ablation. The amount of aerosol that forms is dependent on the size and density of the soil particles. For example, sand does not aerosolize as easily as smaller particulate dust [100]. The strength of binding between soil particles also has a significant effect on plasma formation. A study that incrementally increased the amount of binder to form pellets observed that there is a correlated increase in signal intensity and decrease in standard deviation, possibly due to reduced material scattering [124]. It was also noted that pellets that contained less water yielded lower standard deviations [124, 125]. It is possible that porous membranes like nitrocellulose paper behave similarly to powders.

A few studies have also investigated the effects of heating a sample on optical emissions. It was found that samples heated up to 150 °C have higher ablation volumes, which contribute to greater signal intensity and lower limits of detection [126]. However, changing the temperature of the substrate also changes the stoichiometric composition of the plasma. This effect depends on the volatility of the elements composing the sample. It was also observed that higher substrate temperatures create a low-pressure zone at the surface of the substrate, promoting ablation, plasma expansion, and enhancement of emission lines [127].

1.5.5 LIBS Plasma Morphology

Plasma shape and the distribution of elements in the plume affect the nature of line emissions produced during LIBS. In general, plasma plumes have a balloon shape that can be extended up to 10 mm along the laser path (z axis) and be 10 mm in diameter perpendicular to the laser path (x and y axes) in low-pressure environments[128]. Plasmas between 2 and 10 mm are

desirable for LIBS because they are less optically opaque and fit the specifications of most light-collection optics [94]. Plasma morphology is affected by lenses, pulse energy, and environmental and sample composition.

Lens Effects

Spatial distribution of laser pulse energy has an effect on the formation of the plume. In a study by Bulatov et al., lenses were used to control the spatial distribution of the laser above the sample surface. Short focal length lenses ($f = 150$ mm) broadly distribute the laser energy before densely accumulating it at the focal point. In comparison, long focal length lenses ($f = 1000$ mm) have a higher concentration of energy prior to the focal point. Both extremes yield undesirable results. Short focal length lenses generate small and hot plasma plumes because the high laser-energy density at the focal point rapidly diffuses along the x, y, and z axes. Long focal lengths have “taller” plasmas because the change in energy density is more gradual along the z axis. Under these conditions, the laser interacts with the surrounding gas above the sample. Owing to the high energy density above the sample surface, the interaction between the laser and the gas creates a shield of ionized gas that diminishes the amount of laser energy that reaches the sample surface. Based on the study of these effects, Butalov et al. found that the optimal lens for LIBS has a focal length of 400 mm because it appropriately balances the advantages and disadvantages of long and short focal lengths [94, 129]. Most LIBS studies keep the substrate slightly out of focus to irradiate a larger surface area and sample more material. In addition, most studies prefer longer focal lengths because exact positioning of the substrate along the z axis is not as critical, and possibly because lens contamination by the ablated material is not as severe [130].

Laser Power

The laser power incident on the sample surface also has an effect on plasma morphology. In an early study where the authors used a ruby laser at relatively low power (850 μ s pulse at 1 MW/cm²) on an aluminum-foil sample in air, a plasma was generated that extended past 10 mm above the sample surface. This power regime produced low-intensity background and line-emission signals. At medium power, (10 MW/cm²), line emissions could be detected up to 4 mm above the sample surface. At high power (4000 MW/cm²) the background signal was too intense

to detect line emissions [128]. A similar study using a KrF excimer laser (248 nm, pulse width 30 ns) on a copper-foil target in an argon environment yielded similar results. Copper line-emission intensity increased and decreased along the z axis, the peak being 1.5 mm from the sample surface [131]. Generally, line-emission intensity increases and then decreases along the z axis with a few local maxima, depending on the element. When temperature distribution in the plasma is examined, the hottest zone is found closest to the sample surface, below the area of highest emission intensity [131, 94]. Another study examined the difference in plasma morphology between ns and fs lasers and found that fs pulses expand primarily along the z axis rather than the x-y plane, whereas ns plasmas expand evenly in all directions. The directed expansion of fs pulses was speculated to be due to the strong self-generated magnetic field [102].

Sample Composition

The location on the z axis of highest line-emission intensity is dependent not only on laser energy but also on the elements comprising the plasma. Elements with lower melting points are dispersed farther along the x, y, and z axes than those with higher melting points. For example, in a comparison between copper and lead foils, it was found that high signal-to-background ratios for lead can be found 5 mm above the sample surface, and for copper 2 mm above the surface [132]. Differences between element distributions in plasma can be observed in other studies as well [133, 134].

1.5.6 SIBS Plasma Formation and Emission

Though this dissertation focuses primarily on LIBS, one of the key aspects of the application of LIBS is low cost and portability. For this reason, a technique similar to LIBS, spark-induced breakdown spectroscopy (SIBS), is also considered because it lends itself to a more portable and low-cost design. SIBS and LIBS differ in the types of plasmas and emissions they form such that the principles of one may not always apply to the other. The primary differences exist in the mechanisms of plasma formation and the time-scale of emissions.

The energy pulsed by a SIBS system is comparable to that of LIBS (60-300 mJ). However, a SIBS pulse lasts significantly longer than a LIBS pulse – a LIBS pulse is on the ps, fs, or ns scale depending on the laser, whereas a SIBS pulse is approximately 15-20 μ s in air [135]. It was

previously mentioned that the effect of a ns pulse is significantly different from that of a ps or fs pulse because the ns pulse allows time for heat to diffuse through the substrate, resulting in a larger ablation volume. SIBS pulses persist for much longer, allowing even more time for heat to dissipate throughout the sample. As a result, SIBS has larger ablation volumes than LIBS [94]. As with LIBS, higher SIBS pulse energy yields more ablated material and stronger emissions. It was observed that as pulse energy increased from 50 mJ to 200 mJ, the signal-to-background ratio increased and then plateaued, indicating that more power yields higher emissions, but not necessarily better signal-to-noise ratios [135]. For the study cited, 150 mJ yielded the best signal-to-background ratio, and created a plasma with a temperature comparable to LIBS (6500-7000 °K) [135].

Whereas LIBS generates ions using an electromagnetic field, SIBS uses an electric field. When a few thousand kV are applied to opposing electrodes, electrons transition to higher energy states at the anode and the gas environment between the electrodes is ionized. As electrons accelerate towards the grounded electrode (cathode) an ion channel is formed [136]. Over time, the ion channel expands laterally [137]. When energized electrons in the channel collide with the cathode or a substrate in between the electrodes, electron energy is transferred into the solid material, ionizing the material and increasing the kinetic energy of the system. With sufficient energy, the solid material ablates and an ionic plasma expands radially. In this system, two types of plasmas exist: one originating from the central ion channel, and the other from the solid material [137]. When in air, the voltage pulse lasts approximately 15-20 μs (in soil samples a 4- μs pulse was reported [86]) [135]. After 30 μs , the plasma comprising the ion channel mostly dissipates, and the plasma originating from the substrate radially expands and persists for at least 50 μs after pulse initiation [135]. The substrate plasma in air has a volume of up to 0.07 cm^3 [86], considerably larger than most LIBS plasmas [101]. Line emissions important for substrate characterization are found in the lower-temperature plasma originating from the substrate and not from the high-temperature central ion channel. The plasma from the ion channel instead contains significant background since it is formed primarily by particles in the gas environment [135]. Part of the background originates from the electrodes, also indicating that the electrodes degrade over time. However, it has been shown that electrode degradation over the course of repeated pulses does not cause large variation in the signal (2-17%)[135].

Similarly to LIBS, SIBS applications are primarily in detection of heavy-metal contaminants in soil and air [86, 135]. Though the process of SIBS plasma formation has been described for gaseous samples, studies on solid samples are not as abundant. Compared to SIBS, LIBS offers the advantage of higher signal-to-noise ratios, lower standard deviations, no need for conductive samples, and greater control of the energy source [98]. Although a SIBS energy discharge has little variation (~2%), the sampling location, trajectory of the ion channel, and trajectory of the ablated material are unpredictable and difficult to control [136]. Even so, SIBS offers the advantage of producing stronger emission lines, which may be beneficial for designing a system with a low limit of detection (SIBS detection limits are a few hundred ppm to ppb to ppm; LIBS detection limits are 1 ppm-100 ppm) [138, 95, 139-141]. SIBS also eliminates the complication of laser focusing optics and laser alignment, and offers greater pulse energy per unit of physical size [135]. However, the large standard deviation observed in SIBS makes this detection modality less amenable to quantitative studies. Whereas some aspects of LIBS and SIBS are comparable, sensitivities are difficult to compare because few studies investigate both systems simultaneously [98]. Whether one or the other is applied to a certain application depends on the application goals.

LIBS and SIBS Instrumentation and Configuration for Optimal Sensitivity During Solid-Substrate Analysis

Configuration of LIBS and SIBS instrumentation varies significantly throughout the literature. Each design optimizes multiple parameters (pulse energy, environmental pressure, etc.) to achieve the quality of results needed for the intended application. Owing to the variation in the literature, it is noted that the optimal SIBS/LIBS instrument cannot be described unless referring to a specific application [99]. The studies presented in this section have been selected because they propose instruments capable of sensitive detection of heavy metals in soil or metal alloys. This section starts with a description of excitation sources followed by materials used to direct the energy to the sample and spatial and temporal arrangement of excitation sources.

Current Instrumentation for LIBS, SIBS, DP-LIBS, and SA-LIBS

Excitation sources:

The excitation source for LIBS has mostly been described throughout the text. In summary, typical excitation sources are Nd:YAG lasers and krypton fluoride (KrF) excimer lasers. Albeit rarely, transversely excited atmospheric (TEA) carbon dioxide (CO₂) lasers are also used for LIBS [142, 143]. Typical wavelengths are 1064 nm, 532 nm (both Nd:YAG), 248 nm (KrF excimer), and 10.6 μ m (TEA CO₂). Pulse widths vary from the fs to the ns range. Depending on the application, repetition rates are typically 10 Hz, and pulse energies range from 60 to 200 mJ [103]. Critical components of the SIBS excitation source are the power supply, capacitor, and electrodes. A transformer opens an ion channel by delivering a high-voltage, low-current pulse (15-40 kV). This event significantly reduces the resistance and impedance of the spark gap. A capacitor (~6 nF) charged with a high-voltage power supply (<2000 V, 100 J/s) then discharges energy (200 mJ-5 J) into the gap [86, 140]. Spark generators can either be made in-house or be purchased commercially, such as the Firefly High Power Pulse Generator by Cascodium Inc. (Andover, MA, USA).

To control environmental parameters involved in plasma formation during LIBS and SIBS, some studies use a controlled pressure chamber attached to a supply of air, argon, or helium gas. An alternative method that does not require a chamber involves supplying the sample surface with a laminar flow of gas, ~0.2 5 L/s. This method aids in eliminating aerosolized debris and reducing the degree of laser shielding during subsequent pulses [144, 122].

In LIBS, a series of dichroic mirrors can be used to direct the laser beam to the focusing lens. Focusing lenses commonly used for LIBS are convex, have a diameter of 25-50 mm, and a focal length between 50 and 150 mm. Advantages of using a 50-150 mm focal length (rather than 400 mm as mentioned in a study earlier) is simplicity in laser path design. Lenses typically feature anti-reflective layers to reduce energy loss and have maximum transmission at the laser wavelength [103]. In SIBS, rod-shaped electrodes are used to direct the energy pulse from the capacitor. The spacing between the electrodes is typically 5-6 mm. This distance was determined to be the maximum at which a spark can be reproduced [94] and is common throughout the literature. The material composing the electrode is selected to be resistant to corrosion and ablation, have a high melting point, and consist of elements uncommon to the sample [86]. Electrodes are typically made out of pure tungsten, thoriated tungsten, or graphite [145, 135, 98]. Electrode

shapes are rod-like with diameters that range from 200 μm with a 5- μm pointed tip, to 500 μm with a flattened end, to 3.2 mm with a hemispherical tip [146, 98, 135]. Though at least one study has been conducted on the effect of electrode size and composition on plasma emission, the results are limited to the field of metal detection in aerosols [146]. However, it can possibly be inferred that a larger diameter decreases the reproducibility of the spark because it permits a larger variety of spark trajectories. To improve reproducibility, some studies use a washer made from an insulating material to cover the electrode, leaving only a small area at the tip exposed. A similar strategy involves placing an insulating sheath around the entire electrode except the very tip [135]. The electrodes can be angled towards each other, their ends either placed in the sample or 2 mm above the sample [86, 138]. Electrodes can also be opposing each other, with a conductive or semi-conductive sample between the two ends. In one study using this configuration, the sample was placed directly on the flattened end of the cathode [135].

SIBS and LIBS configurations:

Of the multiple configurations used for SIBS and LIBS, single-pulse laser- and spark-induced breakdown spectroscopy (SP-LIBS) (SIBS) is the simplest and most traditional system to design. Since the development of LIBS and SIBS, combinations of multiple energy sources have been used to improve sensitivity. These configurations can be subdivided into three main categories: collinear double-pulse LIBS (DP-LIBS), orthogonal DP-LIBS, and spark-assisted LIBS (SA-LIBS).

Two types of geometries are commonly used for DP-LIBS. Collinear DP-LIBS utilizes two or more laser beam pulses whose angle of incidence is normal to the sample surface. Orthogonal DP-LIBS instruments consist of one laser beam whose angle of incidence is normal to the sample surface, and a second laser beam that is parallel to the surface [115, 147]. The laser beam parallel to the surface is focused on an area typically 2 mm above the ablation zone. The reasoning behind these geometries is to provide a mechanism by which to either heat the plasma after the plasma forms or heat the air above the plasma before the plasma forms [115]. In either geometry, efficient plasma heating depends on the wavelength, pulse width, energy, and timing. Studies have found that IR wavelengths are more successful than UV wavelengths as a secondary pulse owing to the phenomenon of IB described earlier [148]. In terms of pulse width, a study by Scaffidi et al. shows that a fs (800-nm) ablative pulse followed by a ns (1064-nm) heating pulse has a 30-fold

enhancement in Cu emission-line intensities compared to other fs and ns pulse arrangements [149]. From the perspective of pulse energy, studies by Rai et al. and Benedetti et al. show that line-emission intensities increase when the energy of the second pulse is equal to or greater than the energy of the first pulse [150, 151]. Whereas each of these studies uses an orthogonal configuration to perform an ablation pulse followed by a heating pulse, others switch the order of the two pulses – the first pulse heats the air above the ablation zone and the second pulse ablates the sample. This process yields free electrons in the gas above the ablation zone such that when the plasma is formed, emissions are enhanced as they encounter the heated region above the substrate [115]. Stratis *et al.* found that the use of a pre-plasma heating pulse on a copper foil yields a 33-fold higher line-emission intensity compared to SP-LIBS [152].

Timing is an important component of DP-LIBS. In the studies cited above, signal enhancement was observed when the delay between pulses was within a range from several ps to several hundred μ s [147, 115]. For samples such as glass, steel, copper, and aluminum the best delay time was between 5 and 50 μ s. Another study analyzing similar samples along with silicon found the best delay to be several tens of ns [153, 154]. In the DP-LIBS pre-plasma heating study by Stratis et al. the optimal inter-pulse delay for metal foil samples was 2.5 μ s, with no enhancement being observed between 1 μ s and the maximum delay of 20 μ s [152]. Because the range of inter-pulse delay times in the literature is so broad, the optimal delay must be determined on a case-by-case basis [115]. Greater consensus is found regarding data-collection delay times, which typically range from 0.5 μ s to 1 μ s after the last laser pulse [155].

Like DP-LIBS, SA-LIBS also uses a double excitation process, the first pulse being a laser pulse and the second an electrical spark pulse. The typical arrangement involves two electrodes angled towards each other with a 5- to 6-mm gap between the tips. The electrode tips are approximately 2 mm above the sample. The laser is positioned so that the beam hits the sample at a normal angle between the electrodes [156, 140]. In this configuration, the laser generates an ionic environment that reduces resistance between the electrodes. In a study by Belkov et al. the electrical circuit contained a capacitor charged with 4 kV before the laser pulse. Lasing the sample with a Nd:YAG (1064 nm, 180 mJ, 8-ns pulse width) generated a plasma that completed the circuit and triggered the spark discharge from the capacitor. Using the same system, SP- and DP-LIBS were performed as well. Though the SA-LIBS arrangement does not yield additional material ablation compared to SP-LIBS, the signal is greatly enhanced compared to both SP-LIBS and DP-

LIBS [155]. The study attributes the increased intensity to extended time for plasma evolution and greater plasma volumes. Interestingly, laser energy in SA-LIBS had little impact on signal intensity [155]. A concern with the electrical spark process in SIBS and SA-LIBS is plasma reproducibility. Hou et al. found that reproducibility was improved when a partial barrier was introduced around the sample. The barrier was 1.5 mm tall and encompassed the sample with a diameter of 3 mm [157].

1.5.7 Section Summary

This literature review attempts to outline the mechanism of plasma formation and emission in laser- and spark-induced breakdown spectroscopy as it is applied to the detection of heavy metals in solid samples. Based on our experimental studies, it was observed that many parameters influence plasma formation and emission. These parameters include excitation source, pulse energy, duration, and environmental conditions, among others. Researchers fine-tune the parameters to best suit the specifications of their study. After consideration of these parameters, a design for an emission spectroscopy tool was proposed based on a very specific application that required high line-emission intensities and low background. The application involved detection of metal-labeled biomolecules. By designing a LIBS instrument for biohazard detection, our group is addressing needs in the fields of biodefense and food security for low-cost, field-deployable multivariate-analysis tools.

2. LIBS SYSTEM DESIGNS FOR DETECTION OF DISSOLVED/SUSPENDED METALS DRIED ON NITROCELLULOSE PAPER

2.1 Introduction

While LIBS systems are available commercially, most are still being built in-house. When acquiring a LIBS system for a specific application, both paths require investigation in several key aspects of a LIBS system: the laser, spectrometer, sample holder/chamber, electronics and software, laser optics, and light collection optics. The choice among the options available for each component can be overwhelming, especially since certain components such as the spectrometer and laser can be a financial commitment (\$30,000 for a laser and \$60,000 for a spectrometer). Through the process of investigating six LIBS systems, this study determined that the nature of the sample was the best starting point when designing or purchasing a LIBS system for a specific application. The target application in this dissertation was detection of metal-conjugated antibody labels in nitrocellulose paper-based immunoassays. Six LIBS systems, some built in-house, others commercial, were tested to determine the parameters necessary to detect 1) metals in foils/wafers, 2) metals dissolved in nitric acid and dried on nitrocellulose paper, and 3) metal-conjugated antibodies dried on nitrocellulose paper. The systems are described in chronological order – LIBS System 1 was the first instrument built for the application at Purdue University, while LIBS System 6 represents the final iteration. Over the course of investigating LIBS Systems 1-6, the author gained experience in LIBS design and operation. While not all the LIBS systems described in this document could detect metals on nitrocellulose at the time and in the way they were tested, user experience could have had an effect on the outcome. After gaining four years of experience in LIBS, the author offers retrospective views on each system and its potential for success given certain changes in the design and operation, presented in Appendix A. User experience and data suggest that multiple LIBS parameters should be jointly optimized for the proposed application.

In addition to achieving the desired function of detecting metals on nitrocellulose paper, this investigation also aimed to create a user-friendly LIBS system for general lab use, where experimental parameters could easily be changed, and data collection was fast and automated. In doing so, this system could be not only optimized for the desired application, but also modified to fit the lab's future goals in different application spaces. The final iteration, LIBS System 6, was

designed to serve as a benchmark for future LIBS systems (portable and bench-top) built in our lab for analysis of metal biomolecular labels in paper-based bioassays.

2.2 LIBS System 1

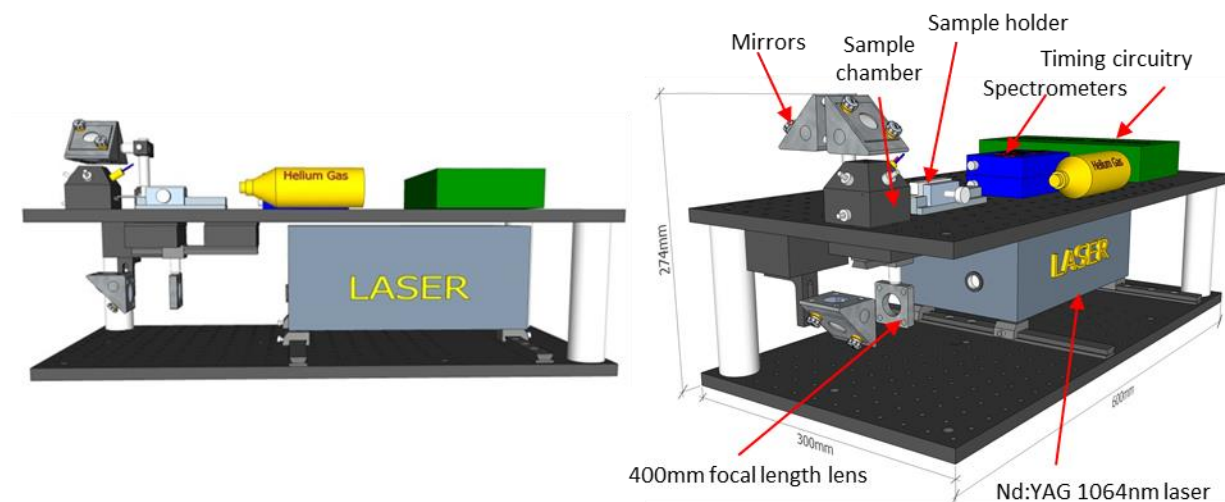


Figure 2.1 Design of LIBS System 1. A 70 mJ pulsed 1064 nm beam was directed to a sample chamber using a series of optics. Plasma emissions were collected by a collimating lens and fiber optics which interfaced with the sample chamber via a SMA connector. Laser water cooler and external power supply not shown.

2.2.1 Laser

An actively Q-switched pulsed laser (SLP-1064-1) was acquired from Chengdu Xinwujieopto Technology Co. Ltd. The system was described by the manufacturer as an Nd:YAG laser producing a 1064 nm beam with a pulse width less than 20 ns, pulse energy of 70 mJ (5% variation), and maximum repetition rate of 5 Hz. The laser came with an external power supply and required an external water cooler. The laser-head dimensions were $28 \times 12 \times 16$ cm and weighed 5.24 kg. Beam quality factor and beam divergence measurements were not provided by the manufacturer. Based on the ablation marks created by the laser, it was determined that the beam was non-Gaussian and had a 5 mm diameter exiting the laser head. For LIBS experiments, a single trigger event generated a single pulse. Triggering of the laser was achieved via a BNC cable connecting the power supply to a custom-made function generator produced by Miftek Inc (West Lafayette, Indiana, USA). The delay between laser triggering and laser firing was

determined to be 96.6 μs with a 2.119 μs jitter. A diagram of how the LIBS configuration is displayed in Figure 2.1 (water cooler and external power supply not shown).

2.2.2 Spectrometer

AvaSpec Mini spectrometers AvaSpec-Mini2048L-U25 and AvaSpec-Mini-VIS-OEM (Avantes, Apeldoorn, the Netherlands) were used for signal acquisition. The Mini2048L-U25 covers the ~ 220 nm to 390 nm range, whereas the Mini-VIS-OEM covers ~ 350 to 600 nm. Both feature a resolution of approximately 0.25 μm and a 2048-pixel Sony CCD array. USB connectors allow data transfer between the spectrometers and a personal computer (PC), while an HDMI connector allowed the spectrometer to be triggered from the custom-made function generator. In triggering the LIBS system, the 3.28 μs internal delay of the spectrometers was accounted for. The AvaSpec Mini spectrometers were compact and light-weight ($95 \times 68 \times 20$ mm, 174 grams), making them a favorable option for a portable LIBS system. The user-controlled integration time (the time over which the CCD array records signal) of the spectrometers ranged from 1 ms to 10 s. For data analysis, spectra from each spectrometer were stitched together by averaging the region of the spectrum from each spectrometer that overlapped, or omitting overlapping data from one of the spectrometers.

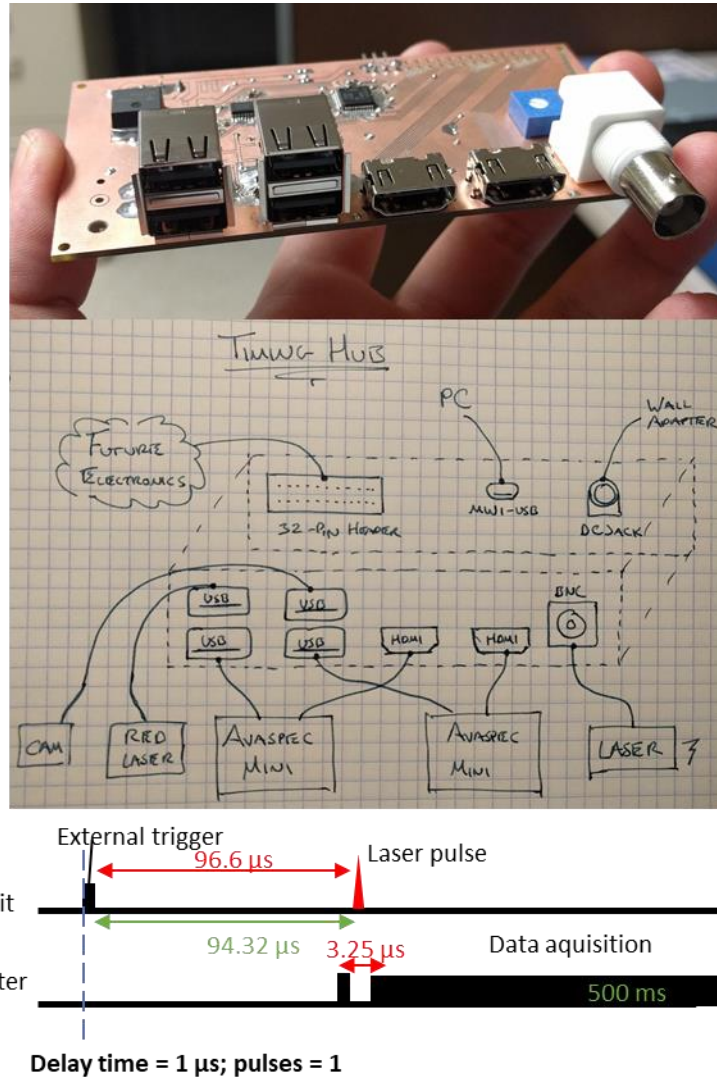
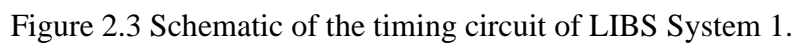


Figure 2.2 Top image: picture of the timing circuit for LIBS System 1. Middle image: Function of each port in the timing circuit. Bottom image: timing diagram. The timing sequence starts with an external trigger pulse sent to the laser from a PC. $96.6 \mu s$ after the trigger pulse, the laser is fired. The internal delay of the spectrometer once it is triggered ($3.25 \mu s$) is considered such that data acquisition begins $1 \mu s$ after the laser pulse. Values in red can be modified by the user, values in green cannot.



2.2.3 Electronics and Software

A custom-made function generator designed and constructed by Keegan Hernandez at Miftek Inc. (Figure 2.2) controlled laser repetition rate and pulse number. A circuit schematic is provided in Figure 2.3. Triggering of the LIBS system was controlled from the custom function generator using a PC and graphic user interface also developed by Miftek Inc. Once the system was triggered from the PC, a TTL signal was sent to the laser and the spectrometers. The timing of the signal sent to the spectrometer was based on the signal sent to the laser. The user could program the spectrometer signal to be sent either before or after the signal sent to the laser. Typically, the signal was sent to the spectrometer 93.32 μs after the signal was sent to the laser, such that spectrometer data acquisition coincided with the laser pulse (calculated by subtracting the internal delay of the spectrometer from the internal delay of the laser; $96.6\mu\text{s} - 3.28\mu\text{s}$) (Figure 2.2). Upon signal acquisition, data from the spectrometers would be displayed in a wavelength vs. intensity plot where the user could quickly assess the results.

2.2.4 Optics

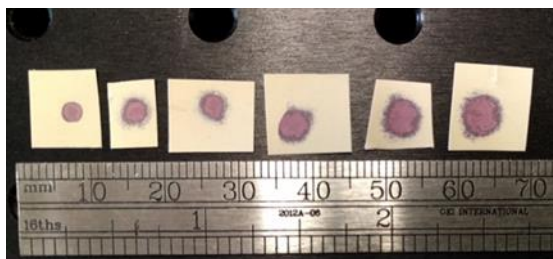


Figure 2.4 Photopaper placed along the path of the laser beam after passing through a 400 mm focal-length lens. The further the beam from the lens, the smaller the ablation marks on the photopaper, indicating beam focusing.

The laser beam was focused using a $f = 400$ mm, 25 mm–diameter lens (33-369, Edmund Optics Barrington, NJ, USA). Using photographic paper, the narrowing of the beam could be observed (Figure 2.4). The ablation marks on the wafer surface placed at the focal point of the beam suggested a non-Gaussian beam profile (Figure 2.5). Whereas most LIBS applications focus a 1064 nm beam to a spot size below 1 mm, the minimum spot size that was achieved with this system was 1 mm. Inability to achieve a smaller spot size could be attributed to either the optics used to focus the beam or the beam profile. Beam quality (M^2) or profile measures were not

provided by the manufacturer, which, along with lack of proper equipment, hindered efforts to identify an explanation for the smallest achievable spot size. Though spot sizes smaller than 1 mm were not obtained, the pulse energy of the laser was sufficient to create a plasma on various material surfaces. While a non-Gaussian beam profile may be appropriate for qualitative LIBS measurements, uneven heating of the sample could result in considerable variability in the data. This concern was supported by an article by Lednev et al. 2013 [158] where multimode beams were shown to produce less reproducible analytical signals than Gaussian beams. The authors of the study hypothesize that the difference is attributed to greater fluence variation of multimode beams and interference effects of sample surface impurities.

For plasma light collection, two UV-VIS fiber optics with a 1mm-diameter fiber bundle (FC-UV1000-1-SR-BX, Avantes) were each fitted with 6 mm collimating lenses (COL-UV/VIS, Avantes). The lens surface was placed 20 mm from the sample surface at a 45° angle. SMA connectors allowed the fiber to connect directly to the spectrometers.

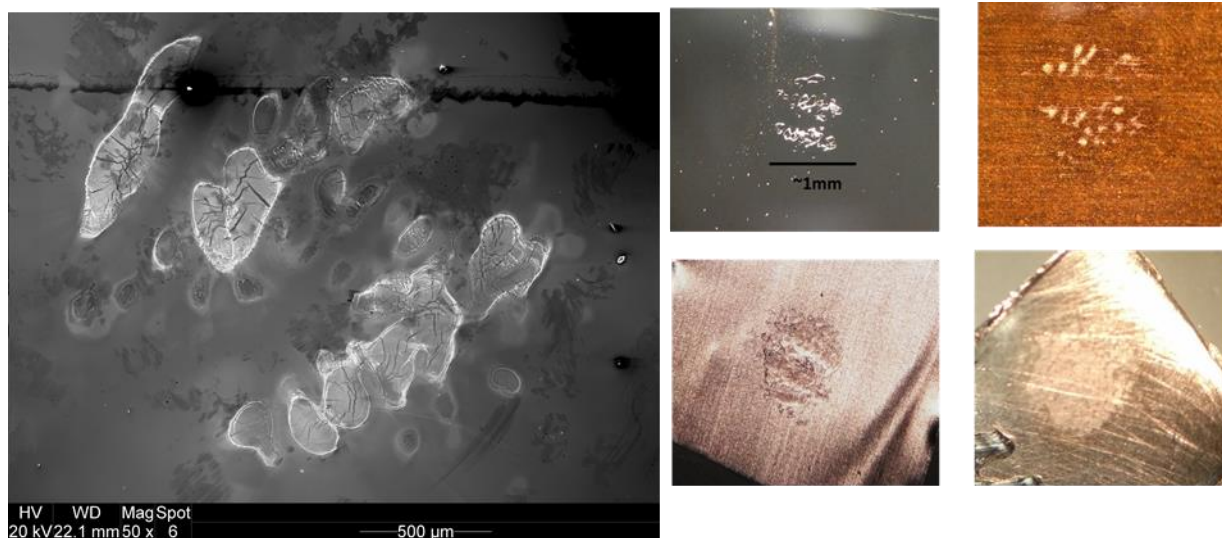


Figure 2.5 Left image, acquired with an electron microscope, represents ablation marks by LIBS System 1 on a silicon wafer. The images on the right (starting clockwise from top left) are stereomicroscope images of ablation marks on a silicon wafer, and foils of copper, aluminum, and nickel respectively.

2.3 Sample Chamber

The sample chamber was designed in SolidWorks (Dassault Systèmes, Vélizy-Villacoublay, France) computer software and printed at the Weldon School of Biomedical Engineering at Purdue University (Figure 2.6). The chamber consisted of two halves. The base was a box with an open top ($43 \times 43 \times 30$ mm). Two opposite ends of the box had a rectangular cut-out (3×5 mm) connected by a rail that would allow the sample holder to enter the box and travel to the opposite opening. The top half was a pyramid ($43 \times 43 \times 17$ mm) with a flat, square top (14×14 mm) having a 5 mm-diameter hole. Each side of the pyramid was designed to interface with collimation lenses or camera. To visualize the sample, an endoscopy camera similar to the 5.5 mm 6 LED Android Endoscope Snake Borescope (GinTai Co.) was used. The intensity-adjustable light-emitting diodes facilitated viewing of the sample by illuminating the chamber interior. The chamber was designed so that the distance between the collimation lenses and sample surface was 20 mm. The 3D-printed sample holder was designed to hold multiple 6×6 -mm samples with a height of up to 2 mm. To move samples, the user would manually slide the sample holder through the chamber as the sample was ablated. The laser beam entered the chamber from the hole at the top, perpendicular to the sample surface.

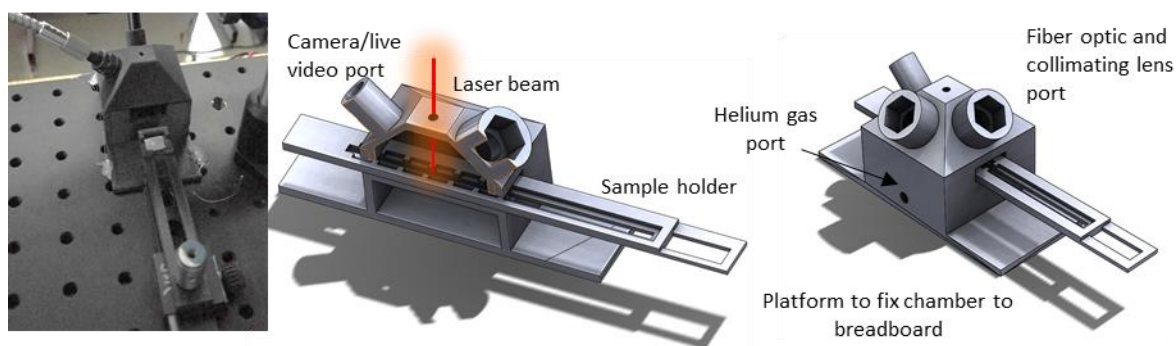


Figure 2.6 A chamber facilitated sample placement in the path of the laser beam while obstructing most external light. Two fiber optics fitted with collimating lenses and a camera were interfaced with the chamber to permit sample viewing and signal acquisition.

2.3.1 Results

Using the SLP-1064-1 laser and Avantes spectrometers, LIBS analysis was performed on three solid metallic surfaces: a silicon wafer, 99.9% pure copper foil (CU-5, Lyon Industries), and aluminum foil (Reynolds Wrap, Reynolds Group Holdings, New Zealand). Eight ablations were performed per material. The averages of the eight spectra are displayed in Figure 2.7. The spectra for silicon and aluminum show distinct emission lines. To identify emission lines, the atomic emissions data base assembled by the National Institute of Standards and Technology was used (NIST) [159]. More details on the NIST atomic spectra database is provided in Section 3.5.1. As an example, NIST [159] lists prominent silicon (I), aluminum (I), and copper (I) emission lines at 288.158 nm, 309.271 nm, and 521.820 nm respectively. For each respective element/emission line, signal intensities and standard deviation produced by the samples were found to be 706.688 a.u. and 799.147 a.u. (Si); 1224.75 a.u. and 1156.150 a.u. (Al); and 1505.66 a.u. and 1111.304783 a.u. (Cu). The signal deviates significantly and is clearly displayed by the Si (I) emission line at 288.158 nm in Figure 2.8. The negative control (detector aperture was blocked) consisted of a signal intensity of -8.875, -6.594 and -14.375 a.u. with a standard deviation of 5.759, 5.741, 2.629 a.u. for Si, Al, and Cu emission lines respectively.

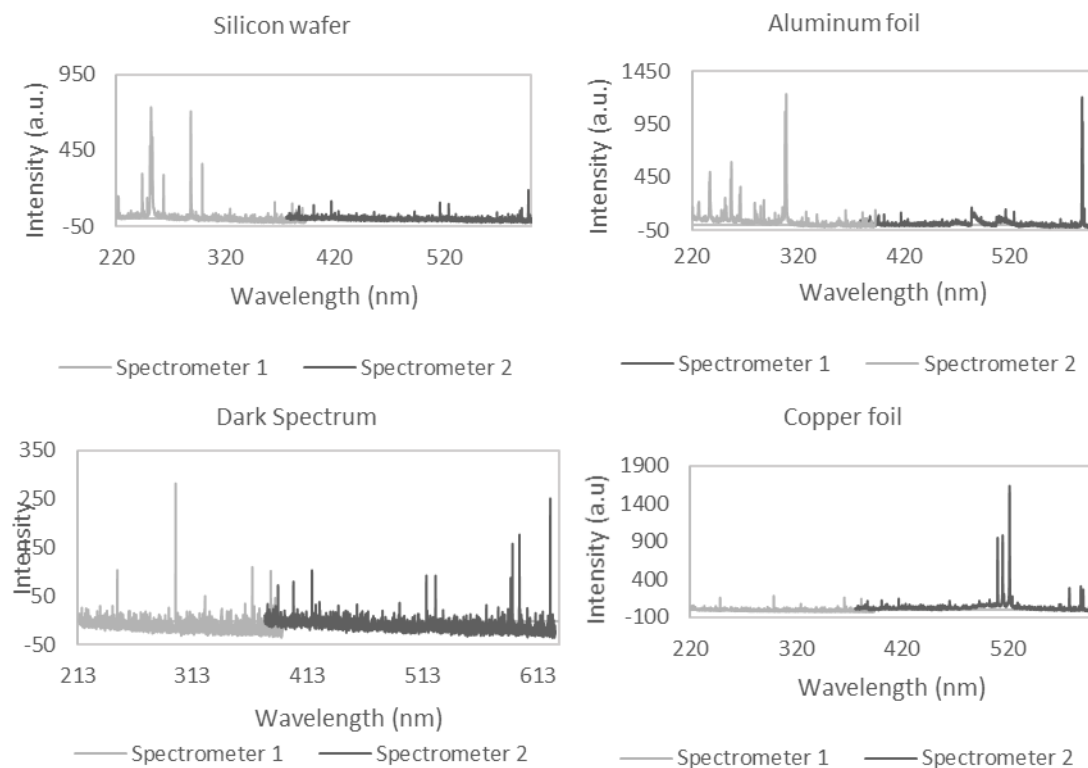


Figure 2.7 Each plot represents the average of spectra produced from eight ablations on the surface of a silicon wafer, aluminum foil, and copper foil. A spectrum of the detector when the entrance was covered is represented as “dark spectrum.” Each plot represents the signal detected by two spectrometers that together cover the wavelength range from 220 to 600 nm.

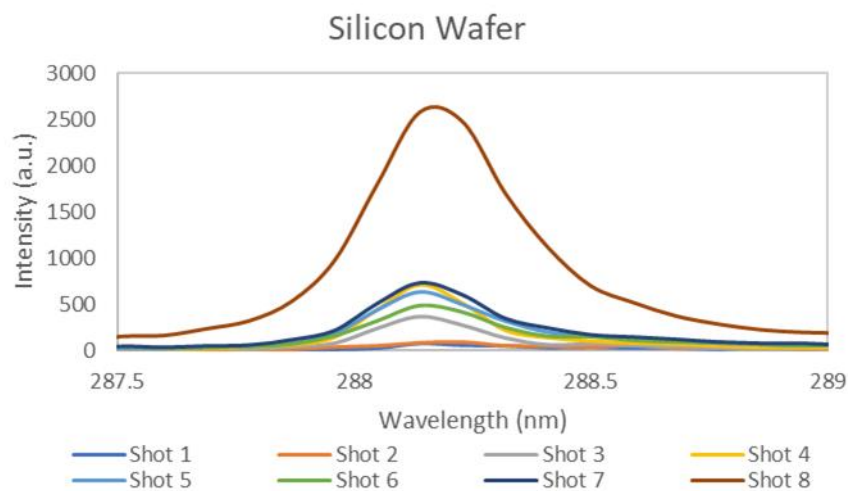


Figure 2.8 Si (I) 288.158 nm emission line varies significantly between laser ablations of a silicon wafer

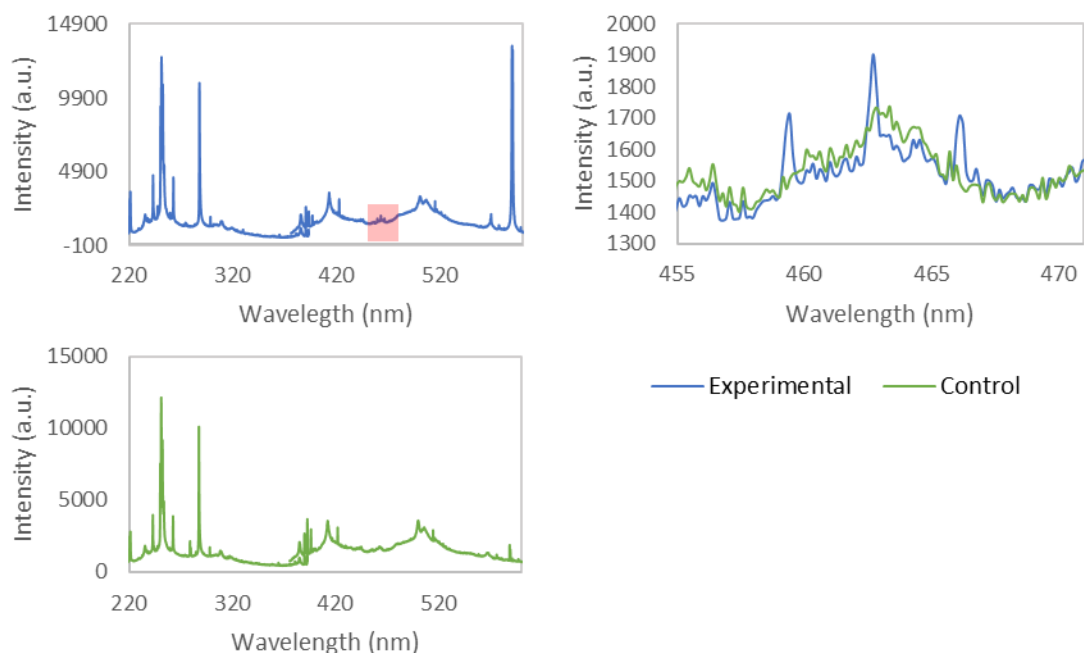


Figure 2.9 Top left: spectrum of Eu-labeled antibodies on a silicon-wafer surface. Bottom left: spectrum of silicon wafer. Top right: Focusing on the region indicated by the red box brings attention to the Eu (I) emission lines at 459.403, 462.722 and 466.188 nm and how they contrast with the silicon wafer background.

LIBS System 1 was also applied to detection of metal-conjugated antibodies dried on a silicon-wafer surface. In a visit to Dr. Gary Nolan's lab at Stanford University, antibodies were conjugated to erbium, europium, gadolinium, neodymium, platinum, ytterbium, and dysprosium using the MaxPar X8 antibody conjugation kit (Fluidigm, San Francisco, CA, USA). Studies using a different LIBS system at Berkeley National Laboratories identified that the metals were present in their respective samples. Detection was also attempted using LIBS System 1. Six microliters of the conjugated antibody were loaded onto a silicon wafer and allowed to dry. Six locations in the area where the metal-conjugated antibody was spotted were subsequently sampled with one ablation per location. Europium-conjugated antibody was the only sample successfully detected. Figure 2.9 shows the average signal produced by the europium-antibody sample. Three europium (I) peaks 459.403, 462.722 and 466.188 nm extended beyond background. The background produced by LIBS ablation of a silicon wafer appeared to be significant, potentially masking signal produced by the metals of interest. To mitigate this effect, an option would be to reduce the integration time of the spectrometer and modify the delay to omit detection of broad-band or

irrelevant atomic emissions. However, the Avantes Mini's minimum integration time of one millisecond (typical LIBS integration time is 500-1000 ns) limited the options for time-gating the signal.

The studies above were the most successful with LIBS System 1 and show potential for qualitative characterization of metal substrates and dried metal solutions. Other studies were conducted to determine if LIBS System 1 could detect metals deposited on nitrocellulose paper. Such experiments were largely unsuccessful. Samples consisted of lanthanide standards, lanthanide-conjugated antibodies, gold nanoparticles, and gold nanoparticles conjugated to antibodies and immobilized on the control zone of a lateral flow assay. Though this dissertation does not provide definitive evidence that explains the inability of LIBS System 1 to detect metals in nitrocellulose, experiential observations suggested that the optical design of the LIBS system and the sensitivity and time-gating limitations of the spectrometer were largely the causes. Had the SLP-1064-1 been paired with the appropriate optics and spectrometer, the system may have been capable of some level of detection of metals on nitrocellulose.

Overall, the laser experienced inconsistencies in operation: the laser would not always fire when triggered. Inconsistent laser function made data collection time-consuming and error prone. In addition, mechanical issues associated with damage during laser shipment consumed significant time and effort for repair. The laser was also observed to produce a significant electro-magnetic field that affected the other electronics. Even so, this system was successful in qualitative analysis of silicon, aluminum, and copper substrates as well as dried Eu-conjugated antibody on a silicon wafer.

2.4 LIBS System 2

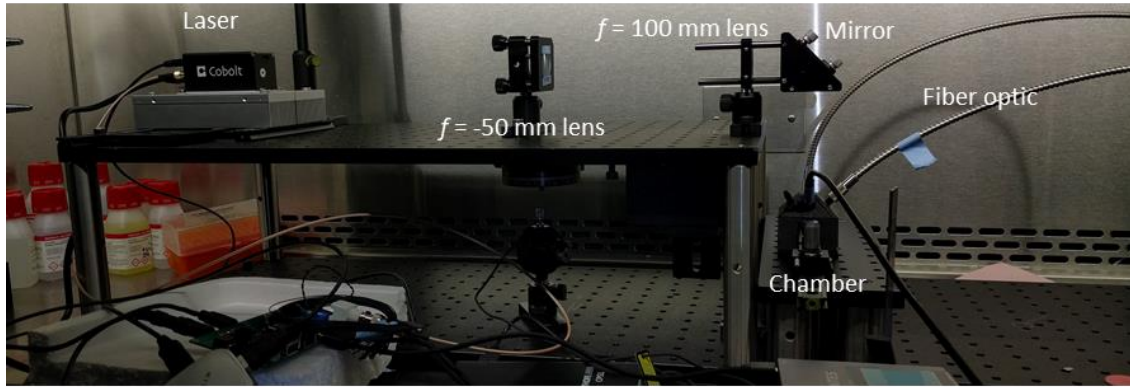


Figure 2.10 Design of LIBS System 2. A 50 μJ pulsed 1064 nm beam was directed to a sample chamber using a series of optics. The beam was expanded using a $f = -50$ mm lens, focused using a $f = 100$ mm lens, and re-directed to the sample chamber using a mirror. Plasma emissions were collected by a fiber optics which interfaced with the sample chamber via an SMA connector.

The Tor XS by Hübner Photonics (Kassel, Germany) is a Nd:YAG 1064 nm 50 μJ actively Q-switched laser with a pulse width of 2-3.5 ns and repetition rate of up to 1 kHz. The beam is approximately circular with a diameter of ~ 3 mm as it exits the laser head, with beam quality factor $M^2 < 1.3$. Unlike other lasers discussed in this dissertation, the Tor XS does not require water cooling. A heat sink placed under the laser head dissipates heat. It is also the smallest ($50 \times 21 \times 29$ mm) and lightest (100 grams) laser discussed, making it favorable for a portable LIBS system design. Delay between laser trigger and laser firing was measured to be 170.68 μs with a 0.41 μs jitter. The repetition rate and the number of laser pulses could be modified under user control. The most common combination of repetition rate and pulse number used for this study was 1000 Hz and 1000 pulses. Triggering of the laser was achieved via an SMA cable connecting it to a custom-made function generator. A diagram of LIBS System 2 is provided in Figure 2.10.

2.4.1 Spectrometer

The same spectrometers used for LIBS System 1 were applied to LIBS System 2. A timing diagram in Figure 2.11 shows an example of the sequence of triggering events used for this LIBS system.

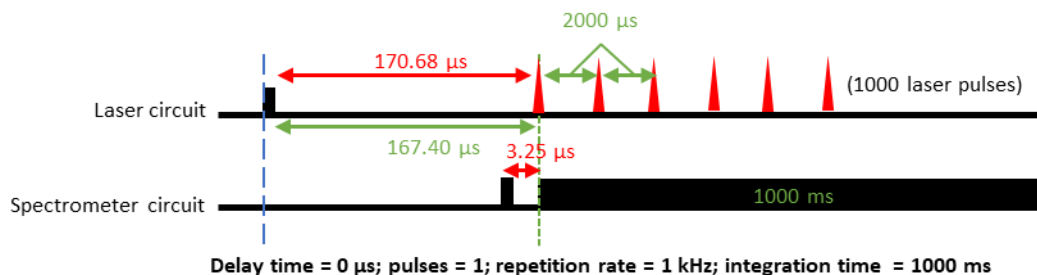


Figure 2.11 Timing circuit of LIBS System 2 shows data acquisition starting at the first of 1000 laser pulses. The laser pulses at 1 kHz for 1000 milliseconds. Data were acquired from the first pulse to the last pulse. Values in red can be modified by the user, values in green cannot.

2.4.2 Electronics and Software

The electronics and software applied to LIBS System 1 were applied to System 2. As opposed to System 1 operation, a single trigger event from the PC triggered either single or multiple laser pulses. The spectrometer was triggered once, irrespective of the number of laser pulses, allowing the collection of atomic emissions generated for a single or across multiple laser pulses. The number and repetition rate of the TTL signal were determined by the pulse number and repetition rate indicated via the graphic-user interface. For the data presented below, integration time was typically 1 ms as the laser pulsed 1000 times at 1 kHz. The delay time was 167.4 μ s (internal delay of the spectrometer subtracted from that of the laser; 170.68 μ s – 3.28 μ s), such that spectrometer data acquisition coincided with the first laser pulse. Upon signal acquisition, data from the spectrometers were displayed as a wavelength vs. intensity plot to allow rapid assessment of results.

2.4.3 Optics

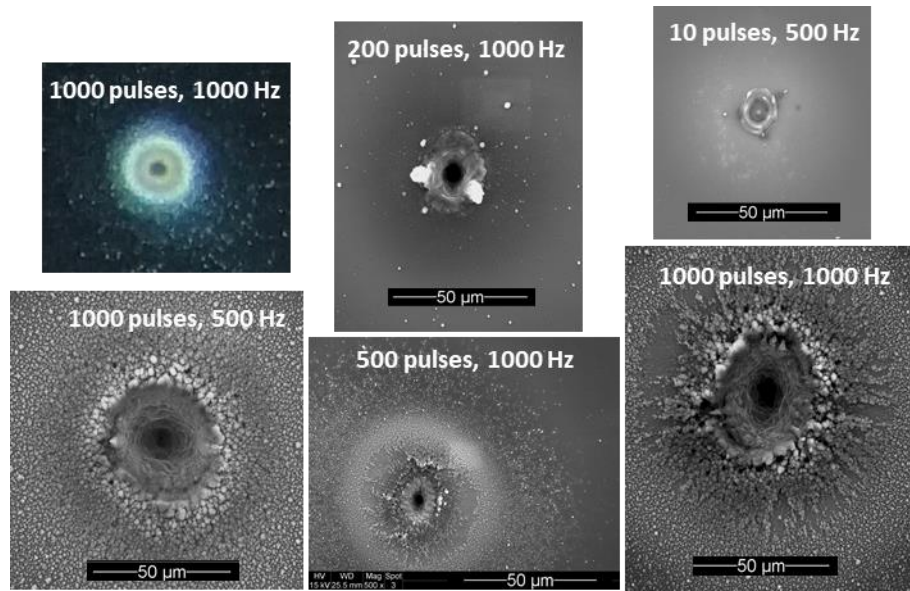


Figure 2.12 Top left is an image taken with stereomicroscopy. All other images were taken with electron microscopy (25.5 mm, 15 kV acceleration voltage, 200x magnification). As the number of the pulses increased, the amount of debris surrounding the crater, the size of the crater, and the apparent depth of the crater increased. Debris is deposited in a ring around the crater.

Optics were selected according to recommendations by Hübner Photonics: a $f = -50$ mm lens (Edmund Optics, 68001) placed 30 cm from the laser head expanded the beam such that beam diameter was approximately 25 mm. After beam expansion, the beam was focused to the sample surface by an $f = 100$ mm lens (Edmund Optics, 67653) placed 47 cm away from the laser head. Following these recommendations, the beam was focused to a ~ 30 μm spot size on the sample surface (Figure 2.12). A stereomicroscope and an electron microscope were used to visualize the craters. In some iterations of the system, a mirror (NB1-K14, Thorlabs) placed between the two lenses re-directed the beam from the horizontal to the vertical plane before it entered the sample chamber. The sample was placed 64 mm from the laser head. To facilitate sample alignment, a visible laser or “alignment laser” (CPS635R, Thorlabs) was placed orthogonal to the Tor XS laser head and directed onto the same optical path as the TorXS laser using a long-pass dichroic mirror (DMLP650, Thorlabs). After being redirected, the alignment laser beam passed through the lenses described previously, focusing onto the sample surface. Though the focal point of the alignment laser ($\lambda = 632$ nm) was different from that of the TorXS beam ($\lambda = 1064$ nm), the approximation

was sufficient to aid in sample placement. For plasma light collection, two UV-VIS fiber optics (FC-UV1000-1-SR-BX, Avantes) were placed 20 mm from the sample surface at a 45° angle. The fibers traveled from the sample chamber directly to the spectrometers.

2.4.4 Sample Chamber

The sample chamber was designed in SolidWorks (Dassault Systèmes) computer software. Similar to System 1, the chamber consisted of two halves of similar dimensions. The main difference was the removal of ports for the Avantes collimating lenses. Instead, the fiber interfaced directly with the box, using an SMA connector. Another modification consisted of a gas entry port 20 mm from the sample surface at a 45° angle. The design of the chamber allowed the distance between the fiber and sample surface to be 20 mm. The sample holder was the same as that used in System 1.

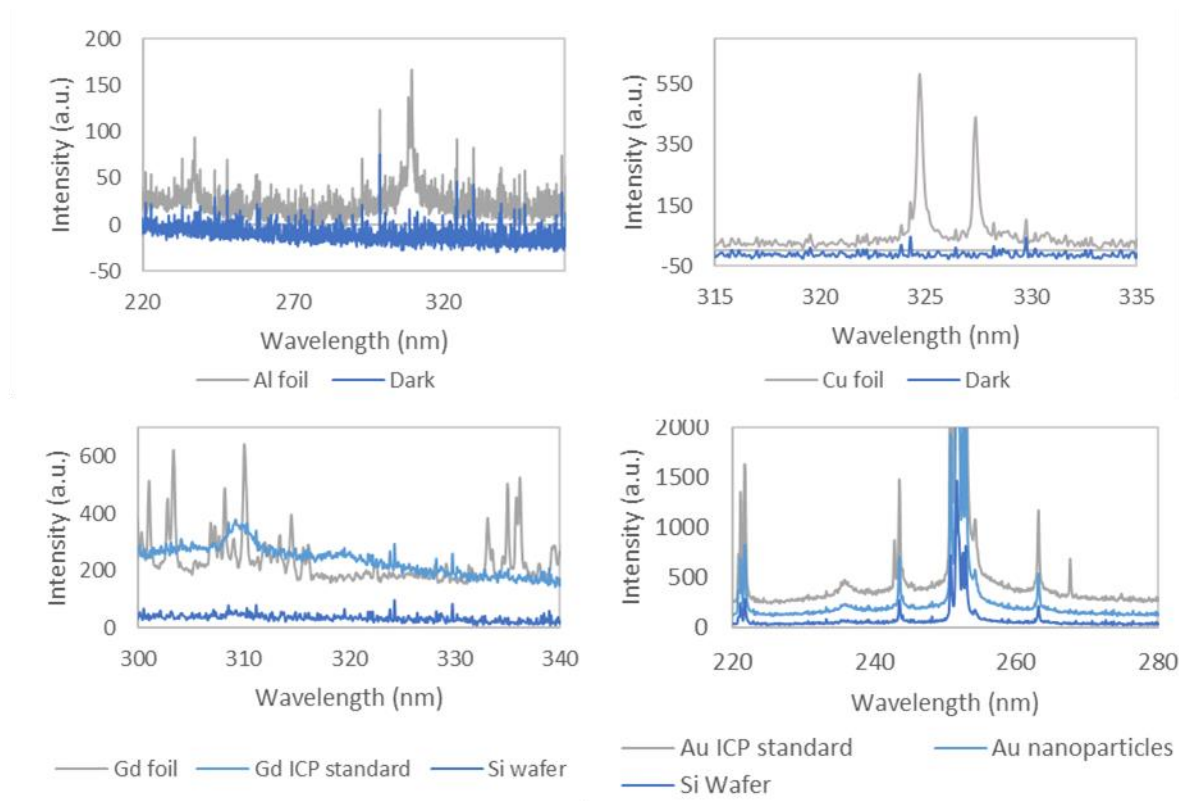


Figure 2.13 Spectra of aluminum foil, copper foil, gadolinium foil, and silicon wafer acquired with LIBS System 2.

2.4.5 Results

This LIBS system was applied to the detection of metal foils and wafers, metal suspensions dried on silicon wafers, and metal suspensions dried on nitrocellulose paper. The LIBS system was adjusted to produce 1000 laser pulses at 1 kHz, and to acquire data for one second – from the first laser pulse to the last. Composition of metal foils and wafers was one of copper, silicon (444, University Wafer) or gadolinium (#693723, Sigma Aldrich). These materials produced emissions characteristic of the corresponding element (Figure 2.13). Emission lines of metals were determined based on the presence of a peak at the wavelengths specified by NIST [159] for the element of interest. In the aluminum sample, two low-intensity peaks were present at 236.705 and 309.270 nm, indicative of Al (I). In the copper foil, peaks were observed at 327.396 and 329.0417, indicative of Cu (I). In the Si wafer sample, peaks were observed at 251.432 and a strong emission at 288.158, indicative of Si (I). The gadolinium sample produced many peaks, a feature common among lanthanides [160]. Some peaks found in the data that matched with the NIST database were Gd (I) 303.284 nm, Gd (II) 310.050 nm, and Gd (II) 335.010 nm [159].

Several metal solutions/suspensions were loaded onto silicon wafers: 10 µl of either Gd or Au certified reference material (CRM) solutions at a concentration of 1000 mg/L (38168-100ML and 05660-100ML, Sigma Aldrich, St. Louis, MO, USA), and gold nanoparticles in citric acid at an optical density greater than 5 (G-20-20, Cytodiagnostics, Toronto, Canada). The solutions were dried on the silicon wafer surface. Au and Gd in nitric acid dried as a clear spot. The gold nanoparticles formed a dense red spot on the silicon wafer surface. Using the Gd foil as a reference, similar emissions were not observed for the Gd CRM standard dried on the wafer. However, the Au CRM solution was detectable based on emission peaks present at 242.795 and 267.595 nm. Interestingly, the gold nanoparticles were not detectable on the silicon wafer surface. Since both Au CRM solution and gold nanoparticles were present on the wafer at high concentration, it is believed that particle shape or adhesion to the silicon wafer surface may have played a role in whether Au could be detected. Figure 2.13 shows the spectrum of each metal solution/suspension on the silicon wafer surface. The CRM solution and the silicon wafer serve as positive and negative controls respectively.

LIBS analysis of metals deposited on nitrocellulose paper was unsuccessful with this system. A strong plasma was not observed to form on the surface of nitrocellulose paper, and any emissions that may have been produced were undetectable by the AvaSpec Mini spectrometers.

For this LIBS system to detect metals on nitrocellulose, a critical modification may be to increase laser power such that a plasma can at least be observed on the surface of the nitrocellulose. The minimum power reported in this dissertation that utilized a Nd:YAG 1064 nm laser and produced a plasma on nitrocellulose was 6 mJ.

2.5 LIBS System 3

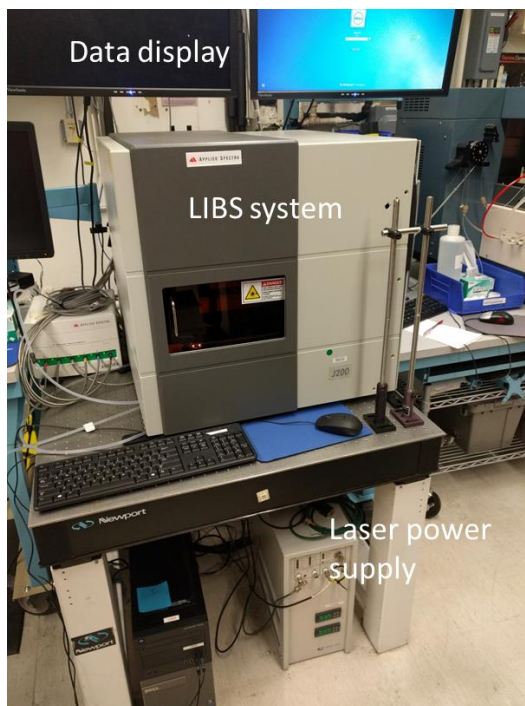


Figure 2.14 The LIBS system designed by Applied Spectra Inc. consisted of a 213 nm, 4 mJ, nanosecond pulsed laser and a 6-channel spectrometer. The laser beam was directed to an enclosed sample chamber. This system allowed environmental gas control (Ar, He or air) and was interfaced with an inductively coupled plasma optical emission spectrometer. Data was displayed on monitors during and after data acquisition, allowing the user real-time data visualization.

Berkeley National Laboratories (LBNL) hosts a laser-technologies group and an array of LIBS systems, many of them custom built. Two of the LIBS systems at LBNL were tested and described here as LIBS System 3 and 4. LIBS system 3 was a version of a commercial LIBS systems sold by Applied Spectra. Given that design specifications are proprietary, this system is not described in the same detail as other LIBS systems.

LIBS System 3 consisted of a water-cooled Nd:YAG 213 nm 4 mJ nanosecond pulsed laser. The system utilized control software for rapid sampling and data analysis. Laser power and spot size (125 μm) could not be modified without opening the system, and therefore were not investigated further. Gas composition (air, argon, or helium) and flow rate inside the enclosed LIBS chamber could also be controlled. Two spectrometers were paired with this LIBS system, a Princeton Instrument 320-mm IsoPlane SCT spectrograph fitted with a PI-MAX ICCD detector (Princeton Instruments, Acton, MA, U.S.A), and the Aurora LIBS Spectrometer utilizing a CCD detector (Applied Spectra, Sacramento, CA, USA). The former spectrometer permitted acquisition of high-resolution data across a 25 nm to 30 nm window and over short (50,000 μs) integration and acquisition delay times (~ 1 μs). The Aurora LIBS Spectrometer covered a broad wavelength range (861nm), had an integration time of 1.05 ms, and an acquisition delay time between 0.2 μs and 1 μs .

2.5.1 Results

LIBS System 3 was applied to the detection of gold foil and gold nanoparticles as well as to CRM solutions dried on a nitrocellulose surface. Again, two spectrometers were used: Applied Spectra Aurora LIBS CCD spectrometer and Princeton Instruments IsoPlane SCT ICCD. Using the Aurora spectrometer, gold foil was observed to produce multiple peaks across the wavelength range that corresponded to the NIST reported wavelength. One such peak displayed in Figure 2.15 was at 583.737 nm [159]. The same peak, or others which corresponded to gold, were not detected when gold nanoparticles on nitrocellulose paper were sampled (Figure 2.15).

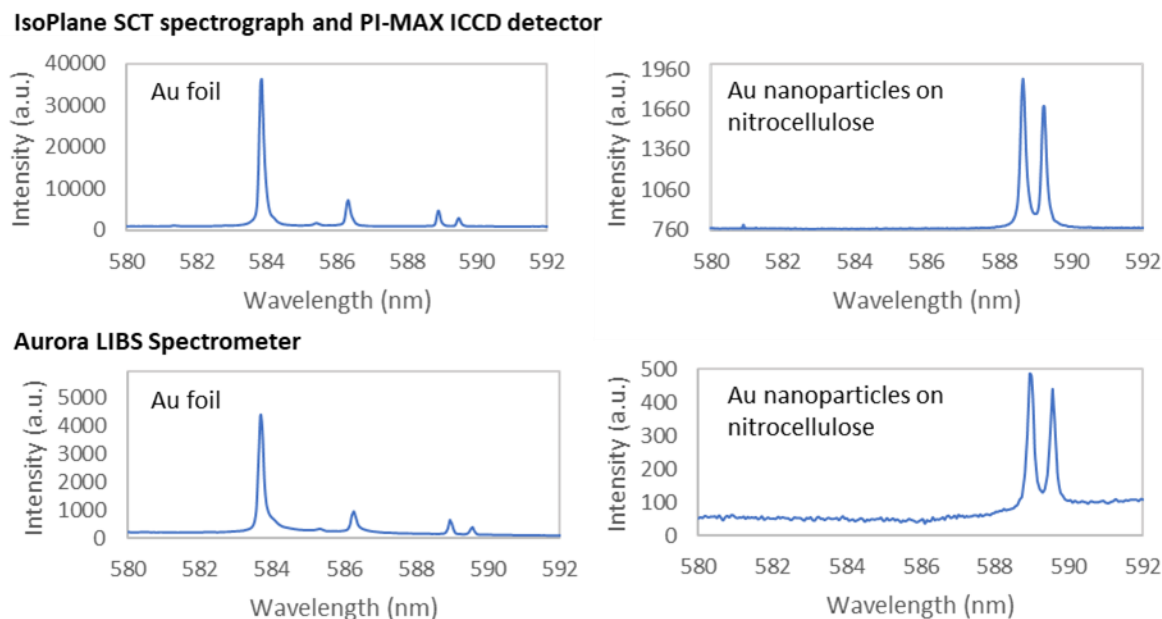


Figure 2.15 Acquisition of plasma emissions on the surface of Au foil using the IsoPlane SCT spectrograph fitted with the PI-MAX ICCD (top left) and the Aurora LIBS spectrometer (bottom left) showed a strong gold peak at 583.737 nm. The same peak was not observed during ablation of Au nanoparticles on nitrocellulose paper (top and bottom right).

The case was similar using the Princeton Instruments IsoPlane SCT ICCD. For both spectrometers, strong emissions were detected at 588.995 nm and 589.592 nm, which correspond to strong sodium (I) lines (Figure 2.15). In another experiment, CRM solutions consisting of Eu, Nd, Dy, Yb, or Pr (PEUN-100, PNDN-100, PDYN-100, PYBN-100, PPRN-100, VHG Labs Inc., Teddington, Middlesex, UK) were not detected on a nitrocellulose surface. The following parameters were altered in an attempt to detect the metals: gas environment, spectrometer acquisition time, and physical properties of the nitrocellulose surface (samples were compressed and/or a glue binder was added to make the substrate more favorable for plasma formation [124]). For every experimental condition, a crater was clearly visible on the nitrocellulose and a plasma was observed to form, indicating that ablation was occurring. However, metals on nitrocellulose were not detectable. Failure to detect metals on nitrocellulose using two types of spectrometers and various environmental conditions indicates that either laser power was insufficient (4 mJ) and/or the laser wavelength (213 nm) was not appropriate for the application.

2.6 LIBS System 4

Compared to LIBS systems described previously, LIBS System 4 was capable of detecting metals on nitrocellulose paper, permitting a more comprehensive study to explore the capabilities of this system. As a secondary measurement method, inductively coupled optical emission spectroscopy was also performed on the samples.

2.6.1 Laser, Spectrometer, Software and Electronics, Optics, Sample Holder

LIBS System 4 was constructed at Lawrence Berkeley National Laboratory by the Laser Technologies Group and consisted of a NewWave Research Tempest 1064 nm actively Q-switched laser. Pulse energy was 18 mJ, with a pulse duration of 3-5 ns. The beam was focused to a spot size of $\sim 100\ \mu\text{m}$ on the sample. The sample was observed using a camera whose focal plane was matched to that of the $100\ \mu\text{m}$ laser spot. A collimating lens and fiber optic directed the LIBS spectral emission to a Princeton Instrument 320-mm IsoPlane SCT spectrograph fitted with a Princeton Instruments PI-MAX ICCD detector (Princeton Instruments, Acton, MA, USA). Figure 2.16 illustrates the design of this LIBS system. The spectra were acquired for 20 μs , 1 μs after the laser pulse. The sample was positioned near the focal point of the beam using an x,y,z stage.

2.6.2 Inductively-coupled Plasma Optical Emission Spectroscopy

As a secondary method of analysis for validation, laser-ablation inductively coupled plasma optical-emission spectroscopy (LA-ICP-OES) was performed using Applied Spectra J200 (Applied Spectra, Fremont, CA, USA) coupled to an Agilent 5100 ICP-OES (Agilent, Santa Clara, CA, USA) system. Samples were ablated with a 213 nm 4 mJ beam focused to a spot size of $125\ \mu\text{m}$. Ablated particulates were carried to the ICP-OES system using argon or helium gas at a flow rate of 0.5 L/min. In the process of ablation, measurements were made continuously, creating signal intensity vs. time data for each element being measured. Using the Agilent ICP-OES software, emission lines of metals used for antibody conjugation (Au, Dy, Pr, Eu, and Nd) were selected for measurement.

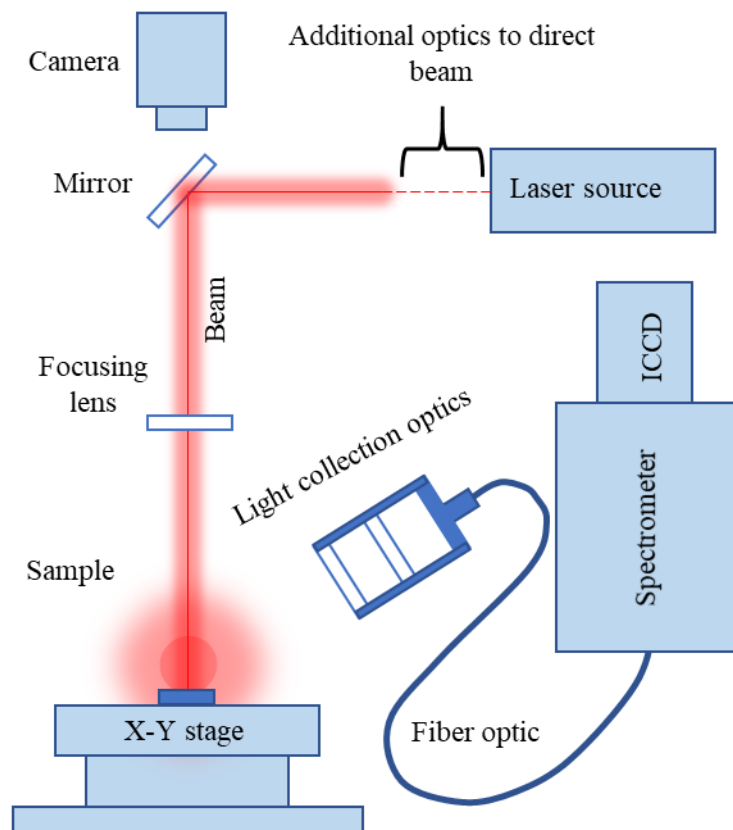


Figure 2.16 Diagram of LIBS System 4. An 18 mJ beam produced by a NewWave Research Tempest 1064 nm Q-switched laser was directed to a sample using a series of optics. Sample position was adjusted using an x-y stage. Plasma emissions were directed to a fiber optic connected to a spectrometer and an ICCD detector. A camera was used for basic sample observation. Diagram not to scale.

2.6.3 Methods for Sample Preparation

For both LIBS and LA-ICP-OES analysis, the general experimental approach was to use a positive control (either a liquid or solid standard) to identify atomic emission lines of elements of interest. Emission lines were cross-validated with the National Institute of Standard and Technology (NIST) atomic database [159] to determine the identity of background emissions produced by the paper sample carrier, and to evaluate whether the experimental sample produced atomic emission lines for elements of interest above background levels. LA-ICP-OES was used to support results obtained by LIBS. This study was not designed to determine whether LIBS and

LA-ICP-OES can be directly compared owing to differences in laser energy and wavelength effects.

Gold-Nanoparticle Paper-based Assay Preparation and Testing

As a proof of concept, off-the-shelf pregnancy tests (Wondfo Pregnancy Test strips, Wondfo W1-S, Guangzhou, China) were used to determine whether LIBS and ICP-OES showed promise as methods for detecting metal-conjugated antibodies on paper. The pregnancy test consisted of a sample introduction pad containing gold nanoparticles targeting a pregnancy hormone, a nitrocellulose strip, and a waste pad. The manufacturer recommends the sample to be introduced to the sample introduction pad, after which it wicks along the nitrocellulose strip, and reaches the waste pad. Along the path of flow, the sample interacts with two distinct regions of the nitrocellulose strip: the first zone immobilizes the pregnancy hormone and associated gold nanoparticles; the second immobilizes only the gold nanoparticles. For the purposes of this study, only the second zone is considered. More details on design of lateral flow assays such as the pregnancy test are provided in Chapter 4.

The LIBS positive control consisted of 99.95% gold foil (Alfa Aesar 7440-57-5, Tewksbury, MA, USA). LIBS was performed on the foil to identify prominent atomic emission lines that correspond to those reported by NIST [159].

To prepare the experimental sample and negative control, water was added to one end of the pregnancy test strip for three seconds according to the manufacturer's instructions. The process was repeated for multiple strips. A single pink line was observed to form on each strip, approximately 41 mm from the submerged end of the strip. The pink line served as the experimental sample, since the color is attributed to the aggregation of gold nanoparticles. The negative control consisted of the white area of paper adjacent to the pink line, 39-40 mm from the end of the strip.

LIBS was performed on the pink line to determine the number of laser pulses that yielded a detectable gold signal. In initial tests, three locations were sampled, with ten pulses per location. The results suggested that a single pulse per location was sufficient; therefore, a single pulse per location was used for all the following samples presented in this paper.

Three strips were prepared as described above and allowed to dry overnight. For each strip, nine locations along the pink line were sampled. This sampling method was also used for the area

adjacent to the pink line (Figure 2.17). To determine whether wet strips would produce a gold signal comparable to that from dry strips, LIBS was performed on three strips immediately after they were immersed in water. Dry strips and wet strips were sampled identically.

As a secondary method to determine the presence of gold on paper, LA-ICP-OES was performed on four dried pregnancy strips. The pink line was ablated in 4 rounds – each round consisting of 65 ablation pulses, one per location. The same sampling method was used for areas adjacent to the pink line. Argon gas was used as the carrier for the particulates. Au emission lines recommended by Agilent’s ICP-OES software database were analyzed (208.2, 242.8, and 267.6 nm).

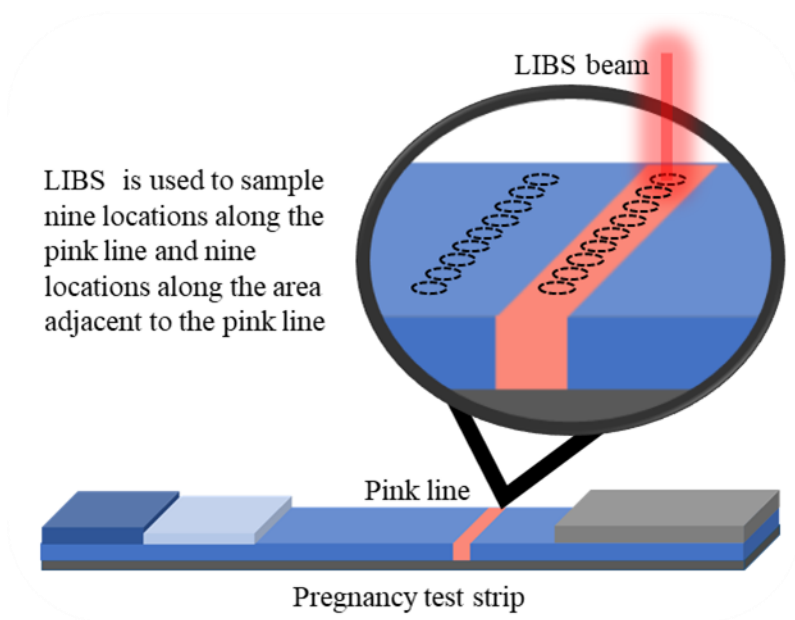


Figure 2.17 Illustration of LIBS sampling approach for pregnancy test strips.
Diagram not to scale.

Lanthanide-conjugated Antibody Preparation and Testing

After testing for gold-conjugated antibodies on paper using LIBS and LA-ICP-OES, a similar experiment was performed on lanthanide-conjugated antibodies.

Anti-*E. coli* antibodies (ab137967, Abcam, Cambridge, MA, U.S.A) were conjugated to Eu, Nd, Dy, Yb, and Pr using the Fluidigm MaxPar metal-labeling kit (Fluidigm, San Francisco, CA, USA). Final antibody concentration was 0.4 mg/ml for Eu-, Nd-, Dy-, Yb-, and Pr-conjugated antibodies, respectively. Based on previous studies, each antibody should be conjugated to 2-3

polymers, each polymer bearing ~30 metal atoms. Experimental samples were prepared by adding 2 μ l of each antibody stock solution to five 6 mm \times 3 mm cutouts of FF120HP plastic-backed nitrocellulose paper (GE Healthcare and Life Sciences, Pittsburgh, PA, USA). This type of paper was chosen because it is common among paper-based bioassays (PBBs)[161]. The antibody solution was observed to distribute across the entire paper, which was dried overnight.

Before performing LIBS on antibody conjugates, lanthanide emission lines were located using a positive control. The positive controls consisted of ICP standards containing either Eu, Nd, Dy, Yb, or Pr (PEUN-100, PNDN-100, PDYN-100, PYBN-100, PPRN-100, VHG Labs Inc., Teddington, Middlesex, UK). A total volume of 240 μ l of each standard (1000 μ g/ml suspended in 2% nitric acid) was dried onto ~25 \times 25 mm sections of FF120HP in aliquots of 60 μ l. Negative control samples consisted of FF120HP with no additives. LIBS was performed on each positive and negative control sample using 15 laser pulses per sample (1 pulse per location). The same method was applied to experimental samples.

The positive control, negative control, and experimental samples used for the LIBS experiments were then used for LA-ICP-OES to further evaluate the presence of lanthanides. Each sample was ablated in 4 rounds – each round consisting of 30 ablation pulses, one per location. Helium was used as the carrier gas. Lanthanide emission lines recommended by Agilent's ICP-OES software database were analyzed: Dy (340.8 and 353.2 nm), Eu (397.2 and 420.5 nm), Nd (401.2 and 406.1 nm), and Pr (390.8 and 417.9 nm). Owing to technical reasons, LA-ICP-OES analysis of samples containing Yb were omitted from this portion of the study.

Peak Identification

Peaks were identified by first acquiring a broad spectrum (250-550nm) of the positive controls. For each element of interest, the region with the most intense and well-resolved spectral peaks was then selected for analysis. Using the NIST Atomic Spectra Database [159], reported emission lines from the metal of interest were cross-checked with the observed peaks in the positive control. To be selected for analysis, peaks in the positive control needed to be of high relative intensity, match reported lanthanide or gold peaks in the NIST database [159], and be absent from the negative control.

Data Analysis

LIBS spectra were analyzed using a custom-developed procedure written in R language for statistical computing. Data were first accumulated for each sampling event. The noise was estimated across the wavelength range by subtracting the result of a sliding median-filtered data. The mean of a second sliding median was then subtracted from the raw data, centering the data on the x-axis. The LIBS spectra were then divided by the estimated noise value, defined as the standard deviation of the estimated noise, providing a local measure of signal to noise (abbreviated as S/N) for the LIBS signal. For samples of gold nanoparticles on nitrocellulose, S/N represented an aggregation of 27 measurements. For each lanthanide on nitrocellulose, S/N represented an aggregation of 15 measurements.

LA-ICP-OES raw data were reported as intensity vs. time for select wavelengths. Shortly following each round of ablations, the signal for carbon (a common element in nitrocellulose paper) peaked. LA-ICP-OES intensities for metals of interest at the time-point where carbon peaked were converted to S/N. Noise was considered as emission intensity reported by the instrument before laser ablation. Standard deviation of the noise was then divided from the signal, yielding S/N. The S/N from the four ablation rounds was averaged, and log-transformed. This process was applied to positive control, negative control, and experimental samples.

2.6.4 Results

Repeated Sampling of Nitrocellulose Paper

To determine the number of laser pulses that would be sufficient to generate a gold signal from GNP PBBs, 3 areas of a dry test-strip pink line were sampled 10 times. A single 18 mJ laser pulse focused to a spot of 100 μm was sufficient to form a visible crater on nitrocellulose and generate a gold emission signal without ablating through all the material. It was noted that the nitrocellulose was easily ablated.

LIBS and LA-ICP-OES Analysis of Gold-nanoparticles in Nitrocellulose Paper

Gold foil was utilized as the positive control for LIBS experiments on gold nanoparticle detection. Ablation of gold foil yielded strong emission peaks at 267.6 nm and 274.8 nm (532 and 315 S/N respectively) (Figure 2.18). Peaks were identified as gold using the NIST database [159].

A study was conducted to determine the number of pulses required to obtain a detectable gold signal from paper without ablating completely through the material. When ablating the same location of a pink line on a pregnancy test with a series of 10 pulses, it was observed that average signal intensity at 267.6 nm and 274.8 nm degraded (Figure 2.19) for each of the 3 tested areas. The plastic backing of the paper was visible after 5-10 laser pulses. Based on this information, all other samples composed of nitrocellulose in this study were ablated once per location.

Differences between gold emission intensity were measured between wet and dry nitrocellulose paper. Wet and dry pregnancy tests were sampled in two locations: the pink line (area of high gold nanoparticle aggregation), and the area adjacent to the pink line (area of low nanoparticle aggregation, defined as the negative control). The raw LIBS spectra are presented in Figure 2.20. The pink line on both the wet and dry pregnancy tests yielded comparable S/N at 267.6 nm (dry: 474 S/N; wet: 475 S/N) and 274.8 nm (dry: 127 S/N; wet: 84 S/N). The area adjacent to the pink line (negative control) on wet and dry samples yielded lower gold-line S/N for each wavelength (267.6 nm – dry: 23 S/N; wet: 37 S/N) (274.8 nm – dry: 7 S/N; wet: 8 S/N). For both wet and dry samples, emission at 267.6 nm were stronger than those at 274.8 nm. Data are graphically presented in Figure 2.20, and S/N values are provided in Table 2.1. Overall, the pink line yielded the strongest gold emission intensities, followed by the area adjacent to the pink line. Results are based on a limited sample size.

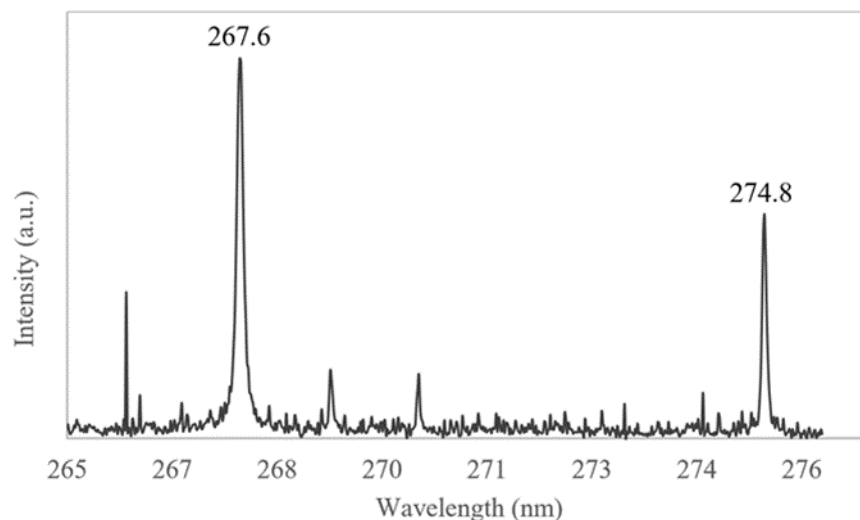


Figure 2.18 Spectrum of gold foil. Gold emission lines, as indicated by NIST [159], were identified at 267.6 nm and 274.8 nm.

In addition to LIBS, LA-ICP-OES was used to measure gold emission on nitrocellulose paper. As with LIBS, the pink line on the dry GNP paper-based assay generated a stronger gold LA-ICP-OES signal than did the area adjacent to the pink line (Figure 2.21).

When ablating the pink line on the nitrocellulose paper, gold line emission signals were detected. Gold emission signals were not detected when ablating the white section of nitrocellulose adjacent to the pink line. In this study, visual detection of gold nanoparticles on paper was supported by LIBS detection of gold nanoparticles. Interestingly, gold emission intensities were comparable between wet and dry nitrocellulose paper. This may imply that water does not have a significant impact on the plasma generation process in nitrocellulose paper, or the laser pulse rapidly evaporates the water before ablating the sample. More replicates and investigation into this topic are required for further evaluation.

LIBS and LA-ICP-OES Analysis of Lanthanides in Nitrocellulose Paper

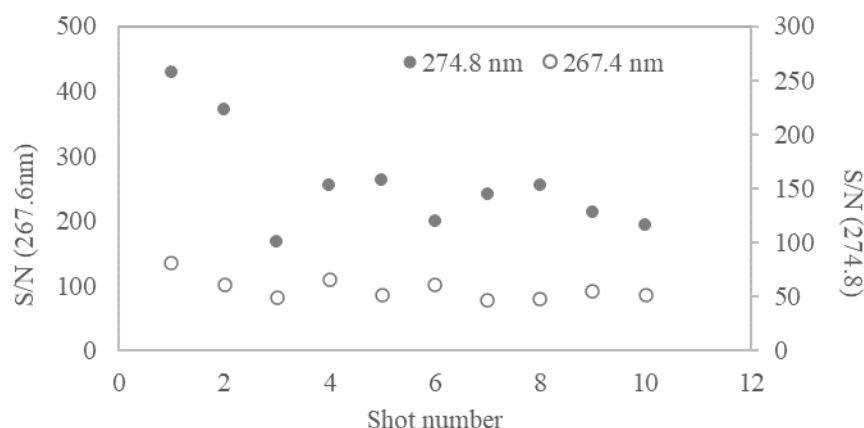


Figure 2.19 Degradation of gold emission lines 267.6 and 274.8 nm as the pink line of a pregnancy test strip was sampled 10 times in the same location. Each data point represents the average of 3 measurements. Standard deviation ranged from 7.7-38.8%.

Lanthanide emission lines were first located along the spectrum using the ICP standard positive controls, and then measured for untreated paper, and paper treated with lanthanide-conjugated antibodies.

Ablation of ICP standards on nitrocellulose yielded a complex emission spectrum. Prominent emission lines were identified as belonging to lanthanides using the NIST database [159] (Eu: 452.3, 459.4, 462.7, and 466.2 nm; Dy: 404.6, 407.8, and 409.4 nm; Pr: 511.0, 512.9, 532.3 nm; Yb: 369.4 and 398.8 nm; Nd: 513.1, 525.0, 532.0, and 535.7 nm). For all samples except dysprosium line 404.6 nm, ICP standard positive controls generated stronger emission signals for the elements of interest than did the experimental treatments (Fig. 9). Though the same quantity of each type of lanthanide ICP standard was added to nitrocellulose paper, some lanthanide ICP standards produced signals with higher S/N than others. The europium ICP standard produced the most intense signal, followed by Yb, Pr, Nd, and Dy. Metal-conjugated antibodies showed a slightly different trend, with Eu producing the most distinct signal, followed by Dy, Yb, Nd, and Pr. Negative controls produced little or no signal at the wavelength locations of interest compared to the positive controls and experimental samples. S/N values for each element and treatment are provided in Table 2.2.

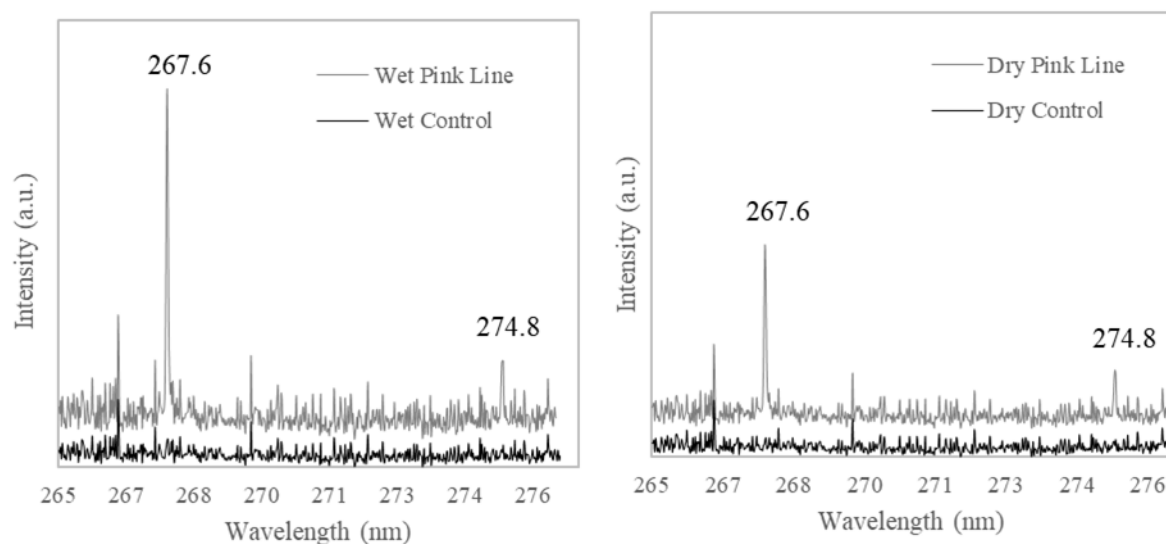


Figure 2.20 Water was added to eight pregnancy test strips. Four were immediately tested with LIBS (left) and the remaining were dried prior to sampling (right). For both wet and dry pregnancy test strips, gold emissions were observed where the pink line was sampled, and not in the area adjacent to the pink line (control). Each data point represents an aggregate of 27 measurements. Experimental and control spectra are offset to facilitate peak comparison.

Analysis with LA-ICP-OES yielded results for Nd, Eu, Dy, and Pr detection that overall reflected the trends observed with LIBS. For all lanthanides, the ICP standard positive control produced the most intense signal, followed by lanthanide-conjugated antibodies, and then untreated nitrocellulose (Figure 2.23).

The results suggest that lanthanide-bearing polymers on nitrocellulose are detectable using LIBS. The positive and negative controls (ICP standards on nitrocellulose and untreated nitrocellulose) were initially used to localize prominent lanthanide emission peaks and determine the background spectrum produced by nitrocellulose. This information was then used to determine the presence of lanthanide-conjugated antibodies on nitrocellulose.

While the results suggested that lanthanide-conjugated antibodies are detectable with LIBS and ICP-OES, this study was not designed to provide quantitative measures of the detection limit. As observed in Figure 2.24, the signal intensity of Eu decreased as different sections of the nitrocellulose paper were sampled. The first peak was associated with ablation along the edge of the paper, whereas subsequent peaks were associated with ablations increasingly close to the center

of the paper. This pattern may be attributed to diffusion properties of liquids containing particulates and suggest that Eu distributed unevenly when dried onto the paper.

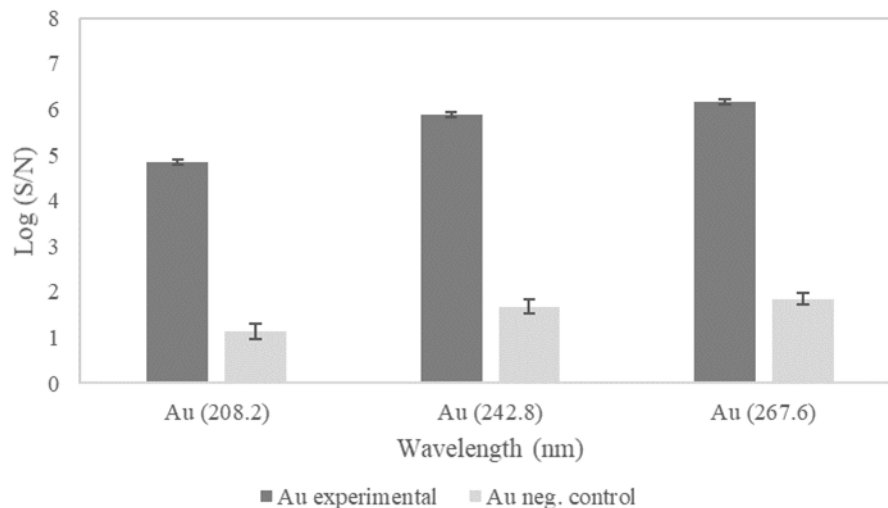


Figure 2.21 LA-ICP-OES was performed on dry pregnancy test strips. The pink line on the strip produced stronger gold emissions at 208.2, 242.7, and 267.6 nm compared to the area adjacent to the pink

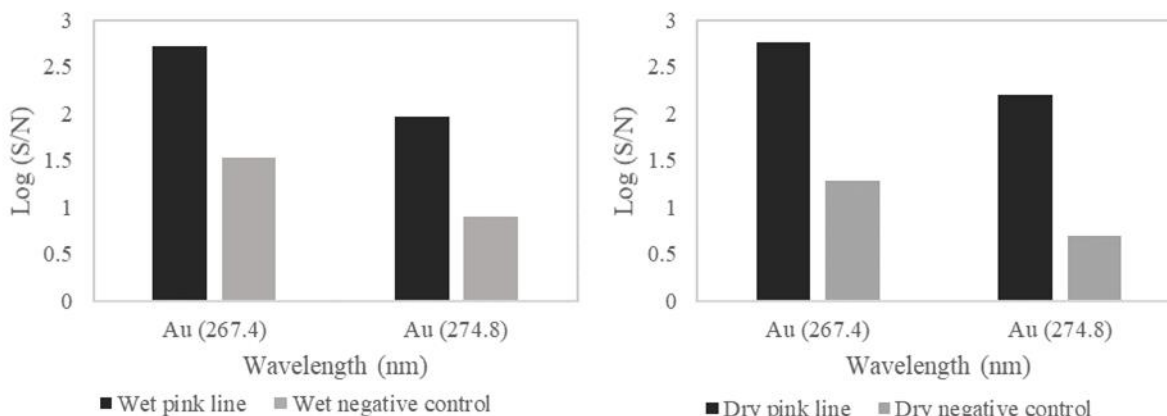


Figure 2.22 Water was added to pregnancy test strips. Three were immediately sampled with LIBS (left plot) and the three were dried prior to sampling (right plot). Two sections (the pink line and area adjacent to the pink line) of each pregnancy test strip were ablated 9 times each. Data on gold emission lines from the same sections of each pregnancy test were aggregated (27 measurements), converted to log of S/N, and plotted. Plot shows that the pink line produced a stronger gold emission line than did the area adjacent to the pink line.

Laser-ablation Inductively Coupled Optical Emission Spectroscopy as a Supporting Analytical Tool

LA-ICP-OES was used as a secondary method of analyzing PBBs and nitrocellulose samples treated with lanthanides. Though this method is not directly comparable with LIBS, the results of the two analytical methods support the same conclusion. LA-ICP-OES can be considered as an acceptable supporting tool for LIBS analysis of PBBs, especially if the same emission lines are compared between both instruments.

Table 2.1 Signal-to-noise ratio was measured for gold emissions lines 267.6 and 274.8 nm among three types of samples: gold foil, dry pregnancy test strips, and wet pregnancy test strips. The gold-foil positive control showed the highest S/N (at 267.6 and 274.8 nm), followed by the pink line, and then the area adjacent to the pink line (negative control).

	Gold foil (S/N)	Dry Pregnancy Test (S/N)		Wet Pregnancy Test (S/N)	
Wavelength (nm)		Pink Line	Adjacent to pink line	Pink Line	Adjacent to pink line
267.6	532	574	20	520	34
274.8	315	160	5	93	8

2.6.5 Summary of LIBS System 4

Compared to the LIBS Systems 1-3, System 4 was capable of detecting metals deposited on nitrocellulose paper. Based on the data collected with the other systems, it can be concluded that both laser power and spectrometer capabilities are key for detecting metals on nitrocellulose paper. Thus, LIBS System 4 at Lawrence Berkeley National Laboratories provided the groundwork for the final instrument design (LIBS System 6), constructed at Purdue University and described in detail in the upcoming sections. While LA-ICP-OES was an interesting option for validating the results obtained with LIBS, the limited availability of these systems made them challenging to access. Therefore, further work using LA-ICP-OES was not pursued.

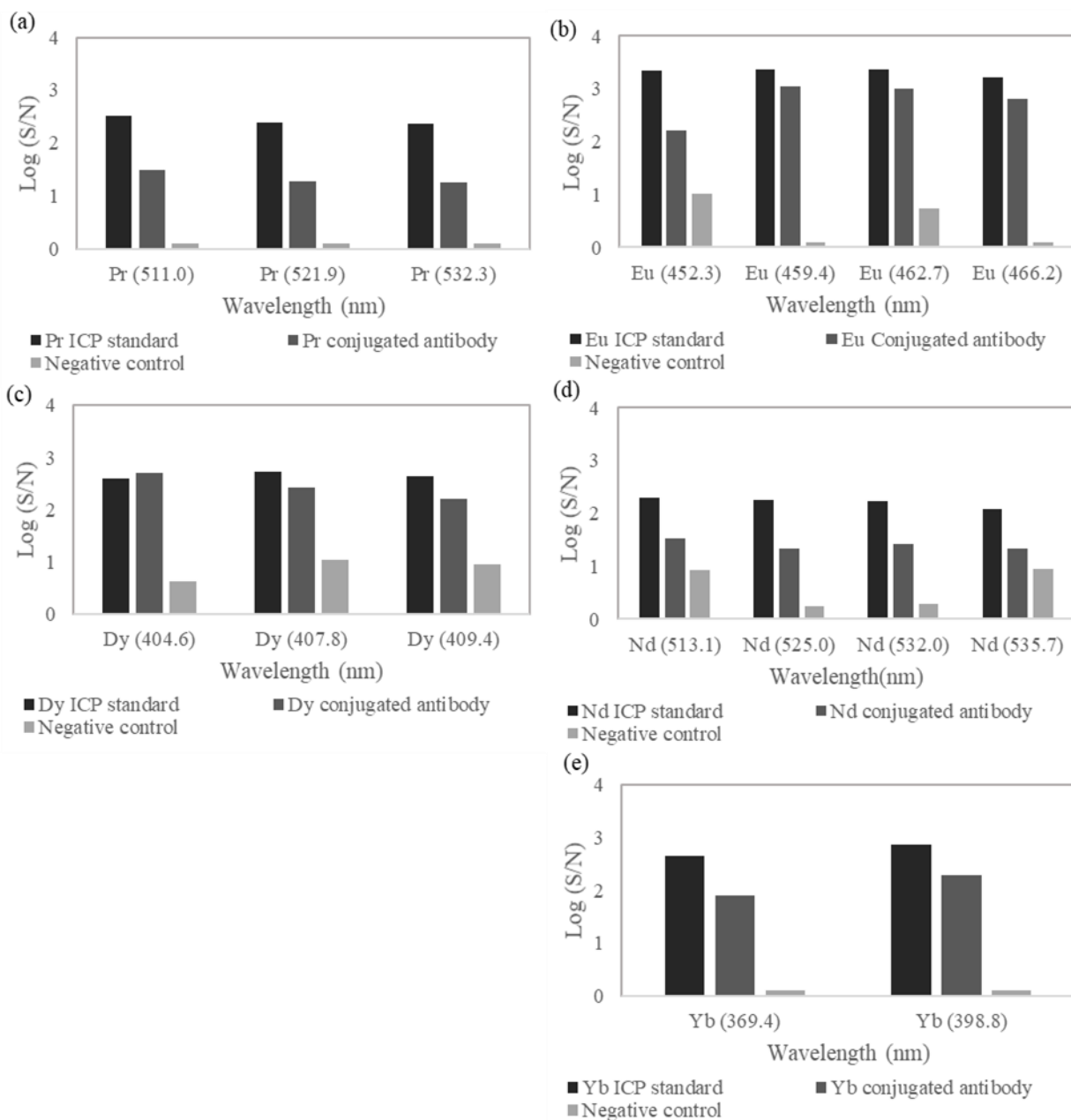


Figure 2.23 LIBS performed on paper samples bearing Pr (a), Eu (b), Dy (c), Nd (d), and Yb (e). For each lanthanide, 3 treatments were tested: ICP standard on paper, lanthanide-conjugated antibody on paper, and untreated paper. All samples were ablated 15 times in different locations. The 15 sampling events were aggregated, converted to S/N in log scale, and plotted. The plots show that for each lanthanide (except the 404.6 nm line of Dy (c)), the ICP standard produced the strongest signal, followed by the lanthanide-conjugated antibody, and then the untreated nitrocellulose.

Table 2.2 Signal-to-noise ratio was measured for lanthanide emissions among three types of samples: ICP standards on paper, lanthanide-conjugated antibodies on paper, and untreated paper. Each value represents S/N calculated from the aggregate of 15 ablations. Both the ICP standards and lanthanide-conjugated antibodies had higher S/N compared to untreated paper.

Wavelength (nm)	ICP Standard (S/N)	Negative control (S/N)	Conjugated Antibody (S/N)
Europium			
452.3	2211	10	167
459.4	2383	0	1106
462.7	2376	5	1030
466.2	1678	0	649
Ytterbium			
369.4	444	0	80
398.8	740	0	197
Dysprosium			
404.6	395	4	522
407.8	532	11	261
409.4	433	9	158
Neodymium			
513.1	203	8	34
525.0	179	2	22
532.0	175	2	27
535.7	120	9	23
Praseodymium			
511.0	338	0	31
521.9	248	0	18
532.3	245	0	18

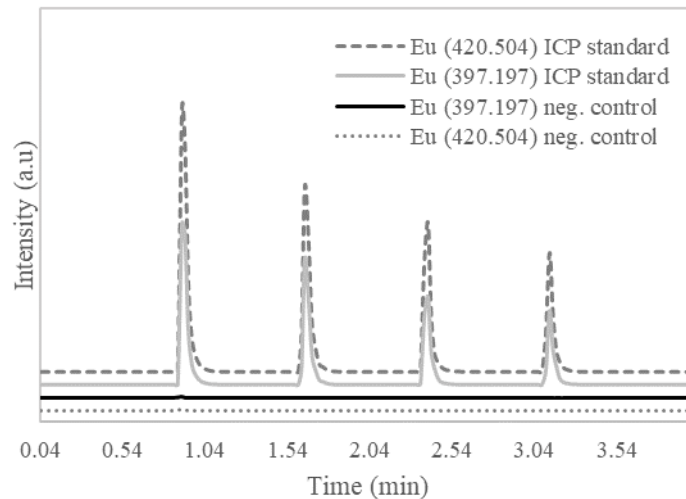


Figure 2.24 LA-ICP-OES was performed on Eu ICP standards on paper in a He carrier-gas environment. The Eu signal in the positive control was observed to spike following each ablation series. Signal was also observed to degrade as the paper was sampled from the edge towards the center. Lines are offset to facilitate peak comparison.

2.7 LIBS System 5



Figure 2.25 LIBS System 5 is a hand-held device sold by SciAps Inc. The LIBS system conveniently fits in a briefcase that can also store spare batteries, argon gas canisters, and supplemental equipment that allows the instrument to be interfaced with a PC or alternative power supplies.

LIBS System 5 (Figure 2.25) was a commercial instrument sold by SciAps Inc. (Woburn, MA, USA). A Z-300 research unit was kindly loaned for evaluation.

2.7.1 Laser, Spectrometer, Optics

The LIBS system was enclosed; most design details were proprietary and therefore are not discussed. The laser consisted of a Nd:YAG 1064 nm Q-switched laser with a pulse energy of 5-6 mJ, pulse width of 1-2 ns, and repetition rate of 50 Hz. For this study, 50 laser pulses were used across a 2×2.5 mm sampling area (one pulse per location). This model of the instrument contained three spectrometers with an acquisition window from 180 to 961 nm and resolution of approximately 0.033 nm. Integration time could be controlled by the user, with a minimum integration time of 1 ms. Spectrometer delay time could also be controlled by the user, with a minimum delay time of 250 ns. Maximum delay and integration times were not reported but were likely to be on the order of several seconds – a time scale that is uncommon in conventional LIBS analysis. Delay time was defined as the time between the laser pulse and signal acquisition. For this study, a 1 ms integration time and 650 ns delay were used. The internal optics of the spectrometer are described in Figure 2.26 [162]. Similar to other LIBS systems in this dissertation, the laser beam was focused onto the sample. A mirror mounted to a stage allows the beam to be moved across the x,y plane. Emissions produced by the sample are focused onto a fiber optic by a series of lenses, directing emissions to a spectrometer.

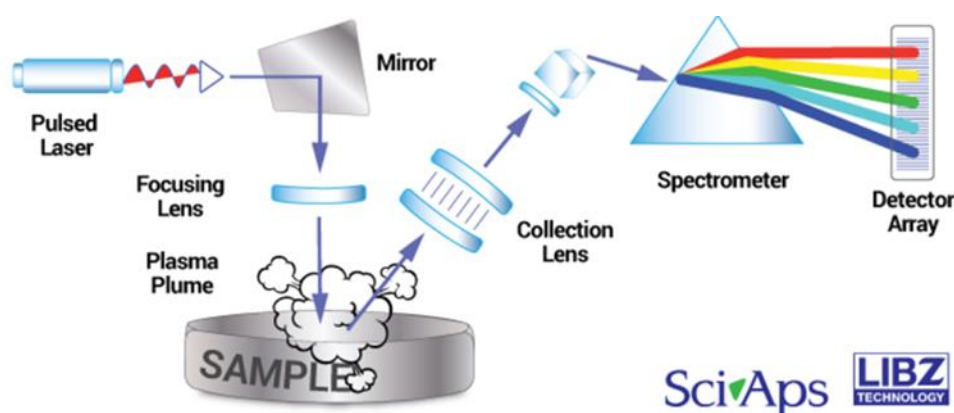


Figure 2.26 Simplified diagram of LIBS System 5 design acquired from SciAps Website.

The unit has a design comfortable for hand-held use. The entire unit is $21 \times 29 \times 11$ cm and weighed 4 lbs with the battery. Control of the system could be achieved through the unit display screen, the trigger button on the unit handle, or a PC with universal serial bus (USB) connection to the unit. The unit contained an argon-gas cartridge that allowed a flush of argon to the sample surface. The time during which argon gas was introduced to the sample surface was user defined. For the studies below, a 1 s argon flush was used. A camera and light-emitting diode (LED) facilitated visualization of the sample. To prevent acquisition of LED emissions, the LED was off during data acquisition. The resulting LIBS emission spectra were visible on the unit display screen or on the computer, allowing the user to quickly assess results.

2.7.2 Sample Preparation and Sample Holder

Samples consisted of a 15-step dilution series of Au, Eu, Lu, and Yb ICP standards from 0.45 to 200 mg/L. The negative control consisted of 2% nitric acid loaded onto nitrocellulose paper. Samples were loaded onto 6 mm \times 6 mm laser-cut Whatman FF120HP nitrocellulose paper and allowed to dry for 2 hrs. Three replicates were made per sample. During ablation, the unit was held upright and samples were pressed against the metal plate where the laser beam exits the unit. It was noted that if the unit was not held upright, debris from the paper would contaminate the quartz plate separating the sample from the laser and light-collection optics. To establish an LOD for Eu, more dilution steps were included such that the minimum concentration was 0.45 mg/L.

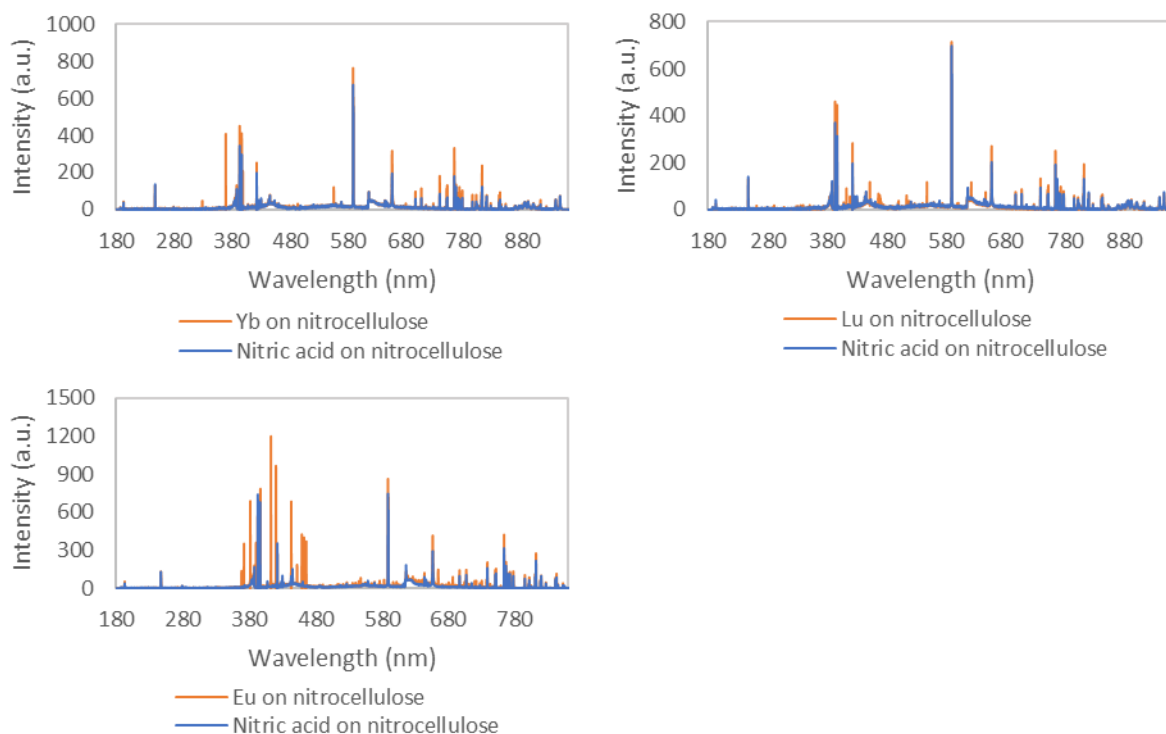


Figure 2.27 Samples of nitrocellulose paper containing Yb, Lu, or Eu CRM solution produced emissions lines that are not observed in the negative control (nitrocellulose treated with nitric acid).

2.7.3 Results

Au was not detectable on nitrocellulose paper, even when higher concentrations of 1000 mg/L were applied to the paper. Conversely, emissions corresponding to Lu, Eu, and Yb were clearly identified in the spectra. Figure 2.27 shows the spectra for Lu, Eu, and Yb on nitrocellulose compared to nitrocellulose treated with nitric acid. The negative control showed multiple emission lines, likely to be associated with carbon, nitrogen, oxygen, and hydrogen (elements composing nitrocellulose and nitric acid). Compared to the negative control, the experimental treatments identified distinct lines not present in the background. Emission lines were selected based on their intensity, and whether the NIST database [159] identified the line as being characteristic to the metals of interest. At the highest concentration (200 mg/L), Eu produced the most intense emission lines at 412.973 and 420.504 nm, followed by Yb at 369.419 nm. Lutetium produced the weakest emissions among the three metals tested.

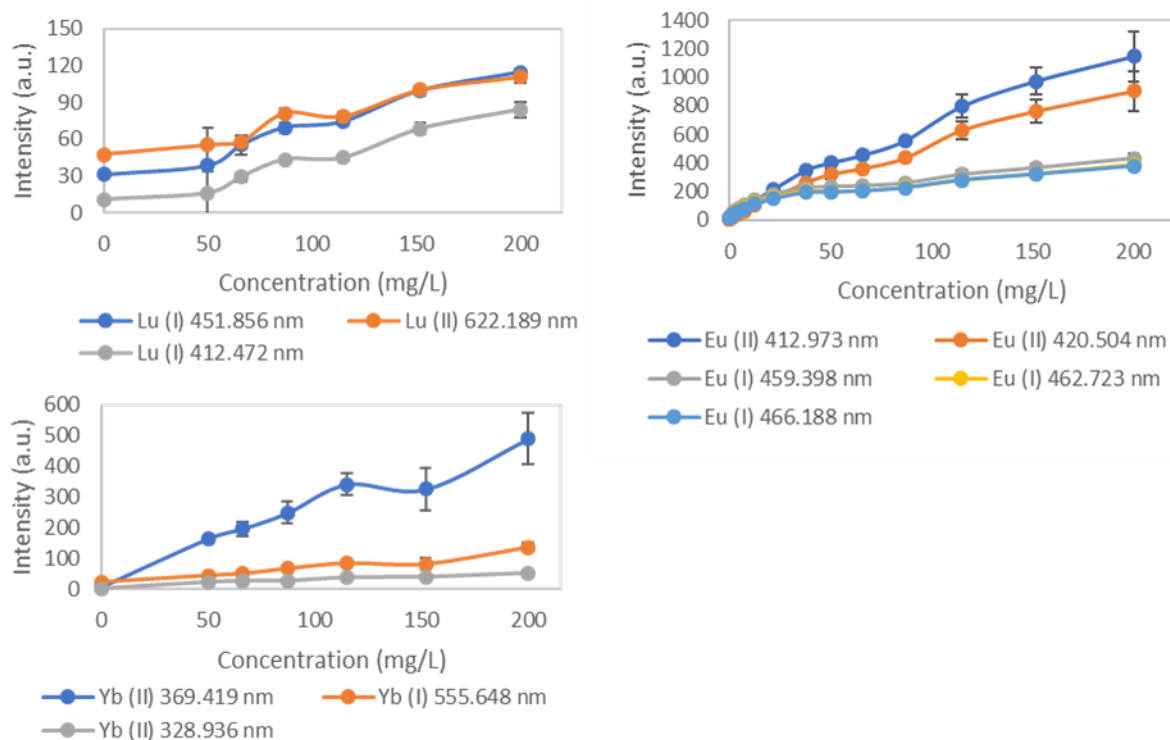


Figure 2.28 As concentration of metal increases, so does the intensity of emission lines indicative of the element. For right-hand graph, data for Eu (I) 462.723 nm is hidden under data for Eu (I) 262.723 nm.

Figure 2.28 shows the intensity of the selected emissions across the dilution series. It was observed that though there was a trend of decreasing signal intensity vs. concentration, the curve was not smooth. Variation in the data could be a result of the method of sample introduction to the laser beam. In the process of manually pressing the sample against the metal plate of the Z-300, it is possible that the sample could have either slightly shifted in the x, y, or z direction during sample acquisition, creating variations in the data. The Z-300 was not designed for the analysis of small paper samples like the 6 × 6-mm nitrocellulose squares in this study and similar material. However, re-designing the interface between the sample and laser would be possible and may result in more consistent data. It was also observed that the negative control in the dilution series did not result in a signal intensity of zero. Broad-band background radiation produced by the sample and captured by the spectrometer is likely to be responsible. A common approach to reduce background signal is by modifying either the acquisition delay or integration time – essentially time-gating the

signal. Though this technique was not applied for LIBS System 5, time-gating experiments were successful for LIBS System 6.

Limit of detection (LOD) was determined for Lu and Eu. For Yb treatments, dilutions were not sufficient to accurately determine the limit of detection. The threshold level (signal intensity) below which the signal was considered undetectable was three standard deviations above the mean. The minimum detectable signal intensity was then applied to the regression line equation of the signal intensity vs. concentration data to determine the minimum detectable concentration. Concentration was then converted to parts per million (ppm) by multiplying concentration by the volume applied to the nitrocellulose (10 μ l) and dividing this value by the mass of nitrocellulose on a 6 \times 6 mm FF120 HP square (1 mg). The detection limit for Eu (I) 462.723 nm and Lu (I) 412.472 nm were determined to be 0.3 and 49.0 ppm respectively.

Overall, the SciAps Z-300 could detect certain metals on nitrocellulose paper. Compared to other LIBS systems described in this chapter, the Z-300 is a hand-held unit. This feature is valuable for the ultimate application of the research in this dissertation – portable detection of metal-labeled bio-contaminants in the field. Aspects that could improve this system's ability to detect metals used for biomolecule labeling are narrower integration times (less than 1 ms) and a design that would facilitate introduction of small nitrocellulose samples to the laser beam. Future experiments would test varying laser energy and spot size to obtain maximum signal intensity from metals in paper samples.

2.8 LIBS System 6

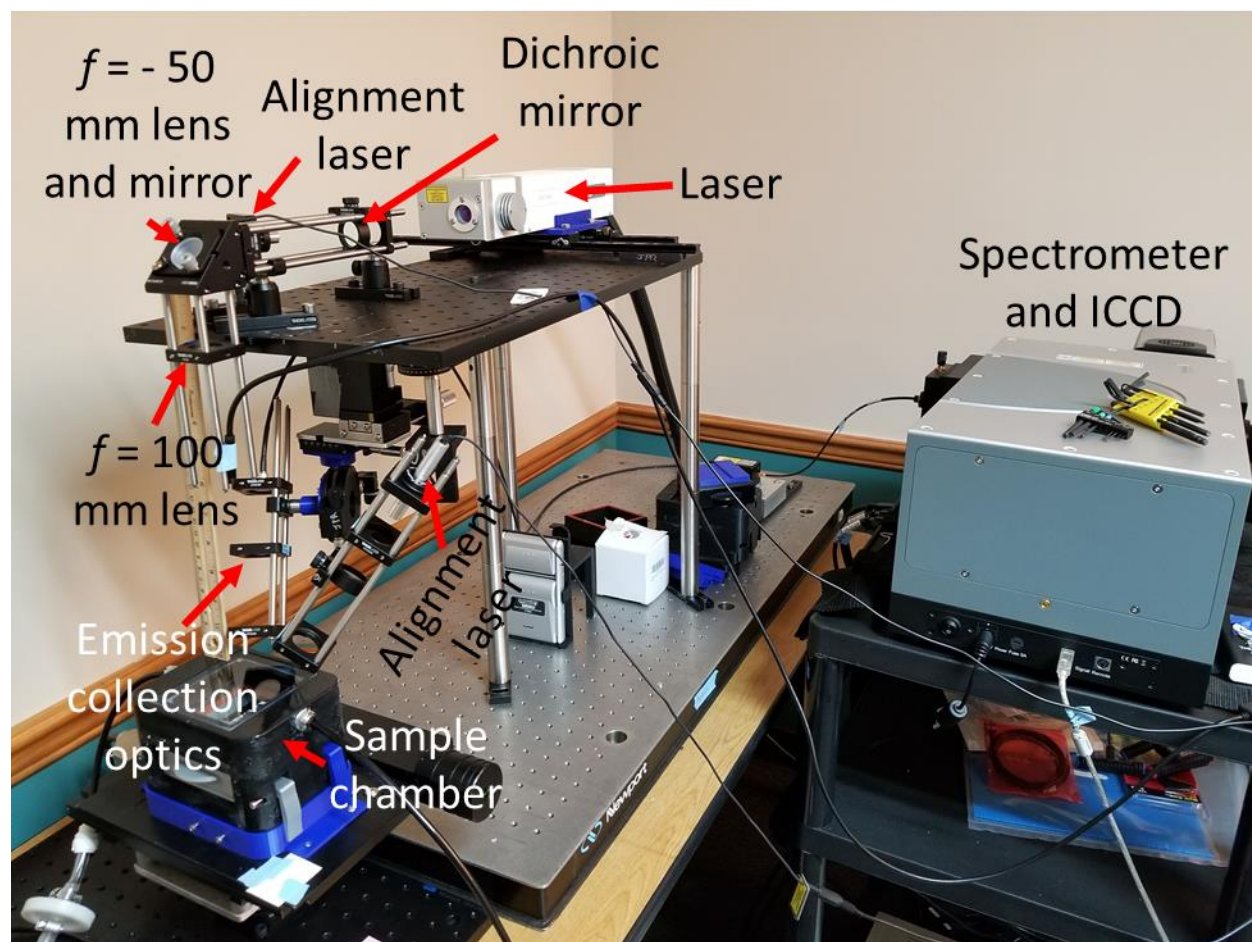


Figure 2.29 The diagram of LIBS System 6 shows the 1064 nm, 150 mJ (maximum), nanosecond laser in line with the optics system. A $f = -50$ mm lens (not clearly visible in the diagram) expands the laser beam, followed by beam-redirection using a mirror. The beam is then focused using a $f = 100$ mm lens into a sample chamber connected to a vacuum pump (not visible in the diagram). Alignment lasers aid with sample positioning. A series of lenses direct emissions to a fiber optic which is connected to a spectrometer and ICCD.

Like LIBS systems 1 and 2, LIBS System 6 (Figure 2.29) was built in-house at Purdue University. This LIBS system was used for most of the studies presented in this document owing to its success in measuring metals on nitrocellulose paper, user-friendly design, and versatility.

2.8.1 Laser

LIBS system 6 utilized the Nano SG 150-10 laser manufactured by Litron Lasers (Rugby, England). The laser consists of a Nd:YAG 1064 nm actively Q-switched laser with a maximum

pulse energy of 150 mJ, pulse width of 4-7 ns, and maximum repetition rate of 10 Hz. As reported by the manufacturer, the laser profile was Gaussian, had an aperture diameter of 4.686 mm, with beam divergence of <0.7 and M^2 of <2 . The laser head dimensions were $\sim 20 \times 8.2 \times 6.2$ cm and the weight ~ 10 lbs. An attenuator also manufactured by Litron Lasers was fitted to the laser head and measures approximately $5 \times 8.2 \times 6.2$ cm. The power supply and water cooler were combined as a single unit. The power supply, water cooler, and laser head can be controlled from a single point using the control box provided by the manufacturer. The controller allows the user to vary repetition rate, pulse number, beam attenuation, q-switch delay, and safety interlocks. It also enables monitoring of the temperature of the Nd:YAG crystal and water being used to cool the laser. With the controller system, the laser can be either fired from the controller, or indicated to fire using an external trigger system designed by the user.

An attenuator consisting of a half waveplate and polarizing filter allows the user to control laser energy. The polarizing filter can be rotated either manually or remotely using the control box. When the laser arrived at Purdue, the gears controlling the rotation of the polarizing filter were not properly secured. Though the problem was unexpected and time consuming, the issue was resolved with the assistance of Litron Lasers technical support. Another method of attenuating the laser beam was to modify the Q-switch delay; however, doing so yielded unstable laser energy output. Therefore, the Q-switch delay was maintained at the manufacturer-recommended 141 μ s.

Nano SG 150-10 design allows the user to monitor the Q-switch flashlamp activation via the power supply. The flashlamp pulses at a rate of 10 Hz and can be monitored using an oscilloscope connected to the flashlamp synchronization port on the power supply. When the laser is indicated to fire using the control box, the Q-switch is internally triggered. Like the flashlamp, activation of the Q-switch can be monitored via the Q-switch synchronization port on the power supply. When the laser was instructed to fire from the control box, the Q-switch was triggered after the flashlamp pulse. The time between the lamp trigger and Q-switch trigger, defined as “Q-switch delay,” was determined by measuring the time between the rising edge of the lamp and Q-switch synchronization pulses (set to 141 μ s). Using the Q-switch sync port and a photodiode placed adjacent to the laser head, it was determined that the time between the Q-switch sync pulse and laser emission was 283 ns (Figure 2.30). Since photodiodes have a short (picosecond) internal delay, the internal delay of the photodiode was not accounted for in this measurement.

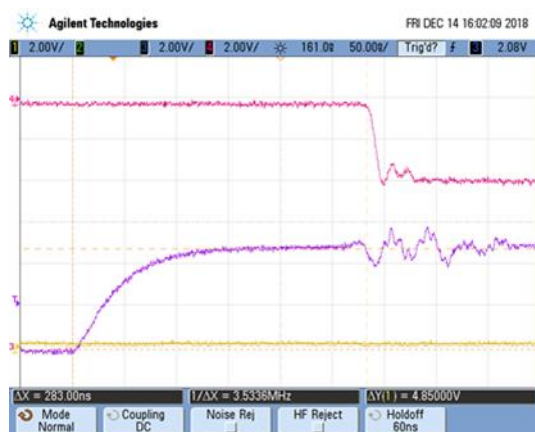


Figure 2.30 Laser synchronization pulses and photodiode readout. Purple line: A voltage rise in the Q-switch synchronization pulse indicated that the laser was about to fire. Pink line: A drop in the photodiode readout indicated that the laser had fired. Yellow line: lamp synchronization pulse rose 141 μ s before the Q-switch pulse (not visible in the displayed scale).

2.8.2 Spectrometer

The primary spectrometer used for LIBS system 6 was the Shamrock 500i imaging spectrograph (SR-500I-B1, Andor, Belfast, UK) fitted with a USB iStar ICCD (DH320T-18F-E3, Andor). The spectrometer contained three gratings, one with a blaze wavelength of 300 nm, and two with blaze wavelengths of 500 nm. The 300 nm and one of the 500 nm blazed gratings had groove spacings of 1200 lines per millimeter (1/mm), whereas the other 500 nm blazed grating had a groove spacing of 600 1/mm. The resolutions of the 500 nm blaze 1200 1/mm grating, 300 nm blaze 1200 1/mm grating, and 500 nm blaze 600 1/mm gratings were 0.095 nm, 0.101 nm, and 0.204 nm respectively [163]. The 1200 1/mm gratings were the primary gratings for the work presented in this dissertation. To detect atomic emissions with a wavelength less than 400 nm, the 300 nm blaze 1200 1/mm grating was used. For emissions above 400 nm the 500 nm 1200 1/mm grating was used. The 400 nm cutoff was determined by measuring the signal intensity produced by a mercury-argon standard light source across the 200 to 600 nm spectrum for each grating, and observing the efficiency of each grating across the wavelength spectrum. Below 400 nm, the 300 nm blaze grating was more efficient. Above 400 nm, the 500 nm blaze grating was more efficient.

The USB iStar intensified charged coupled device (CCD) functioned as a camera and delay generator. The camera has a 1024 \times 256 pixel CCD with a pixel size of 26 μ m. Camera position,

gain, and data-acquisition timing can be controlled from a PC using Andor control software. An oscilloscope can be used to monitor camera function via several reference signals. The arm signal indicates that the camera is ready for data acquisition, the fire signal indicates the time during which the CCD is accumulating charge, and the gate monitor indicates the on/off status of the photocathode. These signals were monitored to determine if the camera was functioning properly (Figure 2.31). The camera's delay generator can be externally triggered. For all the studies presented in this dissertation, the internal delay of the camera – defined as the time between the external trigger and opening of the intensifier (indicated by a voltage change in the gate monitor) – was approximately 35 ns.

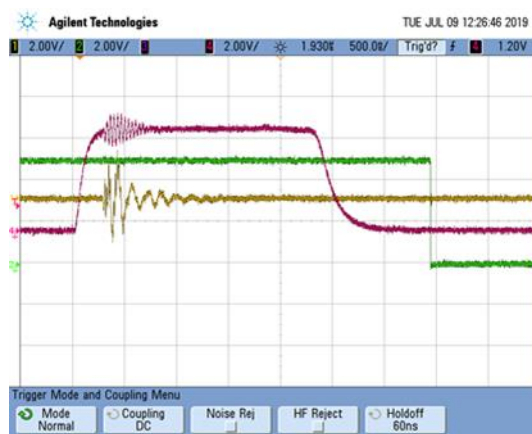


Figure 2.31 Oscilloscope readings of the Q-switch sync pulse from the laser, and ARM and Fire pulse from the spectrometer. Pink Line: laser Q-switch sync pulse – indicated that the laser was about to fire. This pulse goes to the Andor camera external trigger port. Green line: ARM signal – a high voltage indicated that the camera was ready to acquire data. Yellow line: Fire signal – a voltage increase indicated beginning of CCD exposure.

To calibrate the spectrograph, the spectrum of the StellarNet SL2 Mercury Argon Light Source (StellarNet, Tampa, Florida, USA) was acquired once a month. Emission peaks measured by the spectrograph were compared to emissions reported by NIST for mercury and argon [159]. The position of the gratings was then adjusted so that the mercury argon lines were at the same location as the NIST reported lines. In addition to performing monthly quality control using a helium argon light source, controls using CRM solutions at known concentrations were run before every experiment to check the alignment and sensitivity of the spectrometer. The spectrometer and camera could be efficiently controlled using a PC and Andor Solis software package.

The AvaSpec Mini spectrometers AvaSpec-Mini2048L-U25 and AvaSpec-Mini-VIS-OEM described for LIBS System 1 were also used for LIBS System 6. The two spectrometers together acquire across a 400 nm wavelength window with a resolution of 0.25 nm. Whereas LIBS System 1 controlled the AvaSpec Mini spectrometers using software developed at Miftek Inc., LIBS System 6 controlled these spectrometers using the Avantes AvaSoft8 software package. Most studies presented in this dissertation utilized the Shamrock 500i.

2.8.3 Sample Chamber

The sample chamber was designed to completely enclose the sample and hold the sample surface (typically flat nitrocellulose paper) perpendicular to the laser beam. The enclosure was designed on SolidWorks and 3D printed as several separate components: two halves of a box (top and bottom), drawer, drawer platform, platform beams, and handles (Figure 2.31). One side of the bottom half of the box had a rectangular opening where the drawer could be inserted. The top of the box had an opening with a lip lined with a gasket. The drawer was supported by two beams that spanned the width of the bottom half of the box. Between the beams and the drawer exits, a rectangular platform provided a flat surface for the sample drawer. The platform beams were suspended on springs fixed to the bottom half of the chamber. When the handles on the bottom half of the box were rotated, a downward force was exerted on the beams which then compressed the springs. When the springs were compressed, the drawer could be inserted into the box. When the springs were released, the beams and platform pushed the drawer against the gasket. The top half of the box was designed to allow gas to enter and exit the chamber. The exiting gas passed through a high-efficiency particulate air (HEPA) filter to protect the user from aerosols produced during ablation. To allow the laser beam to enter the chamber, the roof of the box consisted of a quartz glass window. Permeability of the chamber was tested by submerging the unit in water. Even after 3-5 minutes of submersion, water did not enter the chamber.

The chamber was fixed to an xyz stage. The stage (TPA-0348A-00 RevX) and control module (TPA-0348A-04 RevX) were manufactured by The Precision Alliance (Fort Mill, SC, USA). Communication with the control module was achieved through the software program EZStepper (Allmotion, Union City, CA, USA). Cole Reynolds, an undergraduate student at Purdue University during summer 2019, improved user-friendly control of the stage by interfacing the control module with a push-button control panel. Mr. Reynolds wrote two programs for the stage:

one which allowed xyz motion, and another that prompted the stage to repeatedly move in a snake-like pattern. The execution of these programs was controlled remotely using the control panel. Automated sample movement greatly improved sampling speed, significantly reducing the time needed to perform experiments.

2.8.4 Electronics and Software

For experiments using the Shamrock 500i spectrometer and USB iStar ICCD, the laser Q-switch synchronization pulse was used as the starting point for all subsequent events. Figure 2.32 shows the timing diagram between the laser and spectrometer. As already noted, the time between the Q-switch sync and the laser pulse was 283 ns, and the internal delay of the camera was 35 ns. For the emissions to be recorded one microsecond after the laser pulse, the delay of the camera was set to 1248 ns. Likewise, for emissions to be recorded two microseconds after the laser pulse, the delay was set to 2248 ns. Once the photocathode was activated, typical integration time was 500 ns. Once an external trigger was sent to the camera, the camera would send a trigger signal to the stage so that it could initiate its programmed motion sequence. Using this sequence of events, data on 25 laser pulses in 25 locations across the sample surface could be acquired in 2.5 seconds when the laser was pulsing at 10 Hz.

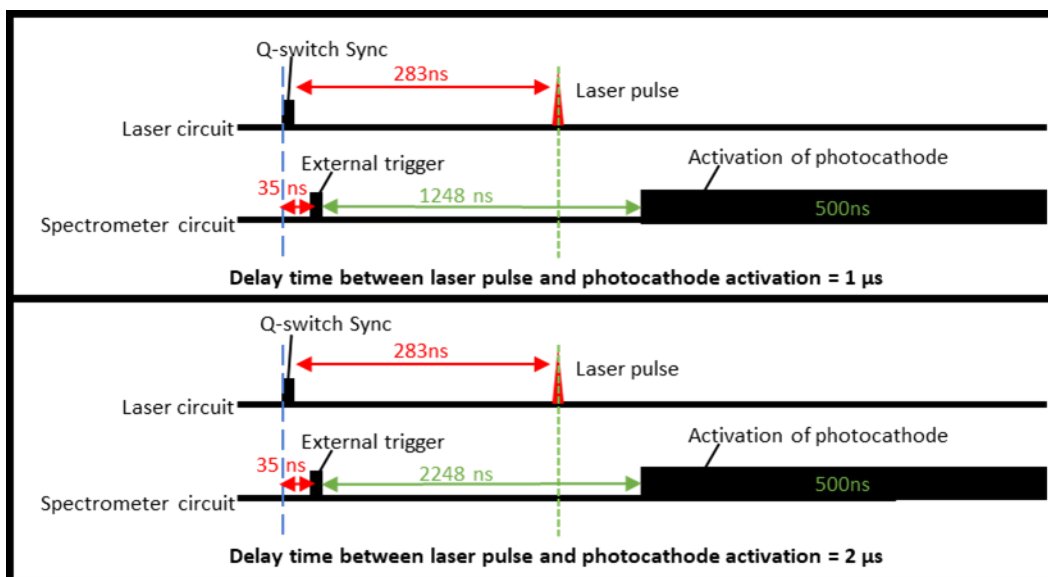


Figure 2.32 LIBS System 6 timing circuit for laser and Andor USB iStar ICCD camera. Values in red indicate internal delays that could not be modified by the user. Values in green could be modified by the user.

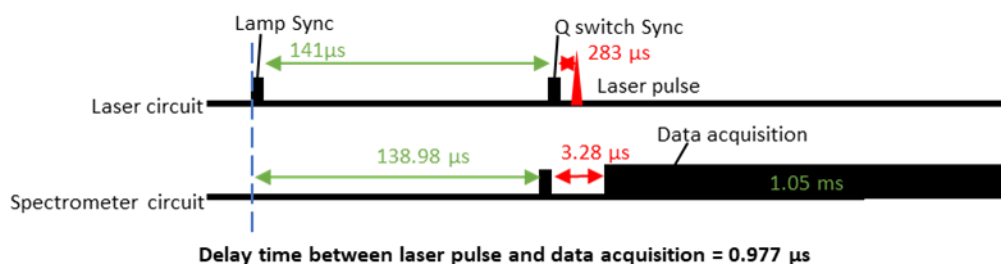


Figure 2.33 LIBS System 6 timing circuit for laser and AvaSpec Mini spectrometers. Values in red indicate internal delays that could not be modified by the user. Values in green could be modified by the user.

For experiments using the Avantes Mini Spectrometers, the sequence of events was different. The spectrometer internal delay was 3.28 μs, whereas the laser internal delay was 283 ns (time difference between the Q-switch synchronization pulse and laser emission) or 141.283 μs (time difference between the lamp synchronization pulse and laser emission). Therefore, to achieve time delays less than ~3 μs, the laser could not be used to trigger the spectrometer. Instead, to control the delays between components, the Sapphire 9200 delay generator (Quantum Composers, Bozeman, MT, USA) was used to externally trigger both laser and spectrometer. For consistent energy output, the flashlamp was internally triggered at 10 Hz. A pulse from the flash lamp served

as the initiation point for triggering other components. Instantly after receiving the flashlamp sync pulse, the delay generator sent a 5 V, 1 ms trigger pulse to the stage, initiating stage movement. 141 μ s after receiving a flashlamp synchronization pulse, the delay generator sent a 5 V, 5 μ s pulse to trigger the laser Q-switch. 138.98 μ s after receiving the flashlamp sync pulse, the delay generator also sent a 5-V, 5- μ s trigger pulse to Pin 5 of the AvaSpec Mini HDMI port (accessed via an HDMI break-out board). Considering that the time between the Q-switch and laser pulse was 283 ns, and the internal delay of the spectrometers was 3.28 μ s, the delay time between the laser pulse and spectrometer data acquisition was 0.97 μ s (Figure 2.33).

2.8.5 Optics

The optical components used for LIBS System 6 are the same as those used for LIBS System 2 with several key differences. In addition to using the 635 nm alignment laser, a 532 nm laser (CPS532, Thorlabs) placed orthogonally to the sample chamber aided with sample positioning. The 532 nm laser was focused onto the sample such that, when the sample surface was at the desired (target) height, the 635 nm and 532 nm lasers intersected on the sample surface. Therefore, when the sample was at the target height, a single yellow spot was observed. If the sample was not at the target height, two spots (red and green) were observed on the sample surface. The target height of the sample was the height at which the spot size on the nitrocellulose surface was approximately 500 - 700 μ m. Determining the optimal sample height is described in Chapter 3.

Another difference between the optics of LIBS Systems 2 and 6 were those used for emission collection. Plasma was collected using a plano-convex 100 mm focal length lens (88-728, Edmond Optics) followed by a plano-convex 50 mm focal length lens (89-179, Edmond Optics) which directed the emission to a UV-VIS fiber optic (SR-OPT-8024, Andor Technologies). The fiber directed emissions directly to the Shamrock 500i spectrometer. In experiments utilizing the AvaSpec Mini spectrometers, the UV-VIS fibers described in LIBS Systems 1 and 2 were used.

2.8.6 Results

The results described here are only for the variation of LIBS System 6 that utilized the Andor Shamrock 500i spectrometer. Ablation of copper foil showed clear emission lines at

510.555, 515.324 and 522.007 nm, which correspond to Cu (I) in the NIST database [159]. It was observed that the background relative to the copper emission line, as well as emission line intensity, changed significantly over the duration of the plasma (Figure 2.34). Early in plasma formation, there was significant background radiation, and copper emission lines were difficult to identify. After a delay of 1 μ s, the peaks were most defined. After 1.3 μ s, peak intensity appeared to decrease while background remained approximately constant. Each line in Figure 2.34 plots represents a single ablation and signal acquisition (260 ns integration time); therefore the standard deviation of the signal at each delay time was not measured. However, the overall trend of copper emission line and background intensity clearly showed a relationship between signal-to-noise ratio and plasma lifetime.

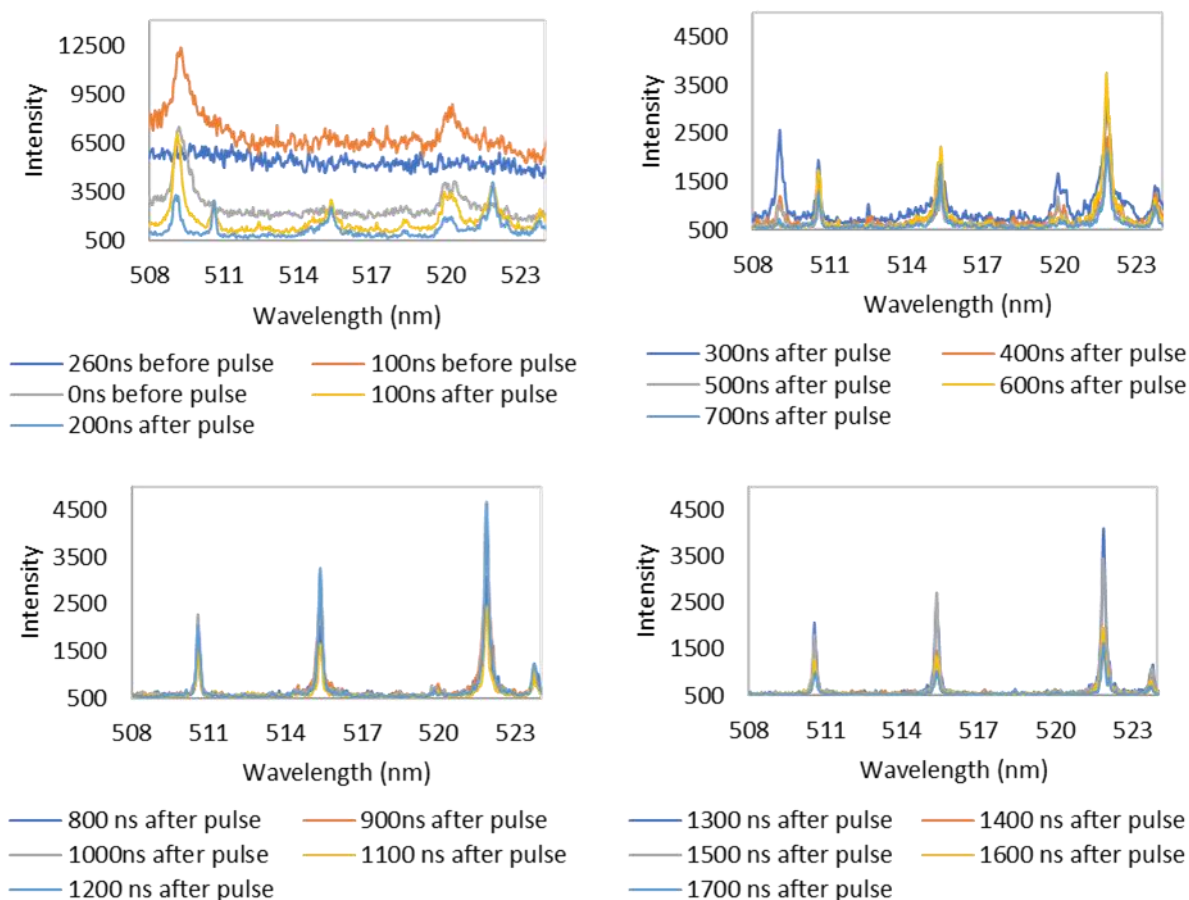


Figure 2.34 Copper emissions from early to late plasma. Over time, continuum radiation decreased, and emission lines appeared. Copper emissions increased in intensity until approximately 1000 ns after the laser pulse, after which emission line intensity decreased.

LIBS System 6 was applied to the detection of metals in nitrocellulose. Solutions consisting of 200 mg metal per liter of 2% HNO_3 were prepared containing Eu, Nd, Pr, Dy, or Gd. 10 μl of each solution was deposited on a 6×6 mm piece of FF120HP plastic-backed nitrocellulose paper. A negative control treatment consisted of 10 μl of 2% HNO_3 . After drying for 2 hrs, each paper was ablated 20 times in 20 different locations and the signal was averaged. Gate delay and integration time were 512 and 50,000 ns respectively. Laser energy was set to 20 mJ. Figure 2.35 shows how the spectra differ between treatments. NIST reports many emission lines for lanthanides [159], complicating the identification of emission lines in the figure. However, several prominent lines matched the NIST database for each element: Nd (II) 401.224, 406.107, and 410.945 nm; Gd (I) 405.364 and 405.821 nm; Gd (II) 409.860 nm; Pr (II) 409.837, 411.845, and 418.948 nm; Dy (I) 418.682 and 421.318 nm; Dy (II) 400.045 nm; Eu (II) 397.197, 412.973, and 420.504 nm. Identification of LIBS emission lines will be discussed further in Chapter 3.

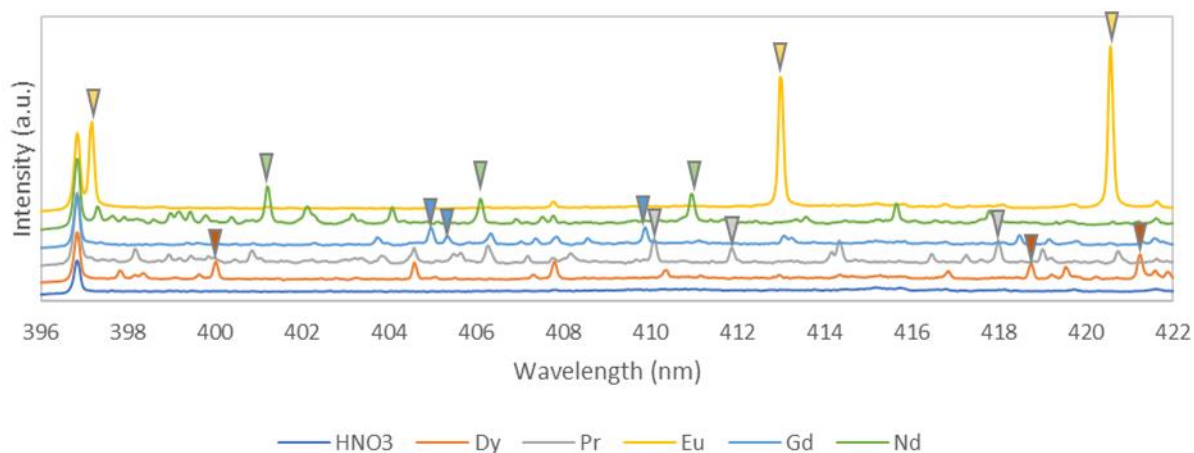


Figure 2.35 Emissions for Dy, Pr, Eu, Gd, and Nd CRM standards on nitrocellulose. Emission lines for each element are indicated by the arrows. Each treatment had a unique spectrum.

2.9 Summary LIBS Systems 1-6

The process of developing a LIBS system for detection of metal biomolecular labels in paper-based bioassays began with LIBS System 1. While this system was capable of characterizing metal foils and wafers, and detecting europium-conjugated antibodies dried on a silicon wafer, it was not capable of detecting europium or other metals embedded in a nitrocellulose paper matrix. Therefore, this combination of components (laser, spectrometer, optics, electronics, and sample

chamber) was not suitable for the application. A similar conclusion is drawn for LIBS Systems 2 and 3, the former being built in-house, the second being a commercial system. LIBS System 4 at Lawrence Berkeley National Laboratories was the first in this series to demonstrate capabilities in detecting metals dried on nitrocellulose paper. Based on the success of LIBS System 4, LIBS System 6 was developed at Purdue University and used similar laser energy, sample chamber design, emission collection optics, and time gating. LIBS System 5 was also successful, and the design had portability as a key advantage over LIBS Systems 4 and 6. Given that each LIBS system used different components, it is challenging to determine which aspects made LIBS Systems 4 and 6 successful in detecting metals dried on nitrocellulose paper. Appendix A hypothesizes reasons behind the differences between each LIBS system's capabilities. Overall, it is evident that the LIBS system must be designed for the material or application, and it is useful to test optimize the parameters of laser, spectrometer, optics, electronics, and sample chamber. While automation is not one of the parameters listed as being key to detection of metals on nitrocellulose, it greatly facilitates the process of system optimization.

3. LIBS SYSTEM CHARACTERIZATION AND OPTIMIZATION FOR QUANTITATIVE LANTHANIDE DETECTION

The previous chapter addressed LIBS system design and ability to detect metals on nitrocellulose. This chapter focuses on LIBS System 6 characterization and optimization for sensitive detection of metals on nitrocellulose. System characterization and optimization involved an assessment of sample preparation, laser power and spot size, data analysis techniques, and establishment of quality-control protocols for the laser, spectrometer, and optics. Key findings were that consistent sample preparation and LIBS system operation were important for reducing variability in the results and improving the quantitative capability and sensitivity of the system. Quantitative, sensitive, and multiplexed detection is valuable for the ultimate application of LIBS System 6 – detection of metal-labeled food contaminants in a paper-based immunoassay. The system's quantitative and limit-of-detection capabilities are explored in this chapter, as well as its ability to perform multiplexed detection. Multiplexed detection of analytes was investigated through LIBS analysis of samples loaded with a variety of metal biomolecular labels. It was found that while quantitative and sensitive detection can be achieved with a single analyte, a mixture of analytes is far more complicated owing to the effect of each analyte on the others.

In the process of LIBS system characterization and optimization, a database of 17 metals was developed for LIBS System 6. Four metals produced distinctly intense emissions – Eu, Lu, Yb, and Ag. The limit of detection of these four metals was compared to that for gold, the material typically used in paper-based bioassays. Limit of detection for Eu, Lu, Yb, and Ag was significantly lower than for gold, suggesting that these metals are appealing biomolecular labels for sensitive LIBS detection of biomolecules in paper substrates.

3.1 Sample Preparation

Our overall research objective was to analyze samples consisting of paper bioassays containing metal-conjugated biomolecular labels. The LIBS systems described in Chapter 2 tested a variety of different samples: metal foils, wafers, and metal suspensions/solutions dried onto nitrocellulose paper.

The metal foils and wafers served as suitable substrates on which to test basic function of the LIBS system and were used to determine if the system “worked” on a basic level. Preparation was fast, often by cutting from the bulk material a section of foil containing a high concentration of the metal of interest. In addition, solid metal was observed to be a substrate that easily generated a plasma, possibly owing to its conductive properties and density. Having a sample that easily generates plasmas is an effective way to perform quality control and troubleshooting on a LIBS system. The substrates presented in Chapter 2 were silicon wafers (444, University Wafers, Boston, MA, USA), copper foil (CU-5, Lyon Industries, Dowagiac, MI, USA), aluminum foil (Reynolds Wrap, Reynolds Group Holdings, New Zealand), gadolinium wafers (693723, Sigma Aldrich, St. Louis, MO, USA), tin foil (265756-9G, Sigma Aldrich), and gold foil (Alfa Aesar 7440-57-5, Tewksbury, MA, USA). Each substrate was placed so that the surface was perpendicular to the incoming laser beam. In the case of gold and gadolinium, each of the metal foils/wafers served as positive controls for experimental samples consisting of gadolinium and gold solutions/suspensions, each of which were loaded onto separate nitrocellulose paper squares. The emission lines generated by the metal foil predicted the location of the emission lines from the experimental samples.

Materials in a paper matrix are more challenging to detect than those in metal foils/wafers. Observing the process of ablation with a camera, it was noted that the nitrocellulose is easily ablated. Nitrocellulose paper is a highly flammable, porous material composed of carbon, nitrogen, hydrogen and oxygen [164]. Nitrocellulose paper used for bio-assays is delicate; where the pores easily collapse if pressure is applied to the structure [165]. The material is not conductive or densely packed like metal foils, and proves a difficult substrate on which to generate plasmas. Even when plasmas were generated, it was challenging to predict whether the metals embedded in the paper would be detectable. An example is a comparison of LIBS Systems 5 and 6. Both systems could easily detect the same quantities of europium on a paper substrate. However, whereas LIBS System 6 could detect gold on nitrocellulose at concentrations as low as 15.968 ppm, gold emissions were not detected with LIBS System 5, even when concentrations were 10,000 ppm (both systems could detect gold in gold foil). This aspect highlights the importance of the substrate and application in the design of a LIBS system.

The primary substrates of interest in this dissertation are bioassays containing metal-conjugated biomolecular labels. However, these assays are time consuming and costly to produce.

To determine if the LIBS system could detect metals on nitrocellulose, a less expensive and faster alternative was used: metals dissolved in nitric or hydrochloric acid and dried onto nitrocellulose paper. The dissolved metals are classified as certified reference material (CRM), and were acquired from either Sigma Aldrich or VHG Labs Inc. The CRMs are described as having either 99.99% purity or impurities at a concentration less than 0.02 ppm at stock concentration. LIBS System 4 tested CRMs containing either Eu_2O_3 , Nd_2O_3 , Dy_2O_3 , Yb_2O_3 , or Pr_6O_{11} acquired from VHG Labs Inc. (PEUN-100, PNDN-100, PDYN-100, PYBN-100, PPRN-100, Teddington, Middlesex, UK). All other LIBS systems used CRMs purchased from Sigma Aldrich that contained Eu_2O_3 (05779-100ML), Nd_2O_3 (1703350100), Dy_2O_3 (68339-100ML), Yb_2O_3 (39956-100ML), Pr_6O_{11} (59947-100ML), Ho_2O_3 (01541-100ML), Au metal (38168-100ML), Cd metal (36379-100ML-F), Cu metal (68921-100ML-F), Er_2O_3 (05693-100ML), Sm_2O_3 (1703480100), Gd_2O_3 (05660-100ML), Ho_2O_3 (01541-100ML), In metal (00734-100ML), Fe metal (43149-100ML-F), La_2O_3 (11523-100ML), $\text{Pb}(\text{NO}_3)_2$ (41318-100ML-F), Lu_2O_3 (03909-100ML), Ni metal (28944-100ML-F), Ag metal (12818-100ML), Tb_2O_3 (44881-100ML), Tm_2O_3 (01496-100ML), and Zn metal (18827-250ML). All metals were dissolved in either 2-5% nitric acid or 2-5% hydrochloric acid (most in nitric acid) at a concentration of 1000 mg/L. Metals were diluted to the desired concentration, typically ranging from 200 – 0.1 mg/L, using the same solvent contained in the stock (either 2% nitric acid or 5% hydrochloric acid). 10 μl of the solutions were then loaded onto 6×6–mm cutouts of FF120HP plastic-backed nitrocellulose (GE Healthcare and Life Sciences, Pittsburgh, PA, USA), dried for at least 2 hours, and analyzed within 12 hrs of drying. Versions of FF120HP nitrocellulose without the plastic backing are also available; however, the plastic backing was useful in preventing solutions from escaping the nitrocellulose material. The nitrocellulose paper was cut using a laser-cutter (VLS3.50, Universal Laser Systems Inc., Scottsdale, AZ, USA) to ensure consistent dimensions between cutouts (Figure 3.2). To determine the amount of nitrocellulose per 6×6–mm square, nitrocellulose on multiple squares was scraped off the plastic backing and weighed. The weight was divided by the number of squares that were scraped. Each plastic-backed nitrocellulose square was calculated to have 0.0010057g of nitrocellulose. Parts per million (ppm) of metal was calculated as the concentration of the metal solution (mg/mL) multiplied by the volume of the solution added to the nitrocellulose (mL) and divided by the mass of the nitrocellulose (kg).

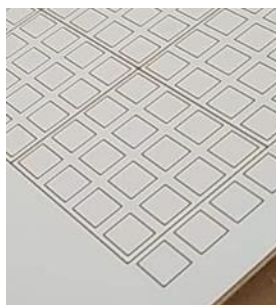


Figure 3.1 Laser-cut nitrocellulose squares, each 6×6 mm. The grooves made by the laser cutter prevented liquid added to a square from seeping beyond the boundaries.

To determine if CRMs on nitrocellulose were suitable for quality control of LIBS System 6, a study was conducted to determine if the CRM solutions evenly distributed across the sample surface, and if they produced a consistent signal day to day. 10 μl of 200 mg/L Eu CRM was loaded onto 15 FF120HP squares and dried for 2 hrs. Each square was ablated 25 times in different locations across the square's surface. Eu(I) signal was measured at 420.504 nm. Among the 25 ablations, the coefficient of variation (COV) is between 1.62% and 2.82% across the 15 samples (within-square COV). When signal from the 25 ablations are averaged per square the COV between squares is 4.55% (between-square COV). To determine day-to-day variations in the LIBS system, 2-3 squares were prepared on each test day using the same protocol as the previous experiment (total of 4 days and 11 samples). Each square was ablated 25 times in different locations. The ablations for all squares on the same day were averaged. Day-to-day COV was measured to be 9.22%. Within-square, between-square and day-to-day COV seemed to be low enough to validate using similarly prepared samples as LIBS system quality-control materials and justify using LIBS System 6 for quantitative detection.

In another study, Gd CRM solution was added to six nitrocellulose paper squares at a concentration of 100 mg/L. Each square was ablated 25 times in different locations across the sample surface in a 5×5 grid. It was hypothesized that the concentration, and therefore the signal intensity, of Gd would be highest at the edges of the paper. This hypothesis was based on the observation of how red food coloring distributed and dried across the nitrocellulose surface – more pigment was present at the edges of the nitrocellulose compared to the center. To determine if the same phenomenon occurred with Gd on nitrocellulose, the signal generated from each column of the grid was averaged and plotted (Figure 3.2). The plot shows a higher concentration of Gd at the

edges of the nitrocellulose. Within-square COV ranged from 17.83 to 20.78%, whereas between-square COV was 8.25%.

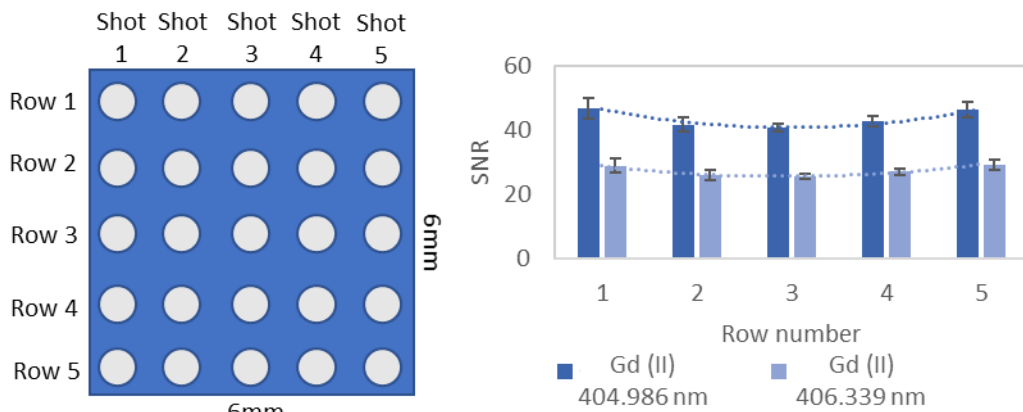


Figure 3.2 Nitrocellulose squares were ablated 25 times in a grid-like pattern composed of five rows and five columns. The average of each row of the grid for two Gd emission lines are demonstrated in a bar chart. The edges of the nitrocellulose produced higher signal intensities than the middle regions.

For the studies conducted with metal solutions on nitrocellulose, the results suggest that variation can be high for different locations within a nitrocellulose square. The recommended approach would be to sample the square across the entire surface and average the signal. Using this method, the coefficient of variance between replicate squares will be approximately 4.55 to 8.25%. Alternatively, a technique for drying liquid solutions on paper more evenly can be employed [25]. Using food coloring, it was found that the solution dries evenly across a surface when placed in a vacuum (0.000263 psi) (Figure 3.3). For the work in this dissertation, equipment to reach this this level of vacuum was not readily available. However, a COV between 4.55 and 8.25% obtained from drying samples at atmospheric pressure was determined to be acceptable for the purposes of this research.

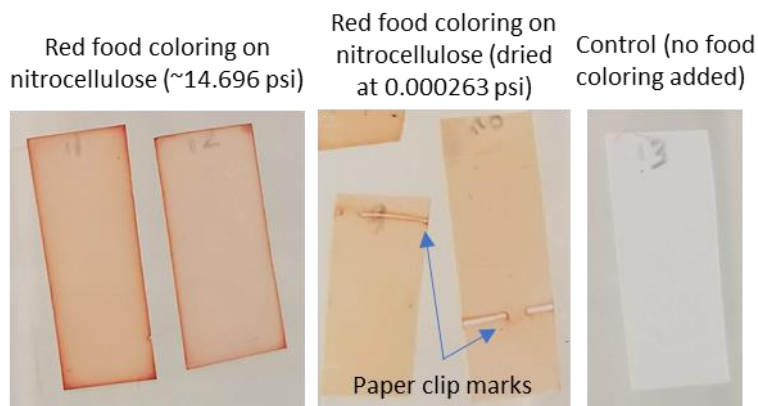


Figure 3.3 Uneven drying of red food coloring on nitrocellulose in air at atmospheric pressure suggested that material gathered at the edges of the nitrocellulose. When nitrocellulose was dried under vacuum, the distribution of red food coloring was more even.

3.2 Laser, Spectrometer, and Optics Quality Control

Before experiments were performed on LIBS System 6, quality control was performed on the laser, spectrometer, and optics. This provided consistency in instrument performance. LIBS System 6 was built in-house over the course of several months. Inconsistent operation of the system at early stages of development yielded inconsistent results for replicate samples tested across different days. However, when the instrument design was finalized with appropriate quality control measures, samples yielded more stable day-to-day consistency.

Spectrograph and camera quality control involved irradiating nitrocellulose paper in the sample chamber with the 635 nm alignment laser. Spectrograph acquisition settings were set to a 0 ns delay time and 200 μ s integration time, with no gain applied to the intensifier. Each grating was set to zero order mode such that all wavelengths were reflected onto the camera's detector. If optics were properly aligned, a peak was visible at center of the detector. Optics were adjusted such that the peak reached a maximum intensity. Maximum peak intensity was recorded across 15 acquisitions and compared to similar data collected across different days to assess variations in spectrometer performance. For future studies it is recommended that noise be measured as well. Some variation in signal intensity was expected owing to environmental fluctuations (temperature, humidity, pressure). Figure 3.4 shows that peak intensity, indicative of spectrometer performance, changes day to day. For studies that compared data collected across different days, variations in

spectrometer performance were accounted for by running replicate treatments of CRM solutions on nitrocellulose each day an experiment was conducted. The type of CRM used depended on the nature of the experiment (e.g., experiments focused on Eu detection used Eu CRM solutions). During data analysis, emission-line signal-to-noise ratios (SNR) were either scaled up or scaled down based on the results from the replicate treatments of CRM solutions.

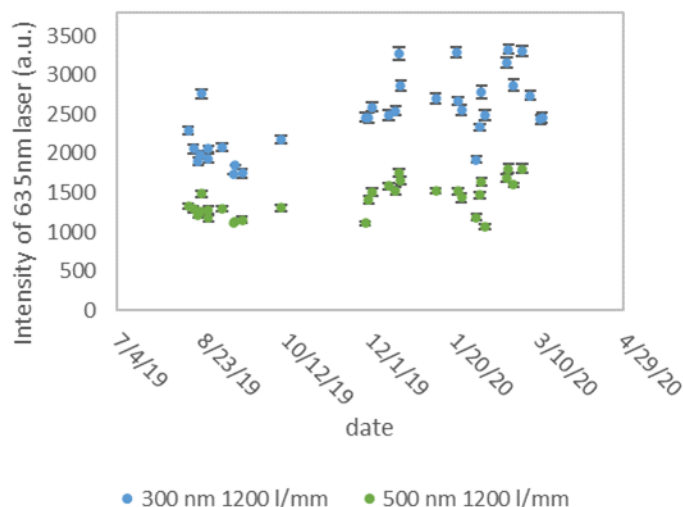


Figure 3.4 Day-to-day measurements of a 635 nm laser reflected on the surface of nitrocellulose were performed as a measurement of optics alignment and spectrometer performance. Variations in signal intensity were observed across months of measurements for two gratings with a 300 nm and 500 nm 1200 l/mm blaze.

Laser quality control was performed by measuring laser pulse energy before an experiment, when the water temperature reached the stabilization point of 39-40 °C. When measuring pulse energy, laser attenuation was kept at 25% (for laser output power of 33.6 mJ) to avoid damaging the sensor (ES111C, Thorlabs, NJ, USA) and the laser was pulsed 25 times at 10 Hz. As additional protection, a neutral-density filter with an optical density of 2 was placed in front of the sensor. Laser energy measurements collected across 13 days show little variation in energy (COV = 0.091%). Variation across 25 pulses was also low (COV = 0.38 to 1.65%).

Quality control of optics involved a visual assessment of whether dust had accumulated on the optical components. If so, optics were cleaned using isopropanol and lens paper. A fluorescing alignment disk (VRC2D05, Thorlabs) was used to check the alignment of the 1064 nm laser beam as it traversed each optical component.

3.2.1 Laser Warm-up Time

Experiments performed with the Litron SG-150 laser showed that laser “warm-up” time affects laser output energy. In the case of the SG-150 laser, “warm-up” referred to the process of the laser’s reaching a stable operating temperature of approximately 40 °C. Laser temperature was displayed on the controller screen of the controller system, allowing the user to monitor laser temperature in real time. Stable operating temperature was determined experimentally by monitoring laser temperature and energy every 5 min as the flashlamp pulsed at 10 Hz for 75 min. Laser energy was measured using the Thorlabs (Newton, NJ, USA) ES111C pyroelectric energy sensor and PM100D hand-held energy meter. The sensor was placed perpendicular to the laser beam. Every 5 min, the sensor recorded 20 laser pulses at a rate of 10Hz. To prevent damage to the energy sensor, a neutral density filter with an optical density of 2 was placed in front of the sensor. Figure 3.5 shows the laser temperature and power over time. The data indicate that over time, output energy and temperature respectively decrease and increase for the first hour and then gradually approach a plateau. Standard deviation in output energy ranges between 1 μ J and 2 μ J. Temperature readings consisted of a one-time measurement and therefore do not have an associated standard deviation. The results suggest that to obtain a stable energy output from the laser, a “warm-up” time of 1-1.5 hours is recommended. Laser energy contributes significantly to the process of plasma formation on a sample (Section 3.3). Litron Lasers does not provide warm-up time recommendations for the SG-150; however, the brochure mentions that the maximum laser energy advertised for their products was measured after a 15-minute warm-up time.

The literature suggests that the practice of laser warm-up is based on anecdotal experience rather than formal studies. Laser distributors such as Coherent often list laser warm-up times in their product description. Fast warm-up times are favorable because they allow more rapid experimentation and may reduce strain on laser components, improving the longevity of the laser. A study by Grayson et al. (2017) addresses the importance of Q-switched Nd:YAG laser warm-up, but from the perspective of beam stability [166]. Though the study by Grayson et al. and this one address the importance of laser warm-up from two different perspectives (beam stability and laser energy), the conclusions are similar – laser warm-up should be performed prior to experimentation. The study by Grayson adds that the Q-switch trigger does not need to be operating during warm-up; pulsing the flashlamp is enough.

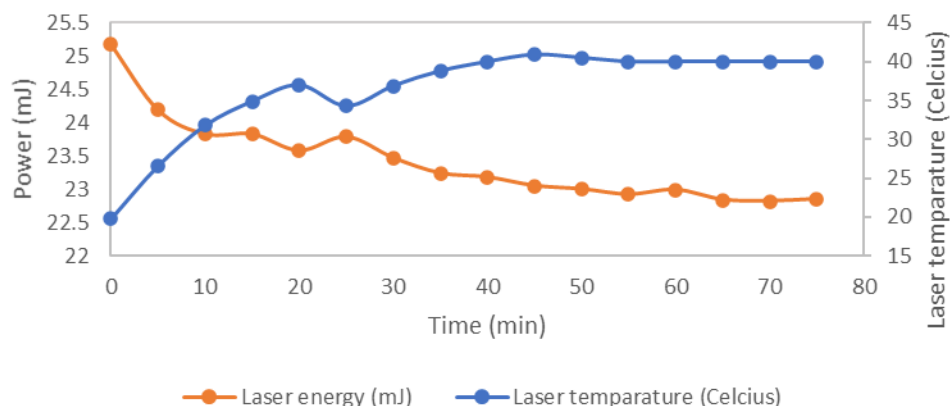


Figure 3.5 The flashlamp of the Litron SG-150 laser was pumped at 10 Hz for 75 min. Over the course of the 75 min, the Q-switch was activated 20 times at 10 Hz every 5 min. When the Q-switch was activated, laser energy and temperature were recorded. Over the course of 75 min, laser energy decreased and stabilized, whereas temperature increased and stabilized.

3.3 Spot Size and Laser Energy

3.3.1 Imaging LIBS Ablation Zone

Three methods were used to determine laser spot size: white-light interferometry (WLI), electron microscopy, and stereomicroscopy. Each method has its advantages. WLI provides a three-dimensional topographic heat map and surface depth profiles that facilitate quantitative measurements between features across the sample surface. The resolution of electron microscopy allows the user to see fine details such as debris deposited at the edges of ablation craters and produces visually appealing images. Stereomicroscopy is easily accessible and fast, permitting rapid data acquisition.

LIBS System 4 was used to ablate the surface of a silicon wafer and nitrocellulose paper (using one pulse per material). When the surface of the silicon wafer was analyzed with WLI, a clear crater mark was observed (Figure 3.6). The crater had distinct walls around the borders. From the borders to the center of the crater, crater depth gradually increased then peaked at $3.75\ \mu\text{m}$. The shape of the crater mimicked what was expected from a Gaussian-shaped beam, where energy sharply increases towards the center of the laser spot. The walls around the crater likely result from the shockwave created as the laser ablates the sample surface. Though the walls may indicate the

diameter of the shockwave, it does not necessarily indicate the diameter of the laser beam. It is also notable that there are two walls formed around the crater. It is speculated that the inner wall (134 μm diameter) resulted directly from the shockwave, whereas the second wall is a ring of material that was re-deposited after the shock wave. A similar pattern can be seen in the electron microscopy images taken of craters formed by LIBS System 2, specifically the treatment where 1000 laser pulses were fired at 1 kHz (Figure 2.12). A wall was observed immediately around the center of the crater followed by a second wall of seemingly deposited debris. Unlike WLI or electron microscopy, stereomicroscopy did not provide as much topographical detail of the ablation zone. Figure 2.12 can be used to compare images of a crater formed by LIBS System 2 taken with electron microscopy vs. stereomicroscopy. Much less detail is observed in the latter case. However, stereomicroscopy at least allows a fast and rough estimation of crater diameter. In most cases, a rough estimation of crater diameter sufficed.

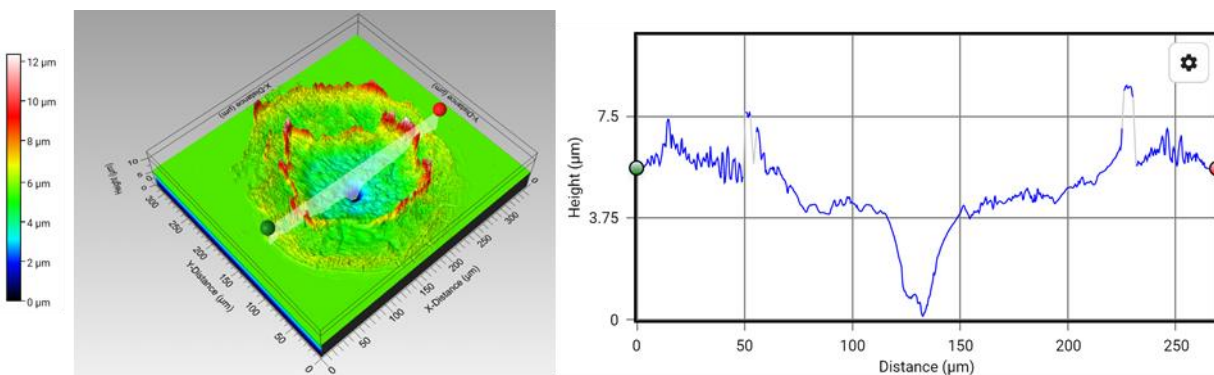


Figure 3.6 White-light interferometry image of a crater produced by LIBS System 4 on the surface of a silicon wafer. The laser beam formed a Gaussian-shaped crater, whose deepest point was approximately 5 μm from the surface. Circling the crater were two rings of material taller than the sample surface, potentially indicating material ablated from and deposited onto the wafer surface.

Interpreting the spot size created by LIBS System 4 on a paper substrate was more challenging. When characterizing the crater using WLI, the porous surface of the paper makes the edges of the crater difficult to discern. In addition, nitrocellulose is lighter and softer than a silicon wafer, which may affect the way the material is ablated and how the shockwave propagates and re-distributes material. A deep crater in the middle of the ablation zone is still observed. In this case, the crater depth was 75 - 150 μm (compared to the silicon-wafer crater depth of 3.75 μm),

indicating that the laser beam ablated through the nitrocellulose layer (100 μm thick) [167] and reached the flat plastic backing (Figure 3.7). The crater diameter on nitrocellulose was 346 μm , significantly larger than that formed on the silicon-wafer surface (134 μm in diameter). Though debris around the crater wall was evident, an inner and outer wall could not be clearly discerned. Electron microscopy was not used to view craters formed in nitrocellulose; however, in separate studies using electron microscopy on nitrocellulose, it was noted the nitrocellulose degrades under the electron beam. While it may be possible to mediate this effect by changing the electron beam voltage, degradation of nitrocellulose while analyzing LIBS crater profiles may lead to an inaccurate characterization of the crater. Stereomicroscopy is an option for measuring crater diameter in nitrocellulose. However, like the case of the silicon wafer, little information on the topography is gained.

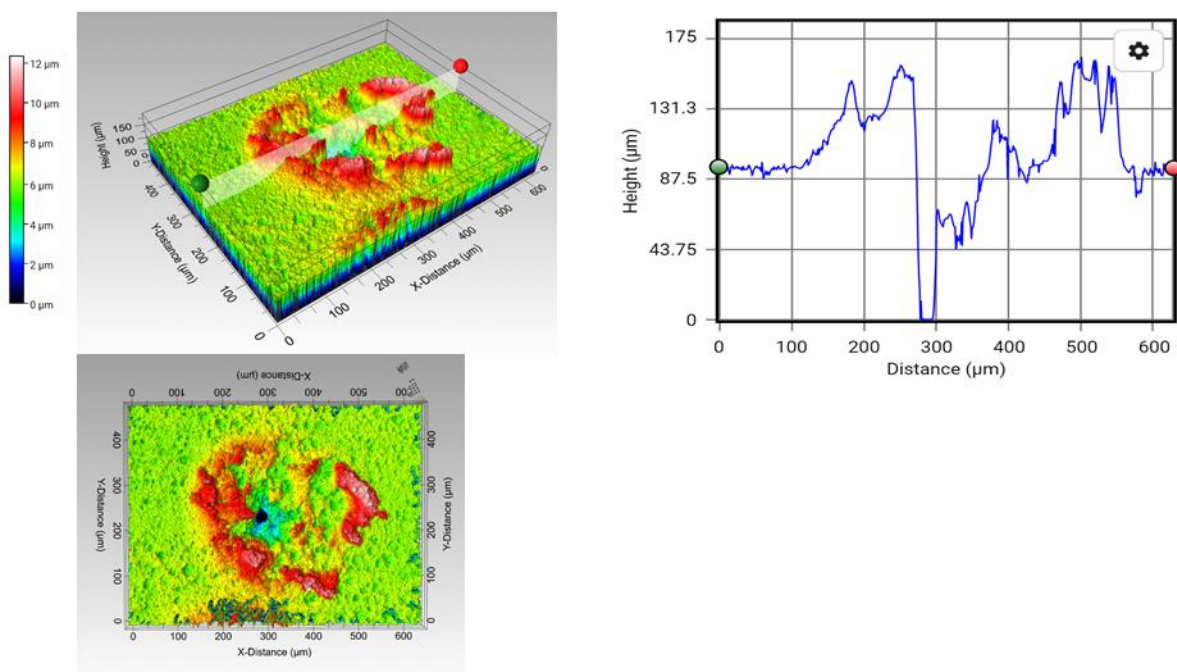


Figure 3.7 White-light interferometry image of a crater produced by LIBS System 4 on the surface of nitrocellulose paper. Maximum crater depth was approximately 88 μm from the sample surface. Circling the crater was an uneven ring of material taller than the sample surface, potentially indicating material ablated from and deposited onto the sample surface.

3.3.2 Spot size, Power, and Irradiance

To understand the relationship between laser energy, spot size, and sample position of LIBS System 6, experiments were conducted by varying each parameter and measuring the size of the ablation mark on a sample surface. The sample consisted of a glass microscope slide colored with ink from a black Sharpie and placed on a sheet of white paper. The laser beam would ablate and remove the pigment, producing a clear circle that sharply contrasted with the black ink surroundings. Using a micrometer and a microscope, the diameter of the spot was measured.

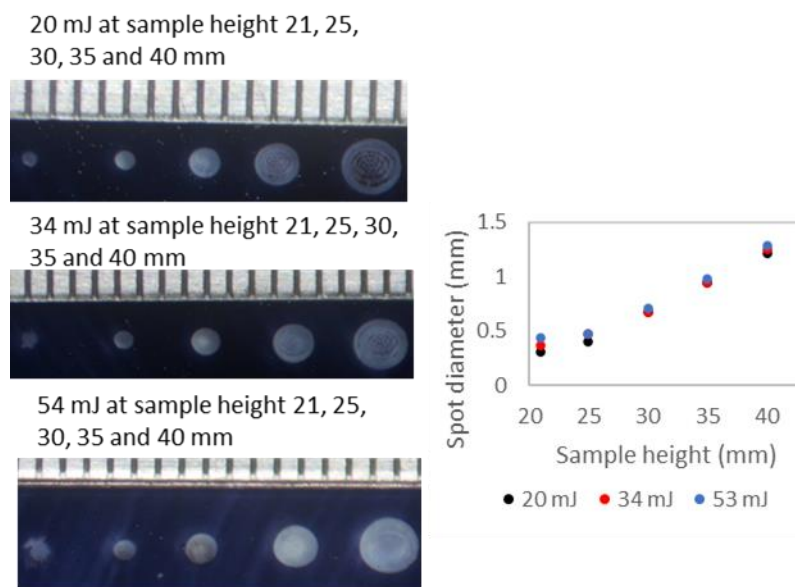


Figure 3.8 A microscope slide colored with a marker provided a convenient substrate on which to measure laser spot size. As laser energy increased, spot size remained the same regardless of sample position relative to the focal plane. As the sample was moved out of the focal plane, spot diameter increased.

The position of the sample relative to the laser focusing lens is referred to as “sample height.” As the sample surface is moved closer to the lens, the sample height increases. A decrease in sample height refers to distancing the sample from the lens. As laser power was increased from 20 to 34 to 53 mJ, spot size remained identical irrespective of sample height (Figure 3.8). However, as sample height increased, spot size increased at the same rate for each power treatment, indicating that the sample surface was moving away from the laser focal plane. A similar technique was applied to determine the minimum spot size of the laser. For this experiment, laser energy was maintained at 20 mJ. The sample, again consisting of a glass microscope slide coated in black ink,

was positioned above and below the presumed focal plane. As the sample was moved into and out of the focal plane, the diameter of the spot decreased, plateaued between sample heights of 20 to 25 mm, and then increased (Figure 3.9). The minimum spot size achieved was 338 μm .

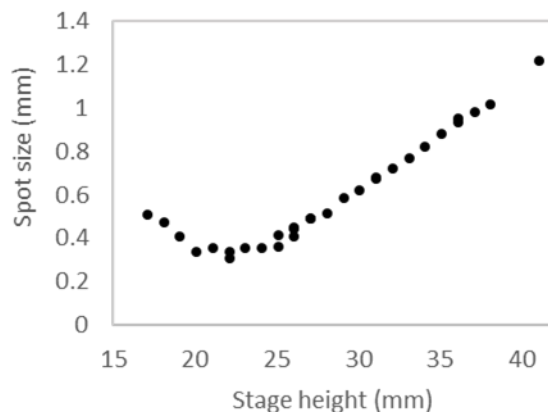


Figure 3.9 As a microscope slide coated in black ink was moved into and out of the focal plane of the laser, spot size decreased, plateaued, and then increased. The plateau indicated the size of the beam waist.

The relationship between spot size and energy is irradiance (energy per unit area). To determine if irradiance had an effect on the signal intensity, gadolinium on a paper wafer was ablated in different locations at different sample heights. To prepare the samples, 10 μl aliquots of a 200 mg/L solution (metal in 2% nitric acid) were loaded onto a 6×6 mm nitrocellulose squares and allowed to dry for 2 hrs. Irradiance was controlled by changing the sample height while maintaining energy constant. Sample size consisted of 5 ablations in 5 locations for each sample-height interval. The process was repeated for 3 energy levels: 20, 34, and 53 mJ. The Gd signal was measured as the peak intensity at 405.364 nm, an emission reported by NIST [159] as being indicative of Gd. Figure 3.10 shows that the irradiance level that produces the most intense signal is dependent on laser energy.

Another interesting aspect was whether signal intensity would increase if irradiance was kept constant while energy and spot size increased. Samples consisted of 10 μl aliquots of 200 mg/L of europium (in 2% nitric acid) added to nitrocellulose. Each treatment consisted of 5 repetitions. As spot size and laser energy increased, Eu (II) signal intensity at 397.197, 412.973, 420.504 nm decreased (Figure 3.11). Trends observed in the studies with gadolinium and europium could be associated with plasma shielding. More material ablated from the sample surface may

cause a denser cloud of material above the sample, inhibiting emissions from Gd or Eu from escaping the plasma and reaching the detector. The phenomenon of plasma shielding is mentioned numerous times in LIBS literature [12, 168, 85].

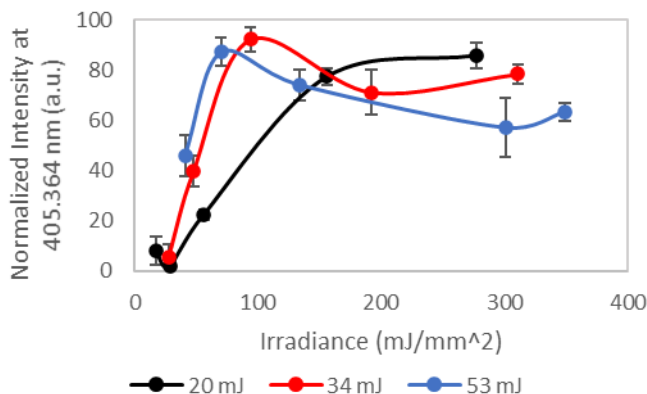


Figure 3.10 Variation in irradiance on a nitrocellulose sample treated with Gd CRM solution yielded changes in signal intensity at 405.364 nm (Gd emission line location). The irradiance level at which the signal peaked was dependent on laser energy.

3.4 LIBS Signal Processing

The data regarding LIBS Systems 1-6 in chapter 2 represent raw signal intensity across a wavelength range. While the raw signal can be useful in assessments of the plasma or instrument performance, applying data-processing techniques can simplify analysis of emission lines and aid in comparing data collected by different instruments or by the same instrument on different days. In the majority of this dissertation, LIBS spectra were analyzed using a custom-developed procedure written in R language for statistical computing [169]. A sliding median filter (using a 101-pixel width) estimated the background across the wavelength range and was subtracted from the raw data. An example is shown in Figure 2.15, where background subtraction is applied to LIBS analysis of three types of samples: Dy dissolved in nitric acid on nitrocellulose paper, Dy-conjugated antibodies dried on nitrocellulose paper, and nitric acid on nitrocellulose paper. Background subtraction reduced bremsstrahlung radiation, essentially leveling atomic emission lines.

After background subtraction, signal to noise ratio (S/N or SNR) was calculated. Two methods were compared for calculating S/N. One method was to measure the signal adjacent to

the emission lines of interest, where there were no interfering atomic emission lines. Continuing with the example of Dy, three regions adjacent to NIST-reported Dy emission lines at 404.597, 407.796, and 409.610 nm (reported in Figure 3.13 as 404.59, 407.58, and 409.95 nm) were selected as noise. Each region represented 50 pixels, 15 pixels away from the base of the peak. To standardize the signal, the intensity of the emission line was then divided by the standard deviation of the adjacent region. The second method was to use a median filter (again using a 101 pixel width) to estimate overall noise of the spectrum. As in the first method, the signal was standardized by dividing the intensity of the emission line by the standard deviation of the median filter. To evaluate the performance of the two methods, both were applied to the analysis of Eu, Yb, Dy, Nd, and Pr CRM solutions dried onto nitrocellulose paper.

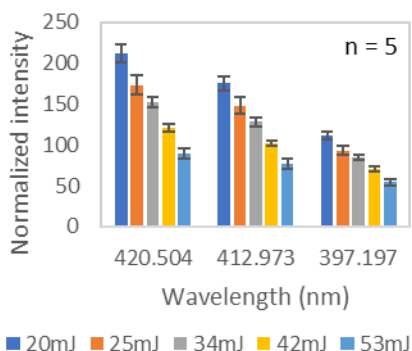


Figure 3.11 Europium peak intensities decreased as laser power increased while maintaining irradiance constant (by increasing spot size).

Overall, method 1 for determining signal to noise performed better than method 2. Most lanthanides have many closely spaced emission lines, compared to other elements. Therefore, in cases regarding lanthanides, the region adjacent to the peak not only may be noise but also could contain an emission line. If this is the case, the adjacent area does not truly represent noise, but a mixture of signal and noise, resulting in an inaccurate representation noise. A higher standard deviation in the noise region caused by the presence of an emission line would affect the denominator in the signal-to-noise ratio calculation. An example is the treatment consisting of Dy CRM solution on nitrocellulose (Figure 3.13). Adjacent to the 404.59 nm peak, in the region considered as noise, there is a clear peak that does not appear in the negative control. As explained earlier, the presence of an emission line in the “noise” region results in an inaccurate representation

of S/N. Another complication with method 1 is the subjective process of choosing a region to designate as noise, allowing the user to intentionally or unintentionally manipulate the signal to noise ratio. Method 1 can be applied for data analysis; however, it may be best suited for spectra with low densities of emission lines.

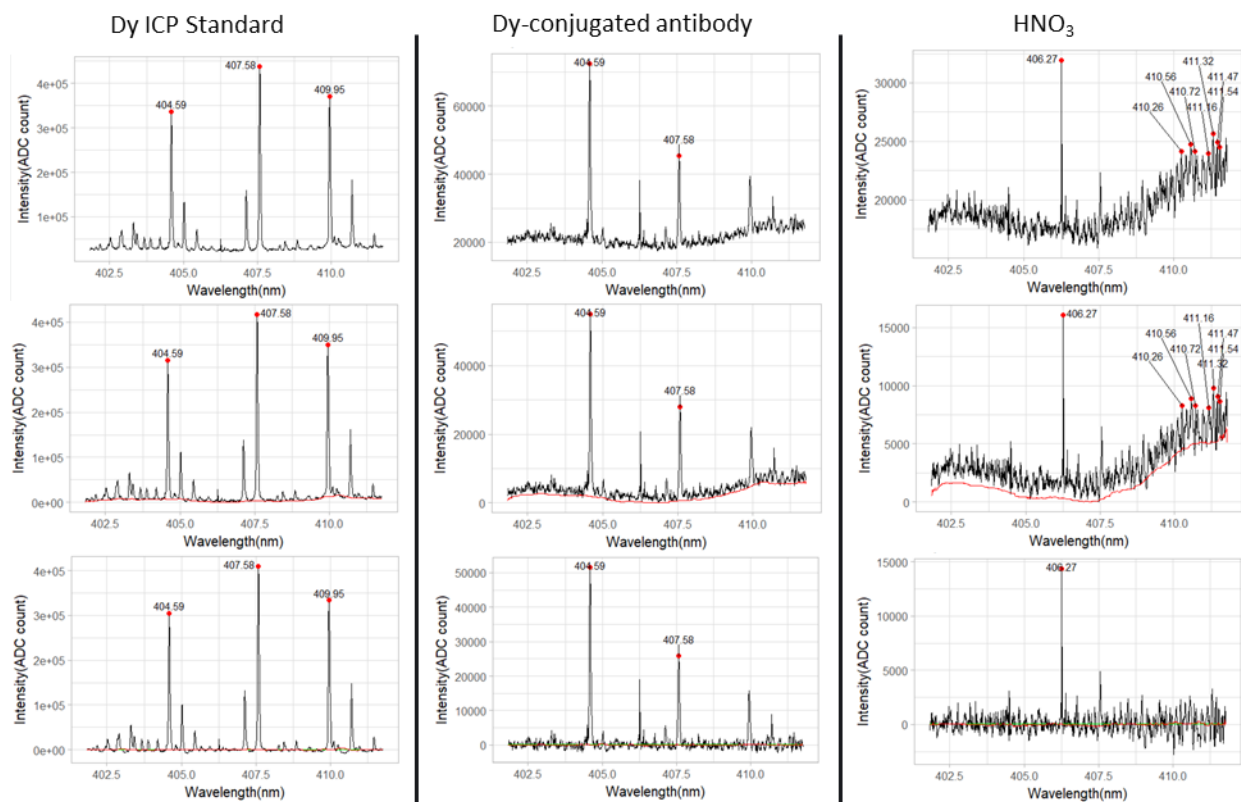


Figure 3.12 The signal-processing approach applied to Dy CRM solution (Dy ICP standard), Dy-conjugated antibody, and a negative control: row 1 displays the raw signal; the red line in row 2 represents a median filter applied to the data; row 3 shows subtraction of the median filter from the data.

Method 2 accounted for the data acquired across the entire width of the detector, removing the need for subjective selection of a region to consider as noise. By using a 101 pixel median filter across the spectrum, overall variations in the data were captured and were minimally influenced by the narrow emission lines. This method seemed effective for complex spectra such as those produced by Dy, Pr, and Nd. Since selection of the noise region was not required for method 1, data analysis using method 2 was faster. Comparing data across treatments and methods shows that method 1 yielded lower S/N compared to method 2 for emission lines identified for Eu, Dy,

Pr, Nd, and Yb (Table 3.1). S/N is greater in method 2 compared to method 1, as well as the difference between the experimental treatments and the negative control.

Given that method 2 was more robust when applied to complex lanthanide spectra, and less vulnerable to user bias compared to method 1, method 2 was the used to standardize the data presented in this dissertation.

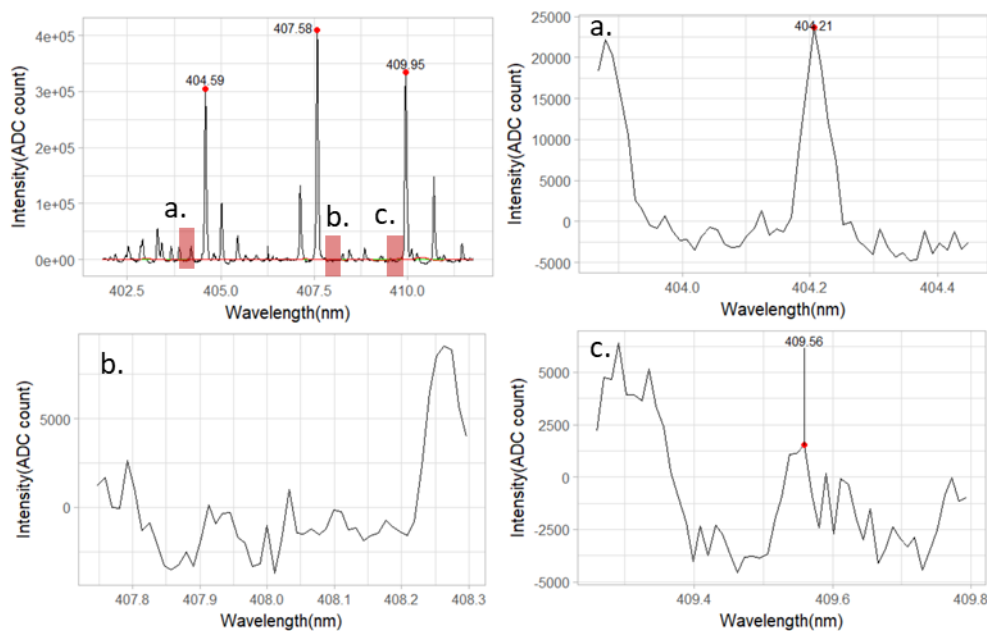


Figure 3.13 Top right: raw spectrum of Dy CRM solution on nitrocellulose. The red areas labeled as “a,” “b,” and “c” indicate regions adjacent to Dy peaks considered noise and used to calculate SNR. A closer view of these regions shows that other unidentified peaks may be present in these regions, indicating that this method of calculating SNR is subject to error.

Table 3.1 Comparison of two methods for calculating emission line SNR for five elements. Method 1 (left) defined noise as the standard deviation of the 50-pixel region near the emission line. Method 2 (right) defined noise as the standard deviation of a median filter applied to 868 pixels of data (the full spectral window). Method 2 yielded much higher SNR for experimental treatments and slightly higher SNR among the negative controls.

Method 1				Method 2			
Wavelength (nm)	ICP Standard (S/N)	Negative control (S/N)	Conjugated Antibody (S/N)	Wavelength (nm)	ICP Standard (S/N)	Negative control (S/N)	Conjugated Antibody (S/N)
Europium				Europium			
452.258	641.7	0.6	63.8	452.258	2211.0	10.4	166.9
459.398	618.1	0	284.6	459.398	2382.9	0.0	1105.7
462.723	665.7	0.3	279.9	462.723	2375.5	5.4	1030.2
466.188	431.6	0	50.9	466.188	1677.7	0.0	648.8
Ytterbium				Ytterbium			
369.419	347.9	0	50.5	369.419	444.4	0.0	80.0
398.799	24.2	0.0	0.9	398.799	739.7	0.0	197.0
Dysprosium				Dysprosium			
404.597	38.7	0.5	53.2	404.597	280.9	4.3	522.0
407.796	132.6	1.3	25.8	407.796	153.7	11.1	260.6
409.610	114.2	0.8	19.0	409.610	97.1	9.0	158.3
Neodymium				Neodymium			
513.059	25.0	0.9	1.7	513.059	202.9	8.4	33.8
525.081	8.5	0.1	2.2	525.081	179.1	1.8	21.9
531.982	39.6	0.2	3.3	531.982	175.3	1.9	26.7
535.697	6.6	0.5	2.7	535.697	120.1	8.8	21.9
Praseodymium				Praseodymium			
511.037	98.5	0	5.7	511.037	334.5	0.0	31.3
521.905	58.1	0	4.7	521.905	238.4	0.0	18.4
532.277	28.8	0	2.5	532.277	232.6	0.0	17.9

3.5 Emission Line Selection

3.5.1 NIST Atomic Spectral Database

The NIST atomic spectral database (ASD) is a compilation of emission lines and associated details compiled across a variety of studies by different authors using different instruments and experimental conditions. While the NIST ASD is extremely useful in providing predictions as to which emission lines to expect in LIBS data, it serves more as a guideline rather than a definitive document. The NIST database provides abundant information in the line table. The information

found to be most applicable to LIBS spectrum analysis was ion identity, observed wavelength, Ritz wavelength, relative intensity, and transition strength.

Ion identity lists the ionization state of the element producing the emission line of interest. The ionization state of most elements reported throughout this study are either neutral (e.g., Eu (I)) or singly ionized (e.g., Eu (II)) since they are the most likely to occur in air [168]. The NIST database reports two wavelengths per emission line – observed and Ritz wavelength. The former is an experimentally determined wavelength, while the latter is calculated based on the upper and lower energy levels of electron transition. This document reports primarily Ritz wavelengths unless they are unavailable, in which case observed wavelengths are reported. Relative intensity is used as a guideline to compare the emission strength of one line to another. Two lines in the line table were considered comparable only if they were reported by the same study. The reason is that relative intensity values are dependent on the equipment (detector, amplifier, etc.) and signal-processing techniques (normalization vs. raw data) used by the author who supplied the data to NIST. Transition strength refers to the probability that an electron will transition from a higher energy level to a lower one. Transition probability is associated with emission line strength. As an example, the Eu (II) emission line at 420.504 nm was one of the strongest among the lanthanides tested in this study and had a reported transition probability of $7.1 \times 10^7 \text{ s}^{-1}$. For some emission lines, like most of those associated with Gd, transition probability is not reported. In this dissertation, emission lines for metal elements were identified if they 1) appeared in the experimental sample as a single, narrow peak and did not appear in the negative control, 2) were less than 0.5 nm from a NIST-reported emission line, and 3) the NIST-reported line identified the ionic state of the element, Ritz wavelength, relative intensity, and transition strength. Exceptions were made in some cases (like Gd) where only observed wavelength was available or transition strength was unavailable.

The most effective method to identify emission lines was found to be a combined approach of utilizing positive experimental controls composed of CRM solution on nitrocellulose, negative controls, and the NIST ASD. Relying solely on the NIST ASD yielded uncertain results because reported emission lines did not always appear in the experimental spectrum. Less often, emission lines in the experimental spectrum were not reported by NIST. This could be due to the different instrument and environmental conditions under which the reported data and experimental data were acquired. It may be an appropriate approach for LIBS users to develop an element library for

their own instrument, using the NIST ASD as a guideline, rather than relying solely on the NIST ASD.

3.5.2 LIBS System 6 Atomic Spectral Database

To build a database for LIBS system 6, the spectra of 17 metals from 200 to 600 nm were acquired. The metals of interest were those found to be commonly used for biomolecular labeling (Tm, Lu, Dy, Tb, Ho, Sm, Er, Pr, Gd, Nd, Yb, Eu, Zn, Cd, Au, Ag, and Fe). Most of these elements are lanthanides, which are used for antibody labeling and are commercially sold as part of antibody conjugation kits by Fluidigm Co. (San Francisco, CA, USA). The kits sold by Fluidigm allow the user to attach metals, presumably in a form similar to the CRM solutions, to polymers, and subsequently to antibodies. Other elements such as Au, Ag, and Fe are commonly used in LFIAs, often in the form of nanoparticles that are then coated by biomolecules. Elements like Zn and Cd are found in quantum dots, which are also sold in kits for antibody conjugation. The method for developing the database depends on the LIBS system used to acquire the database. For LIBS System 6, the spectrometer defined the process for acquiring the database. A portion of this data can also be found in “Detection of *E. coli* labeled with metal-conjugated antibodies using lateral-flow assay and laser-induced breakdown spectroscopy”, published in *Analytical and Bioanalytical Chemistry* (DOI:10.1007/s00216-019-02347-3).

Some spectrometers investigated in this document (Avantes AvaSpec Mini and Applied Spectra Aurora Spectrometer) are capable of acquiring across spectral windows that are several hundred nanometers wide. An advantage of having a wide spectral window is rapid data acquisition across a wide spectrum (milliseconds). The gratings applied to the Andor Shamrock 500i in LIBS System 6 can acquire only 30-60 nm windows, a significantly narrower window than the AvaSpec Mini or Aurora spectrometers. Therefore, to acquire a 200 to 600 nm spectrum, multiple 30 nm windows were collected from 200 to 600 nm and then stitched together to create the full spectrum. After some automation of the system, the process took 30 min, significantly longer than acquiring the data with the AvaSpec Mini or Aurora spectrometers. The advantages of having a narrow spectral window and an ICCD detector (Andor USB iStar) are: 1) acquisition of highly resolved spectra (~0.1 nm resolution) and 2) short integration times – on the order of nano- and microseconds vs. milliseconds. This feature permits studies investigating changes in emission-

line intensity in response to 0.5-1 μ s changes in acquisition delay time when the integration time is 0.5-1 μ s.

Samples were prepared by loading nitrocellulose paper squares with 10 μ l of 200 mg/L metal CRM solutions (20 squares per metal) and following the protocol outlined in Section 3.2, *Sample Preparation*. 100 squares were prepared per element, and each square was ablated 25 times in different locations across the square. Delay time was set to 0.5, 1, 2, 3, and 4 μ s. Integration time was maintained at 500 ns. Signal from each square (25 acquisitions) underwent baseline correction, standardization, and averaging. After sampling a square, the spectrograph grating was moved to collect across a new spectral window.

The negative control consisted of nitrocellulose paper treated with the diluent used for the CRM (2% HNO_3 or 5% HCl). Pure nitrocellulose is composed of C, N, O, and H; therefore these lines were anticipated in the LIBS spectrum of the negative control (Figure 2.17). Impurities in the nitrocellulose, naturally found in the starting material or introduced through proprietary processing methods, were also important aspects to consider. For example, prominent sodium lines were observed in the spectrum (Figure 3.14). Understanding the emissions of nitrocellulose helped distinguish it from the emissions produced by the CRMs loaded onto the nitrocellulose. Emissions produced by the nitrocellulose were most intense at 0.5-3 μ s delays. C, H, and Na lines were often observed to be more intense than the lines produced by the CRM solution. Lines from the CRM that overlapped with lines originating from the nitrocellulose were not considered for analysis. The negative control against which the experimental CRM treatments were compared in Figure 3.15- Figure 3.19 consisted of an average of the nitrocellulose spectrum across each delay time.

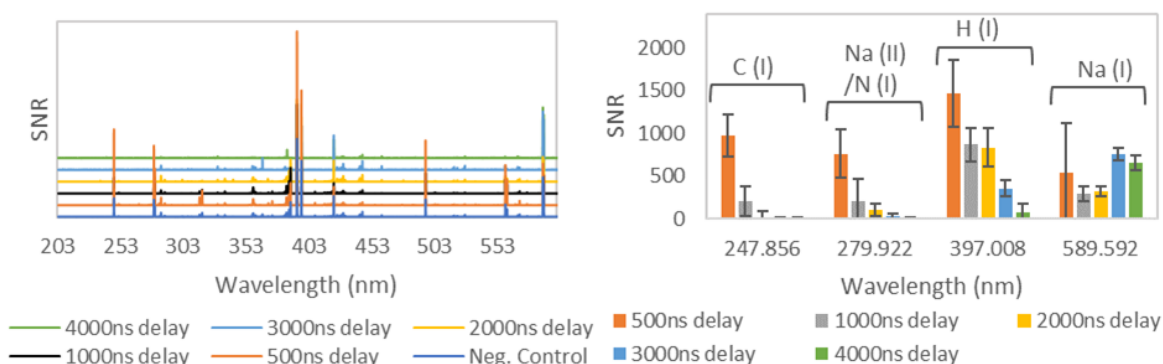


Figure 3.14 Spectrum of nitrocellulose paper at delay times of 0.5, 1, 2, 3, and 4 μ s. C (I), Na (II), N (I), and H(I) were observed to produce some of the strongest emission lines from nitrocellulose. An average of the spectra across all delay times was used as the negative control for treatments consisting of CRM solutions on nitrocellulose.

Acquiring the 200 to 600 nm spectrum of 17 elements demonstrated that each element has a unique spectrum. Figure 3.15-Figure 3.19 show the spectrum of 17 elements across five delay times. The scale of each plot was adjusted to emphasize the lines produced by the CRM rather than the intense emission lines of the nitrocellulose – hence, some of the strong lines produced by the nitrocellulose are not fully visible in the plot.



Figure 3.15 Spectra of Ho, Tm, Zn, and Ag on nitrocellulose paper at delay times of 0.5, 1, 2, 3, and 4 μ s.

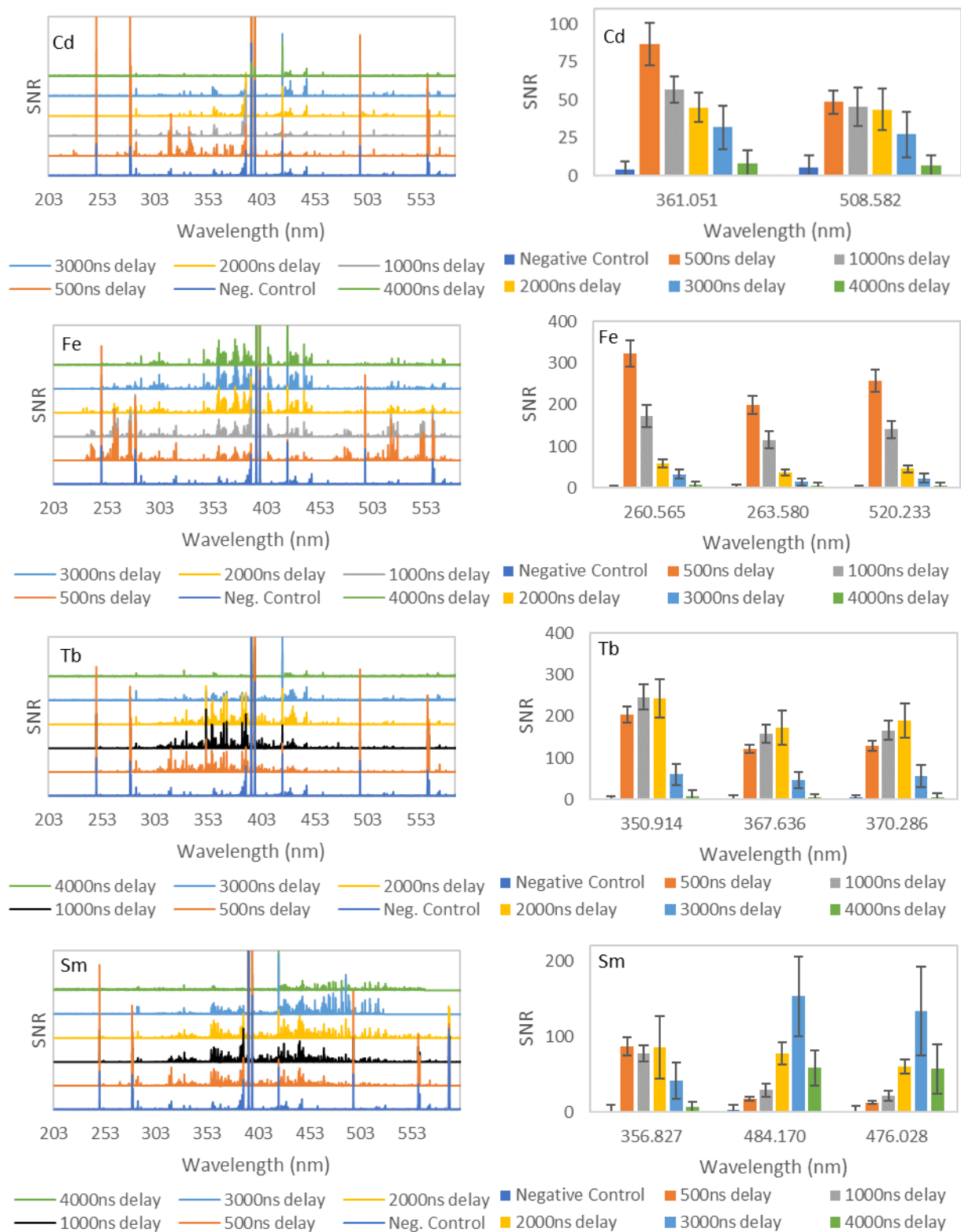


Figure 3.16 Spectra of Cd, Fe, Tb, and Sm on nitrocellulose paper at delay times of 0.5, 1, 2, 3, and 4 μ s.

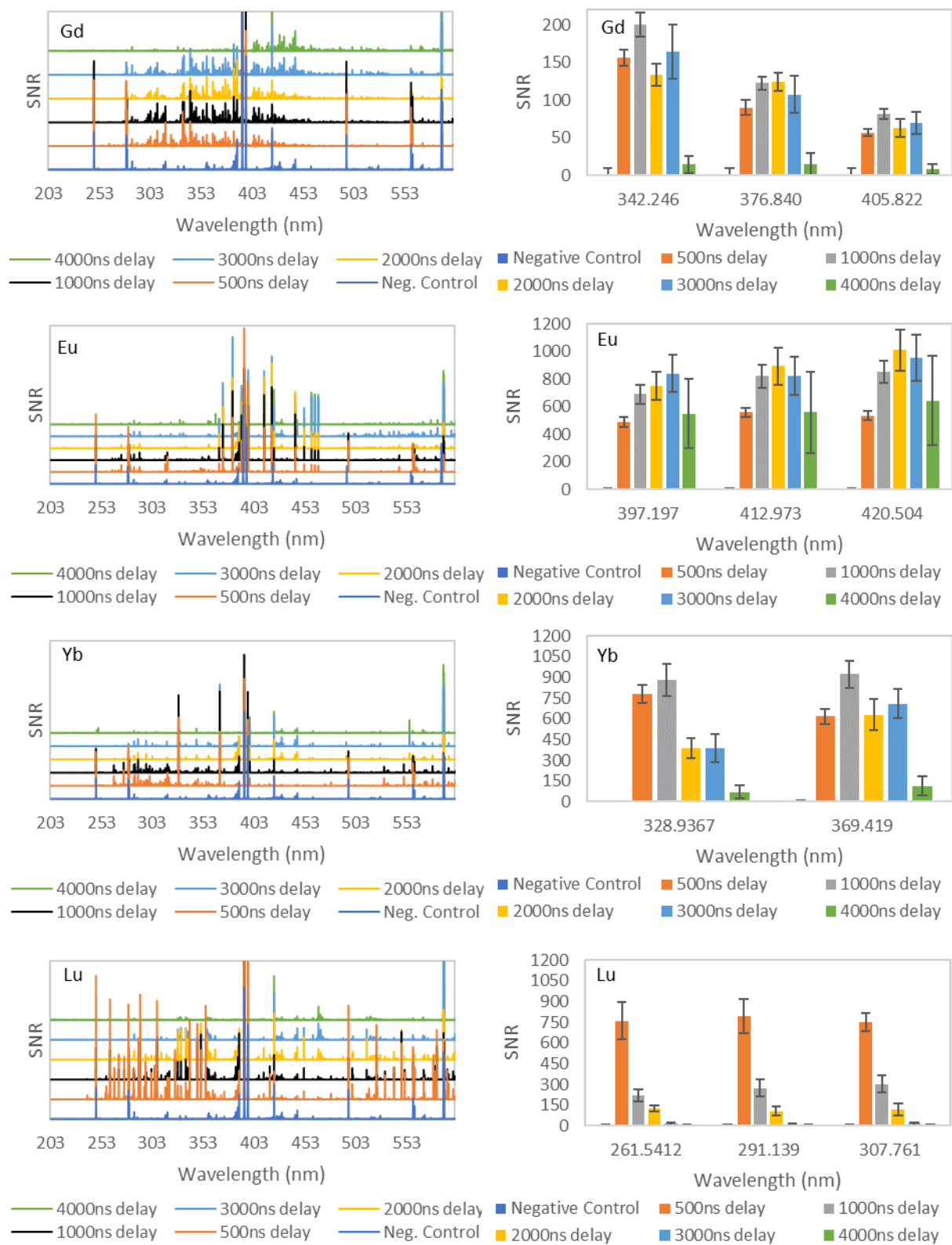


Figure 3.17 Spectra of Gd, Eu, Yb, and Lu on nitrocellulose paper at delay times of 0.5, 1, 2, 3 and 4 μ s.

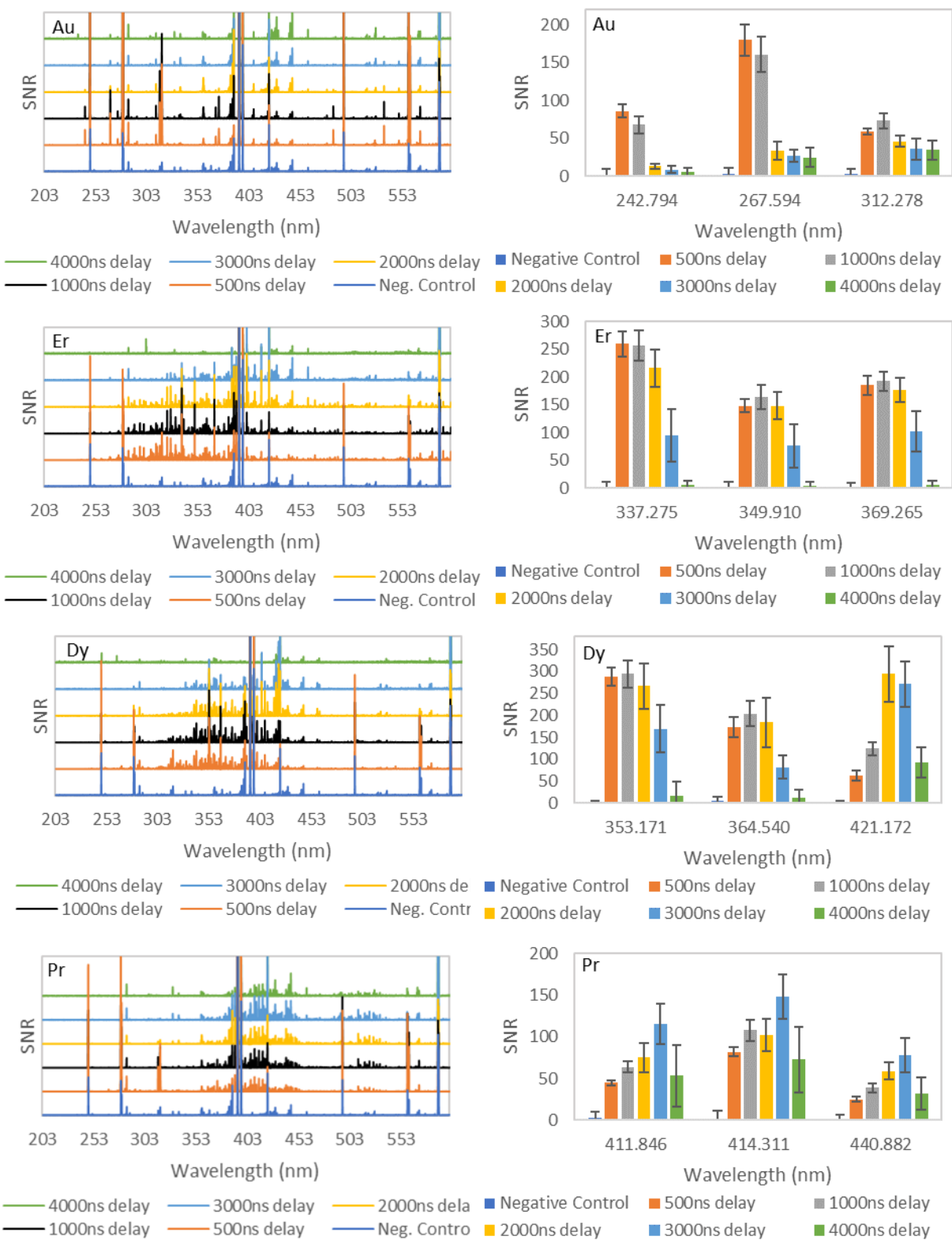


Figure 3.18 Spectra of Au, Er, Dy, and Pr on nitrocellulose paper at delay times of 0.5, 1, 2, 3, and 4 μ s.

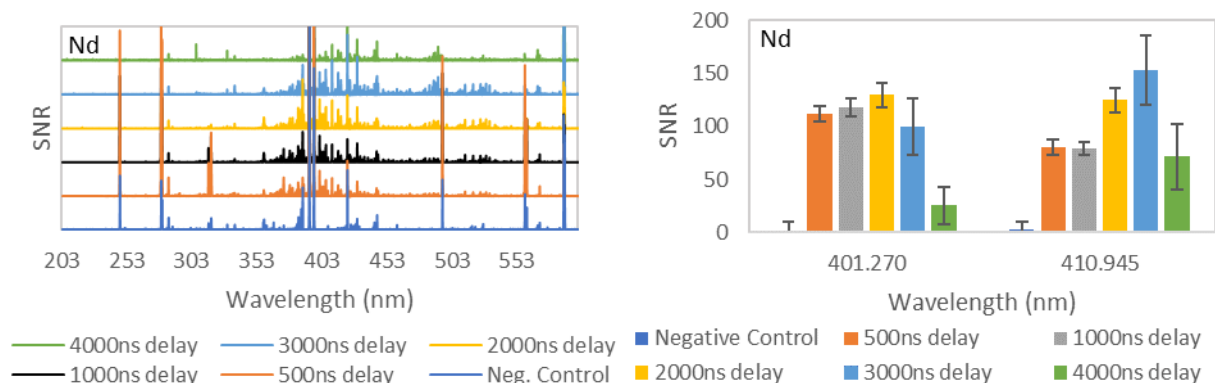


Figure 3.19 Spectra of Nd on nitrocellulose paper at delay times of 0.5, 1, 2, 3, and 4 μ s.

To illustrate the relationship between SNR and delay time, two to four of the most intense peaks were chosen for each element based on the criteria described in the previous section and plotted as a bar chart. Line selection was based on high SNR and low interference with the nitrocellulose background. For most elements, the strongest emission lines were produced between 300 and 450 nm. Some elements like Ag, Fe, and Lu had strong emissions below 300 nm. Fe and Sm had strong emission lines above 450 nm. Most metals (Nd, Pr, Dy, Er, Ag, Gd, Sm, Tb, Fe, Cd, Zn, and Ho) had an SNR of 150-300 for their strongest emission lines. Tm produced emission lines of intermediate SNR – between 300 and 400 SNR. Eu, Lu, Yb, and Ag produced the strongest emissions between 750 and 1500 SNR, which were 2.5-6 times stronger than most of the other metals tested. In general, lanthanides produced many high-density and low-SNR emission lines. The exceptions were Eu, Yb, and Lu, which produced few such emission lines. The literature suggests similar findings of certain lanthanides having multiple high-density emission lines [160].

Discrepancies were observed between the acquired spectra and the NIST ASD. Many strong emission lines (100 SNR or higher) observed in the experimental spectra were not listed in the NIST ASD. The discrepancy was most notable with Gd. The experimental spectrum of Gd is rich with lines; however, few of these emission lines correlated with NIST-reported lines with associated transition probabilities. Many other lines are reported for Gd in the NIST ASD, but little information other than ionization state, observed wavelength, and relative intensity are provided. The NIST database is a compilation of studies investigating atomic emissions. In its description it states that gaps or errors in data are a possibility. The spectral library acquired in this study could be used to enrich the NIST ASD.

Table 3.2 Emission lines for 17 elements and the delay time at which they were found to have the highest SNR. Limits of detection are listed for 7 elements, Lu having the lowest. *Identifies an element emission line with high standard deviation at the specified delay time.

Element	Ionic state	Wavelength (nm)	Peak Delay (μm)	LOD (ppm)	Element	Ionic state	Wavelength (nm)	Peak Delay (μm)	LOD (ppm)
Lu	II	291.139	0.5	0.004	Fe	I	260.565	0.5	NA
Lu	II	307.761	0.5	0.047	Fe	I	263.58	0.5	NA
Ag*	I	328.068	0.5	0.217	Fe	I	520.233	0.5	NA
Ag*	I	338.289	0.5	0.628	Gd	II	342.246	1	NA
Eu	II	420.504	2	1.052	Gd	I	405.822	1	NA
Yb	II	369.419	1	1.577	Gd	II	376.83961	2	NA
Yb	II	328.937	1	1.684	Ho	II	347.425	1	NA
Eu	II	412.973	2	3.200	Ho	I	410.38	2	NA
Eu	II	397.197	3	15.309	Ho	I	416.302	2	NA
Au	I	242.794	0.5	15.968	Ho	II	339.895	1	NA
Au	I	267.594	0.5	34.371	Lu	II	261.5412	0.5	NA
Nd	II	401.224	2	152.826	Sm	II	356.827	0.5	NA
Nd	II	406.108	3	205.522	Sm	I	476.028	3	NA
Pr	II	411.846	3	1528.197	Sm	I	484.17	3	NA
Pr	II	440.882	3	1766.937	Tb	II	350.914	2	NA
Pr	II	414.311	3	2145.206	Tb	II	367.636	2	NA
Cd	I	361.051	0.5	NA	Tb	II	370.286	2	NA
Cd	I	508.582	0.5	NA	Tm	I	376.807	2	NA
Dy	II	353.171	1	NA	Tm	I	379.854	2	NA
Dy	II	364.54	1	NA	Tm	I	409.418	3	NA
Dy	I	421.172	2	NA	Tm	I	410.273	3	NA
Er	II	337.275	0.5	NA	Zn	I	328.232	0.5	NA
Er	II	349.91	1	NA	Zn	I	334.501	0.5	NA
Er	II	369.265	1	NA					

Figure 3.15-Figure 3.19 show a clear and unique relationship between emission-line SNR and delay time. Different emission lines for the same element peaked at different delay times. Out of the 48 emission lines selected across 17 elements, 16, 11, 12, 9, and 0 emission lines were found to peak at 0.5, 1, 2, 3, and 4 μs respectively. Most emission lines belonging to the same element peaked at the same time. Some emission lines had short lifetimes, characterized by a sharp spike in signal intensity across the delay times. This pattern was most dramatic for emission lines associated with Lu, suggesting that achieving the lowest limit of detection (LOD) for Lu may involve a 0.5 μs acquisition delay and a brief integration time (500 ns). Other emission lines, like those for Eu, have long lifetimes, suggesting that the lowest LOD for Eu may be achieved using a 0.5 μs acquisition delay and a broad acquisition window (2-3 μs).

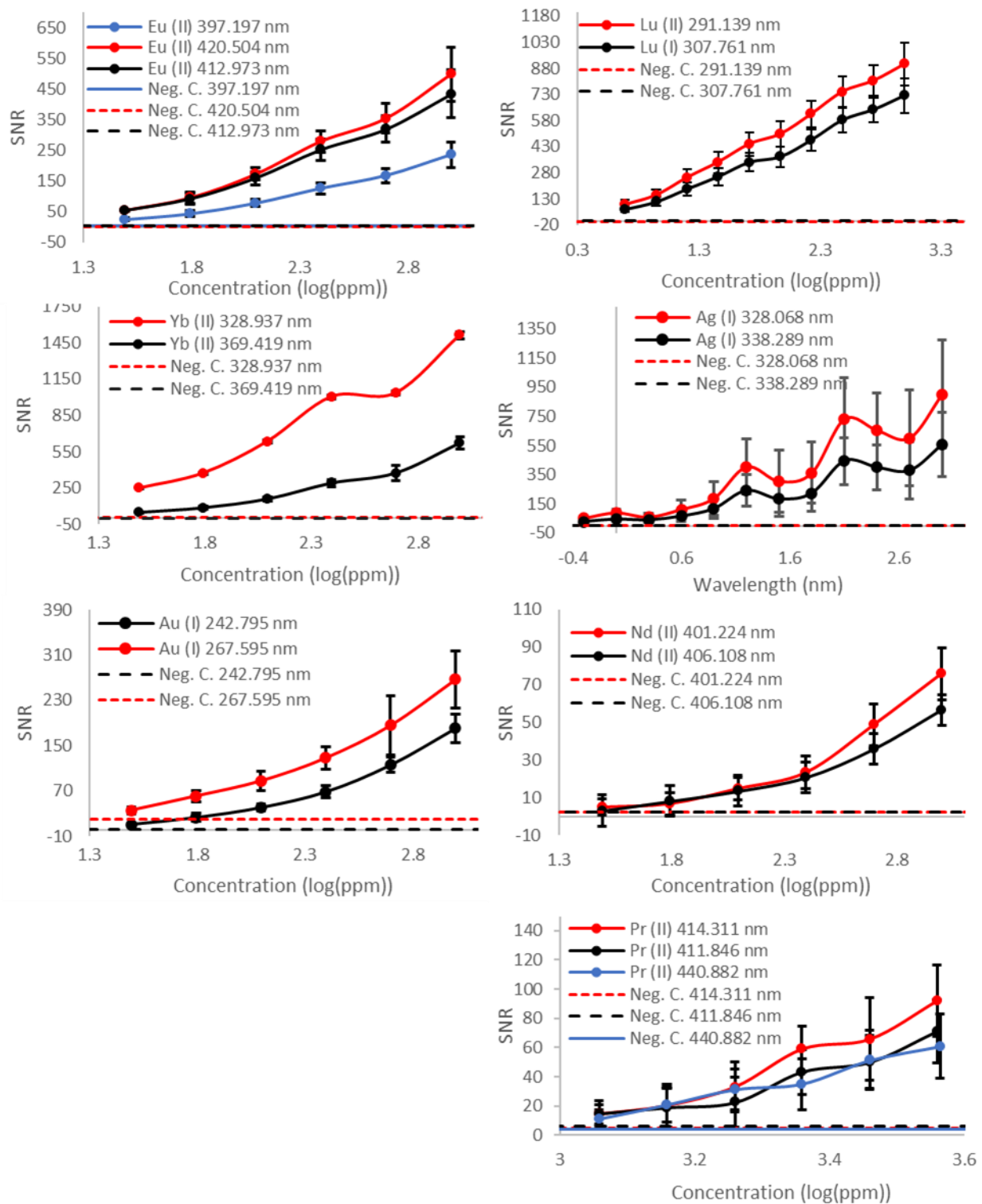


Figure 3.20 Dilution curves for Eu, Lu, Yb, Ag, Au, Nd, and Pr were used to determine the detection limit of LIBS System 6 for each element.

The spectra acquired for 17 elements across five delay times provides a reference library for future studies utilizing LIBS System 6. Four elements (Eu, Lu, Yb, and Ag) were identified as promising biomolecular labels since they produced the most intense emission lines. Two to three emission lines for Eu, Lu, Yb, Ag, Au, Pr, and Nd and their corresponding delay times were used to determine the LOD of each metal (listed in Table 1). A limit-of-detection study for each of these metals provided more information as to which would yield the most sensitive detection of a biomolecule in a paper-based immunoassay.

3.5.3 Limit of Detection

Limit-of-detection (LOD) studies were performed for four elements with the strongest emission lines: Eu, Lu, Yb, and Ag. Additionally, LOD was determined for Au, Pr, and Nd owing to their frequent use for antibody labeling. Identifying which element yielded the lowest LOD ranked them as candidates for sensitive detection of biomolecules. A dilution series was made for each metal. 10 μ l of each dilution step was loaded onto nitrocellulose squares and dried for 2 hrs (2-3 replicates per dilution step). As a negative control, 10 μ l of 2% HNO₃ or 5% HCl was added to nitrocellulose squares. Each nitrocellulose square was shot 25 times, 1 shot per location. LOD values were reported as ppm, defined as milligrams of metal per kilogram of nitrocellulose. The average weight of nitrocellulose per 6×6 mm laser-cut section was 1 mg.

Limit of detection was determined by applying the following formula to a dilution series of the metal standard:

$$LOD = ((3.3 \times SD_0 + \mu_0) - b)/m \quad \text{Equation 3.1}$$

where SD_0 is the standard deviation of the SNR in the area adjacent to the test line, μ_0 is the mean SNR of the emission line in the negative control, b is the y-intercept of the regression line, and m is the slope of the regression line. The regression-line equation was derived from a linear fit of the log-transformed SNR vs. log-transformed concentration data for each analyte.

The measured LODs (Table 3.2) were compared to determine which metal would be the best candidate as a biomolecular label in a LFIA analyzed with LIBS. A positive non-linear relationship was observed between metal concentration and SNR for the selected lines for each metal. A log transformation of both SNR and concentration yielded a linear fit between $R^2 = 0.93$

and 0.99 for all emission lines except Ag ($R^2 = 0.83$). Ag displayed a particularly high standard deviation at most dilution steps. The delay time study shown in Figure 3.15 also shows a large standard deviation of Ag signal at 0.5 μ s, the timing parameter used for the LOD study. The standard deviation is less at later delay times. Further investigation is required to understand the source of the variation. The slope of the relationship between SNR and log-transformed concentration (ppm) depended on the emission line (Figure 3.20). The Lu (II) 291.139-nm emission line offered the best LOD at 0.004 ppm, followed by Ag, Eu, Yb, and Au.

For Au, the best emission line was found to be 242.795 nm, with an LOD of 15.97 ppm. LODs for other metals and their select lines can be found in Table 3.2. While the LIBS LOD for Au reported in the literature is 0.8-2.6 ppm in ores, few if any studies refer to the LOD of Au on nitrocellulose paper [27]. Since many LFIAs use nitrocellulose paper as the platform on which to concentrate and label analytes, it is important to determine the optimal parameters for gold detection on this material. After optimization, we achieved a limit of detection of 15.97 ppm. This serves as a benchmark for comparing other metal labels to determine which offers the best LOD.

In LIBS articles that refer to detection of the lanthanides Lu, Pr, Yb, Eu, and Nd, the matrices and instrument parameters such as laser energy and wavelength, diffraction grating, and detector vary significantly [170, 171]. The variation among these factors led the authors of those studies to choose, out of the many emissions produced by lanthanides, those that will yield the best LOD. To select appropriate emission lines for this study, the 200 nm to 600 nm spectrum of five lanthanides on paper were collected at different delay times. While Eu, Au, and Yb had simple spectra, Nd and Pr had many closely spaced emission lines. The literature suggests similar findings of certain lanthanides having multiple high-density emission lines [160]. Two or three intense lines that had high SNR, little interference with the nitrocellulose background, and low proximity to other lines belonging to the same element were selected for further examination at their optimal delay time. Literature-reported LIBS detection limits for Lu, Eu, Yb, Nd, and Pr were 20, 1-209, 1-156, 11-500, and 3-40 ppm respectively, depending on the material, acquisition parameters, and data-analysis approach [170, 172-174, 171]. We found that our best LODs were 0.004, 1.1, 1.5, 152.8, and 1528.2 ppm for Lu, Eu, Yb, Nd, and Pr, respectively. The data show that different emission lines for the same metal have different rates of decay across the dilution series, indicating that just because an emission line is the most intense at a high concentration does not mean it will have the best LOD. When comparing the LOD of Ag and lanthanides to gold, it was found that

Ag, Eu, and Yb have LODs more than 10 orders of magnitude less than that of Au. Ag produced a 0.217 ppm limit of detection, which is on the lower end of the values reported by the literature that range from 0.2-110.8 ppm [175]. A particularity about the signal produced by Ag at early delay times was the high standard deviation – a finding that encourages follow-up and could affect quantitative LIBS detection. Overall, based on the results of this study, LFIAs analyzed with LIBS may be able to achieve more sensitive detection of the bio-analytes when they are labeled with Ag, Eu, and Yb rather than the same quantity of the standard label, Au.

So far, all experiments have considered only a single metal element on nitrocellulose. Utilizing these single-metal samples, spectra could easily be examined for atomic emission lines, and dilution series yielded predictable curves. When other heavy metal elements are present in the sample, matrix effects and emission-line overlap may complicate data analysis. The next section involves analysis of mixed heavy-metal samples.

3.6 Multiplexed Heavy-Metal Data-Analysis Techniques

The following section was published in SPIE Proceedings as “Multiplexed detection of lanthanides using laser-induced breakdown spectroscopy: a survey of data analysis techniques” (DOI: 10.1117/12.2521453). Imaging spectroscopy is used extensively in the field of remote sensing, which encompasses both passive and active sensing. Passive systems detect energy originating from an external source such as sunlight, whereas active systems like lidar (light detection and ranging) and radar (radio detection and ranging) produce an optical signal that is then reflected and measured [176, 177]. A common detector used for remote sensing is a charged coupled device (CCD). The pixels of the CCD array are photoactive, transmitting an electrical signal proportional to the intensity of electromagnetic radiation incident on the pixel surface [178]. In hyperspectral imaging, information on a scene such as a large region of the Earth’s surface is collected over a broad range of wavelengths and transmitted to a much smaller CCD pixel array. Limitations in imaging resolution means that each pixel contains a mixture of information that needs to be deconstructed in order to understand the contribution of each wavelength to the image. Similarly, when two distinct materials produce the same or similar signals, their accumulated signal is detected as a single measurement on a pixel [177]. The accumulated signal can be deconstructed to determine the relative contribution of each material. Deconstructing the

information contained in each pixel of an array is termed spectral unmixing and is a fundamental process in the field of remote sensing [177], biological imaging [179], and flow cytometry [180].

In this study, spectral unmixing techniques have been applied to LIBS. Each element produces emissions at specific wavelengths allowing the user to perform multi-elemental characterization of the source material [181]. In many cases, atomic emissions from different elements partially overlap. Therefore, each pixel is detecting signal produced by one or more material components – a scenario classic to many remote-sensing applications. This paper applies to LIBS algorithms used for spectral unmixing.

Spectral unmixing of a LIBS signal is being studied by our group for the downstream goal of identifying food-borne pathogens labeled with unique metal-conjugated antibodies. The metal conjugates act as biomarkers and are typically used for mass cytometry or luminescence detection [11, 14, 8, 16]. Such biomarkers are commonly applied to biological assays in polystyrene multi-well plates and paper-based assays [3, 8, 182-184]. Paper-based assays are a particularly promising diagnostic tool for food borne-pathogen detection because they are easy to use, low cost, and portable [1-3]. Their primary drawbacks are lack of multiplexing capability, low sensitivity, and difficulty in producing quantitative measurements by observation of color change [2]. To improve the multiplexing capability of paper-based diagnostics, we initiated studies applying LIBS analysis of paper-based diagnostics that utilize panels of metal biomarkers for multi-contaminant labeling. Our downstream goal is to use LIBS and paper-based bioassays to perform multiplexed detection of food-borne contaminants. A critical step in LIBS analysis of multiplexed paper diagnostics is spectral data processing and interpretation. Therefore, the aim of this section is to investigate spectral unmixing models (non-negative least-squares, Poisson, and negative binomial unmixing) for the purpose of detecting mixtures of metal biomarkers in a paper matrix.

3.6.1 Sample Preparation

Metal CRM solutions for Gd, Eu, Dy, Nd, and Pr were each diluted to a final concentration of 0.2 mg/ml. Since Eu generates particularly intense emission lines relative to the other metals at the stated settings, a dilution series of Eu (2.8, 2, 1.6, 1.2, 0.8, 0.4, 0.2, and 0 mg/ml in 2% HNO₃) was made to identify the concentration that yielded a signal on the same scale as Gd, Dy, Nd, and Pr. These treatments are referred to as “pure metal” treatments.

A mixture of all five metal standards was prepared such that the final concentration of each metal was 0.2 mg/ml, and the total metal concentration was 1 mg/ml. Mixtures of different combinations of four metals (Eu, Gd, Nd, Pr; Dy, Gd, Nd, Pr; Dy, Eu, Nd, Pr; Dy, Eu, Gd, Pr; Dy, Eu, Gd, Nd) were prepared such that the final concentration of each metal was 0.2 mg/ml, and the total metal concentration was 0.8 mg/ml. In a separate set of treatments, the same combinations of metals were prepared such that the final concentration of each metal was 0.2 mg/ml, with the exception of Eu, which was 0.02 mg/ml. In the five-metal mixture the total metal concentration was 0.820 mg/ml, and in the four-metal mixtures 0.620 mg/ml. These treatments are referred to as “mixed-metal” treatments. A negative control treatment consisted of 2% nitric acid. 10 μ l of each treatment was added to 6 x 6 mm sections of plastic-backed nitrocellulose paper (GE Lifesciences, FF120HP PLUS, Pittsburgh, PA, USA) and dried for >2 hours.

LIBS System 6 was applied to the analysis of the samples. LIBS System 6 utilized a Nd:YAG 1064 nm laser with 30 mJ pulse energy; laser spot size between 500 μ m and 700 μ m; an Andor Shamrock 500i spectrometer with a 500 nm blazed, 1200 l/mm grating; Andor USB iStar ICCD that detected signals after a 1 μ s delay across a 50 μ s integration time with no gain applied to the intensifier. A chamber surrounded the sample to prevent user exposure to harmful aerosols. Samples in the sample chamber were ablated 20 times in different locations for each treatment.

3.6.2 Data Analysis

Analysis of individual peaks characteristic of each element was performed. For each treatment replicate, data were baseline corrected by subtracting a median filter from the raw data. The data were then normalized by dividing the data by the standard deviation of a second median filter. Values that were one standard deviation below the mean were considered noise and set to zero. The data from each replicate were averaged and plotted. To identify emission lines belonging to the metals of interest, the atomic emission database provided by (NIST) [159] was compared to the spectra of pure metal treatments. The emission lines selected for each metal had the least overlap with emissions from other metals. The base-corrected and normalized intensity of each emission line of interest was compared across treatments.

Multivariate data-analysis strategies employed were based on complex signals originating from the material being analyzed. The signal collected by the spectrometer contains a mixture of

signals originating from the constituent elements. Unless a transfer of energy occurs due to matrix effects or self-absorption, the total signal can be expressed as a linear mixture of component signals:

$$\mathbf{r} = \mathbf{M}\mathbf{a} + \mathbf{e}, \quad \text{Equation 3.2}$$

where \mathbf{r} is the spectral vector to be unmixed (a mixed-metal treatment), \mathbf{M} is the mixing matrix describing the spectra of the constituent elements (pure-metal treatment) as detected by the spectrometer, \mathbf{a} is the vector of abundances, and \mathbf{e} is the noise vector describing the uncertainty of the measurement. The noise, \mathbf{e} , is assumed to be normally distributed and leads to the least-square estimation of \mathbf{a} :

$$\hat{\mathbf{a}} = \left(\mathbf{M}^T \mathbf{M} \right)^{-1} \mathbf{M}^T \mathbf{r} \quad \text{Equation 3.3}$$

However, the model of \mathbf{e} must take into account the physical reality modeled via Equation 3.2. The measurement of a spectral signal formed by the plasma plume involves registering the intensity of the incoming light, so values cannot be negative. In addition, the uncertainty of light measurement in the LIBS experiment can be only Poissonian or super-Poissonian, but not Gaussian. Therefore, the model better accommodating the underlying physics could be expressed as

$$\hat{\mathbf{a}} = \arg \min_{\mathbf{a}} \left\{ 2\mathbf{j}^T \left(\mathbf{r} \circ \log \left(\mathbf{r} \circ \overline{\mathbf{M}\mathbf{a}} \right) - (\mathbf{r} - \mathbf{M}\mathbf{a}) \right) \right\}, \quad \text{Equation 3.4}$$

where \mathbf{j} is an $L \times 1$ sum vector of 1, and \mathbf{j}^T is its transpose (the sum vector is used to find the sum of the elements of the computed vector), $\mathbf{M}\mathbf{a}$ is a vector of reciprocal values to the elements of vector $\mathbf{M}\mathbf{a}$ (Hadamard inversion), and \circ denotes element-wise multiplication (Hadamard product).

Further, a more realistic super-Poissonian case can be approximated by a negative-binomial regression model:

$$\hat{\mathbf{a}} = \arg \min_{\mathbf{a}} \left\{ 2\mathbf{j}^T \left(\mathbf{r} \circ \log \left(\mathbf{r} \circ \overline{\mathbf{M}\mathbf{a}} \right) - (\mathbf{r} + \theta^{-1}) \log \left((1 + k\mathbf{r}) \circ \overline{(1 + \theta\mathbf{M}\mathbf{a})} \right) \right) \right\} \quad \text{Equation 3.5}$$

where θ is an additional dispersion parameter, which can be provided or estimated from the data.

3.6.3 Results: univariate analysis

Each treatment produced unique spectra. The raw data, averaged across replicates, are displayed in Figure 3.21. Prominent Pr peaks (406.28, 410.07, 414.31nm), Eu peaks (420.51, 412.97, 397.20 nm), Gd peaks (404.99, 406.34, 409.86 nm), Dy peaks (400.05, 404.60 nm) and Nd peaks (401.23, 406.11, 410.95 nm) were identified by comparing the spectra to the NIST database [159]. The peaks with the least overlap with other metals in the study were Pr 410.07 nm, Eu 412.97 nm, Gd 404.99 nm, Dy 400.05 nm, and Nd 410.95 nm. Among treatments containing a single metal, Eu was observed to have the strongest emission lines of all metals in the study, followed by Nd, Pr, Dy, and Gd in order.

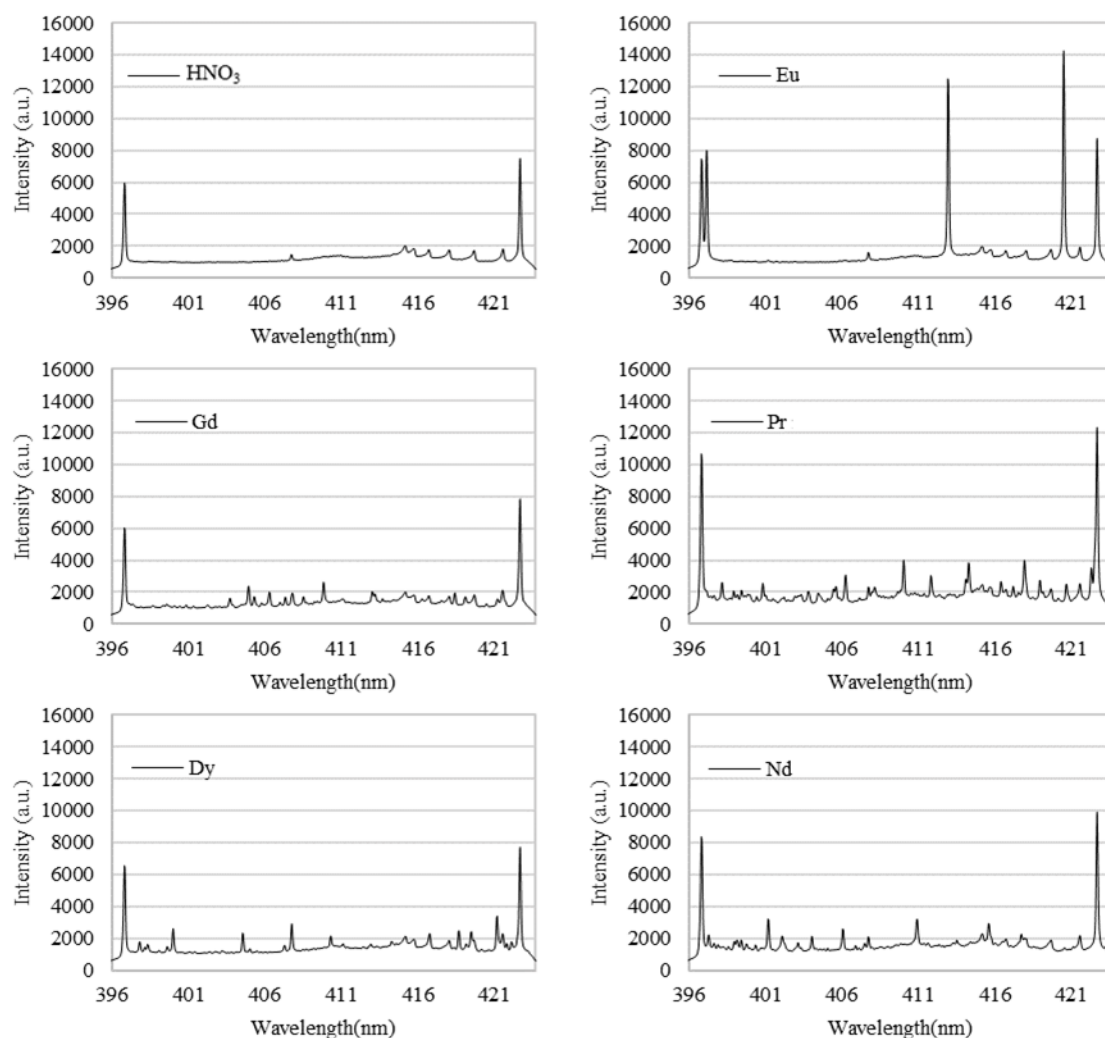


Figure 3.21 Raw spectra of pure metal solutions (Eu, Gd, Pr, Dy, and Nd) dried on nitrocellulose paper. HNO₃ dried on nitrocellulose paper serves as a negative control.

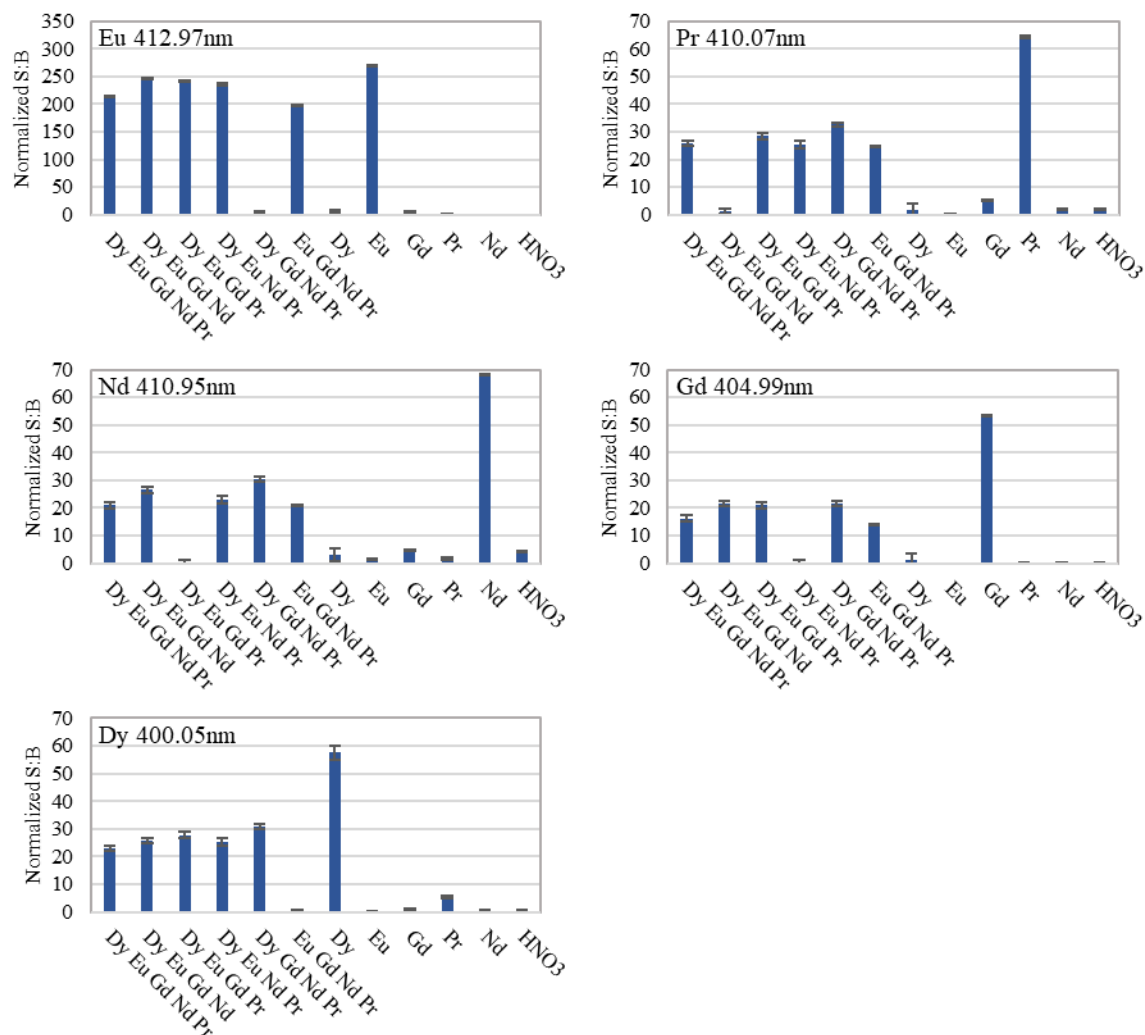


Figure 3.22 Intensity of emission lines for Eu, Pr, Nd Gd, and Dy across treatments. Treatments consist of pure lanthanides and mixtures of four or five in which each lanthanide is at a concentration of 0.2 mg/l. Metals on nitrocellulose at 0.2 mg/ml generate a stronger signal in pure samples vs. mixed samples.

The signal of Eu decreased significantly when in a mixture of other lanthanides, despite Eu concentration's remaining constant. The same trend was observed for each lanthanide in pure vs. mixed samples (Figure 3.22). This phenomenon has been observed in other LIBS studies and is termed matrix effects [185, 12, 94, 186]. Matrix effects are due to a variety of factors, including irradiance, atom density, temperature, and electron density. Self-absorption is another common phenomenon [12, 186] and may explain the non-linear trend in signal intensity observed across the Eu dilution series (Figure 3.23) – at a concentration of 0.2 mg/ml Eu (the 7th dilution step), the signal plateaus. Matrix effects and self-absorption significantly complicate quantitative LIBS

analysis [185, 186]. In bioassays for contaminant detection, quantitative or semi-quantitative measures are often valuable [187]. This suggests that if LIBS is to be used for quantitative bioassay analysis, self-absorption and matrix effects should be considered when determining which combinations of metals to use as biomarkers, and during instrument calibration as well.

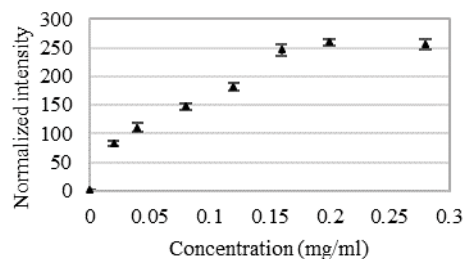


Figure 3.23 Signal intensity at 412.97 nm across a dilution series of Eu. Signal positively correlates to Eu concentration, and plateaus at a concentration of 0.2 mg/ml.

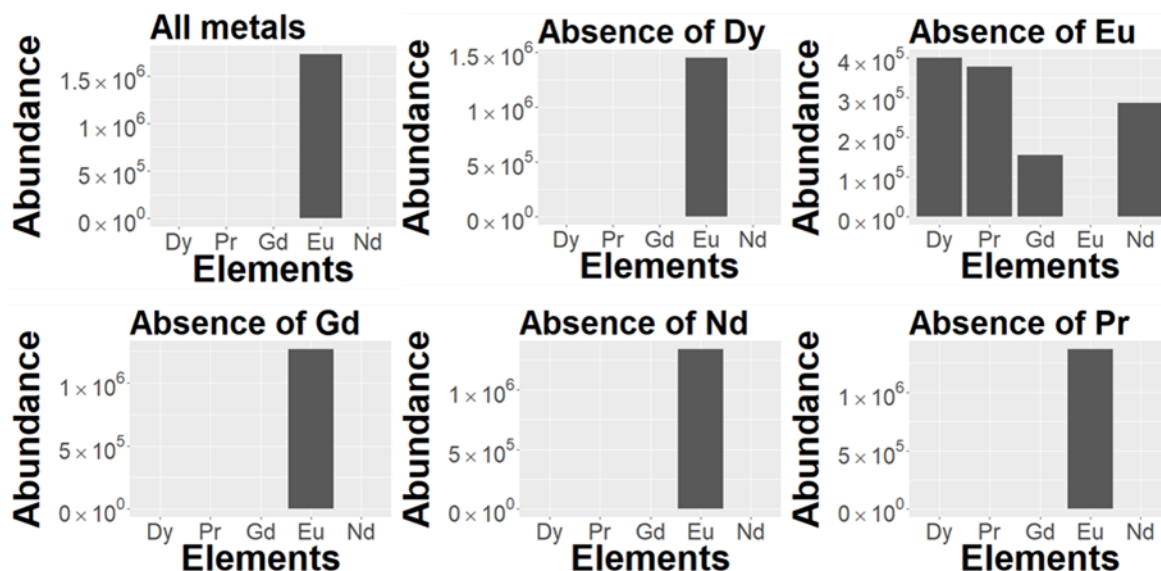


Figure 3.24 NNLS unmixing across mixed metal treatments for case 2. The mixing matrix M consists of data from pure-metal treatments, where each metal is present at a concentration of 0.2mg/ml, with the exception of Eu, which is at a concentration of 0.02 mg/ml. r is a vector representing a mixture of four or five metals, with each metal present at a concentration of 0.2 mg/l. False negatives result from each treatment, except for the mixture lacking Eu.

3.6.4 Results: multivariate analysis

A common method for spectral unmixing is through least-squares solutions [188, 186]. In this study, we use non-negative least squares (NNLS), Poisson, and negative binomial unmixing methods. We observed that dominant signals in the mixed spectra have a significant effect on the unmixing results. Among the treatments of pure lanthanides, the signal generated by Eu was approximately four to five times higher than those of all other metals at the same concentration (0.2 mg/ml) (Figure 3.22). For Eu to generate a signal of approximately equal intensity, it was diluted to 0.02 mg/ml. Spectral unmixing was performed using either high (0.2 mg/ml) or low (0.02 mg/ml) concentrations of Eu in the pure- and mixed-metal treatments.

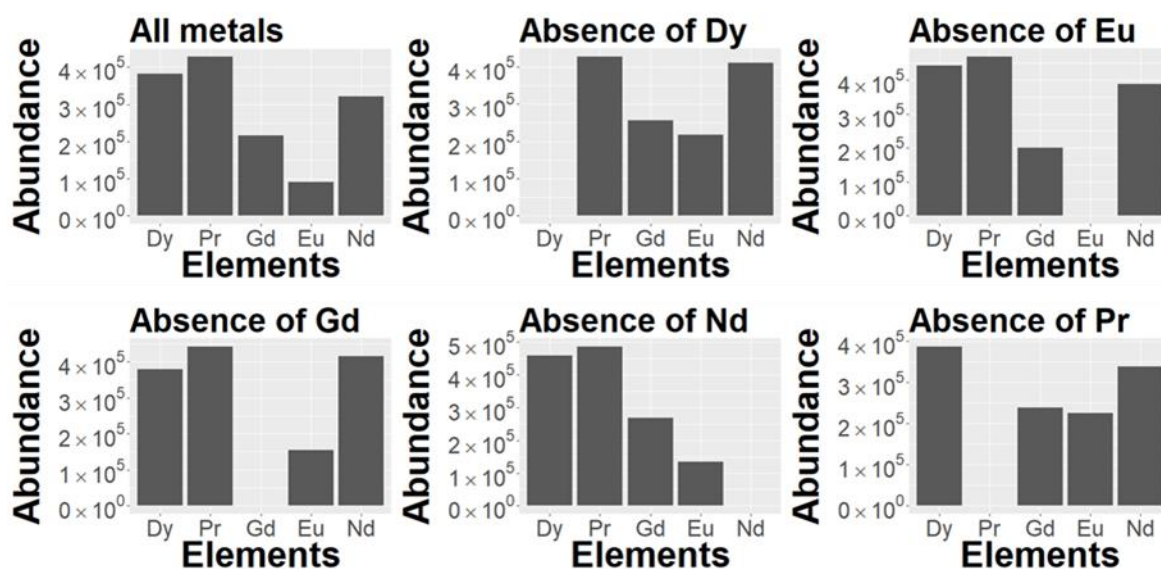


Figure 3.25 NNLS unmixing across mixed metal treatments for case 3. The mixing matrix \mathbf{M} consists of data from pure-metal treatments, where each metal is present at a concentration of 0.2 mg/ml, with the exception of Eu, which is at a concentration of 0.02 mg/ml. \mathbf{r} is a vector representing a mixture of four or five metals, with each metal present at a concentration of 0.2 mg/ml, with the exception of Eu which is at a concentration of 0.02mg/ml. False negatives were not observed.

In case 1, \mathbf{M} is composed of treatments containing 0.2 mg/ml of pure metal, and \mathbf{r} is a vector representing a mixture of four or five metals, each with a concentration of 0.2 mg/ml. In this case, the dominant Eu signal obscured signal produced by other lanthanides when NNLS (Figure 3.26), Poisson, and negative binomial unmixing models were applied. This phenomenon can lead to false negative results. For example, in the treatment containing Eu, Gd, Nd, and Pr, Dy

was reported missing (correct), and Gd was reported missing (false negative). Likewise, in the treatment containing Eu, Gd, Nd, Pr, and Dy (all metals), Gd was reported missing (false negative).

In case 2, \mathbf{M} is composed of treatments containing 0.2 mg/ml of pure metal, except for Eu, which is at 0.02 mg/ml. \mathbf{r} is a vector representing a mixture of four or five metals, each with a concentration of 0.2 mg/ml. Similar to case 1, the results contain false negatives (Figure 3.24). Only the treatment lacking Eu was successfully unmixed, suggesting that in all other treatments, the dominance of the Eu signal interfered with spectral unmixing. The results were similar across the three unmixing approaches.

In case 3, \mathbf{M} is composed of treatments containing 0.2 mg/ml of pure metal, except for Eu, which is at 0.02 mg/ml. \mathbf{r} is a vector representing a mixture of four or five metals, each with a concentration of 0.2 mg/ml, except for Eu, which is at 0.02 mg/ml. Unlike case 1 and case 2, NNLS (Figure 3.25) and other models successfully unmixed the spectra.

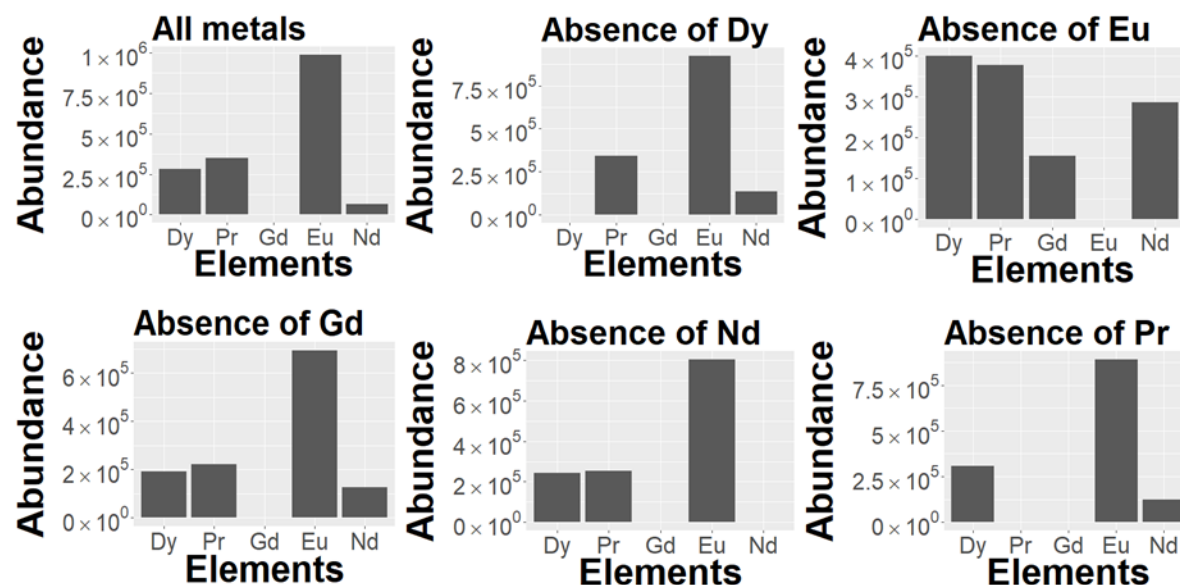


Figure 3.26 NNLS unmixing across mixed metal treatments for case 1. The mixing matrix \mathbf{M} consists of data from pure-metal treatments, with each metal present at a concentration of 0.2 mg/ml. \mathbf{r} is a vector representing a mixture of four or five metals, with each metal present at a concentration of 0.2 mg/l. False negatives result from each treatment, except for mixtures lacking Gd or Eu.

3.6.5 Discussion

In this study, pure and mixed lanthanide solutions were dried onto nitrocellulose matrices and tested using LIBS. Univariate and multivariate approaches were used to simultaneously detect each lanthanide component in mixed solutions. The goal was to evaluate these approaches in their ability to detect lanthanide biomarkers in paper-based bioassays. Paper-based assays are being developed in our group to capture food contaminants and label them with metal-conjugated biomarkers. These bioassays are being designed to capture and label either a single contaminant or many contaminants. In the latter case, each contaminant will be uniquely labeled using a lanthanide specific to the contaminant and detected using LIBS. In this multiplexed detection scheme, the data-analysis approach must be capable of identifying different combinations of lanthanide labels. We have chosen to evaluate univariate and multivariate analytical methods for multiplexed detection of lanthanide standards loaded onto nitrocellulose paper.

The univariate approach was mostly successful in determining the composition of mixed samples. It was noted that in pure samples, where only one lanthanide was present, emissions of other lanthanides absent from the sample were present, albeit weak. This highlights an important aspect that will be considered in future work – spectral overlap between emission lines can produce misleading results when using univariate analysis approaches if the appropriate controls are not tested.

As in other studies, matrix effects were observed to have a significant influence on the intensity of emission in pure vs. mixed samples, complicating the potential for the LIBS system to perform quantitative measurements [186, 185]. For contamination detection, quantitative or semi-quantitative measures have been described to be of value depending on specific circumstances [2, 189]. While this study suggests that LIBS analysis of paper-based assays may have potential in the realm of multiplexing, the potential for quantitative measures is still being investigated. Future studies consist of evaluating the role of matrix effects on lanthanides at lower concentrations.

A multivariate approach using NNLS, Poisson, and negative binomial spectral unmixing models successfully identified the metal compositions of each mixed metal solution only when the intensity of the signals in the \mathbf{M} matrix and \mathbf{r} vector were of comparable intensity. In situations where the spectra were dominated by a very intense emission line, the models failed. Simply lowering the intensity of the dominant signal in the \mathbf{M} matrix may not suffice in correcting the model since the abundance of components in the \mathbf{r} matrix is often unknown. This interesting result

brings attention to the limitations of linear unmixing on complex signals. Spectral unmixing models must be used with care when applied to spectra with very intense emission lines, since the outcome of the model can be misleading. Hence, when designing a bioassay using lanthanide biomarkers for simultaneous detection of multiple analytes, the panel of markers should be chosen according to the expected abundance of the analyte. Rare analytes can be marked with lanthanides that produce a strong signal, like Eu, more common analytes with Gd, Dy, or Nd.

In conclusion, multiplexed detection of lanthanides on a paper matrix can be achieved using univariate and spectral unmixing methods. In both cases, attention must be given to spectral overlap, relative signal intensities, matrix effects, and self-absorption. Future studies include spectral unmixing at lower metal concentrations and applying the technique to real biological samples for the purpose of food-contaminant detection.

3.7 Promising Biomolecular Labels Eu, Lu, and Yb: self-absorption, matrix effects, and recommendations for multiplexed detection

As mentioned in the previous section, matrix effects and self-absorption factor heavily in LIBS, complicating quantitative detection of metals. This chapter has identified Eu, Lu, and Yb as promising biomolecular labels in nitrocellulose for detection with LIBS. Future applications involve either individual or simultaneous detection of each label in a paper-based assay. It is possible that in future applications, these metal labels will be used simultaneously with gold labels. Therefore, this section examines Eu, Lu, and Yb emissions from several standpoints: concentration effects on self-absorption, emission-line selection for multiplexed detection of Eu, Lu, and Yb, and the effect of gold on Eu signal intensity.

To examine the effects of self-absorption in relation to concentration, a 0.5 mg/L to 1000 mg/L dilution series of Eu, Yb, and Lu was made, and 10 μ l were applied to the 6 \times 6 mm FF120HP nitrocellulose paper squares and allowed to dry for 2 hrs (2 replicates per dilution step). LIBS System 6 was applied to the analysis of the samples. LIBS System 6 utilized a Nd:YAG 1064-nm laser with 33.6 mJ pulse energy; laser spot size between 500 μ m and 700 μ m; an Andor Shamrock 500i spectrometer with a 300 nm blazed, 1200 l/mm grating; Andor USB iStar ICCD that detected signals at the optimum delay time for each emission line (Table 3.2) across a 500 ns integration time with no gain applied to the intensifier. A chamber surrounded the sample to prevent user exposure to harmful aerosols. Samples in the sample chamber were ablated 25 times in different

locations. The emission lines examined were Eu (II) 520.504, Yb (II) 369.419, and Lu (II) 291.139 nm.

Graphical representations of the relationship between concentration and SNR are displayed in Figure 3.27. It was found that each emission line generally follows a log-logistic distribution. The signal gradually increases at low concentrations, followed by a near linear increase at intermediate concentrations, and peaks after 100 mg/L (1000 ppm) followed by a plateau or decrease in signal. Each line saturates at a different concentration. For Eu (II) 420.504 nm, Lu (II) 291.139 nm, and Yb (II) 369.419, the saturation points are approximately 450, 100, and 200 mg/L respectively (4,500, 1,000, 2,000 ppmw).

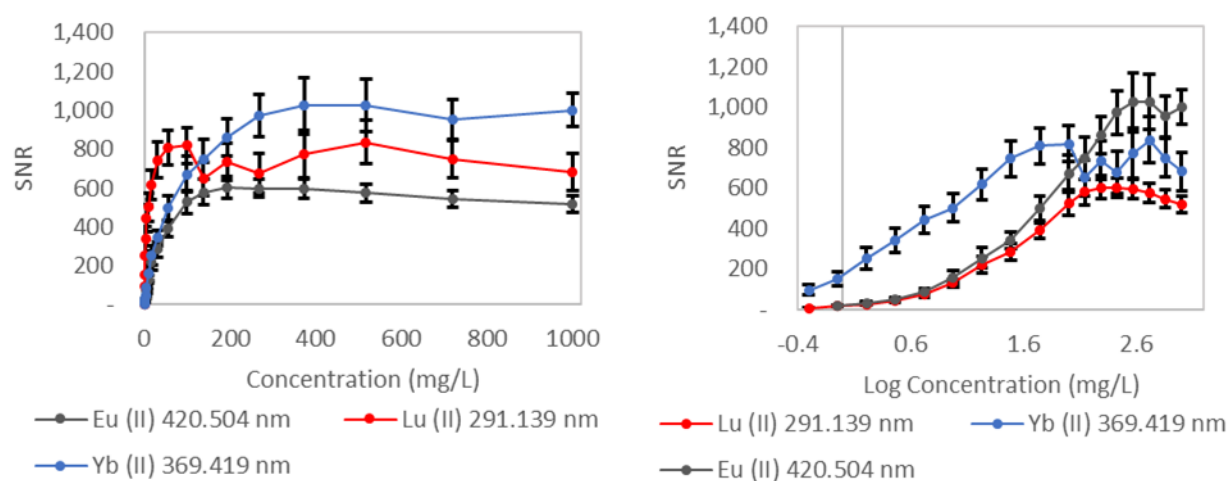


Figure 3.27 Top graph: A positive relationship was observed between concentration (mg/L) and SNR until concentrations reached 100-200 mg/L, after which the signal peaks and plateaus or decreases. Left graph: relationship between signal-to-noise ratio and the log-transformed concentration (mg/L) for better representation of data at lower concentrations. Each emission line was observed to follow a log-logarithmic distribution.

Signal saturation observed in the data reflects a phenomenon referred to in the literature as self-absorption. Self-absorption occurs more frequently in plasmas with high optical density. The plasma can be visualized as a near-spherical cloud extending above the surface of the sample, along the path of the laser beam. The periphery of the plasma, exposed to air, cools faster than the interior of the plasma. The ‘cooler’ atoms are those closer to or at the ground state and absorb emissions of the excited atoms in the center of the plasma, essentially blocking them from the detector. Energy absorbed by the ‘cooler’ atoms can be lost either as thermal, kinetic, or photon-emission energy. As a given element is most likely to absorb an emission produced by an atom of

the same species since emission lines are element specific, a high density of the same element in a plasma can yield self-adsorption [12]. Lanthanides have a high quantity and density of atomic emission lines, some of which overlap. It is postulated that one must be wary of the effects of self-adsorption in samples containing mixtures of lanthanides, even if the concentration of the individual elements is low. Evidence of these effects may be observed in Figure 3.22, where a single lanthanide element on nitrocellulose produces a more intense signal than the same amount of the element in the presence of other lanthanides. Another cause for these trends may be changes in heat absorption associated with changes in the density of the matrix material. A higher density of materials on the nitrocellulose, attributed to adding more lanthanides, may require more energy to transition the same volume of material to a plasma; recall that nanosecond lasers produce plasmas mainly through thermal effects. A method to investigate whether this phenomenon occurs could be to measure ablation mass and SNR as the concentration of one metal remains constant while the concentration and diversity of other metals vary. This type of study was not fully pursued in this dissertation; a simpler version was conducted using europium and gold nanoparticles.

The effects of matrix composition on atomic emission-line intensity was measured across mixtures of gold and europium. Europium produces a strong emission line at 420.504 nm. Au(I) and Au(II) produce few emission lines compared to other lanthanides and do not produce an emission line at or near 420.504 nm [159], theoretically reducing the possibility that gold would adsorb the Eu (II) 420.504 nm emission line. It was hypothesized that as gold was added to a sample of nitrocellulose, Eu signal would decrease despite the concentration's remaining constant. A mixtures of gold nanoparticles (G-20-20, Cytodiagnostics, Toronto, Canada) and Eu CRM (05779-100ML, Sigma Aldrich) solution were made such that the final concentration of Eu was 100 mg/L for every treatment and the final concentration of gold had an optical density of 0.5, 0.125, 0.063 or 0.031 depending on the treatment. 10 μ l of each treatment were added to 6 \times 6-mm nitrocellulose squares and dried for 2 hours (3 replicates per treatment). A negative control consisted of 10 μ l of OD = 1 gold nanoparticles dried onto nitrocellulose paper with no europium added. LIBS System 6 parameters were described previously.

The results suggest that Eu (II) 520.504 nm signal intensity is affected by the concentration of gold nanoparticles present on the nitrocellulose (Figure 3.28). Whereas the previous study observed a plateau and slight decrease in Eu signal intensity due to self-adsorption, in this case, decrease and plateau of Eu signal intensity is believed to be attributed to matrix effects. As the

concentration of gold increases in the sample, the sample material properties – heat conductivity, adsorption of the laser wavelength, and vaporization temperature – change [12]. These changes in the sample properties affect plasma formation, ultimately affecting the signal produced by Eu. Matrix effect is also defined by variations in the density of other materials in the plasma and presence of easily ionizable elements. In summary, composition of the sample can have a significant effect on emission-line intensity.

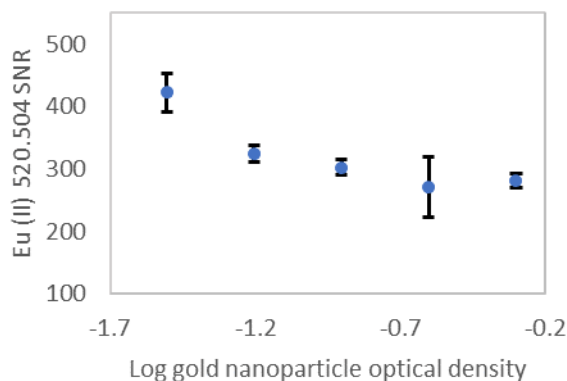


Figure 3.28 Eu (II) 520.504-nm SNR in response to concentration of gold nanoparticles on nitrocellulose. Eu concentration remained constant across treatments. As gold nanoparticle concentration increased, Eu signal decreased, indicating that the matrix composition had an effect on Eu signal intensity.

Together, self-adsorption and matrix effects pose a significant challenge to quantitative analysis with LIBS. The broader goal of the project represented by this dissertation is sensitive, quantitative, and multiplexed detection of biomolecules labeled with metals on nitrocellulose. However, evidence shows that quantitative and multiplexed detection may be challenging given the complex effects that label concentration and diversity have on the signal they produce.

Despite the challenges of quantitative and multiplexed metal label detection, there is still value in qualitative multiplexed detection. Though less informative than knowing how much of a contaminant is present, a yes/no evaluation is enough to trigger a response in the public health community. Most commercial lateral-flow immunoassays provide a yes/no answer and are applied to detection of food contaminants. In the following experiment, the spectra of Yb, Eu, and Lu are compared to determine what spectrometer parameters would be best suited for multiplexed detection of these elements.

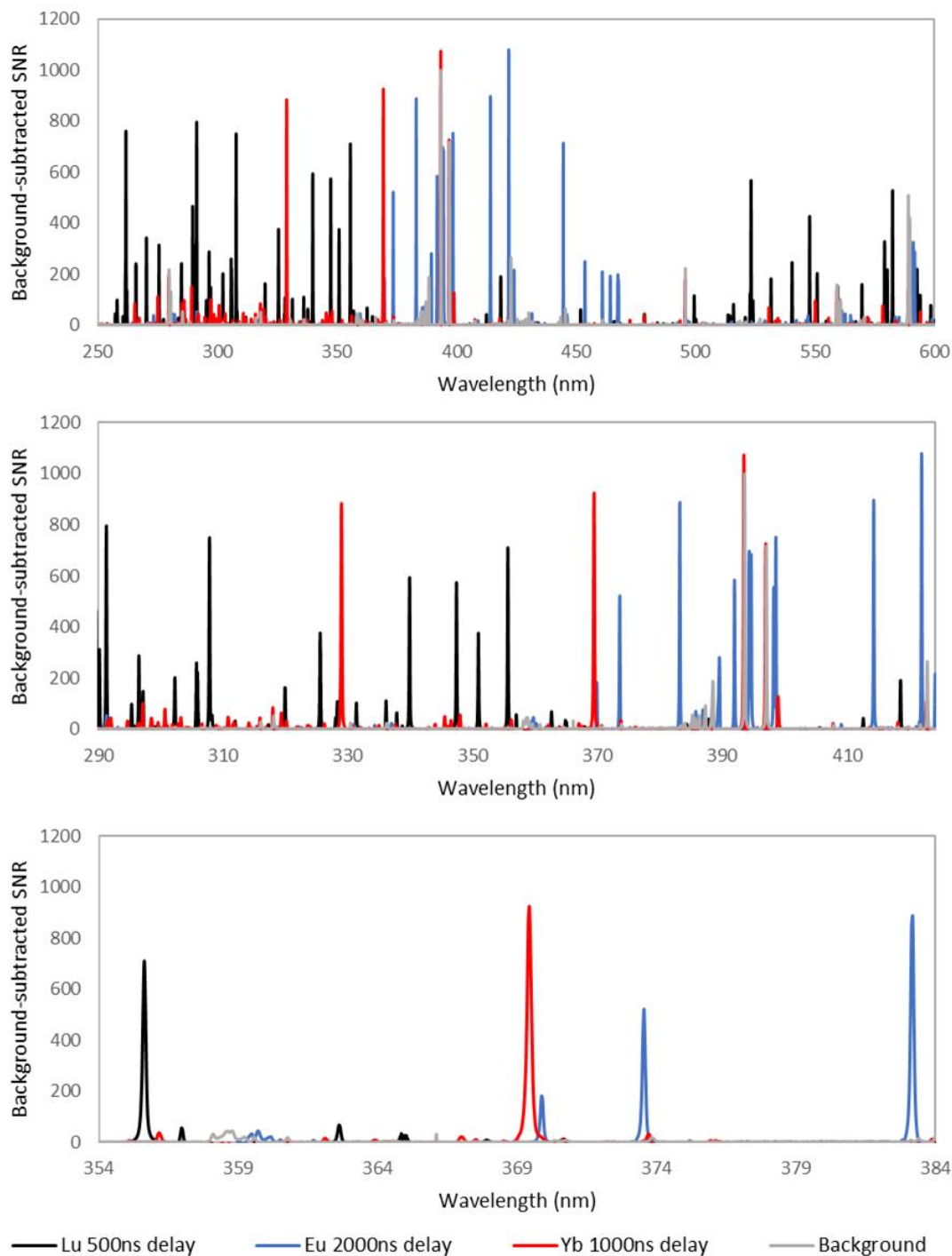


Figure 3.29 Each graph represents the spectrum of Lu, Eu, and Yb on nitrocellulose at their optimum delay time. To more clearly distinguish Lu, Eu, and Yb peaks, the nitrocellulose background was subtracted from each spectrum. The nitrocellulose background is also represented on each plot. All three plots represent the same data, but on different wavelength scales to allow more clear visualization of peaks.

This study simply overlaps data acquired from the experiment presented in section 3.3.3. Figure 3.29 shows the overlapped spectra of background-subtracted Eu, Lu, and Yb, as well as the background. Ideally, a LIBS system would employ a spectrometer with the highest resolution and widest wavelength range available on the market. However, this comes at significant financial cost. For sensitive multiplexed detection of Eu, Lu, and Yb on nitrocellulose, a spectrometer that covers the 290 to 424 nm range with a resolution of 0.5-1 nm may be sufficient. For multiplexed detection of Eu, Lu, and Yb with less sensitivity, but possibly lower spectrometer cost, detection can encompass the 354 to 384 nm range with a 0.2 nm resolution. This study does not account for emissions produced by the food samples to which the Yb, Eu, and Lu labels are being applied. Further study is needed to determine the emission lines produced by the food samples being analyzed, and their effects on Eu, Lu, and Yb emission-line intensity.

3.8 Summary of Chapter 3

This chapter covers a diversity of topics, beginning with basic LIBS system operation and characterization followed by applying the LIBS system to perform fundamental studies on analyte concentration and diversity effects. Each experiment was performed with the intent to understand LIBS System 6's capability for sensitive, multiplexed, and quantitative detection of metal-labeled biomolecules on paper-based assays. Consistent system operation and sample preparation were found to be important aspects of developing a quantitative system. For nitrocellulose treated with Eu CRM solution, the coefficient of variance within samples, between samples, and across different days were determined to be 1.62%-2.82%, 4.55%, and 9.22%. For nitrocellulose treated with Gd CRM solution, these values were higher. The difference may be attributed to signal-intensity and emission-line susceptibility to other factors such as plasma opacity or matrix effects. Based on the data, a method of LIBS sampling was chosen that would allow accurate comparisons between treatments and across different days, with a coefficient of variance between 4.55 and 8.25%. Using these methods and information acquired about laser spot size and power, the 200 to 600 nm spectra of 17 metals were acquired. After identifying several promising emission lines and conducting limit-of-detection experiments, it was found that Ag, Lu, Eu, and Yb were promising candidates for biomolecular labels, since they have the lowest limits of detection. Used individually, these labels could be applied to quantitative detection since they have predictable relationships between concentration and SNR. Self-adsorption occurs when the concentration of

the label is high; therefore, when applying these labels to biomolecular detection assays, it is important to determine if the amount of metal that labels the biomolecules falls within a concentration range that is not affected by self-adsorption. It was also shown that multiplexed detection introduces interesting challenges such as matrix effects. Though matrix effects may hinder quantitative analysis, qualitative detection of food contaminants is still useful and may be achieved with spectral unmixing techniques.

4. APPLICATIONS OF LIBS TO BIOLOGICAL SCIENCES AND FOOD ANALYSIS

4.1 Introduction

This chapter explores the application of laser-induced breakdown spectroscopy (LIBS) for analysis of standard lateral-flow immunoassay (LFIA) platforms and LFIA platforms modified with lanthanide biomolecular labels. The combination of these technologies primarily offers advantages for rapid, portable, and multiplexed biomolecular detection. Such a detection modality is particularly useful in food inspection and forensics, where rapid in-field identification of food contaminants such as *E. coli* has wide-spread public-health impacts.

LFIAAs have become popular field-deployable diagnostic tools because they are simple, portable, and low cost [1-3]. LFIAAs are well described in scientific literature [3, 4]. A common example is the pregnancy test strip, which utilizes gold nanoparticles (GNPs) coated in antibodies for colorimetric detection of human chorionic gonadotropin hormone. Configurations of LFIAAs vary greatly, but a common approach is to use a two-step lateral-flow assay design [5]. In this design, an antigen-containing suspension is mixed in a tube with an antigen label. The solution is introduced to one end of a nitrocellulose strip, and capillary forces wick the labeled antigen along the strip. A defined area downstream of the sample introduction zone displays antibodies that immobilize the labeled antigen, but not the background material, which is removed as it continues to travel downstream. Label that is not bound to a target is captured downstream at the control line. The concentrated label at the test and control lines are then detectable, typically through colorimetric means. Similar designs are common in commercial products, many of which have applications in food science, such as bacterial, allergen, and toxin detection [4]. While commercial LFIAAs are not stand-alone assessments of analyte presence, ongoing advancements and the advantages of LFIAAs in portability and cost suggests a promising future, especially for in-the-field detection.

Increasing the sensitivity and quantitative multiplexing capability of LFIAAs is a key aspect of improving LFIA performance [4, 2]. Multiplexed LFIAAs for food-contamination detection are uncommon because of sample complexity, limited number of antigen labels (e.g., gold, silver, latex), reagent chemistry on the paper substrate, and spatial design [2]. A common multiplexing approach is to spatially differentiate each antigen across a test cartridge. However, the footprint of

the test cartridge increases and becomes more cumbersome as the multiplexing capability increases [2, 3]. An alternative is to use unique labels to differentiate each antigen while maintaining the size of the footprint. This approach would permit a smaller test-cartridge design and smaller sample volumes.

Labels typically used among commercial LFIAs are gold, silver, and latex beads, which visually contrast the background of the assay substrate and biological matrix by localized surface plasmon resonance [2]. In immunochemistry, fluorochromes are widely used labels because of their specificity and excellent signal-to-noise capacity [6] [7, 8]. However, multiplexing either fluorochromes or gold, silver, or latex particles is challenging for most detection modalities owing to overlapping emission or color profiles, short lifetimes, and background effects [9-11, 8]. These features make it challenging to develop detection modalities that are portable and highly multiplexed.

This study proposes a method to overcome the challenges of multiplexed LFIAs by introducing a new detection modality, LIBS – a multi-analyte detection tool [12, 13]. The large number of available labels for LFIAs creates opportunities for highly multiplexed assays that can be used as field-deployable or bench-based diagnostic tools. Existing labels that lend themselves to LIBS analysis are polymer-complexed metals, mostly lanthanides (e.g., europium, ytterbium, praseodymium, and neodymium), which have been developed in the last several years for use in immunoassays analyzed by mass cytometry for discoveries primarily in the field of hematology [11, 14]. The diversity of metal labels and the bandwidth of mass cytometry permits highly multiplexed immunoassays [9, 15, 16]. To date, metal-complexed polymers have not been applied to LFIAs, possibly because the size, cost, and sample preparation requirements of mass spectrometry precludes their transition into the field of low-cost or portable diagnostics [17]. With the rapid advancements being made in laser and optical-sensor technologies, LIBS is becoming increasingly portable [13]. It has potential to become a portable analytical tool for highly multiplexed LFIAs that use polymer-complexed metals for antigen labeling.

LIBS is a technique for simultaneous multi-element identification that relies on the generation and spectral analysis of a laser-induced plasma [12]. While it originated as a bench-top instrument, it has recently been developed into a hand-held commercial product, predominantly applied to characterization of soils, rocks, and scrap metal [13, 18]. Significant effort has been undertaken to apply LIBS to biological applications such as microbial identification

and toxin detection [19, 20, 13, 21-23]. In a few instances, portable LIBS systems were designed for biocontaminant detection [24, 19]. Some studies apply LIBS to analysis of clinical or biological samples, where analytes are labeled with metal tags [25-27, 23]. These studies primarily apply gold, iron, titanium, and silicon micro- and nanoparticles as bio-labels detected with LIBS on a porous membrane-like paper.

This chapter seeks to introduce a wider diversity of metal tags to the intersection between LIBS and analysis of clinical, biological, and environmental samples. Fluidigm Corporation has designed a kit for labeling antibodies with a wide diversity of lanthanides. The first part of this chapter uses LIBS to assess the efficiency of the conjugation kit and determine an estimate for the number of metals conjugated per antibody. The conjugated antibodies are then successfully applied to a LFIA for antibody detection. The product of this experiment serves as a positive control for the next series of experiments that apply lanthanide-labeled antibodies to detect Gram-negative bacteria on a LFIA. A similar test was conducted with gold labels, and a detection limit for *E. coli* using LIBS was established and compared to conventional LFIA detection methods. Most of the studies described in this dissertation used a bench-top LIBS system to analyze LFIA. Since the ultimate goal of this research was focused on portable LIBS detection of biomolecules, it was valuable to determine if hand-held LIBS units could detect lanthanide labels in an immunoassay. A handheld LIBS system was successfully applied to detection of lanthanide-labeled antibodies in an antibody-detection LFIA. This is the first study to report the use of LIBS to detect antigens on a LFIA, and the first to introduce metal-complexed polymers to LFIA. The cumulation of the work in this chapter sets the stage for future work in pairing LIBS with a wide diversity of metal-labeled antibodies and LFIA for sensitive, multiplexed, and portable detection of biomolecules.

4.2 Characterizing the Efficiency of Fluidigm MaxPar X8 Using LIBS

4.2.1 Background

Antibodies are often used for antigen recognition in immunoassays using antibody-conjugated labels that produce signals indicating their presence, and therefore the presence of the antigen. In mass cytometry, commonly used labels are polymer-complexed lanthanides. Fluidigm Corporation is a pioneer in the field of producing instruments and reagents for mass cytometry. Among their products is a conjugation kit that allows the user to covalently bind metals to polymers

and metal-complexed polymers to antibodies. Detailed explanation is provided by the company of the procedures for conjugation [190]. The complete kit comes with a proprietary polymer, buffers, and metal suspension. The polymer contains approximately 30 repeats of 1,4,7,10-tetraazacyclododecane-1,4,7,10-tetraacetic acid (DOTA) chelator and a maleimide group at one end [191]. The protocol for conjugation begins with suspending a lyophilized polymer pellet in a solution of buffer, and then mixing it with a purified metal isotope in solution at an unknown concentration. After incubation between the polymer and metal, excess unconjugated metal is removed via centrifugal filtration. The efficiency of the metal and polymer conjugation process is not described or disclosed by Fluidigm. The metal-complexed polymer is then added to an IgG antibody suspension where the thiol groups have been reduced by tris(2-carboxyethyl)phosphine (TCEP). The maleimide on the polymer covalently binds to the reduced thiol groups on the antibody, with two to four polymers binding to a single antibody. Again, unconjugated reagent is washed away through centrifugal filtration. It is within the interest of the user to not have unconjugated material in the final conjugation product, especially for sensitive detection modalities like mass cytometry. An excess of unlabeled antibody can yield a less sensitive immunoassay, whereas an excess of unconjugated metal can create read-out noise. To obtain maximum output from the conjugation process, it is also beneficial to reduce reagent loss through filter membranes. However, the extent of reagent loss to the filters is unknown.

Chapter 2 examined 17 metals commonly used as antibody labels in immunoassays. Four of the 17 metals, Eu, Lu, Yb, and Ag, have relatively intense emissions and low limits of detection. Eu, Lu, and Yb are sold by Fluidigm as part of their MaxPar X8 conjugation kits. The efficiency of the kits for conjugating Eu, Lu, and Yb to anti-mouse antibodies was evaluated using LIBS. Key measurements obtained were 1) amount of metal provided by the kit, 2) amount of metal lost in the multi-step conjugation process, 3) amount of metal conjugated to the antibody, and 4) metal lost to the centrifugal filter membrane. Section 4.3 covers functionality of the conjugated antibody.

4.2.2 Materials and Methods

MaxPar X8 kits were used to conjugate anti-mouse antibody (A16092, ThermoFisher, Waltham, CA, USA) to 151Eu, 175Lu, and 171Yb (201151B, 201175B, and 201171B, Fluidigm Corporation, San Francisco, CA, USA). There are three key differences between the protocol applied here compared to the protocol recommended by Fluidigm [190]: 1) 200 µg of antibody

was used per conjugation rather than 100 µg; 2) two polymer tubes were used per conjugation rather than one; and 3) in the final steps, the conjugated antibody was recovered from the filter walls using two 100 µl to 200 µl washes rather than a single 80 µl wash. The modifications were recommended by Dr. Gary Nolan's laboratory (personal communication), where the students and staff have extensive experience in the use of MaxPar X8 conjugation kits.

For conjugation to a metal, 95 µl of proprietary L buffer from the conjugation kit was added to one polymer tube, then transferred to another polymer tube. 10 µl of metal supplied by the kit's metal stock solution was then added to the polymer mixture. Following these initial steps, standard Fluidigm procedure was followed until step 32[190], where the antibody was suspended for recovery. In the process of washing the metal-polymer solution using centrifugal filtration, the Fluidigm protocol indicates disposal of the wash waste [190]. However, the waste was instead saved for LIBS analysis. In total, the reaction solution containing the metal went through six wash steps, and therefore six waste products were saved for LIBS analysis. After the sixth wash (step 31) [190], 100 µl buffer were used to wash the walls of the centrifugal filter unit. Each filter wall was washed 10 times without touching the filter membrane with the pipette tip. The unit was inverted into a microcentrifuge tube and spun at $1000 \times g$. The wash, inversion, and centrifugation steps were repeated using an additional 100 or 200 µl buffer. The final volume of antibody suspension was 200-320 µl. After conjugation was complete, antibody concentration was measured using a NanoDrop 2000 (ND-2000, Thermo Fisher Scientific). The final product was diluted with antibody stabilizer (131 050, Candor Bioscience, Wangen, Germany) and 0.2% sodium azide such that the antibody concentration reached the highest round value.

For analysis of MaxPar conjugation efficiency, four types of samples were tested with LIBS: 1) the Max Par X8 metal stock solution; 2) the washes; 3) the final product of the conjugation; and 4) the membranes in the filter units. To determine the original concentration of the metal stock solution, a dilution series of the stock concentration was compared to a standard curve. To determine the amount of metal lost during each wash step, the material collected in the waste containers was analyzed. To determine the amount of metal in the final product, 10 µl of a 50% dilution of the product was loaded onto nitrocellulose squares. Diluents used for the metal stock solution and conjugation product were nitric acid and a proprietary MaxPar X8 kit buffer respectively. Negative controls consisted of nitric acid or kit buffer dried on nitrocellulose squares.

With the exception of the filter units, samples consisted of 10 μ l aliquots loaded onto 6 \times 6 mm nitrocellulose squares, with 1-2 replicates per treatment.

For detection of metals on the centrifugal filter units, the bare membranes of the unit were ablated with the laser 45 times, 3 times per location. The structure of the filter unit was a conical plastic tube where two opposing sections of the interior walls constitute membrane filters. To make the membranes accessible to the laser, the unit was divided into two parts, where each half had undamaged membrane. Like the nitrocellulose squares, the membranes were placed perpendicular to the incoming laser beam. Two types of filters were used per conjugation: filters with 3 kDa and 50 kDa particle-size cutoffs. The 3 kDa filter was used during conjugation of metal to the polymer, allowing unconjugated metal to flow through the filter and into the waste chamber, but not the larger polymer. The 50 kDa filter was used during conjugation of metal-complexed polymer to antibody, allowing the metal-complexed polymer to flow through the filter and into the waste chamber, but not the antibody. As a negative control, untreated 3 kDa and 50 kDa filters were used.

To convert LIBS signal intensity to concentration and mass of metal present in experimental samples, a standard curve was made using a 1 mg/L to 100 mg/L dilution series of Yb, Eu, and Lu CRM solutions. Like experimental treatments, 10 μ l aliquots were dried onto nitrocellulose squares. The standard curve was used to calculate metal concentration for all experimental samples except filter membranes. The filter membranes were made out of different material than the nitrocellulose on which the other experimental samples and CRM solutions were dried. Since LIBS is strongly affected by material type, the standard curves were only compared to other treatments that use the same type of nitrocellulose sample holder.

The LIBS system used for sample analysis was LIBS System 6, described in Chapter 2. In brief, LIBS System 6 utilized: a Nd:YAG 1064 nm laser with 33.6 mJ pulse energy; laser spot size between 500 μ m and 700 μ m; an Andor Shamrock 500i spectrometer with a 300 nm blazed, 1200-l/mm grating; Andor USB iStar ICCD that detected signals at the optimum delay time for each emission line (Table 3.2) across a 500 ns integration time with no gain applied to the intensifier. Chapter 3 details the process of selecting the emission lines and delay times that were then applied to this study: Eu (II), Yb (II), and Lu (II) emission lines 420.504, 369.419 and 291.139 nm with delay times of 2, 1, and 0.5 μ s respectively.

To verify the LIBS-estimated concentration of Eu in the stock metal solution provided by the kit, the solution was digested in 70% nitric acid for 24 hours and diluted to 0.017% and 0.002%

of the original concentration using 2% nitric acid. Negative controls consisted of nitric acid and water used to make the dilutions as well as the buffer in which the final kit product was suspended at the end of conjugation. The latter was also digested and diluted in 70% and 2% nitric acid, like the experimental treatment. As a positive control and for instrument calibration, a standard CRM solution (MS68A-100, Exaxol Corporation, Clearwater, FL, USA) at a concentration of 10 mg/L was used. The samples were analyzed using inductively-coupled plasma mass spectrometry at the Analytical Mass Spectrometry Facility at Purdue University. The results are reported in ppb derived from subtracting signal intensity of the blank from signal intensity of the experimental samples and converting the resulting signal intensity to concentration using a standard curve.

4.2.3 Results and Discussion

Determining Stock Concentration of Metal in the Fluidigm Kit

The results of the standard curve were similar to those observed in Chapter 3 for Eu, Lu, and Yb. There was a positive relationship between log-transformed concentration and signal intensity (Figure 4.1). Like the dilution curves in Chapter 3, which cover a similar concentration range, the trend observed for Lu tends to be more linear than that of Eu or Yb. A second-order polynomial function was applied to the curves and later used to calculate the concentration of metal in samples of unknown concentration.

To estimate an acceptable concentration range for the experimental samples, a dilution curve of the stock metal solution was analyzed. The dilution series of stock metal exhibits a log-logistic relationship between log-transformed concentration and signal intensity (Figure 4.2). A similar trend was observed in Chapter 3 among metal CRM solutions when the concentration range was between 1 and 1000 mg/L (10-10,000 ppm). MaxPar metal solutions at concentrations between 0.02 and 0.99% of the stock concentration produced signal intensities within the range of the standard curve. Dilutions at 0.087, 0.141, 0.23, 0.374, 0.61, and 0.993% of the original concentration were used to calculate the concentration of the MaxPar metal stock solutions. For Yb, Eu, and Lu the stock concentration was determined to be 10,661, 7,460, and 1,845 mg/L respectively, indicating that 106.61, 74.60, and 18.45 μg of Yb, Eu, and Lu were used for conjugation.

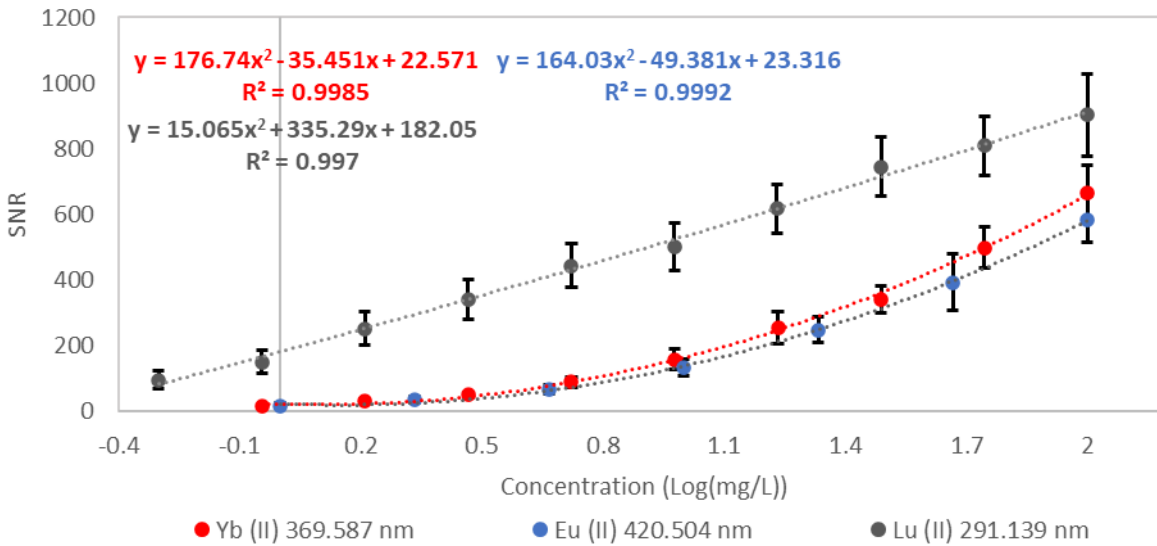


Figure 4.1 Standard curve of Eu, Lu, and Yb CRM solutions.

Mass spectrometry results parallel LIBS results. According to LIBS estimates of Eu concentration, Eu MaxPar stock at 0.017 and 0.002% of the original concentration is equivalent to 1.26 and 10.10 ppb respectively. According to mass spectrometry, the concentration of Eu at the same percent dilutions are 2.58 and 22.33 ppb respectively. Therefore, the concentration of undiluted MaxPar Eu stock is 106,610 ppb according to LIBS and 131,353 ppb according to mass spectrometry (21% difference). During the mass analysis, the signal intensity produced by the blanks was minimal (e.g., blank signal intensity was between 25 and 55 units, CRM standard signal intensity was 3,695,261 units). Mass spectrometry measurements were performed only with MaxPar kit Eu stock solution and should be performed with MaxPar kit Yb and Lu stock solutions.

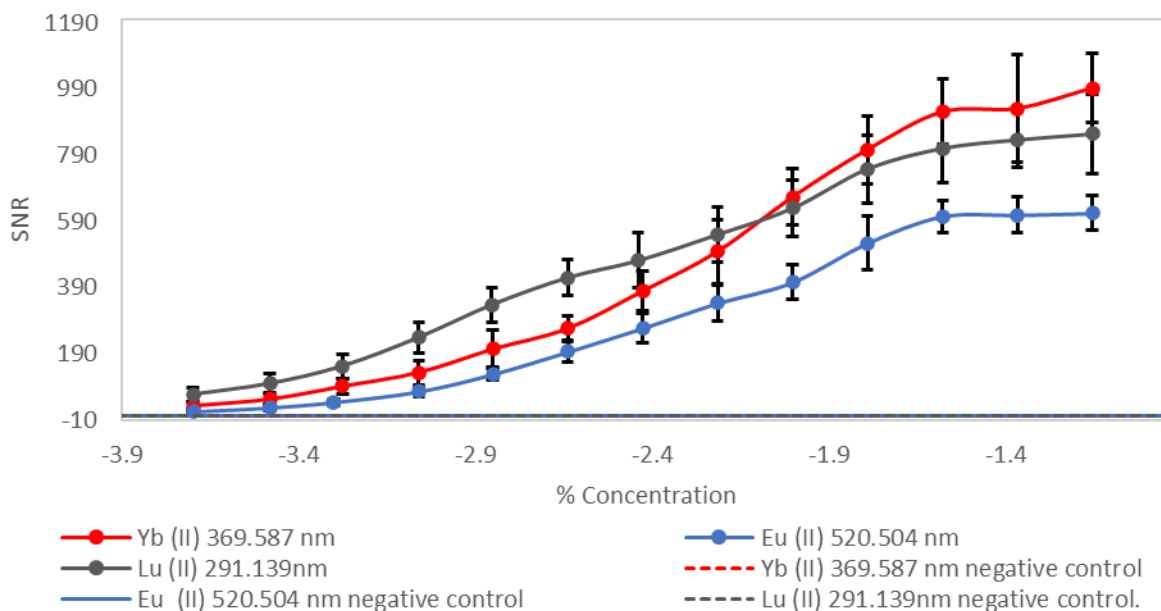


Figure 4.2 Dilution curve of MaxPar X8 metal stock solutions containing Eu, Lu, and Yb. Curves show a log-logistic trends. Negative controls for each treatment overlap.

Centrifugation Steps and Antibody Conjugate Product

Centrifugation steps used 300-400 μ l of wash buffer provided by the kit to remove unconjugated material from the reaction solution. The material that was collected in the waste chamber was analyzed with LIBS. Using the standard curve, signal intensity was converted to milligrams of metal in the wash solution. This value was subtracted from the starting amount of metal to determine how much was left in the reaction solution after each wash (Figure 4.3). LIBS analysis showed that the waste obtained from washes 1-6 contained metal, indicating that unconjugated metal was being removed from the reaction solution.

In Figure 4.3, post wash 1 and post wash 2 represent the amount of metal left in the reaction solution during the conjugation steps where the metal was being chelated to the polymer. 6-13% of the metal was lost in the first two washes. Percent efficiency of metal conjugation to the polymer was 78.13 (Yb), 67.01 (Eu), and 81.39% (Lu) (Table 4.1). 71-83% of metal lost during metal chelation occurs during the first wash.

The product of the conjugation between metal and polymer was added to 200 μ g of antibody. Assuming that unconjugated metal was completely washed out of solution, the amount of metal-complexed polymer added to the antibody solution was 83.30 μ g for Yb, 49.98 μ g for Eu,

and 15.01 μg for Lu. After addition, the reaction solution underwent several more washes. The loss of metal from the reaction solution in between washes was approximately linear (Figure 4.3). In the last wash (wash 6), metal was still found in the waste solution, suggesting that either not all the unconjugated metal had been removed from the final product, or the final product was being lost through the filter and collected in the waste chamber.

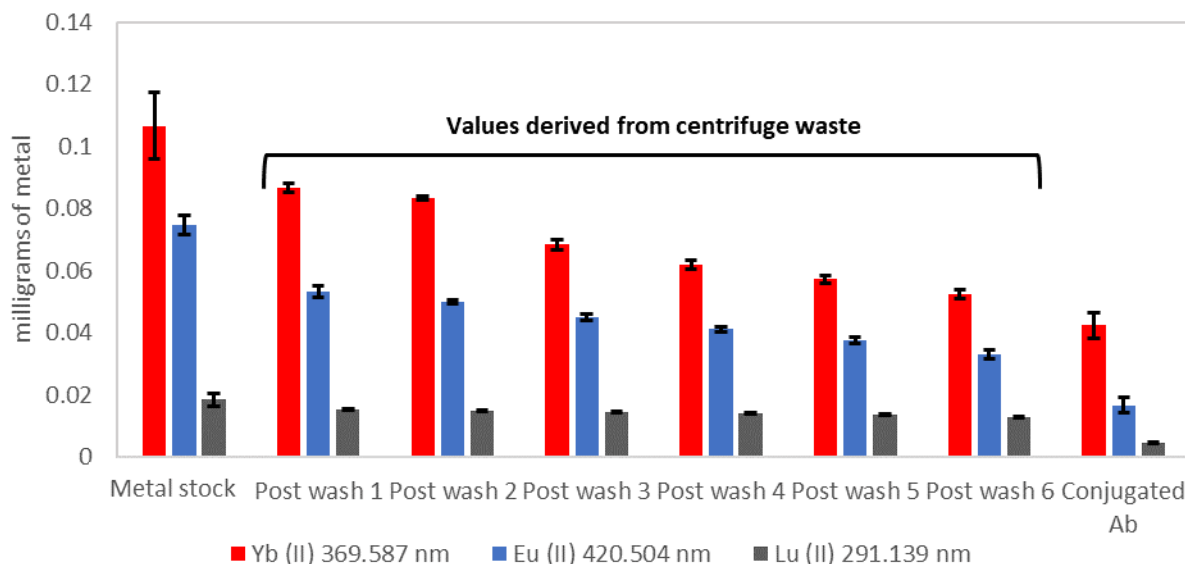


Figure 4.3 SNR of Yb, Eu, and Lu in the metal stock and conjugated antibody (Ab) solution were measured by drying the solutions on nitrocellulose paper followed by LIBS analysis. SNR was converted to milligrams of metal using a standard curve. Milligrams of metal in post washes 1-6 was measured by drying the waste from each wash step on nitrocellulose, followed by LIBS analysis, unit conversion, and subtracting the amount of metal found in the waste solution from the amount of metal in the reaction solution. Post washes 1-6 represent an estimate of the amount of metal in the reaction solution.

Ideally, the final product should consist only of metal-chelated polymer conjugated to an antibody. The final product was measured with LIBS and the signal converted to micrograms of metal using the standard curve. Based on the assumption that there was no unconjugated material in the final product, there was 42.4 μg of Yb, 16.6 μg of Eu, and 4.58 μg of Lu conjugated to antibodies. Based on the amount of metal determined to be used for conjugation after wash 2 (post wash 2 in Figure 4.3), retention of metal-complexed polymer during conjugation to the antibody was determined to be 50.92, 33.32, and 30.51% for Yb, Eu, and Lu respectively (Table 4.1).

Table 4.1 Percent efficiency of MaxPar X8 conjugation kit for antibody (Ab) and metal retention. Overall Ab and metal retention values represent the percent of each material retained from the beginning of the protocol to the final product. Metal retention for chelation represents the percent of each material retained in the reaction solution between the beginning of the protocol to post wash 2. Metal retention for Ab conjugation represents the percent of each material retained in the reaction solution between post wash 2 to the final product.

	Ab retention % overall	Metal retention % overall	Metal retention% (for chelation)	Metal retention% (for Ab conjugation)
Yb	73	39.79	78.13	50.92
Eu	63	22.33	67.01	33.32
Lu	78	24.83	81.39	30.51

Table 4.2 Quantity of metal and antibody in the final product of MaxPar X8 conjugation. Based on these values, mg of metal, mol of metal, and atoms of metal per antibody were determined.

	Metal (μg) in conjugation product	Ab (μg) in conjugation product	Number of Abs (based on IGG weighing 2.49E-16 mg)	mg of metal per Ab	mol of metal per Ab	atoms of metal per Ab
Eu	16.65	126.16	5.06E+14	3.29E-23	2.16E-22	130.26
Lu	4.58	155.10	6.23E+14	7.36E-24	4.20E-23	25.31
Yb	42.42	146.63	5.89E+14	7.21E-23	4.16E-22	250.68

Using the NanoDrop2000 spectrophotometer, the amount of antibody in the final product was determined to be 155.10 μg, 126.16 μg, and 146.63 μg for the Yb, Eu, and Lu conjugations respectively (Table 4.2). Based on the starting amount of antibody used for conjugation (200 μg), the kit's antibody retention efficiency was determined to be 73, 63, and 78% (Table 4.1). Considering Avogadro's constant (6.02E23 atoms/mol), the atomic mass of Yb (173.04 g/mol), Eu (151.964 g/mol), and Lu (174.967 g/mol), and the mass of an IgG antibody (2.49E-19 g), it was found that the number of Yb, Eu, and Lu atoms conjugated to each antibody were 250.68, 130.26, 25.31 atoms/antibody respectively. Recall that Fluidigm reports approximately 60 atoms/antibody [191]. However, the efficiency of conjugation potentially depends on the metal, the amount of starting material, and subtle differences in the protocol. In this case, the kit for Yb conjugation contained the most metal starting material, followed by the Eu and Lu kits. Likewise, the Yb-antibody conjugate contained the most metal, followed by the Eu and Lu kits. Assuming that there was no unconjugated metal or metal-complexed polymer in solution, the MaxPar Yb conjugation kit was the most efficient at conjugating metals to the antibody used for this study, followed by the Eu and Lu conjugation kits.

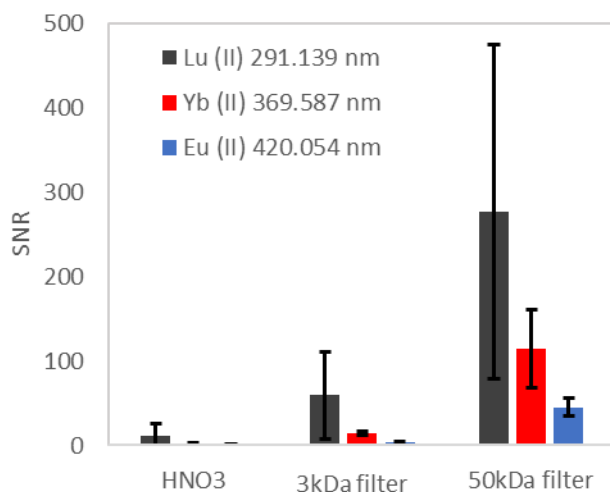


Figure 4.4 3 kDa and 50 kDa centrifugal filter units were used to remove unconjugated reagent from the reaction solution. To determine if metal remained embedded in the membranes of the filter units, the membrane surface was tested with LIBS. The material remaining in the filter could be metal-complexed polymer or metal-labeled antibody, indicating that reaction efficiency may have been impacted by product loss to the filters.

In Figure 4.3 there is a notable drop in the amount of metal contained in the reaction solution between post wash 6 and the final product. Recall that the values represented in post wash 1 were calculated by subtracting the amount of metal found in the waste from the amount of metal measured in the previous reaction solution. The amount of metal contained in the final product was instead measured directly with LIBS. The drop between post wash 6 and the final product could be attributed to metal lost to the filters or pipettes during washing, and therefore not accounted for in the waste. LIBS was performed on the membranes within the filters to determine if there was embedded metal. The first LIBS pulse displayed little or no metal signal from either Eu, Lu, or Yb. The second pulse yielded a strong signal from each metal. The third pulse displayed little or no metal signal. The second pulse across 15 locations along the filter are represented in Figure 4.4. Note that the plotted values are of signal intensity, not quantity of metal, indicating that metal is present, but not the amount of metal. The plot shows that there is more of each metal attached to the 50 kDa filter than to the 3 kDa filter, indicating that more product loss may be attributed to the former filter than the latter. IgG antibodies are generally recognized to be 150 kDa [192], significantly larger than the 50 kDa filter membrane. The size of the polymer produced by Fluidigm is proprietary, therefore unknown, but estimated to be between 3 and 50 kDa. It is

presumed that the polymer conjugated to the antibody becomes entangled with the porous 50 kDa filter membrane, unable to continue passage through the membrane during centrifugation owing to the larger antibody acting as an anchor. The same entanglement does not occur in the 3 kDa filter, because the polymer is too large to become entangled in the membrane pores. As a result, higher signal is detected in the 50 kDa filter, indicating that product is lost owing to entanglement with membrane.

Since the material composition of the membrane in the filter is different from that used to make the standard dilution curve, the percent of metal lost to the membrane during conjugation was not determined. However, it was determined that there was loss of metal to the membranes. Quantitative measure of the amount of metal in the membrane can be achieved by creating a standard curve of CRM solution on filter membranes; however, it was not pursued in this study.

4.2.4 Section Summary

The goal of this section was to characterize the Fluidigm MaxPar X8 kit using LIBS and provide support for some of the results using mass spectrometry (MS). A form of mass spectrometry, mass cytometry, is commonly paired with detection of MaxPar X8 conjugation products applied to immunoassays. This study shows that, similar to MS, LIBS can also detect the product of the MaxPar X8 kit, and therefore could be an alternative detection modality in immunological studies that do not require isotope identification. The advantage to LIBS detection is that the sample does not require the same sterility applied to MS samples, as well as being less expensive and capable of analyzing different material types like those featured here: liquids dried on nitrocellulose and membrane components of centrifugal filters. LIBS has been known to be applied to analysis of liquids as well [18]; however, this was not pursued here. Characterization of the MaxPar X8 kit sets the stage to the application of the kit product to a LFIA.

4.3 LIBS Detection of Metal-labeled Antibodies Applied to a LFIA

4.3.1 Background

A study was conducted to determine if the antibodies conjugated in the previous section were 1) functional post conjugation, and 2) could be used and detected in an LFIA that would later be applied to bacteria detection. Lateral-flow assays for Gram negative bacteria detection are a

part of WaterSafe® bacteria test kits (Silver Lake Research, Azusa, CA, USA). The kit comprises lyophilized gold nanoparticles that bind to Gram negative bacteria in solution, followed by introduction to a lateral-flow assay that immobilizes the gold-labeled bacteria at the detection zone (test line). Excess gold label binds to the control zone (positive control line). Conventional analysis of the strip involves visual or image-based analysis of the pink nanoparticles clustered at the test line. In this experiment, only the strip and not the gold nanoparticles were used. It was hypothesized that the test and/or control line consisted of anti-Gram negative antibodies raised in mice. To test the hypothesis, gold nanoparticles conjugated to anti-mouse antibodies were applied to the strip. The appearance of a pink line at the detection and control zone indicated that the reagents in these zones were either antibodies raised in mice, or material that nonspecifically reacted to the anti-mouse antibody. A similar experiment applied anti-mouse antibodies conjugated to Eu and Lu to the strip. Unlike the gold nanoparticles, the Eu and Lu labels were not visible. LIBS determined that Eu- and Lu-conjugated antibodies had been immobilized at the test and control line. Data for Eu-conjugated antibodies applied to WaterSafe® can also be found in “Detection of *E. coli* labeled with metal-conjugated antibodies using lateral-flow assay and laser-induced breakdown spectroscopy”, published in *Analytical and Bioanalytical Chemistry* (DOI:10.1007/s00216-019-02347-3).

4.3.2 Materials and Methods

Gold Nanoparticle Conjugation

Anti-mouse antibodies (A16092, ThermoFisher Scientific) were passively absorbed onto the surface of gold nanoparticles and applied to the test strip. Absorption reactions were performed at different pH and antibody concentrations. The most successful treatment was applied to WaterSafe® strips. For the first step of conjugation, 5, 15, and 22.5 µl of 100 mM Na₂HPO₄ in 150 mM NaCl at pH 8 were added to 15 ml Falcon tubes labeled “1”, “2” and “3.” Two, six, and nine µg of antibody (0.75, 2.26, 3.39 µl respectively) were added to the Falcon tubes such that the final concentration of antibody in each tube was 0.35 mg/ml. One milliliter of 20 nm gold nanoparticles (OD = 1) (G-20-20, Cytodiagnostics, Toronto, Canada) mixed with 40 µl of Na₂HPO₄ at pH 7, borate buffer at pH 8, and borate buffer at pH 9, were added to tubes 1, 2, and 3 respectively while vortexing briefly. Tubes were set on a rotator at room temperature and allowed

to incubate for 30 minutes. Fifty microliters of 10% BSA was added to each tube after incubation. Solutions were transferred to microcentrifuge tubes and centrifuged at $6,500 \times g$ for 25 min. Supernatant was carefully removed without disturbing the gold-nanoparticle pellets. Pellets were resuspended in 100 μ l storage buffer (20 mM Tris (pH 8.0), 150 mM NaCl, 1% (w/v) BSA, 0.025% Tween 20). This process was repeated three times per treatment for a total of nine samples.

To evaluate if conjugation was successful, 50 μ l of each treatment was loaded into the wells of a 96-well flat-bottom transparent plate (655101, Greiner Bio-One, Kremsmünster, Austria), and absorbance was measured using a spectrophotometer (SpectraMax M5, Molecular Devices, San Jose, CA). Absorbance of unconjugated nanoparticles and storage buffer were also measured as controls.

To determine if the test and control line on the WaterSafe® LFIA were composed of mouse antibodies, first the plastic covering on the strip was removed to expose the glass fiber pad. Conjugated gold nanoparticles were diluted in storage buffer such that the OD = ~1. Sixty μ l of the gold nanoparticle solution was added to the lateral flow assay (sample size = 1). After 10 minutes the strip was visually analyzed to determine if a pink line had developed at the detection and positive control zones.

Lanthanide-Labeled Anti-mouse Antibodies on LFIA

Since binding of gold nanoparticles coated with anti-mouse antibodies was observed at the test and control lines (discussed further in the results section), anti-mouse antibodies conjugated to Eu and Lu using the method and protocol described in Section 4.2 were also applied to a WaterSafe® assay to see if the results would be similar.

Sixty μ l of a 15 μ g/ml solution of Lu-conjugated antibodies were added to the sample introduction pad of the WaterSafe® Strip after the plastic covering was removed. The solution was observed to wick along the strip to the waste pad. After 10 minutes, the conjugate and waste pad were removed from the strip to prevent reagent from back-washing into the nitrocellulose strip. After drying for 2 hours, three areas on the strip were analyzed with LIBS: the test line, control line, and the area adjacent to the test line.

In a similar test, 30 μ l of 160 μ g/ml Eu-conjugated anti-mouse antibodies were added to a WaterSafe® LIFA. Unlike the previous test, this test also introduced *E. coli* into the antibody

solution, as well as WaterSafe® lyophilized gold nanoparticles, which target Gram negative bacteria. The mixture was incubated for 1 hour.

The same LIBS System 6 parameters described in the previous section were applied here. Ablations were made across the width of the nitrocellulose strip at the test, positive-control, and negative-control line/zone. Six ablations, each in a different location, were used per line/zone.

4.3.3 Results and Discussion

Gold Nanoparticle Conjugation

For all treatments applied to the conjugation between antibody and gold nanoparticles, absorbance peak shifted from 516 nm (unconjugated 20 nm gold nanoparticles) to 520-526 nm, indicating successful conjugation (Figure 4.5). Figure 4.5 shows the coloration of the gold nanoparticles after incubation at 30 min. Red coloration and absence of nanoparticle aggregates were also an indicator of successful conjugation as the protocol was being completed.

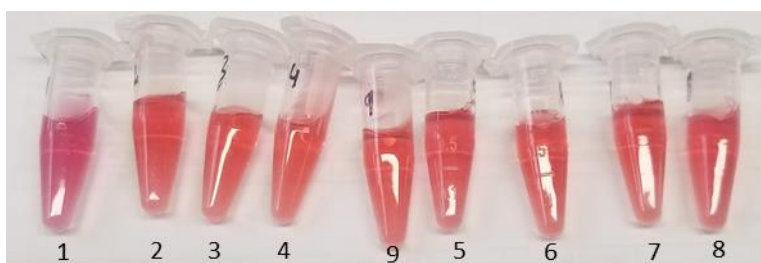


Figure 4.5 20 nm gold nanoparticles after 30 minutes of incubation with antibody and buffer. Numbers indicate the treatment. Coloration of the nanoparticles was used as an indicator of conjugation success. A red hue (absorbance = 516 nm) indicated little aggregation, whereas a purple hue (absorbance > 516 nm) or clumps indicated nanoparticle aggregates and precipitation.

Gold nanoparticles conjugated to antibodies in treatment 5 were selected for use in the WaterSafe® assay. After 10 minutes of being applied to the assay, gold nanoparticles were observed to bind to the detection and control zones. The test line was observed to have a darker coloration than the control line, indicating a higher concentration of gold nanoparticles (Figure 4.6). Binding indicated that the reagents at the detection and control zones were either antibodies raised in mice or reagents nonspecifically reacting with the antibodies on the nanoparticle. Similar

but separate experiments confirmed that unconjugated gold nanoparticles and gold nanoparticles conjugated to anti-Gram negative antibodies did not bind to the test and control line, supporting the hypothesis that the reagents at the detection and control zones were antibodies raised in mice.

In the previous experiment, anti-mouse antibodies conjugated to gold nanoparticles successfully reacted with the test and positive-control line on a WaterSafe® strip. The same antibodies were conjugated to Eu- and Lu-complexed polymers in section 4.2. Since the antibody-conjugated gold nanoparticles successfully reacted with the detection and control zones, it was hypothesized that the same antibodies conjugated to Eu- and Lu-complexed polymers would do the same. Unlike gold nanoparticles, Eu- and Lu-complexed polymers do not produce a visual signal, so the strips required LIBS analysis. Similar to test strips treated with gold nanoparticles, the test line had the highest concentration of Eu- and Lu-labeled antibodies, followed by the control line and the area adjacent to the control line (Figure 4.7).

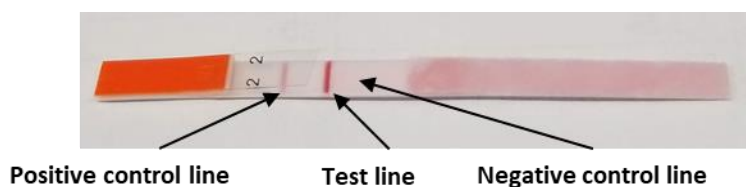


Figure 4.6 WaterSafe® assay for detection of Gram-negative bacteria. The plastic covering of this strip was removed to expose the sample absorption pad (right). Anti-mouse antibodies conjugated to gold nanoparticles were added to the sample absorption pad and were observed to wick along the strip. After 10 minutes of incubation, test and control lines were observed on the strip, indicating that the reagents immobilized to these areas by the manufacturer were either antibodies raised in mice or reagents that cross-reacted with the anti-mouse antibody.

A study to assess the functionality of Yb-labeled anti-mouse antibody has yet to be conducted. However, based on the success of the Eu- and Lu-conjugated anti-mouse antibodies in a simple immunoassay on a WaterSafe® test strip, it was anticipated that the Yb-conjugated anti-mouse antibodies would be successful as well. The results from these experiments suggested that 1) the reagents on the WaterSafe® test and control line were antibodies either raised in mice or ones that cross-reacted with Novex A16092 anti-mouse antibodies; 2) antibodies labeled with lanthanide-complexed polymers could be used in a WaterSafe® assay; 3) anti-mouse antibodies labeled with lanthanides and applied to a WaterSafe® assay could be used as a positive control for future experiments testing the functionality of lanthanide-labeled antibodies that target microbes

in a WaterSafe® assay. The third point in this list of results was applied to the next section of this chapter, which tested Eu-labeled anti-*E. coli* and anti-Gram negative antibodies in a WaterSafe® LFIA with *E. coli* present.

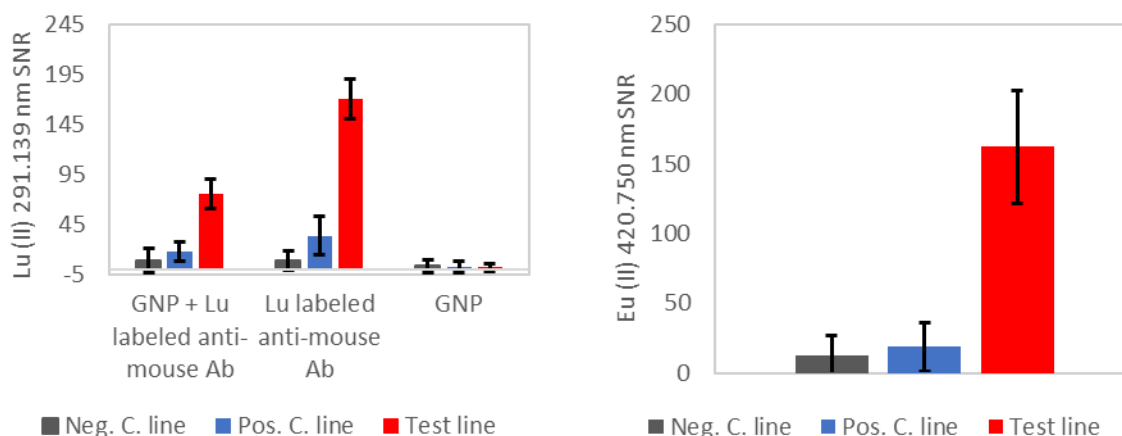


Figure 4.7 Lu-labeled antibodies (left) and Eu-labeled antibodies (right) applied to WaterSafe® detection strips. The goal of the assay was to determine if the anti-mouse antibodies would bind to the test and positive control lines as did gold nanoparticles (GNPs) conjugated to the same antibodies. The strongest Eu and Lu emissions were found at the test line, followed by the control line and the negative control line. For the study with Lu-labeled antibodies, signal intensity was lower in the presence of gold nanoparticles. Signal intensity was minimal in the treatment where Lu-labeled antibodies were absent.

4.3.4 Section Summary

This section applied the lanthanide-labeled antibodies created and described in the previous section to a simple antibody-detection immunoassay that took place on a lateral flow strip. Using LIBS, it was found that the lanthanide-labeled anti-mouse antibody binds to the test and control line of a commercial Gram negative–bacteria detection strip. Using visual detection, binding was verified using gold nanoparticles conjugated to anti-mouse antibodies. This suggested that the strip test-line used anti-Gram negative capture antibodies raised in mice. Though the performed assay was simple, it established an important positive control for future experiments in which the WaterSafe kit was modified so that, instead of gold nanoparticles to detect Gram-negative bacteria, antibodies labeled with lanthanides were used instead. Based on the results in Chapter 2, Eu, Yb, Lu, and Ag labels will yield more sensitive LIBS detection than Au labels.

Table 4.3 Gold-nanoparticle conjugation treatments were described by the quantity of antibody used and pH of the conjugation buffer. Conjugation success was determined using peak absorbance measurements. A right shift in absorption wavelength indicated conjugation. Compared to unconjugated nanoparticles, all other treatments except the negative control displayed a right shift in absorbance.

Tube ID	Quantity of antibody used (ug)	pH buffer	Final OD	Peak absorbance (nm)
1	2	7 (Na ₂ HPO ₄)	0.64	524
2	6	8 (borate)	0.82	524
3	9	9 (borate)	0.71	524
4	2	7 (Na ₂ HPO ₄)	0.80	522
5	6	8 (borate)	0.76	524
6	9	9 (borate)	0.77	524
7	2	7 (Na ₂ HPO ₄)	0.86	520
8	6	8 (borate)	0.79	526
9	9	9 (borate)	0.82	524
Storage buffer	0	8 (Tris buffer)	0.08	423
Unconjugated	0	Citric acid	0.36	516

4.4 LIBS Detection of Gram-negative Bacteria Applied to a LFIA

4.4.1 Background

Sections 4.2 of this chapter covered Eu, Lu, and Yb conjugation to lanthanides. Section 4.3 determined that lanthanide-conjugated antibodies could be used for a simple antibody-detection assay in a commercial assay for detection of Gram negative bacteria. This section goes a step further – instead of performing an antibody-detection assay, the assay is applied to Gram negative bacteria (*E. coli*) detection. Labels used for Gram negative bacteria detection are gold nanoparticles supplied by the WaterSafe® detection kit, and anti-*E. coli* antibodies conjugated to Eu and Lu. This was the first study to report the use of LIBS to detect labeled bacteria on a LFIA. LIBS and visual detection of *E. coli* using Au particles was successful. The results suggested that LOD for Au-labeled *E. coli* detection was comparable between LIBS and image analysis. In theory, the LIBS detection limit could be improved using an Eu, Lu, Yb, or Ag label, making it more sensitive than visual/image analysis. This section attempts to replace the gold nanoparticles supplied by the WaterSafe kit with anti-*E. coli* and anti-Gram negative antibodies conjugated to Eu. Though the outcome of this last experiment did not yield binding between *E. coli* and

lanthanide-labeled antibodies, it can be used as a guideline for future experiments. Most of the work presented in this section was published in “Detection of *E. coli* labeled with metal-conjugated antibodies using lateral-flow assay and laser-induced breakdown spectroscopy” (*Analytical and Bioanalytical Chemistry*, DOI:10.1007/s00216-019-02347-3).

4.4.2 Materials and Methods

Bacteria Detection Using WaterSafe® Gold Labels

WaterSafe® bacteria test strips use Au to label Gram negative bacteria like *E. coli*. While the strips are typically interpreted visually or with image analysis, we attempt to compare this modality to a LIBS system optimized for gold detection.

A colony of *E. coli* K12 was selected from a tryptic soy agar culture plate and suspended in phosphate-buffered saline (PBS), from which a dilution series was prepared. The number of colony forming units (CFU)/ml of the stock was determined by plating the last four dilution steps and colony counting after a 24-hr incubation period at 37 °C. 100 µl each of *E. coli* suspensions with a concentration of 3.50E6, 3.50E5, 1.75E5, 3.51E4, 7.35E3, 4.23E3, 9.43E2, and 0 CFU/ml were mixed with 100 µl of gold nanoparticles from WaterSafe® bacterial test kits suspended in purified water (optical density (OD) = 0.4) for 5 min. WaterSafe® bacterial test strips from the kit were introduced to the solutions (three replicates per dilution) for 10 min. A pink color at the control line developed on each strip, indicating that the assay was functioning properly. A pink coloration at the test lines was also observed to form; the intensity of the pink line decreased with decreasing *E. coli* concentration.

The nitrocellulose portion of the test strip was separated from the conjugate and waste pad, and air-dried for 2 hrs. The membranes were then imaged using a stereomicroscope. Images were then used for analysis. Image analysis of WaterSafe® strips utilized ImageJ [193] to first perform background subtraction followed by image inversion. “Background” was considered the area adjacent to the test line in the treatment with 0 CFU/ml *E. coli*. Integrated density, or the product of area and mean gray value, was determined for each test line and area adjacent to the test line.

LIBS was performed after imaging using a 0.5 µs delay time and 500 ns integration time. Of the three wavelengths identified for Au, 242.795 nm and 267.595 nm lines were selected because they had the best LODs and fit within the same 30 nm acquisition window. Two to three

regions of the strip were analyzed: the test line, area adjacent to the test line, and the positive-control line (Figure 4.5). Each of these areas was shot 6-8 times across the width of the strip (one pulse per location).

Bacteria Detection Using Lanthanide Labels

Similar to the previous study that used gold nanoparticles, a suspension of *E. coli* was made and applied to each of the treatments listed. The experimental treatment consisted of 240 μ l *E. coli* suspension mixed with 60 μ l of 0.5 mg/ml Eu-labeled anti-*E. coli* antibodies (Ab31499, Abcam, Cambridge, United Kingdom) and incubated for 1 hour at room temperature in a microcentrifuge tube. The negative control treatment consisted of Tris buffer supplemented with BSA (240 μ l of 20 mM Tris (pH 8.0), 150 mM NaCl, 1% (w/v) BSA, 0.025% Tween 20) mixed with 60 μ l of 0.5 mg/ml Eu-labeled anti-*E. coli* antibodies and also incubated for 1 hr. Treatment 3 consisted of a variation of the positive control developed and tested in section 4.3: 120 μ l *E. coli* was mixed with lyophilized gold nanoparticles supplied by the WaterSafe® Kit, and then supplemented with 30 μ l of 0.5 mg/ml Eu-labeled anti-mouse antibody. The experimental and negative control treatments were incubated for 1 hour. The positive control treatment was incubated for 10 minutes.

A variation of the experiment described in the previous paragraph was repeated, but with Eu-labeled anti-Gram negative antibodies (Ab41201, Abcam) instead of labeled anti-*E. coli* antibodies. *E. coli* (preparation described previously) was incubated with 15 μ l of 0.1 mg/ml Eu labeled anti-Gram negative antibody in 100 mM Na₂HPO₄ buffer at pH 7 and 8, and a borate buffer at pH 9.

Both experiments were tested with LIBS using the same methodology as the previous section. Image analysis was not performed since the metal-complexed polymers did not produce a visual signal.

4.4.3 Results and Discussion

A LIBS system with low LOD is particularly important when attempting to detect rare analytes. Food contaminants can be extremely hazardous even in minute quantities, and therefore detection modalities must be sensitive and fast. *E. coli* is a common food and water contaminant, and acceptable concentrations of *E. coli* in drinking water and food vary according to strain. As an

example, for generic *E. coli* detection the U.S. Department of Agriculture states that chicken rinsate containing ≥ 1000 CFU/ml during industrial processing is unacceptable [194]. Concentrations below this value are considered either acceptable or marginally acceptable.

The present study utilized WaterSafe® bacteria detection strips to detect Gram negative bacteria, in this case *E. coli*, using Au labels. The LOD reported by the manufacturer for these strips is 1000 CFU/ml, enough to potentially distinguish between acceptable and unacceptable concentrations of *E. coli* in chicken rinsate. Strips were introduced to a dilution series of *E. coli*. As with many LFIA's that use gold, latex, or silver labels, the result of the dilution series was assessed by detecting the label at the test line with image analysis. A positive linear relationship was found between integrated density and log-transformed *E. coli* concentration ($R^2 = 0.99$). LOD with image analysis was found to be 8.89×10^3 CFU/ml, on the same order as the manufacturer's reported LOD, 1000 CFU/ml. To determine if LIBS could achieve a better LOD, the pink detection zones were analyzed for the presence of Au using an optimized system. LIBS analysis of the Au 242.795 nm line also showed a positive linear relationship but with a worse linear fit ($R^2 = 0.93$). The resulting LOD was comparable to image analysis (1.03×10^4 CFU/ml). There is significant potential for improving LIBS limit of *E. coli* detection by using a label that produces a more intense signal than Au. Yb, Lu, Eu, and Ag are good candidates because they are already widely used in the field of immunochemistry for antigen labeling and produce a more intense LIBS signal than Au.

In experiments that utilized anti-*E. coli* and anti-Gram negative Eu-labeled antibodies, the strongest Eu signal was produced by the positive control line. The test line and area adjacent to the test line were observed to produce signals of similar intensity (Figure 4.8 and Figure 4.9). The results indicate that, although *E. coli* may have bound to the test line, Eu-labeled antibodies did not bind to the *E. coli*. In other words, a sandwich between the capture antibody on the assay, the antigen, and the detection antibody was unlikely. Changing pH of the reaction buffer had minimal effects on the signal intensity measured in each region. Unlike the experiment that yielded successful detection of *E. coli* using WaterSafe® reagents and gold labels, the Eu-labeled antibodies and reagents used here were purchased from a separate supplier and not optimized for use in the WaterSafe® strip. There are many possible reasons for their incompatibility, among which are reaction kinetics of the antibodies, salt concentration, type, and volume, and effect of lanthanide conjugation on antibody function.

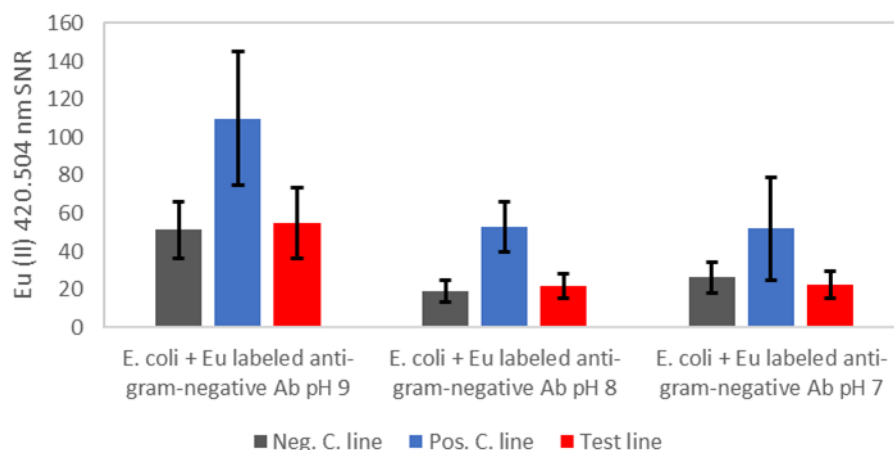


Figure 4.8 Eu-labeled anti-Gram negative antibodies were applied to WaterSafe® Gram-negative bacteria detection strips in the presence of *E. coli* and buffers at different pH levels. In each case, the signal was strongest at the positive control line and equivalent at the test and negative-control lines.

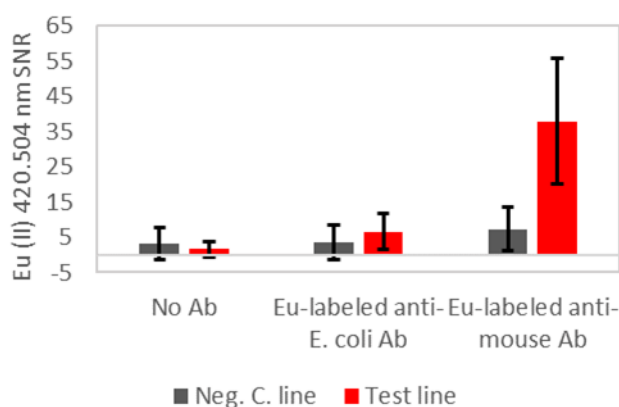


Figure 4.9 Eu-labeled anti-*E. coli* antibodies were applied to WaterSafe® Gram-negative bacteria detection strips in the presence of *E. coli*. As a positive control, Eu-labeled anti-mouse antibodies were similarly applied to the strip. As a negative control, neither Eu-labeled antibody nor *E. coli* was added to the strip. In the experimental treatments, the signal was equivalent at the test and negative-control lines. In the positive-control treatment, signal was strongest at the test line. In the negative-control treatment, signal was equivalent at the test and negative-control lines.

4.4.4 Section Summary

This section investigated whether metal-labeled antibodies could be used to detect bacteria at a concentration that is relevant to food safety. It was found that LIBS can be used to detect *E. coli* at a limit equivalent to that of visual detection on a WaterSafe LFIA. When the kit reagents for antigen detection were exchanged for Eu-labeled anti-*E. coli* and anti-Gram negative antibodies, detection of *E. coli* was unsuccessful. For similar studies in the future, it is recommendable to carefully assess antibody compatibility with buffers, substrates, and antigen. The selection of antibody, buffer, and substrate can be accomplished using gold nanoparticles since they are rapidly conjugated to antibodies and binding success can be quickly and visually determined. Once an appropriate antibody is found, it could be conjugated to a metal that produces a strong LIBS signal (Eu, Lu, Yb, or Ag), applied to a LFIA, and detected with LIBS. Despite the failure of detecting *E. coli* using lanthanide-labeled antibodies in a LFIA, the success achieved with gold nanoparticles shows that LIBS can detect labeled *E. coli* at concentrations relevant to public health. This success and the success of previous studies using lanthanide-labeled anti-mouse antibodies suggest a more promising outcome if the correct pairing of antigen, antibody, and substrate is found.

4.5 Hand-held LIBS Detection of Metal-labeled Antibodies Applied to a LFIA

4.5.1 Background

So far, the experiments in this chapter utilized LIBS System 6 for sample analysis. LIBS System 6 is strictly a bench-top instrument that has the advantage of permitting the user to tune parameters to optimize the system for the substrate. This section explores whether the SciAps LIBS system (described as LIBS System 5 in chapter 2) can also perform detection of lanthanide-labeled antibodies in a WaterSafe® bacteria detection strip. Though this instrument is primarily for scrap-metal analysis, if successful in detecting metal labels in nitrocellulose, it would suggest a promising future for a hand-held LIBS system designed specifically for the analysis of LFIA.

4.5.2 Materials and Methods

Two colonies of *Escherichia coli*, *Klebsiella pneumoniae*, and *Salmonella enterica* were each sampled from cultures growing on a tryptic soy agar culture plate after a 24 hr incubation period at 36 °C and suspended in 4 ml water (stock solution). Bacteria were further diluted by adding 275 μ l of the stock bacteria suspension to 1 ml water (concentration of bacteria was unknown). 100 μ l of each bacterial suspension was added to the well of a 96-well plate. 50 μ l gold nanoparticles from WaterSafe® Kit suspended in PBS were added to each well and allowed to incubate for 10 min at room temperature. 150 μ l of 0.1 mg/ml Eu-labeled anti-mouse antibody was added to each well and incubated for 1 hour at room temperature. After incubation, WaterSafe® strips were introduced to the wells. The suspensions were observed to wick up the strip. After 20 minutes, the strips were removed from the solution, and the sample absorption and waste pads were removed to prevent backwash into the nitrocellulose strip. The nitrocellulose was allowed to dry for 2 hours and then tested with the hand-held SciAps LIBS system described as LIBS System 5 in Chapter 2. In summary, this LIBS system utilized a Nd:YAG 1064 nm laser with a pulse energy of five to six mJ, pulse width of one to two ns, and repetition rate of fifty Hz. Fifty laser pulses were used across a 2×2.5 mm sampling area (one pulse per location). Two regions of each nitrocellulose strip were analyzed with LIBS: the test line and the area adjacent to the test line (negative control). Ablation marks made on the strip can be observed in Figure 4.9. The SciAps output data include an average of the data, but not the standard deviation; therefore, the results for each strip (three strips total, one per treatment) were represented as averages of 50 ablations, with no standard deviation bar.

4.5.3 Results and Discussion

Ten to 20 minutes after the WaterSafe® strips were introduced to the solutions of bacteria, gold nanoparticles, and Eu-labeled antibody, pink lines were observed to form at the test and control lines. This indicated that a sandwich had formed between the antibodies immobilized on the test line and the gold nanoparticles. It also indicated that a sandwich had formed between the antibodies immobilized on the positive-control line and excess gold nanoparticles. The area adjacent to the test line was near-white, indicating that not many gold nanoparticles remained in this region of the strip. Whether Eu-labeled antibody was also present in the test line and area

adjacent to the test line was determined with LIBS. LIBS analysis showed a stronger Eu signal at the test line than in the area adjacent to the test line for all treatments (Figure 4.10). This outcome matches the results obtained with the bench-top LIBS system. The role of the bacteria in this experiment is uncertain, however, since lanthanide-labeled anti-mouse antibody was shown to bind to the test line even in the absence of the bacteria; it is suspected that the bacteria played a minor role in the outcome. Even so, the results show that Eu-labeled antibodies can be detected in a LIFA using a hand-held LIBS system. Future experiments that use SciAps hand-held LIBS and WaterSafe® bacterial test strips can utilize lanthanide-labeled anti-mouse antibodies as a positive control to compare against experimental treatments. Appropriate experimental treatments for future experiments consist of anti-*E. coli*, -*K. pneumoniae*, and -*S. enterica* antibodies labeled with Eu, Lu, and Yb respectively. The bacteria and labels can be added either to separate WaterSafe® test strips for single-plex detection, or to the same test strip for multiplexed detection.

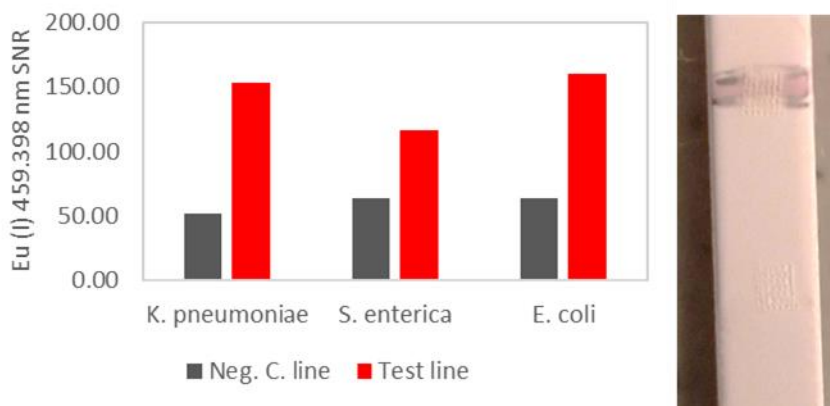


Figure 4.10 (Right) Ablation marks on the test (pink line surrounded by pencil marks) and negative-control lines (white region) of the WaterSafe test strip were visible. (Left) Hand-held LIBS analysis of three detection strips treated with Eu-labeled anti-mouse antibodies showed a strong Eu signal at the test line compared to the negative-control line. Each strip was also treated with a different bacterial species, but it is believed that the bacteria had minimal impact on the outcome of the assay. The LIBS spectrum was not analyzed for detection of graphite from the pencil marks.

4.5.4 Section Summary

This section covers the application of a hand-held LIBS system originally designed for soil, rock, and scrap metal analysis to analysis of a LFIA. Although the system was not optimized for a paper immunoassay substrate, the outcome of the assay was measurable with LIBS. A hand-held unit designed specifically for sensitive and multiplexed detection of metal-labeled antibodies on a paper substrate has potential to become a device used by food-safety and defense agencies to screen for biohazards in the field. While the experiment presented here is based upon an antibody-detection assay, the protocol can be used as a positive control for future studies that utilize the lanthanide-labeled antibodies for Gram negative bacteria detection on a WaterSafe test strip.

4.6 Investigation of Standard ELISA and Vertical Flow Assays for Toxin Detection

So far, lateral flow assays and antibody conjugation to metal-complexed polymers and gold nanoparticles have been discussed. In this section, vertical flow immunoassays (VFIA) and enzyme-linked immunosorbent assays (ELISA) were also tested, as well as a alternative nanoparticle conjugation methods. The goal was to explore assay approaches other than LFIAs that could be paired with LIBS as a direction for future work.

4.6.1 Lanthanide-labeled Antibody Conjugation to Gold Nanoparticles

Throughout the previously described work, it was found that assays utilizing gold nanoparticles and lanthanide conjugated antibodies were viable substrates for LIBS analysis. This section examines the possibility of conjugating lanthanide-conjugated antibodies to the surface of gold nanoparticles. In theory, this would provide two advantages over each technique (lanthanide conjugation and gold nanoparticle conjugation) used independently since the gold nanoparticles are an easy visual target for LIBS and sensitive and multiplexed detection may be achieved using lanthanide labels.

Using the antibodies complexed to Er, Pt, Dy, Eu, Nd and Yb at Stanford University, an experiment was performed to determine if these antibodies could be passively adsorbed onto gold nanoparticles. The intent of performing this chemistry was to establish a dual-labeling method (label 1 and label 2) for antigens on a paper substrate. Label 1, the gold nanoparticle, have several advantages: bioconjugation can be achieved using a variety of methodologies, conjugation results

can be assessed using several rapid analytical methods (e.g. LIBS, visual, and absorbance), and gold nanoparticles produce a LIBS signal that may permit instrument calibration for future experiments. The disadvantage of label 1 (gold nanoparticles), is the weak LIBS signal produced by gold nanoparticles, and limited multiplexing options. These disadvantages are counter-balanced by Label 2, the lanthanide-complexed polymer. Label 2 cannot be visually detected; however, Eu, Lu and Yb produce an intense LIBS signal relative to gold and may be used for multi-analyte detection in multiplexed assays. This dual labeling system would theoretically provide the user with the benefits of each label: visual confirmation of assay functionality (using label 1), and sensitive and multiplexed detection of the assay targets (using label 2).

To achieve the dual-labeling method, an antibody/lanthanide/gold conjugate was developed. Anti-*E. coli* antibodies were conjugated to Dy, Yb, Nd, Eu, Er and Pt using a similar protocol to the one described in section 4.2. The concentration of the lanthanide conjugated antibody was 0.4 mg/ml for Dy, Yb, Nd and Eu conjugates, 0.17 mg/ml for Er conjugates, and 0.2 mg/ml for Pt conjugates. 22 µg of each antibody was added to microcentrifuge tubes and mixed with 66 µg of BSA (in a 10% w/v solution). The total volume of each solution was brought up to 22 µl using protein suspension buffer from Cytodiagnostics. The protein solutions were then conjugated to 20 nm gold nanoparticles through the passive adsorption protocol described in section 4.3.

Vertical flow immuno-assays were used to assess conjugation success. Details on single-layer VFIA construction are as follows: 1 MedMedmira plastic cartridge shell, a 25 mm × 27.5 mm × 1 mm plastic frame with a 8mm diameter hole cut in the center (a component that originally belonged to the complete MedMira cartridge), two sheets of CF6 (GE Lifesciences catalog # 8116-2250) cut in 25 mm × 27.5 mm rectangles, one sheet of CF7 (GE Lifesciences catalog # 8117-2250) cut into a 1 cm x 1 cm square, and one sheet of Protran BA79 (GE Lifesciences # 10402096) cut into a 1 cm x 1 cm square. The CF6 layers go into the bottom half of the MedMira cartridge shell, followed by the CF7 and then the Protran BA79, and the plastic rectangle. The top half of the MedMira cartridge was then sealed onto the bottom half, enclosing the layered paper substrates. Three regions of the Protran BA79 layer were each spotted with 1 µl of 1 mg/ml anti-mouse antibody, and in a different region with 1µl of 1 mg/ml anti-rabbit antibody. The nitrocellulose dried for 40 min, after which it was blocked with three drops of MedMira Universal Buffer. Regions of the nitrocellulose cartridge treated with anti-mouse capture antibodies (test region) targeted meal-conjugated anti-*E. coli* antibodies. Regions of the nitrocellulose treated with anti-

rabbit capture antibodies (negative control region) served as a negative control. Regions of the nitrocellulose paper that did not contain capture antibody (background region) also served as a negative control. To each assay cartridge, a solution of lanthanide-conjugated antibodies passively absorbed onto the surface of gold nanoparticles were added (one assay was performed per lanthanide conjugate). It was hypothesized that successful conjugation between lanthanide-conjugated antibody and gold nanoparticle would be represented by an intense pink spot forming in the regions of the nitrocellulose treated with anti-mouse capture antibody when compared to the background or negative control.

The appearance of bold pink spots relative to the background were visually observed in regions of the nitrocellulose treated with anti-mouse capture antibodies, and not in the region treated with anti-rabbit capture antibodies for each metal conjugate with the exception of Pt (Figure 4.11). Treatments where pink spots were observed at the test regions suggested that antibody/lanthanide/gold conjugates had formed and could be immobilized at the test regions of the nitrocellulose.

Although there was a strong contrast between the test and background regions, the latter was observed to have a pinkish hue compared to untreated nitrocellulose (where conjugate solution was not added), suggesting that the antibody/lanthanide/gold conjugate was being trapped in the membrane. This effect may be explained by unspecific interactions between the polymer-lanthanide label and the nitrocellulose. Personal communication with Cytodiagnostics Inc. suggested that polymers may unspecifically interact with nitrocellulose, indicating that the lanthanide-complexed polymer component of the antibody/lanthanide/gold conjugate was partially inhibiting the conjugate from completely flowing through the nitrocellulose paper. Unspecific binding or entanglement may explain why the regions of the paper not functionalized with capture antibody would assume a pinkish hue (compared to untreated paper). To optimize signal to background ratio, the background should be reduced by preventing unspecific binding or entanglement. An interesting topic for future work would be to explore pre-treatment of the nitrocellulose with blocking agents that will prevent unspecific binding between the nitrocellulose and antibody/lanthanide/gold conjugate and/or using a membrane with a larger pore size, allowing the conjugate to more effectively flow through the membrane.

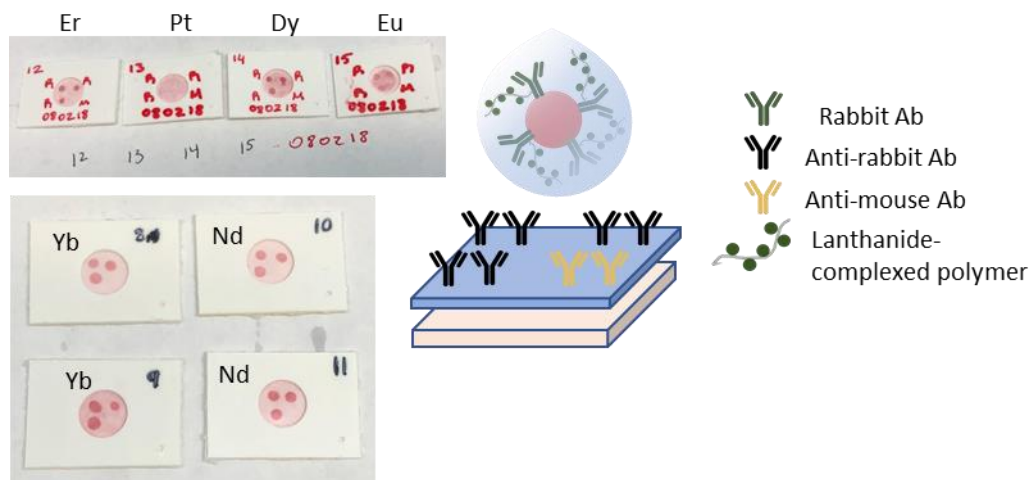


Figure 4.11 Immuno-dot-blot tests for lanthanide-labeled antibodies conjugated to nanoparticles. An illustration of the bioassay is displayed to the right, the results are displayed to the left.

No spots appeared for Pt labeled antibodies (Figure 4.11) suggesting that the formation of an antibody/Pt/gold conjugate was unsuccessful. Future work would investigate why Pt antibodies did not conjugate to nanoparticles. A few options to improve conjugation success are tuning the reaction pH and the relative concentration of protein (antibody and BSA) to create an environment optimal for conjugation using optimization protocols similar to those presented in sections 4.6.3. Future work would also explore whether the antibody/gold/lanthanides conjugates thought to be immobilized in the test region can be detected with LIBS. LIBS analysis would help confirm that an antibody/lanthanide/gold conjugate was formed rather than an antibody/gold conjugate.

4.6.2 Vertical Flow Assay Cartridge Design: single and multi-layer detection

Single-layer vertical flow immuno-dot-blot test using antibodies complexed to lanthanides and gold nanoparticles (described in section 4.6.1) may be an option for developing multiplexed assays using a diversity of metal labels. One drawback of this strategy is loss in sensitivity as the assay's multiplexing capability increases. The loss in sensitivity would be attributed to the nitrocellulose paper's antibody binding capacity. To increase the assay's multiplexing capability, antibodies against a greater variety of targets would be added to the nitrocellulose. Therefore, the concentration of antibodies against a single target will decrease. If a LIBS system has a fixed sampling size of approximately 100 μ m, increasing the assay's

multiplexing capability would decrease its sensitivity since element emission intensity is linearly correlated to the concentration of the element [12].

To avoid the issue of sensitivity loss with increasing multiplexing, the assay cartridge can be re-designed. A vertical flow assay cartridge typically features one layer of nitrocellulose paper spotted with detection and control antibodies. The single layer is exposed so the user can visually evaluate the assay results. It may be possible to have multiple stacked layers of nitrocellulose spotted with detection and control antibodies, where each layer is for detecting one or a set of antigens (Figure 4.12). However, multi-layer detection is impractical using standard detection tools because most cannot evaluate the assay past the first layer. However, LIBS can be used for depth profiling since it is destructive and removes material as it samples – essentially digging through each layer. Therefore, if multiple nitrocellulose layers were stacked, the LIBS system could sample the control and detection spot of the top layer, and then every layer underneath (Purdue University disclosure # D2017-0364). This approach avoids the issue faced in a single layer assay of decreased sensitivity with increased multiplexing. Challenges of using this approach include obstruction of the LIBS signal by the crater that is formed and bleeding of nanoparticles between detection and control spots in different layers. The first challenge may be addressed by applying a emission-collection design specifically for LIBS depth profiling. The second challenge may be addressed by not stacking detection and control spots directly on top of each other – instead, they can be staggered so one does not bleed onto another.

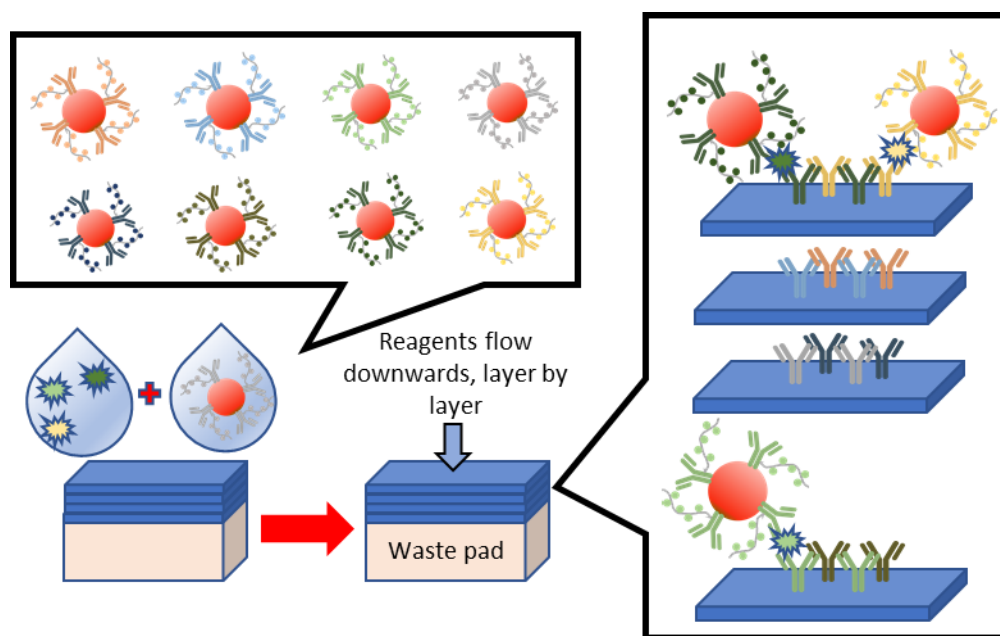


Figure 4.12 Design concept of a multi-layer vertical flow assay cartridge that utilizes nanoparticles conjugated to lanthanide-labeled antibodies

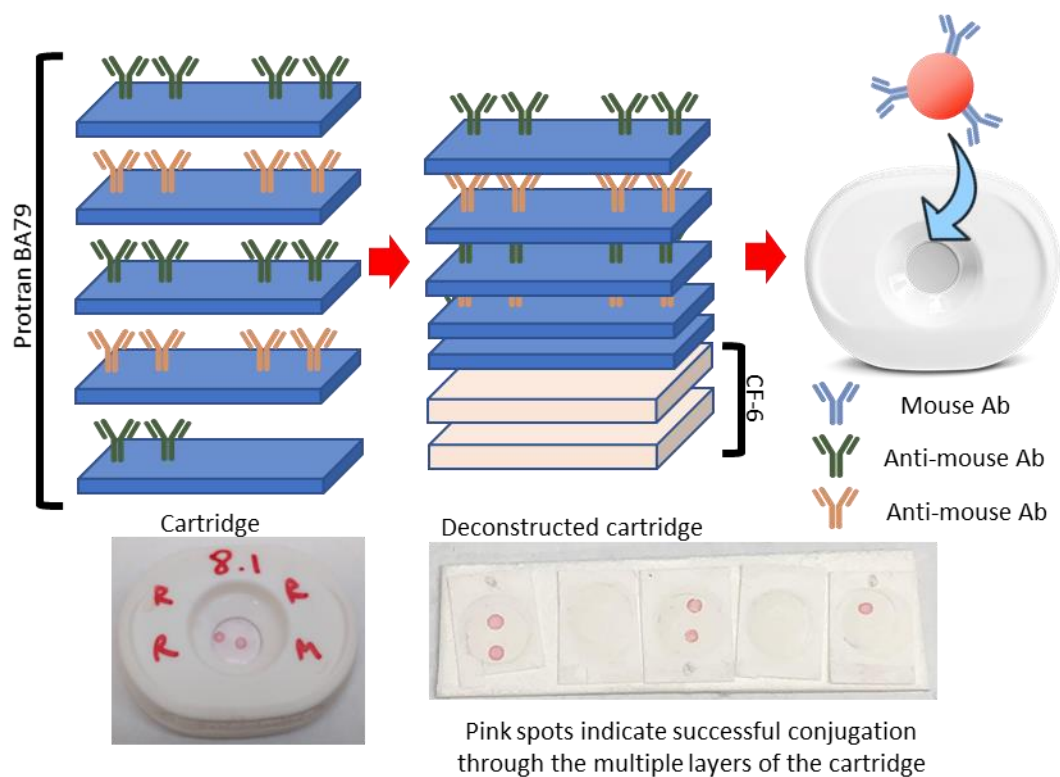


Figure 4.13 Proof-of-concept for multi-layer vertical flow assay cartridge. Pink spots indicate successful immobilization of nanoparticles on nitrocellulose paper.

A similar cartridge as described in section 4.6.1 was used to develop a multi-layer detection vertical flow assay cartridge, with the following key differences. Five pieces of 1 cm × 1 cm Protran BA79 were prepared – each piece termed “layer”. Layer 1 and 3 were spotted in two locations with 1 µl of 1mg/ml anti-mouse antibody. Layer 2 and 4 were spotted in two locations with 1 µl of 1mg/ml of anti-rabbit antibody. Layer 5 was spotted with in one location with 1 µl of 1mg/ml anti-mouse antibody (Figure 4.13). All layers were dried for 40min. The layers 1 (top layer) - 5 (bottom layer) were stacked onto each other, making sure that the spotted areas of each paper did not sit directly on top of each other. Layers were then placed on top of two sections of CF6, and under the plastic frame. The stack was put into the plastic MedMira shell. The nitrocellulose was blocked with three drops of Universal Buffer. Once the blocker went through the nitrocellulose, 200 µl of conjugated nanoparticles were added, followed by a wash of Universal Buffer. Prior to addition of the nanoparticles to the cartridge, the nanoparticles were conjugated to 22 µg of mouse Stx2-2 antibodies and 66 µg of BSA using a protocol similar to that described in section 4.3. The cartridge was then deconstructed. Each layer of nitrocellulose was carefully separated and given additional washes using a solution of 5 mM Na₂HPO₄ 0.01% w/v SDS.

The multi-layer detection vertical flow assay design showed a distinct pink color on each layer where the anti-mouse antibody was spotted, and minimal color where the control anti-rabbit antibody was spotted. This pilot experiment showed that multi-layer vertical flow assay cartridges could potentially be used for antigen immobilization. Here, the outcome of the assay was assessed visually. Future work involves determining whether LIBS can be used to analyze each layer of the assay via depth profiling.

4.6.3 Antibody Conjugation to Carboxylated Silica Beads and Polystyrene Beads

Silica and polystyrene microparticles are often used as a surface for antibody conjugation. If used for bio-conjugation, silica particles are often coated in carboxyl, amine, streptavidin or biotin functional groups [195]. These groups covalently bind to certain regions of a protein. For this study, carboxyl groups on the surface of 1 µm silica particles were used for bioconjugation using carbodiimide chemistry. Carbodiimide reactions are easy and versatile, making them a popular method for protein conjugation.

Carbodiimide reactions are a two-step process and can produce several by-products. One product is the desired amide bond between a carboxyl group on the nanoparticle surface and an

amine on the protein.[196] The second product, typically considered waste, is an isourea derivative. For the carbodiimide reaction to start, EDC (also EDAC 1-ethyl-3-(3-dimethylaminopropyl) is added to a solution of carboxylated particles. The carbon between the two nitrogen atoms reacts with the oxygen on the carboxyl group. The intermediate that forms is O-acylisourea [196]. This reaction is reported to occur best in a pH of 3.5 to 4.5 [197]. O-acylisourea is either hydrolyzed, forming the waste isourea derivative, or can react with an amine on a protein group. Reactions with an amine are reported to be optimal in a pH of 4-6 [197]. Though other strong nucleophiles such as sulfhydryl can also react with the intermediate, the major competing reaction is hydrolysis by water, which creates the isourea derivative [198]. The rate of hydrolysis decreases as the pH approaches 6 [197]. Hydrolyzed O-acylisourea groups can further react, creating either more unwanted by-products, in some cases when an excess of EDC is present, or the desired amide bonds [197]. On an antibody, there are multiple amines and carboxylate groups. As a result, when an amine on an antibody binds to the carboxyl group on one particle, another amine on the same antibody can simultaneously bind to another particle, causing particle aggregation (a process influenced by reagent concentration) [196]. A variation of the EDC chemistry involves reaction of the O-acylisourea intermediate with a sulfo-NHS group. The reaction creates a sulfo-NHS ester intermediate that is more stable (hydrolyzes at a lower rate) and is more reactive to nucleophiles such as the amine groups on an antibody.[196] Since some of the amines on an antibody are near the antigen binding site [199], binding can compromise the antibody's functionality due to steric hinderance [196]. The many pathways of the carbodiimide reactions may be the cause for different degrees of success among those who have used it for conjugation [196].

Protein can also be absorbed onto surfaces. Adsorption onto polystyrene surfaces is an easy and quick method for antibody attachment to solid substrates. Like in EDC chemistry, antibody orientation is random [200]. Unlike EDC chemistry, antibodies can be displaced in the presence of a competing molecule. Passive absorption onto polystyrene particles or plates (e.g. ELISA plates) is determined by hydrophobic binding forces (Van der Waals). The hydrophobic regions on the antibody bind to the hydrophobic polystyrene surface. Changing pH of the solution affects antibody conformation, therefore changing the availability of hydrophobic zones and subsequently antibody binding capability [201]. Interestingly, the pH at which the antibody is conjugated affects its functionality [202]. Therefore, special consideration to the buffers must be taken when passively conjugating antibodies. One study suggests that antibodies adsorbed onto polystyrene

surfaces at a pH of 2.8 had significantly higher functionality than those adsorbed at a higher pH (7.5 and 9.5) [202]. However, this may also be contingent on the type of antibody.

An experiment led by Dr. Eva Biela was performed at the Agricultural Research Services center in Albany, CA to conjugate anti-Shiga (Stx 2-1 and Stx 2-2), and anti-botulinum (BoNT1 and BoNT2) antibodies to silicon and polystyrene beads and determine antibody functionality post conjugation.

In the first experiment, botulinum toxin integrity was evaluated. Two toxins were tested, one supplied by and stored at the USDA, and a sample acquired commercially and kept in a diluted and refrigerated state. A standard ELISA was carried out. 50 µg of 2 µg/ml BoNT1 in 0.05 mM sodium carbonate buffer (pH 9.6) was added to each well of a standard ELISA plate and incubated overnight. The wells were then blocked with 300 µl of 3% Non-fat dry milk in TBST. Wells A1:D12 were treated with botulinum toxin. Each of the first 9 columns in rows A1:D12 received 1000 pg, 500 pg, 250 pg, 125 pg, 62.5 pg, 31.25 pg, 15.63 pg, 7.81 pg, 3.91 pg of toxin respectively (toxin was suspended in 200 µl of 3% Non-fat dry milk in TBST). Wells E1:H12 underwent a similar treatment but received toxin freshly de-frosted and diluted from the USDA stock supply. Each of the first 9 columns in rows E1:H12 received 10000 pg, 5000 pg, 2500 pg, 1250 pg, 625 pg, 312.5 pg, 156.3 pg, 78.1 pg, 39.1 pg of toxin respectively. The plate was incubated for an hour and then washed with TBST. 100 µl biotinylated BoNT2 detection antibody at 5 µg/ml in TBST was added to each well of the plate. Using a luminescence kit by (ThermoFisher, MA, catalog#: 34078) the success of the ELISA was evaluated. The results suggested that, even though the toxin from Purdue was at 10x higher concentration than the toxin from the USDA, the latter performed significantly better (Figure 1). This discrepancy may be a result of toxin degradation during extended storage in a tube at dilute concentrations. Personal communication with experts in the field indicate that toxins must be stored at high concentrations (no less than 100 µg/ml). If diluted, the toxin must be used within 24hrs in containers specific for preventing protein attachment to container walls. Toxins remains intact for years if stored at -80°C. In this experiment, controls were run in wells A10:H12 to ensure that binding did not occur between antibodies in the absence of the antigen.

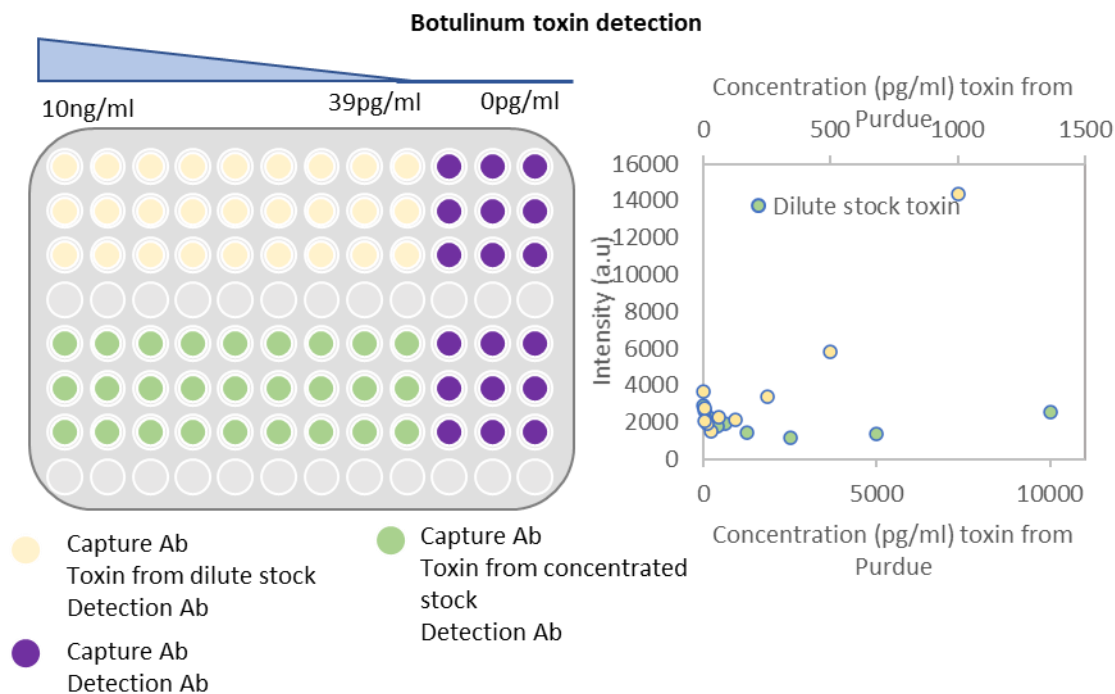


Figure 4.14 Assay design to test binding of botulinum toxin to anti-botulinum antibodies. Two types of toxin were tested – one from Purdue (stored for extended time in a diluted state) and one from the USDA (frozen and freshly diluted). Results indicate that the freshly diluted toxin outperformed toxin stored in a diluted state.

A second experiment replicated the former; however, freshly thawed and diluted Stx2-1 and Stx 2-2 toxin was used instead of toxin that had been stored for extended time in a dilute state. Toxin concentration for columns 1:9 were 1000 pg, 500 pg, 250 pg, 125 pg, 62.5 pg, 31.25 pg, 15.63 pg, 7.81 pg and 3.91 pg respectively. The experiment indicated a positive correlation between toxin concentration and luminescence signal (Figure 4.14).

In a third experiment, conjugation was performed on polystyrene and silica beads rather than a polystyrene ELISA plate. For antibody conjugation to silica beads, the 130 μ l of 1 μ m carboxylated beads (0.1 g/ml in ethanol) were washed with MOPS buffer at a pH of 5.2. 15 mg of NHS in 50 μ l of MOPS was simultaneously prepared and mixed with 10 mg of EDC. 20 μ l of the NHS EDC solution was added to the beads and incubated for 15 min. Beads were then washed and re-suspended in 300 μ l of MOPS 5.2. 200-500 μ g of protein (a mixture of antibody and BSA) was added to the bead solution followed by a 2hr incubation. 50 mM Ethanolamine was then added at MOPS pH 8.2 and incubated for 1 hr. Beads were stored at 4°C in 138 mM NaCl, 2.7 mM KCl, 10 mM Na₂HPO₄, 0.05% (w/v) Tween-20, 0.05% (w/v) Pluronic F127, 0.05% (w/v) n-dodecyl β -

D-maltoside and 7.6 mM NaN₃, 0.1% (w/v) BSA. Conjugation to 1µm polystyrene beads was performed using a variation of the chemistry described previously. Detailed notes on the concentration of antibodies used for each conjugation were not recorded.

To determine success of antibody conjugation to silica and polystyrene beads as well as antibody functionality, an ELISA-like assay was performed in a multi-well plate with filter-bottom wells (Acrowell Catalog# 5020). Botulinum toxin was added as a 100 µl solution to columns 1-9 in the following quantities: 1000 pg, 500 pg, 250 pg, 125 pg, 62.5 pg, 31.25 pg, 15.63 pg, 7.81 pg and 3.91 pg. 100 µl of polystyrene beads coated in BoNT1 were added to each well in rows A1:D12. 100 µm of silica beads conjugated to the same antibody were added to wells E1:H12. Concentration of both silica and polystyrene beads was unknown. Plate was incubated for 1hr at 37°C. Suction added to the bottom of the plate removed the diluent and excess antibody, while the beads were blocked by the filter. Beads were then washed in 300 µl in TBST 3 times using the same diluent removal technique. Beads were re-suspended in 100 µl of TBST containing 1 µg/ml of biotinylated BoNT F1-51. After 1 hr of incubation at 37°C and a series of washes, luminescence was determined using the same technique described previously. A positive correlation was found between toxin concentration and luminescence intensity for both silica and polystyrene beads. The same procedure was applied to a Shiga toxin detection assay with similar results (Figure 4.15).

In summary, these experiments test antibody functionality using a standard ELISA, and an ELISA-like assay on silica and polystyrene beads. The results indicate that if reagents are stored properly, botulinum and Shiga toxin can be detected by both assay formats.

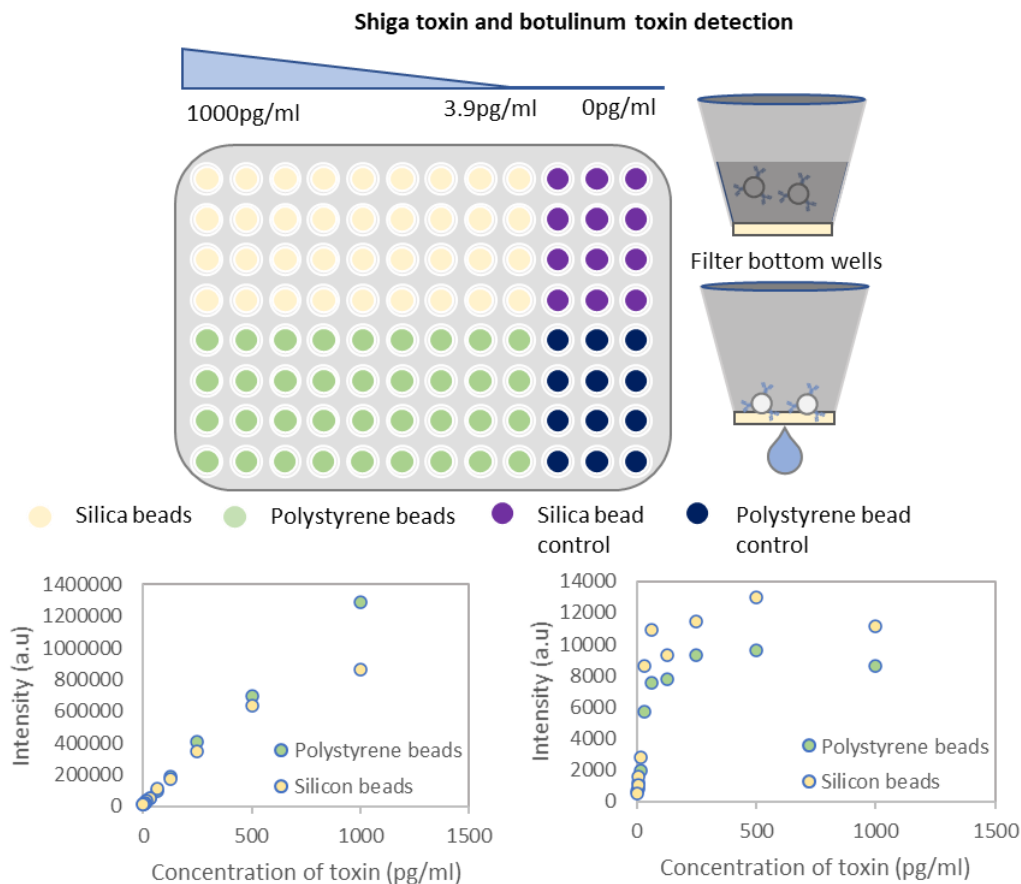


Figure 4.15 Bead-based ELISA assay designed to test binding of Shiga and botulinum toxin to anti-Shiga and botulinum toxin antibodies. Results indicate successful binding between beads, antibodies and toxin (Shiga toxin left plot, botulinum toxin right plot).

4.6.4 Antibody Conjugation to Gold Nanoparticles

Similarly to silica microparticles, gold nanoparticles can be purchased commercially from a number of vendors and used for antibody conjugation [203]. Silica and polystyrene particles are near-transparent when suspended in water. This makes bead assays like the one previously described challenging, especially when the beads need to be washed multiple times. However, gold nanoparticles have a pink, purple or blue appearance, making them easy to visually identify [204]. Their distinct color and ability to conjugate to biomolecules, makes them amenable for use in paper-based diagnostics [204]. Gold nanoparticles can either be used for passive or covalent conjugation. For covalent protein conjugation, nanoparticles can be functionalized with carboxyl,

N-hydroxysuccinimide (NHS) or other reactive groups. For passive conjugation, ionic and hydrophobic interactions guide binding between the nanoparticle and protein [203].

Gold nanoparticles synthesized via citrate reduction and stored in sodium citrate can spontaneously and non-covalently bind to protein via electrostatic and hydrophobic interactions [205, 204]. In electrostatic interactions the positive sites on the protein interact with the negatively charged nanoparticle. During hydrophobic interactions, the hydrophobic regions of the antibody bind to the metallic surface of the nanoparticle. The disadvantage of non-covalently or “passively” binding antibodies to nanoparticle surfaces is the potential for antibody disassociation from the nanoparticle as the solution’s pH increases, neutralizing the negative charges on the nanoparticle [203].

Thiol groups strongly adsorb onto gold nanoparticle surfaces via a sulfur-gold interaction [206, 207]. This interaction provides venues by which antibodies can be bound to nanoparticle surfaces [207]. Polyethylene glycol (PEG) polymers capped on one end with a thiol group and a -COOH or -NHS (or other antibody-binding) group on the other end can be conjugated to nanoparticle surfaces. The thiol group on one end of the polymer binds to the nanoparticle surface while an activated -COOH or -NHS group binds to the antibody [206]. The PEG group helps provide space between the antibody and nanoparticle, reducing the chances for steric hindrance during antibody-antigen interactions. Conjugation of antibodies to thiol-PEG-COOH polymers on gold nanoparticles functions similarly to the reaction described for carboxylated silica microparticles. Whereas thiol-PEG-COOH can be stored in solution, thiol-PEG-NHS functionalized particles must be lyophilized for storage. NHS groups are quickly hydrolyzed, making them unreactive.[196] However, they also form covalent bonds with the amine groups on antibodies. The protocol for NHS-mediated conjugation is simple and rapid, making it a convenient mode for antibody conjugation. In this study, both covalent and passive conjugation was explored. For covalent conjugation, thiol-PEG-NHS functionalized nanoparticles were initially used. However, due to the cost of these nanoparticles, the more economic passive conjugation approach was selected.

Anti-*E. coli*, Stx2-2 and Stx2-1 were passively conjugated to 20 nm gold nanoparticles. For each antibody, different reaction pH and concentrations were tested. 1ml of OD1 20 nm gold particles synthesized by Cytodiagnostics were incubated with antibody treatments for 15 min at 23°C. 50 µl of 10% BSA was added to each reaction solution and incubated for 5 min. 2.6 µl of

10% Tween was added and solutions were centrifuged for 25 min at 10,000 g. At the end of centrifugation, gold nanoparticles were pelleted in a dark red mass at the bottom of the tube. The supernatant was removed and the solution was re-suspended in 1%BSA 1%PBS and 0.025% Tween 20 until the final OD was 1.3. The conjugated nanoparticles were stored at 4°C overnight. To test the success of conjugation, 10 cartridges were spotted with 1 µl of 1 mg/ml anti-mouse and anti-rabbit antibody. Spots were allowed to dry for 30 min. Three drops of Universal Buffer was added to the cartridge. Once the Universal Buffer was fully absorbed, 150 µl of nanoparticles were added to the cartridge, 1 treatment per cartridge.

The results of the immuno-dot-blot test can be interpreted by observing the intensity of the spot (Figure 4.16). A uniform, bold red spot indicates successful conjugation, a blotchy or blue spot indicates less successful conjugation and nanoparticle aggregation, no spot indicates little or no conjugation. Peak absorbance of the nanoparticles can also be used as an indicator of conjugation, though this measure is influenced by both conjugation (indicated by a 2-5 nm right shift in peak absorbance compared to unconjugated nanoparticles) and aggregation (also indicated by a right-shift in peak absorbance and peak broadening compared to mono-dispersed particles). Cytodiagnosics specialists suggest that, between the two methods of evaluating conjugation success, the immuno-dot-blot test is best.

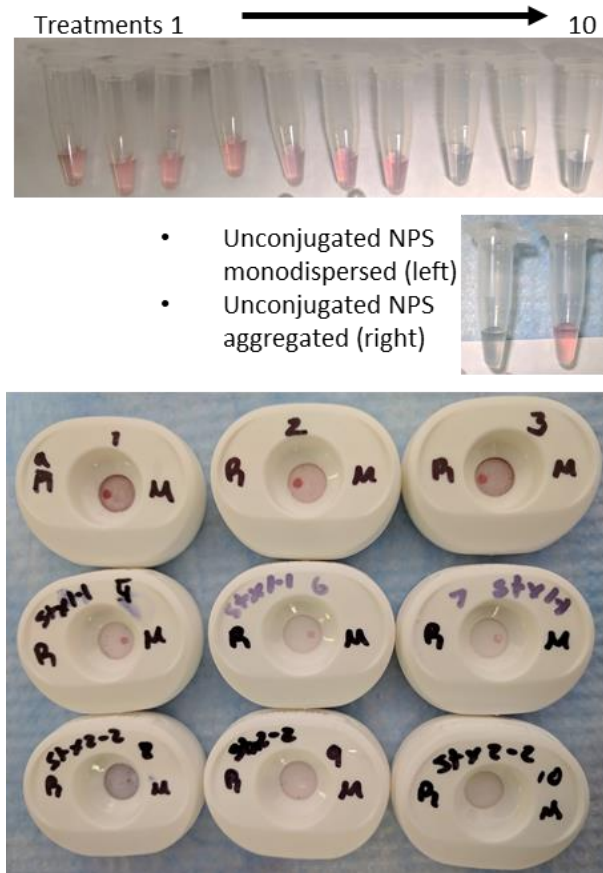


Figure 4.16 Top two images - Differences between treatments can be observed during the process of conjugation. Solution with a more blueish tint imply particle aggregation. Bottom image – immuno-dot-blot tests. Top row of cartridges show successful conjugation of rabbit anti-*E. coli* antibodies to nanoparticles. Bottom two rows indicate less successful conjugation of stx 2-1 and stx 2-2 to nanoparticles.

Immuno-dot-blot results suggest that rabbit anti-*E. coli* antibodies successfully conjugated to the gold nanoparticles, as indicated by the bold red spot where anti-rabbit antibodies were spotted onto nitrocellulose. The region where anti-mouse antibodies were spotted remained blank, indicating no unspecific binding. Based on visual assessment, there was little or no relationship between pH and binding success. Mouse anti-Shiga toxin 2-1 conjugated less successfully, indicated by the fainter and more blue appearance of the spot. Conjugation does seem to be influenced by pH, with pH 7 being most successful. No unspecific binding was observed, as indicated by the blank region where anti-rabbit was spotted. The-immuno dot-blot test for anti-Shiga toxin 2-2 was least successful, with no bold red spots being observed.

The immuno-dot-blot test for anti-Shiga toxin antibody 2-2 to was optimized by adding BSA to the antibody solution during conjugation. Ideally, there should be enough antibody in solution to fully coat the gold nanoparticle. However, when insufficient antibody is present, it was hypothesized that the nanoparticles would aggregate, changing the optical properties and making the immuno-dot-blot more difficult to evaluate. BSA was used to block areas of the nanoparticle surface that remained unconjugated to antibodies. In one experiment, pH was maintained at 8.2 between treatments. Antibody amount per treatment was 0, 2.2, 4.4 or 8.8 μg as indicated by Figure 5, in a total volume of 22 μl . Amount of BSA per treatment was 0, 6.6, 4.4, 44, 66 or 88 μg (Figure 4.17). Similar protocols as those used for the previous passive conjugation were used. Controls to check for unspecific binding were included on every cartridge by spotting 1mg/ml of anti-rabbit antibody. Another control consisted of nanoparticles only conjugated to BSA to ensure BSA was not non-specifically binding to the spotted antibodies.

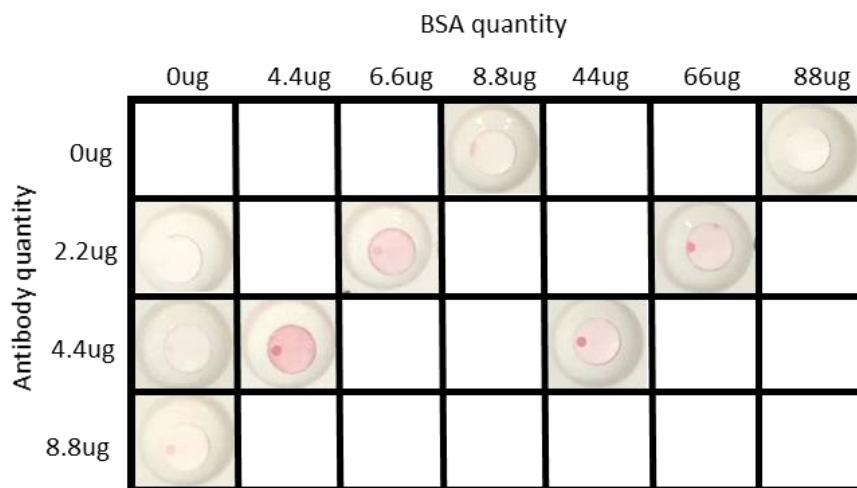


Figure 4.17 Illustration of 10 treatments conditions and results. Rows and columns correspond to the amount of antibody and BSA added to a 1ml solution of 20nm gold nanoparticles (OD1). The total volume of the BSA-Antibody mixture was 22 μl for each treatment.

Interestingly, the treatments with a large quantity of BSA (44 and 66 μg of BSA) performed very well. The immuno dot-blot test displayed bold red dots where anti-mouse antibody was spotted. BSA helped with the performance of the immuno-dot blot, as can be observed in Figure 4.17. In treatments with a larger quantity of BSA less background was observed. The controls showed no occurrence of non-specific binding between the spotted antibodies and conjugated BSA,

or the spotted antibodies and conjugated antibodies (blank areas where anti-rabbit antibodies were spotted). The results supported the conclusion that aggregation of nanoparticles may be prevented by using BSA to block the surface of the nanoparticle not occupied by an antibody. Doing so may have prevented nanoparticles from sticking together as salt concentration of the solution was increased, and the negative charges on the nanoparticle surface neutralized. These results show significant improvement from the conjugation performed previously using Stx2-2. Subsequent experiments further showed that adding BSA to the antibody solution helped in obtaining easily interpretable immuno-dot-blot results.

4.6.5 Section Summary

In this section, different protocols for antibody conjugation were explored, as well as assay designs which utilized these conjugates. Though LIBS is was not used for assay analysis in the experiments presented in this section, it represents a major topic of future work. Here, an ELISA assay was successfully used to detect Shiga, ricin and botulinum toxins using luminescent tags. Substituting the luminescent tags with lanthanides may yield a new methodology of detection which might be more sensitive. There is a possibility to make ELISA assays more multiplexed using lanthanide labels and LIBS. In a single well of an ELISA, a user may detect multiple categories of antigen by labeling each category with a unique lanthanide and detecting them simultaneously with LIBS. Though this concept was not explored in this dissertation, it represents an exciting idea for the future. Likewise, a single or multi-layer vertical flow assays offer an interesting platform for multiplexing. By drilling through the nitrocellulose layers of a multi-layer vertical flow assay, LIBS can potentially analyze the different categories of target captured at each layer. Each of the assay options described in this section provide interesting opportunities for future LIBS applications.

4.7 Chapter Summary

The intersection between LIBS, LFIA, and metal-labeled antibodies has been relatively unexplored. Investigation in this area offers significant potential for portable and multiplexed detection of biomolecules at a sensitivity level that is relevant for food safety. This chapter explores a method for labeling antibodies with lanthanides, and then applies the labels to LFIA for either

antibody or bacteria detection. It was found that LIBS can be used to characterize the MaxPar X8 kit for Eu, Lu, and Yb conjugation. Further follow-up and validation of results using MS is recommended for this study. When applied to an immunoassay, the lanthanide-labeled anti-mouse antibodies were found to successfully flow through the paper substrate and bind to reagents immobilized on a paper strip, indicating that the reagents in the strip consisted of antibodies raised in mice. More importantly, it was determined that MaxPar X8 kit products can be used in lateral-flow assays. Detection of the assay outcome was measured with both benchtop and portable LIBS, showing that portable LIBS has potential to be applied to LFIA analysis. The antibody-detection assay can serve as a positive control for future studies that use a different antibody target, such as *E. coli* or Gram negative bacteria. In experiments that utilized Eu-labeled anti-*E. coli* and Gram negative bacteria, a sandwich between the LFIA capture antibody, antigen, and detection antibody was not successful. However, it is likely that selection of the appropriate reagents (antibodies, buffers, and substrates) will yield a different outcome. Additionally, assay options such as paper-based VFIA and filter-plate-based ELISAs using beads as a conjugation substrate were also explored. Each of these assay formats (LFIA, VFIA, and ELISAs) when combined with LIBS, particularly portable LIBS, provide promising venues for portable, sensitive and multiplexed detection of labeled biomolecules.

5. CONCLUSION

This documented collection of investigations centered on the development of laser-induced breakdown spectroscopy (LIBS) for analysis of paper-based biological assays that utilize metals as biomolecule labels for detection. Chapter 1 provided a broad overview of the literature regarding LIBS (portable and benchtop) as a multi-element characterization tool and its application as a biosensor. Whereas extensive research has been performed on the use of LIBS to analyze biological material in general, a gap was identified in the use of LIBS as a portable biosensor. Chapter one identifies the wide range of biosensors available, investigating the strengths and weaknesses of each approach. I determined that paper-based diagnostics are a solution for portable, rapid, and low-cost detection of target analytes across a diversity of fields such as clinical testing, forensics, food science, and biothreat defense. Among paper-based diagnostics, lateral-flow immunoassays (LFIA) show particular promise owing to their ability to concentrate a target analyte to a specific region on a piece of paper while also labeling the analyte with a detectable material. The future of LFIA is dependent upon improving their sensitivity, as well as their quantitative and multiplexing capabilities. Given the potential of LFIA and the capabilities of LIBS, particularly hand-held designs, the pairing of LIBS and portable LFIA appears to be a natural fit – an effective way to fill the literature gap and potentially provide the world with a new diagnostic tool.

The beginning of these developments, presented in Chapter 2, centered heavily on determining LIBS system parameters that would permit detection of metals deposited on nitrocellulose paper, a substrate commonly used for LFIA. The process involved the partnership of industry such as Cobolt Lasers (now Hübner Photonics), Avantes, SciAps, and organizations like the United States Department of Agriculture, who provided not only instrumentation but also guidance in the theory and operation of LIBS. The Laser Technologies Group at Lawrence Berkeley National Laboratories played a major role in teaching the author about LIBS system design during a one-month internship at their facility. Similarly, Dr. Prasoon Diwakar provided guidance in the understanding of LIBS. The input received from external sources was critical for our group, who was new to the field of LIBS, and permitted investigations of the various LIBS systems described in Chapter 2. Each design featured a different combination of lasers, spectrometers, electronics, software, optics, and sample chambers. Through a process of trial and

error, a combination of parameters was identified to enable the detection of metals on nitrocellulose paper.

Once a LIBS design was established and constructed at Purdue University, fundamental LIBS studies were pursued, as represented in Chapter 3. Quality-control protocols for laser and spectrometer operation were established, improving data replicability. To aid comparability of day-to-day experiments, standard samples were made and characterized to ensure their function as standards. These standard samples were composed of the same material as the LFIA experimental samples. Since LIBS relies heavily on sample composition, the use of standards representative of the material in the LFIA was prioritized. To better understand the relationship between sample composition and LIBS, mini studies (not all presented in this document) were conducted, which examined crater formation on different substrates, laser energy, and the relationship between irradiance and signal. Attention was then directed towards evaluating several methods for data analysis, specifically emission-line selection and signal-to-noise calculation. Using the National Institute of Standards and Technology (NIST) Atomic Spectra Database (ASD) as a guide, an instrument-specific library was developed for 17 metals relevant to the field of biomolecular labeling. Emission lines selected for the limit-of-detection (LOD) studies yielded LOD values comparable and sometimes better than those in the current literature. Among the 17 metals relevant to the field of biomolecular labeling, Ag, Eu, Lu, and Yb proved to be the best candidates for sensitive detection of biomolecules. It was found that by selecting the appropriate instrument parameters, these metals could be used for single-analyte or multi-analyte detection of biomolecules. Results suggested that while quantitative analysis of single-analyte assays would be feasible, analyses of multi-analyte assays were better suited for qualitative detection owing to matrix effects. Even so, qualitative detection of biomolecule targets should not be undervalued given that similar tests (e.g., the pregnancy tests) have had a significant positive impact on public health.

Chapter four pursued single-analyte LIBS detection using Eu-, Lu-, and Yb-labeled antibodies applied to a LFIA (use of LIBS-detected Ag labeled antibodies was already covered in the literature). The first step was antibody conjugation to the lanthanide. The process of conjugation was made less complex by companies like Fluidigm who provide kits with the necessary reagents and instructions. While very convenient, these kits were also a “black box”; information on reagent composition, concentration, or kit efficiency was not readily available. In

creating a LFIA for LIBS analysis, it was considered important to know the efficiency of conjugation and the amount of lanthanide that labeled each antibody. Such information could be used as a benchmark for improvement. Results showed that kits for Eu, Lu, and Yb differed in the amount of metal provided for conjugation by the kit, kit efficiency, and the amount of metal estimated to be tagged per antibody, as well as providing clues on how to make the kit more efficient by identifying where reagents were being lost. The next task was to determine if the antibody remained functional after conjugation and in a paper matrix. A simple antibody-detection assay analyzed with both portable and benchtop LIBS confirmed functionality and compatibility with paper. The success of the hand-held LIBS system was exciting, suggesting that this technology may have a future in field-deployable biomolecule detection. An antibody-detection protocol was used as a positive control for the next series of experiments that attempted to detect Gram negative bacteria labeled with Au and Eu in a LFIA. Experiments with Au were successful, suggesting that the LIBS limit of detection for *E. coli* is on a par with conventional colorimetric LFIA analysis, and could be improved if a more intense label like Eu were used. However, experiments with Eu-labeled antibodies were unsuccessful, presumably owing to the incompatibility of the antibody with the assay. These experiments yielded an appreciation for the time and effort needed to select the appropriate reagents and materials for a functioning LFIA.

The driving force behind this research was the need for rapid, sensitive, multiplexed, and quantitative detection of biomolecules or microbes for applications like food safety. Future work will complete this objective by building on the foundation described here. Among the work that should be pursued is exploring other biomolecule labels. This dissertation explores 17 metals used for conjugation, but there are more, the most obvious of which are silicon, titanium, and platinum [27]. Other metals include boron [208], iodine [209], lead [210], mercury [210], and indium [211]. This list is not exhaustive, as research for biomolecule labels is on-going. Using hand-held LIBS systems to detect these labels in portable paper assays is particularly appealing for applications regarding field-deployable detection of biomolecules. While this study briefly explores the use of hand-held LIBS for label detection, the subject should be pursued further. In the process of doing so, one should take full advantage of the many antigen, antibody, and label combinations available for LFIA. Goals should not be restricted to LFIA. Biomolecule labeling and detection is an enormous area of research, encompassing many types of assay substrates (glass, plastic, nylon,

silicon), targets (DNA, RNA, protein, viruses, bacteria) and reagents. The opportunities for LIBS to be included in the field of biology are abundant and each very exciting.

The work represented by this dissertation is featured in two publications [212, 70]. This dissertation does not encompass all the author's research in the five years of her doctorate. LIBS studies in collaboration with Dr. Bartek Rajwa on food authenticity were pursued by examining the spectral emissions of cheeses and applying machine-learning algorithms to differentiate between different cheese types. This study will be summarized and submitted for publication. Attention was also directed towards cadmium detection in potatoes and pesticide detection in paper and vegetation. Work on spark-induced breakdown spectroscopy (SIBS) in collaboration with Iyul-Joon Doh and Dr. Huisung Kim was a central aspect for the first two years of the doctorate and produced a peer-reviewed article[181]. While each of these research topics focuses on atomic spectroscopy, the author also invested effort in learning about flow-cytometry data analysis and produced two book chapters on the subject[213, 214]. The culmination of experiences set the stage for a future in the expanding and fascinating field of analytical instrumentation development.

APPENDIX A. OVERVIEW OF LIBS SYSTEMS 1-6: PERSPECTIVES ON LIBS DESIGN

Chapter 2 discusses six LIBS systems applied to characterization of metal foils and metals dried on nitrocellulose paper. In the early stages of the project, the author used LIBS System 1 to build an understanding for LIBS design and fundamentals. As the project progressed, the author gained LIBS experience that led to the final design of LIBS System 6. The following represents perspectives from the author regarding the critical properties of a LIBS system design, with emphasis on the laser, spectrometer, sample chamber electronics, and optics/optomechanics.

Lasers

There were several aspects in laser selection that were observed to be particularly helpful when building a LIBS system for quantitative analysis. Valuable data from the manufacturer were laser energy, wavelength, repetition rate, water-cooling, beam profile, divergence, and standard deviation. In this study, a Gaussian beam produced data with less signal variability than a multi-mode beam. Likewise, a beam that produced a consistent energy output would also yield more precise data, suggesting that a quantitative LIBS system would benefit from a Gaussian laser with low pulse-to-pulse variation. Repetition rate was determined to be another important aspect. Ten Hz was found to be a practical repetition rate for scanning the surface of a sample when the sample was moved by a motorized stage. For surface scanning, faster repetition rates require faster stage movement. It was important to consider both repetition rate and stage speed if the application involved scanning the surface of a substrate. Alternatively, rather than moving the sample, a motorized mirror could have been used to change the laser path while maintaining the sample in a fixed position. In contrast to most of the LIBS systems discussed in this study, the SciAps Z-300 used a motorized mirror and a repetition rate of 50 Hz to raster the sample. Choosing between repetition rates and motorized optics/stage components depends on the application. Hand-held devices used for rapid surface sampling or bench-top devices used for LIBS imaging may benefit from a motorized mirror and high (10-50 Hz) repetition rate. For bench-top research devices, a motorized stage and a moderate repetition rate of 10 Hz may be appropriate. Lasers with high repetition rates (e.g., 1000 Hz) may be practical for imaging and depth profiling.

During repeated firing, the laser head required heat dissipation. Many Q-switched lasers come with a water cooler. For a bench-top unit, a water cooler was appropriate. However, for a hand-held unit, a water cooler would increase device weight and bulkiness. To avoid the need for a water cooler, a passive Q-switch laser was considered. Passively Q-switched lasers are practical for hand-held devices since they are small, produce several millijoules of power, and do not necessarily require water cooling. Since delay between pulses is variable, LIBS devices with passively q-switched lasers would benefit from a photodiode which detects the laser pulse. Upon detecting laser emissions, the photodiode would trigger the spectrometer, and therefore the spectrometer internal delay should be 1 μ s or less.

When it came to laser power and LIBS, “too much” and “too little” were found to negatively affect detection. An examination of LIBS Systems 1-6 shows that laser energy of 50 μ J was not sufficient to generate a plasma on nitrocellulose paper with a spot size of 30 μ m. A 70 mJ pulse, even with a spot size of 1 mm, was excessive energy and may have resulted in plasma shielding, making the signal challenging to detect. Attenuating the 70 mJ pulse may have helped in detecting metals in nitrocellulose paper but was not attempted. An advantage of using a high-powered laser for LIBS is the option of beam attenuation. However, higher-powered lasers typically require more safety regulations and water cooling, and are more expensive.

Wavelength may also have had an impact on whether metals were detectable on nitrocellulose. It was observed that a LIBS system with a 213 nm laser and 4 mJ pulse energy was unable to detect certain metals on nitrocellulose (two spectrometers were tested), whereas a 1064 nm laser with a 6 mJ pulse energy was easily able to detect the same metals on nitrocellulose.

Wavelength, pulse energy, and beam quality are factors that seemed to affect detectability. For fast and efficient data collection, repetition rate, user-friendly design, and a multi-functional control system were very important. LIBS System 1 required the user to manually trigger the laser for every laser pulse. Between each laser pulse, the sample was moved to ablate a different location of the sample surface. The software for controlling data acquisition would intermittently freeze, further delaying data acquisition. This LIBS design was cumbersome and time consuming. A LIBS system should take advantage of the repetitive pulse features and motorized functions offered by most lasers and stages available on the market. LIBS System 6 provided a more efficient design. Laser-pulse repetition rate and number were easily modified such that, upon a single trigger signal from the user, multiple laser pulses would fire at a maximum of 10 Hz. There were several options

for laser triggering (internal, external, Q-switch, flash lamp), allowing for versatile integration with other electronic components. The laser also offered synchronization pulse outputs to trigger other devices like the spectrometer. A motorized xyz stage was triggered by the laser to move in a pre-specified pattern as the laser pulsed, removing the need for manual stage movement. With LIBS System 1, data acquisition across 25 sample locations would take 2-2.5 minutes. Using LIBS System 6, this would take 2.5 seconds.

Laser selection for LIBS was found to be an overwhelming task with the number of options available on the market. The guiding parameters were determined to be laser power, beam characteristics, repetition rate, options for triggering (input and output), active vs. passive Q-switching, and cost.

Spectrometers

Like lasers, many options exist among spectrometers and detectors. They vary significantly in cost, sensitivity, and resolution. Likewise, there is large variation in detectors and their functions. Details that were considered when purchasing a spectrometer were ease of integration with a LIBS system, time-gating capabilities, grating efficiency across the wavelength range, and resolution. This study found that most lanthanides had many closely spaced emission lines. Using a high-resolution spectrometer, elements were identified using two methods: emission-line identification and spectral unmixing. Though the following hypothesis was not tested, it may be possible to use a low-resolution spectrometer and spectral unmixing to identify elements like lanthanides. For the purposes of this study, a high-resolution spectrometer facilitated verifying observed peaks with the NIST ASD. The next step would be to apply a low-resolution (1-2 nm) spectrometer to the system and determine if element identification would be possible using spectral unmixing techniques. Overall, to identify spectral-resolution requirements for a LIBS system, it was found that prior knowledge of the background spectrum of the negative control (e.g., nitrocellulose) material, and the analyte of interest (e.g., lanthanides) should be well understood.

Choosing the spectrometer spectral window is closely related to resolution. Generally, the higher the resolution of the spectrometer, the narrower the window. For this study, a 30 nm window was occasionally insufficient, especially when the goal was to acquire the 200 nm 600 nm spectrum of 17 metals. A high-resolution, wide spectral window would be best for measuring atomic emissions across such a range, but this was not common for spectrometers with ICCD detectors.

This study determined that most emissions for the 17 metals of interest (discussed further in Chapter 3) produced strong emission lines from 300 to 450 nm. The optimal width depended on the metals being analyzed. For example, a 354 to 384 nm window was sufficient to capture intense Lu, Yb, and Eu emissions.

One of the major factors in acquiring components for a LIBS system was whether to purchase a spectrometer with a CCD or ICCD detector. CCD detectors, like the one in the Avantes AvaSpec Mini, are less expensive, more compact, acquire data across a ~200 nm wavelength range, and have a resolution practical for lanthanide detection (0.25 nm). However, a factor that may have contributed to LIBS System 1's inability to detect most lanthanides dried on nitrocellulose and silicon wafers was this unit's inability for high-resolution time-gating. ICCD detectors like the USB iStar by Andor Inc. could rapidly (in ~30 ns) begin data acquisition after triggering and acquire data for either very short (2 ns) or long periods of time. This level of high-resolution time gating was not observed among CCD detectors.

It was found that the ability to trigger spectrometer/detector acquisition to perform its function was critical. Without accurately timed triggering, LIBS data would feature high variability. A source of acquisition-time inaccuracy was the cleaning cycle of the CCD. While in some spectrometer models, the cycle of removing charge buildup can be interrupted, in other models acquisition only begins once the cleaning cycle is complete. Interrupting the cleaning cycle for more accurate timing in data acquisition may yield additional noise in the data. Understanding the limitations in the timing accuracy of the spectrometer/detector was an important factor in LIBS system design. For some spectrometers/detectors, the status of the CCD as well as the photocathode can be monitored. The data were helpful in affirming detector function and troubleshooting. Another useful spectrometer output signal was one that could trigger other devices.

Electronics, Software, and Data Analysis

Emphasis has been placed throughout the dissertation on LIBS timing parameters. Accurately timed triggering of all LIBS was found to improve data reproducibility. A useful device in accomplishing this task is a delay generator that can time between signal input and multiple output pulses. For LIBS System 1, a delay generator was built by Miftek Inc. For in-house LIBS System 6, either the Sapphire 9200 delay generator by Quantum Composers or the Andor USB iStar ICCD

was used. Ease of integration into the LIBS system and user interface were found to be the two important aspects. The prototype delay generator for LIBS System 1 required circuit board modifications and software code re-writing so that it could interface with different LIBS components. The Sapphire 9200 had an easy user interface that allowed the device to be either internally or externally triggered followed by a user-defined series of signal outputs. The case was similar with the USB iStar ICCD, though it was not always convenient to have the delay generator paired with the detector, especially when it is not the detector being used for data acquisition.

Both Andor Solis and Avantes AvaSoft8 were found to be user-friendly software for spectrometer/detector control and data visualization. Immediate data visualization post laser ablation was especially useful for troubleshooting and result evaluation. A feature that could improve the software is immediate identification of atomic emission lines. Once data were acquired, the format in which data were exported often dictated down-stream processing for data analysis. ASC files were a convenient export format since they were easy for external programs to read. While both software types could perform analysis of the spectra, data were preferably analyzed using a custom R software for statistical computing (Appendix B).

Sample Chamber

Several sample chambers were tested in this study. LIBS System 1 featured a sample chamber with a simple design meant to position the optics and sample for ablation and emission collection. To change ablation location on the sample, the sample was manually moved within the chamber. This design posed several challenges. First, manual movement of the sample was cumbersome and prone to error. Second, the chamber was not designed to remove aerosols from the chamber, accumulating debris that could have blocked the laser beam as well as emissions, and potentially permitted hazardous inhalation of debris by the user. To prevent inhalation of debris, LIBS systems using this chamber design were in a fume hood, which unfortunately made the hood unavailable for other tasks. LIBS System 6 used a sample chamber on a motorized xyz stage. Unlike the previous chamber, emission collection optics were not connected to the chamber. This allowed the chamber containing the sample to be moved relative to the stationary LIBS laser and emission collection optics. This approach facilitated the design of an enclosed chamber connected to an air filter and vacuum pump to remove debris. Safe removal of debris removed the need for a fume hood, while motorized stage control facilitated remote sample placement.

Optics and Optomechanics

The studies presented in this dissertation work did not involve an in-depth comparison between optical components and designs. However, several observations were of note. For LIBS System 2, which utilized a low-powered LIBS laser, the number and type of optics placed between the laser head and the sample affected whether a plasma was generated on a silicon wafer surface. This observation was likely attributed to laser energy lost across each optical component and highlighted the importance of optics design and selection for low-energy LIBS lasers. In addition, optics placed too close to the sample surface were at risk of contamination with debris. Distance of the optics from the sample surface was dependent on laser energy, sample type and airflow. For dry paper samples a distance of 20-30 mm sufficed. At this distance, debris from wet food samples (not discussed in this dissertation) contaminated the surface of optical components. Throughout this dissertation, quartz windows, mirrors, lenses and other optical components were kept clean to avoid unintentional obstruction of the laser beam or plasma emissions. Positioning of optics was achieved using mechanical components purchased mostly from Thorlabs Inc. The cage system by Thorlabs was especially useful for aligning optics.

APPENDIX B. R CODE FOR LIBS DATA ANALYSIS

The following code was written in R language for statistical computing to analyze LIBS data output by the Andor iStar ICCD. Data was saved as an ASC files and consisted of wavelength and intensity information across multiple acquisitions. An explanation of the data analysis process is provided in Section 3.4.

```

require(baseline)
library(ggplot2)
require(hyperSpec)
library(readr)
library(dplyr)
library(lubridate)
library(ggpmisc)
library(ggrepel)
library(ggspectra)
library(signal)
library(pracma)
require(gtools)
require(tidyverse)
library(xlsx)
library(rJava)
library(xlsxjars)
require(gtools)

##Set filepath
Folder_0 <- 'C:/Users/CarmenGondhalekar/Dropbox/'
Folder_1 <- 'LIBS System/'
Folder_2 <- 'LIBS Instrument/'
Folder_3 <- 'Experiments LIBS SIBS/'
Folder_4 <- 'Experiments with Litron Laser and Andor Spec and ICCD/'
Folder_5 <- '020220 Eu antiGram on LFIA/'
Folder_6 <- 'ASC files' #Folder data is stored in. Data stored as ASC file fo
rmat.
folder_name_1 <- paste0(Folder_0, Folder_1, Folder_2, Folder_3, Folder_4, Fol
der_5, Folder_6)

setwd(folder_name_1)
getwd() #used to check file path

file_list <- list.files()
file_list <- mixedsort(sort(file_list))
file_list

```

```

for (myfile in file_list){

  # if the merged dataset doesn't exist, create it
  if (!exists("dataset")){
    #####
    my_vec <- read.csv(myfile, header = FALSE, skip = 49, sep = "\t")
    my_vec <- my_vec[-c(1:155, 870:1024),] #select range of data for analysis
    Wavelength <- (my_vec[,1])
    data_set_1 <- my_vec[, -c(1, (length(my_vec)-1), length(my_vec))]
    data_mean_1 <- rowMeans(data_set_1)
    data_SD_1 <- apply(data_set_1, 1, sd)

    ###Baseline Subtraction
    run_med_df <- as.data.frame(apply(data_set_1, 2,
function(x){runmed(x,101)}))
    run_med_df_mean <- rowMeans(run_med_df)
    data_set_2 <- (data_set_1)-(run_med_df)
    data_mean_2 <- rowMeans(data_set_2)
    data_SD_2 <- apply(data_set_2, 1, sd)

    ###Centering data on X axis
    filtered_signal.mean <- apply(data_set_2, 2,
function(x){mean(runmed(x,101))}) #calculates the mean of the background
    filtered_signal.mean
    data_set_3 <- sweep(data_set_2,2,filtered_signal.mean,'-')#puts mean of
data on the y axis
    data_mean_3 <- rowMeans(data_set_3)
    data_SD_3 <- apply(data_set_3, 1, sd)

    ###Thresholding data
    filtered_signal.sd <- apply(data_set_3, 2,
function(x){sd(runmed(x,101))}) #calculates the standard deviation of the
background
    filtered_signal.sd
    threshold_level_func <- function(SD){SD*filtered_signal.sd} #establishes
threshold
    threshold_level <- threshold_level_func(0) #finds the threshold level in
units of intensity
    threshold_level
    data_set_4 <- t(apply(data_set_3, 1, function(x){
      x[x<threshold_level] <- 0
      x
    })))
    data_set_4 <- as.data.frame(data_set_4)
    data_mean_4 <- rowMeans(data_set_4)
    data_SD_4 <- apply(data_set_4, 1, sd)

    ###Normalizing data

```

```

data_set_5 <- t(apply(data_set_4, 1, function(x){x/filtered_signal.sd}))
#converts intensity values to standard deviations
  data_set_5 <- as.data.frame(data_set_5)
  data_mean_5 <- rowMeans(data_set_5)
  data_SD_5 <- apply(data_set_5, 1, sd)

  data_set_export <- data.frame(mean2 = data_mean_5, SD2 = data_SD_5)
  dataset <- data_set_export
}
# if the merged dataset does exist, append to it
if (exists("dataset")){
  my_vec <- read.csv(myfile, header = FALSE, skip = 49, sep = "\t")
  my_vec <- my_vec[-c(1:155, 870:1024),]
  Wavelength <- (my_vec[,1])
  data_set_1 <- my_vec[, -c(1, (length(my_vec)-1), length(my_vec))]
  data_mean_1 <- rowMeans(data_set_1)
  data_SD_1 <- apply(data_set_1, 1, sd)

  ###Baseline Subtraction
  run_med_df <- as.data.frame(apply(data_set_1, 2,
function(x){runmed(x,101)}))
  run_med_df_mean <- rowMeans(run_med_df)
  data_set_2 <- (data_set_1)-(run_med_df)
  data_mean_2 <- rowMeans(data_set_2)
  data_SD_2 <- apply(data_set_2, 1, sd)

  ###Centering data on X axis
  filtered_signal.mean <- apply(data_set_2, 2,
function(x){mean(runmed(x,101))}) #calculates the mean of the background
  filtered_signal.mean
  data_set_3 <- sweep(data_set_2,2,filtered_signal.mean,'-')#puts mean of
data on the y axis
  data_mean_3 <- rowMeans(data_set_3)
  data_SD_3 <- apply(data_set_3, 1, sd)

  ###Thresholding data
  filtered_signal.sd <- apply(data_set_3, 2,
function(x){sd(runmed(x,101))}) #calculates the standard deviation of the
background
  filtered_signal.sd
  threshold_level_func <- function(SD){SD*filtered_signal.sd} #says that
the threshold should be a certain number of standard deviations above the
mean of the background
  threshold_level <- threshold_level_func(0) #finds the threshold level in
units of intensity
  threshold_level
  data_set_4 <- t(apply(data_set_3, 1, function(x){
    x[x<threshold_level] <- 0

```

```

}))
  data_set_4 <- as.data.frame(data_set_4)
  data_mean_4 <- rowMeans(data_set_4)
  data_SD_4 <- apply(data_set_4, 1, sd)

  ###Normalizing data
  data_set_5 <- t(apply(data_set_4, 1, function(x){x/filtered_signal.sd}))
#converts intensity values to standard deviations
  data_set_5 <- as.data.frame(data_set_5)
  data_mean_5 <- rowMeans(data_set_5)
  data_SD_5 <- apply(data_set_5, 1, sd)

  data_set_export <- data.frame(mean2 = data_mean_5, SD2 = data_SD_5)
  temp_dataset <- data_set_export
  dataset<-cbind(dataset, temp_dataset)
  rm(temp_dataset)
}
}

###Treatment names
treatment_names <- gsub(".csv", "", file_list)
treatment_names <- gsub(".asc", "", treatment_names)
###Drop first two columns of the dataset because they are repeated values
dataset2 <- dataset[,-c(1,2)]
###Separate means from SDs and give columns titles
odd <- function(x) x%%2 != 0
odd <- odd(1:length(dataset2))
even <- function(x) x %% 2 == 0
even <- even(1:length(dataset2))
odd_num <- which(odd, arr.ind = TRUE)
even_num <- which(even, arr.ind = TRUE)
means <- dataset2[,odd_num]
SDs <- dataset2[,even_num]
names(means)[1:length(means)] <- treatment_names
names(SDs)[1:length(SDs)] <- treatment_names
###Add wavelength and order data according to wavelength
means <- cbind(Wavelength, means)
order.means <- order(means$Wavelength)
means <- means[order.means, ]
SDs <- cbind(Wavelength, SDs)
order.SDs <- order(SDs$Wavelength)
SDs <- SDs[order.SDs, ]

###Save Data
write.csv(means, paste0(folder_name_2, "Normalized_mean.csv"))
write.csv(SDs, paste0(folder_name_2, "Standard deviation.csv"))

###Find peaks
column_num <- 18 #column of data containing the positive control for the

```

element of interest

```
peak_num <- 10
Wavelength_2 <- as.data.frame(Wavelength)
my_peaks <- findpeaks(means[,column_num], npeaks=peak_num, threshold=2, sorts
tr=TRUE)
my_peaks <- data.frame(Wavelength = Wavelength_2[my_peaks[c(1:peak_num),2],1]
, Index = my_peaks[c(1:peak_num),2], Intensity = my_peaks[c(1:peak_num),1], S
D = SDs[my_peaks[c(1:peak_num),2],column_num])
my_peaks #outputs a list of peaks found in the data
```

###Pooled mean calculation

```
pool_mean_SD <- function(start_col, rep_num, sample_size, peak_ID) {
  tn <- rep_num*sample_size;
  sum_x1 <- means[peak_ID, start_col:(start_col+rep_num-1)]*sample_size;
  sum_x_sq1 <- (SDs[peak_ID, start_col:(start_col+rep_num-
1)])^2*(sample_size-1)+((sum_x1)^2/sample_size);
  tx1 <- sum(sum_x1);
  txx1 <- sum(sum_x_sq1);
  pool_mean <- tx1/tn;
  pool_SD <- sqrt((txx1-(tx1)^2/tn)/(tn-1));
  pool_SE <- pool_SD/sqrt(sample_size)
  pool_COV <- pool_SD/pool_mean*100;
  c(treatment_names[start_col-1], rep_num, sample_size,
(rep_num*sample_size), means[peak_ID, 1],
  pool_mean, pool_SD, pool_SE, pool_COV)
}
```

```
start_col <- c(2:24) #A list of the first column of each replicate
rep_num <- 1 #number of replicates per treatment
sample_size <- 6 #sample size per replicate (number of laser shots)
Wavelength_ID <- 31 #ID of wavelength of interest (refer to the my_peaks)
```

```
for(i in start_col) {
  if (!exists("my_pool")){
    pool <- pool_mean_SD(i, rep_num, sample_size, Wavelength_ID)
    my_pool <- data.frame(treatment = pool[1], rep_num = pool[2], sample_size
= pool[3], total_sample_size <- pool[4], Wavelength = pool[5], pool_mean =
pool[6], pool_SD = pool[7], pool_SE = pool[8], pool_COV = pool[9])
  }
  if (exists("my_pool")){
    pool <- pool_mean_SD(i, rep_num, sample_size, Wavelength_ID)
    temp_pool <- data.frame(treatment = pool[1], rep_num = pool[2],
sample_size = pool[3], total_sample_size <- pool[4], Wavelength = pool[5],
pool_mean = pool[6], pool_SD = pool[7], pool_SE = pool[8], pool_COV =
pool[9])
    my_pool <- rbind(my_pool, temp_pool)
    rm(temp_pool)
  }
}
```

```

    }
  }
  Summary <- my_pool[c(-1),]

###Make excel spreadsheet with mean, SDs and Summary
make_xlsx <- function (file, ...)
{
  require(xlsx, quietly = TRUE)
  objects <- list(...)
  fargs <- as.list(match.call(expand.dots = TRUE))
  objnames <- as.character(fargs)[-c(1, 2)]
  nobjects <- length(objects)
  for (i in 1:nobjects) {
    if (i == 1)
      write.xlsx(objects[[i]], file, sheetName = objnames[i])
    else write.xlsx(objects[[i]], file, sheetName = objnames[i],
                     append = TRUE)
  }
}

```


REFERENCES

1. Zhao W, Ali MM, Aguirre SD, Brook MA, Li Y. Paper-Based Bioassays Using Gold Nanoparticle Colorimetric Probes. *Analytical Chemistry*. 2008;80(22):8431-7. doi:10.1021/ac801008q.
2. Liana DD, Raguse B, Gooding JJ, Chow E. Recent advances in paper-based sensors. *Sensors (Basel)*. 2012;12(9):11505-26. doi:10.3390/s120911505.
3. Bahadır EB, Sezgintürk MK. Lateral flow assays: Principles, designs and labels. *TrAC Trends in Analytical Chemistry*. 2016;82:286-306. doi:10.1016/j.jim.2014.10.010.
4. Posthuma-Trumpie GA, Korf J, van Amerongen A. Lateral flow (immuno)assay: its strengths, weaknesses, opportunities and threats. A literature survey. *Analytical and Bioanalytical Chemistry*. 2009;393(2):569-82. doi:10.1007/s00216-008-2287-2.
5. Wild DG. 7.3.1 Pregnancy Tests. *Immunoassay Handbook - Theory and Applications of Ligand Binding, ELISA and Related Techniques (4th Edition)*. Elsevier.
6. Giepmans BNG, Adams SR, Ellisman MH, Tsien RY. The Fluorescent Toolbox for Assessing Protein Location and Function. *Science*. 2006;312(5771):217.
7. Zhang J, Li B, Zhang L, Jiang H. An optical sensor for Cu(ii) detection with upconverting luminescent nanoparticles as an excitation source. *Chemical Communications*. 2012;48(40):4860-2. doi:10.1039/C2CC31642K.
8. Xu S, Dong B, Zhou D, Yin Z, Cui S, Xu W, Chen B, Song H. Paper-based upconversion fluorescence resonance energy transfer biosensor for sensitive detection of multiple cancer biomarkers. *Scientific Reports*. 2016;6:23406. doi:10.1038/srep23406.
9. Yao Y, Liu R, Shin MS, Trentalange M, Allore H, Nassar A, Kang I, Pober JS, Montgomery RR. CyTOF supports efficient detection of immune cell subsets from small samples. *Journal of immunological methods*. 2014;415:1-5. doi:10.1016/j.jim.2014.10.010.
10. Resch-Genger U, Grabolle M, Cavaliere-Jaricot S, Nitschke R, Nann T. Quantum dots versus organic dyes as fluorescent labels. *Nature Methods*. 2008;5:763. doi:10.1038/nmeth.1248.
11. Kanje S, Herrmann AJ, Hober S, Mueller L. Next generation of labeling reagents for quantitative and multiplexing immunoassays by the use of LA-ICP-MS. *Analyst*. 2016;141(23):6374-80. doi:10.1039/C6AN01878E.
12. Cremers DA. *Handbook of laser-induced breakdown spectroscopy*. Chichester, West Sussex, England: John Wiley & Sons; 2006.

13. Rakovský J, Čermák P, Musset O, Veis P. A review of the development of portable laser induced breakdown spectroscopy and its applications. *Spectrochimica Acta Part B: Atomic Spectroscopy*. 2014;101:269-87. doi:10.1016/j.sab.2014.09.015.
14. Majonis D, Herrera I, Ornatsky O, Schulze M, Lou X, Soleimani M, Nitz M, Winnik MA. Synthesis of a functional metal-chelating polymer and steps toward quantitative mass cytometry bioassays. *Analytical Chemistry*. 2010;82(21):8961-9. doi:10.1021/ac101901x.
15. Yang JY, Herold DA. Chapter 13 - Evolving platforms for clinical mass spectrometry A2 - Nair, Hari. In: Clarke W, editor. *Mass Spectrometry for the Clinical Laboratory*. San Diego: Academic Press; 2017. p. 261-76.
16. Tanner SD, Baranov VI, Ornatsky OI, Bandura DR, George TC. An introduction to mass cytometry: fundamentals and applications. *Cancer immunology, immunotherapy : CII*. 2013;62(5):955-65. doi:10.1007/s00262-013-1416-8.
17. Maher S, Jjunju FPM, Taylor S. Colloquium: 100 years of mass spectrometry: perspectives and future trends.(Report). 2015;87(1):113-30. doi:10.1103/RevModPhys.87.113.
18. Galbács G. A critical review of recent progress in analytical laser-induced breakdown spectroscopy. *Analytical and bioanalytical chemistry*. 2015;407(25):7537-62. doi:10.1007/s00216-015-8855-3.
19. Gottfried JL, De Lucia FC, Munson CA, Miziolek AW. Standoff Detection of Chemical and Biological Threats Using Laser-Induced Breakdown Spectroscopy. *Appl Spectrosc*. 2008;62(4):353-63. doi:10.1366/000370208784046759.
20. Barnett C, Bell C, Vig K, Akpovo AC, Johnson L, Pillai S, Singh S. Development of a LIBS assay for the detection of *Salmonella enterica* serovar Typhimurium from food. *Analytical and Bioanalytical Chemistry*. 2011;400(10):3323-30. doi:10.1007/s00216-011-4844-3.
21. Rehse S, Miziolek A. Recent advances in the use of laser-induced breakdown spectroscopy (LIBS) as a rapid point-of-care pathogen diagnostic. *Proceedings of SPIE - The International Society for Optical Engineering*. 2012;8371:1. doi:10.1117/12.919256.
22. Samuels AC, DeLucia FC, McNesby KL, Miziolek AW. Laser-induced breakdown spectroscopy of bacterial spores, molds, pollens, and protein: initial studies of discrimination potential. *Appl Opt*. 2003;42(30):6205-9. doi:10.1364/AO.42.006205.
23. Modlitbova P, Farka Z, Pastucha M, Porizka P, Novotny K, Skladal P, Kaiser J. Laser-induced breakdown spectroscopy as a novel readout method for nanoparticle-based immunoassays. *Mikrochim Acta*. 2019;186(9):629. doi:10.1007/s00604-019-3742-9.
24. Jr FC, Samuels A, Harmon R, Walters R, McNesby K, LaPointe A, Jr RJ, Miziolek A. Laser-induced breakdown spectroscopy (LIBS): A promising versatile chemical sensor technology for hazardous material detection. *Sensors Journal, IEEE*. 2005;5:681-9. doi:10.1109/JSEN.2005.848151.

25. Markushin Y, Sivakumar P, Connolly D, Melikechi N. Tag-femtosecond laser-induced breakdown spectroscopy for the sensitive detection of cancer antigen 125 in blood plasma. *Analytical and Bioanalytical Chemistry*. 2015;407(7):1849-55. doi:10.1007/s00216-014-8433-0.
26. Markushin Y, Melikechi N, O. AM, Rock S, Henderson E, Connolly D, editors. LIBS-based multi-element coded assay for ovarian cancer application. SPIE BiOS; 2009: SPIE.
27. Yuri Markushin NM. Sensitive Detection of Epithelial Ovarian Cancer Biomarkers Using Tag-Laser Induced Breakdown Spectroscopy, Ovarian Cancer. InTech; 2012.
28. Geissler E, Moon JEvC. Biological and toxin weapons : research, development, and use from the Middle Ages to 1945. Oxford; New York: Oxford University Press; 1999.
29. Christopher GW, Cieslak TJ, Pavlin JA, Eitzen EM, Jr. Biological warfare. A historical perspective. *Jama*. 1997;278(5):412-7.
30. Lim DV, Simpson JM, Kearns EA, Kramer MF. Current and Developing Technologies for Monitoring Agents of Bioterrorism and Biowarfare. *Clinical Microbiology Reviews*. 2005;18(4):583-607. doi:10.1128/CMR.18.4.583-607.2005.
31. Török TJ, Tauxe RV, Wise RP, et al. A large community outbreak of salmonellosis caused by intentional contamination of restaurant salad bars. *Jama*. 1997;278(5):389-95. doi:10.1001/jama.1997.03550050051033.
32. A History of Anthrax. Centers for Disease Control and Prevention. <https://www.cdc.gov/anthrax/resources/history/index.html>. Accessed 10/9/18.
33. Schirone M, Visciano P, Tofalo R, Suzzi G. Editorial: Biological Hazards in Food. *Frontiers in Microbiology*. 2016;7:2154. doi:10.3389/fmicb.2016.02154.
34. National Outbreak Reporting System. Centers for Disease Control and Prevention. <https://wwwn.cdc.gov/norsdashboard/>.
35. Aathithan S, Plant JC, Chaudry AN, French GL. Diagnosis of Bacteriuria by Detection of Volatile Organic Compounds in Urine Using an Automated Headspace Analyzer with Multiple Conducting Polymer Sensors. *Journal of Clinical Microbiology*. 2001;39(7):2590-3. doi:10.1128/jcm.39.7.2590-2593.2001.
36. Deisingh AK, Thompson M. Biosensors for the detection of bacteria. *Canadian journal of microbiology*. 2004;50(2):69-77. doi:10.1139/w03-095.
37. Pavlou AK, Magan N, McNulty C, Jones JM, Sharp D, Brown J, Turner APF. Use of an electronic nose system for diagnoses of urinary tract infections. *Biosensors and Bioelectronics*. 2002;17(10):893-9. doi:[https://doi.org/10.1016/S0956-5663\(02\)00078-7](https://doi.org/10.1016/S0956-5663(02)00078-7).

38. Magan N, Pavlou A, Chrysanthakis I. Milk-sense: a volatile sensing system recognises spoilage bacteria and yeasts in milk. *Sensors and Actuators B: Chemical*. 2001;72(1):28-34. doi:[https://doi.org/10.1016/S0925-4005\(00\)00621-3](https://doi.org/10.1016/S0925-4005(00)00621-3).
39. Keshri G, Voysey P, Magan N. Early detection of spoilage moulds in bread using volatile production patterns and quantitative enzyme assays. *Journal of applied microbiology*. 2002;92(1):165-72.
40. Greenwood JE, Crawley BA, Clark SL, Chadwick PR, Ellison DA, Oppenheim BA, McCollum CN. Monitoring wound healing by odour. *Journal of Wound Care*. 1997;6(5):219-21. doi:10.12968/jowc.1997.6.5.219.
41. Chandiok S, Crawley BA, Oppenheim BA, Chadwick PR, Higgins S, Persaud KC. Screening for bacterial vaginosis: a novel application of artificial nose technology. *Journal of clinical pathology*. 1997;50(9):790-1.
42. Keshri G, Magan N. Detection and differentiation between mycotoxigenic and non-mycotoxigenic strains of two *Fusarium* spp. using volatile production profiles and hydrolytic enzymes. *Journal of applied microbiology*. 2000;89(5):825-33.
43. Ivnitski D, O'Neil DJ, Gattuso A, Schlicht R, Calidonna M, Fisher R. Nucleic acid approaches for detection and identification of biological warfare and infectious disease agents. *Biotechniques*. 2003;35(4):862-9.
44. Empowering the Development of Genomics Expertise (EDGE) Fact Sheet. In: Agency DTR, editor.
45. Stephanie Buehler AD, Zachary Willenberg, Karen Riggs. Idaho Technology Inc. R.A.P.I.D.® System for the detection of *Francisella tularensis*, *Yersinia pestis*, *Bacillus anthracis*, *Brucella suis*, and *Escherichia coli*. In: Agency EP, editor. Columbus, Ohio 2004.
46. Pinsky BA, Sahoo MK, Sandlund J, Kleman M, Kulkarni M, Grufman P, Nygren M, Kwiatkowski R, Baron EJ, Tenover F, Denison B, Higuchi R, Van Atta R, Beer NR, Carrillo AC, Naraghi-Arani P, Mire CE, Ranadheera C, Grolla A, Lagerqvist N, Persing DH. Analytical Performance Characteristics of the Cepheid GeneXpert Ebola Assay for the Detection of Ebola Virus. *PLOS ONE*. 2015;10(11):e0142216. doi:10.1371/journal.pone.0142216.
47. Higgins JA, Cooper M, Schroeder-Tucker L, Black S, Miller D, Karns JS, Manthey E, Breeze R, Perdue ML. A Field Investigation of *Bacillus anthracis* Contamination of U.S. Department of Agriculture and Other Washington, D.C., Buildings during the Anthrax Attack of October 2001. *Applied and Environmental Microbiology*. 2003;69(1):593-9. doi:10.1128/aem.69.1.593-599.2003.
48. Peruski AH, Peruski LF. Immunological Methods for Detection and Identification of Infectious Disease and Biological Warfare Agents. *Clinical and Diagnostic Laboratory Immunology*. 2003;10(4):506-13. doi:10.1128/cdli.10.4.506-513.2003.

49. Alim Fatah RA, James Peterson, Charlotte Lattin, Corrie Wells, Joseph McClintock. Guide for the Selection of Chemical Detection Equipment for Emergency First Responders, 3rd Edition. In: Security H, editor.2007.
50. Lin A, Kase J, Moore M, Son I, Tran N, Clotilde L, Jarvis K, Jones K, Katsuri K, Nabe K, Nucci M, Wagley G, Wang F, GE B, Hammack T. Multilaboratory Validation of a Luminex Microbead-Based Suspension Array for the Identification of the 11 Most Clinically Relevant Shiga Toxin–Producing Escherichia coli O Serogroups. *Journal of Food Protection*. 2013;76(5):867-70. doi:10.4315/0362-028x.jfp-12-468.
51. Hindson BJ, Brown SB, Marshall GD, McBride MT, Makarewicz AJ, Gutierrez DM, Wolcott DK, Metz TR, Madabhushi RS, Dzenitis JM, Colston BW. Development of an Automated Sample Preparation Module for Environmental Monitoring of Biowarfare Agents. *Analytical Chemistry*. 2004;76(13):3492-7. doi:10.1021/ac035365r.
52. Fact Sheet for Healthcare Providers: Interpreting xMAP® MultiFlex™ Zika RNA Assay Test Results. Luminex Corporation.
<https://www.fda.gov/downloads/MedicalDevices/Safety/EmergencySituations/UCM515134.pdf>. Accessed 10/9/18.
53. Alim Fatah RA, Tesema Chekol, Charlotte Lattin, Omowunmi Sadik, Austin Aluoch. Guide for the Selection of Biological Agent Detection Equipment for Emergency First Responders, 2nd Edition In: Security H, editor.
54. Peruski AH, Johnson LH, Peruski LF. Rapid and sensitive detection of biological warfare agents using time-resolved fluorescence assays. *Journal of immunological methods*. 2002;263(1):35-41. doi:[https://doi.org/10.1016/S0022-1759\(02\)00030-3](https://doi.org/10.1016/S0022-1759(02)00030-3).
55. Ching KH, He X, Stanker LH, Lin AV, McGarvey JA, Hnasko R. Detection of Shiga Toxins by Lateral Flow Assay. *Toxins*. 2015;7(4):1163-73. doi:10.3390/toxins7041163.
56. Koczula Katarzyna M, Gallotta A. Lateral flow assays. *Essays in Biochemistry*. 2016;60(1):111-20. doi:10.1042/EBC20150012.
57. Seok Y, Joung H-A, Byun J-Y, Jeon H-S, Shin SJ, Kim S, Shin Y-B, Han HS, Kim M-G. A Paper-Based Device for Performing Loop-Mediated Isothermal Amplification with Real-Time Simultaneous Detection of Multiple DNA Targets. *Theranostics*. 2017;7(8):2220-30. doi:10.7150/thno.18675.
58. Schramm EC, Staten NR, Zhang Z, Bruce SS, Kellner C, Atkinson JP, Kyttaris VC, Tsokos GC, Petri M, Sander Connolly E, Olson PK. A quantitative lateral flow assay to detect complement activation in blood. *Analytical Biochemistry*. 2015;477:78-85. doi:10.1016/j.ab.2015.01.024.
59. Carrio A, Sampedro C, Sanchez-Lopez J, Pimienta M, Campoy P. Automated Low-Cost Smartphone-Based Lateral Flow Saliva Test Reader for Drugs-of-Abuse Detection. *Sensors*. 2015;15(11):29569-93. doi:10.3390/s151129569.

60. Moreno MdL, Cebolla Á, Muñoz-Suano A, Carrillo-Carrion C, Comino I, Pizarro Á, León F, Rodríguez-Herrera A, Sousa C. Detection of gluten immunogenic peptides in the urine of patients with coeliac disease reveals transgressions in the gluten-free diet and incomplete mucosal healing. *Gut*. 2015;66(2). doi:10.1136/gutjnl-2015-310148.
61. De Giovanni N, Fucci N. The Current Status of Sweat Testing For Drugs of Abuse: A Review. *Current Medicinal Chemistry*. 2013;20(4):545-61. doi:10.2174/0929867311320040006.
62. Haushalter KJ, Vetcha S, Haushalter RC. Multiplex Flow Assays. *ACS Omega*. 2016;1(4):586-99. doi:10.1021/acsomega.6b00188.
63. Simon S, Worbs S, Avondet M-A, Tracz D, Dano J, Schmidt L, Volland H, Dorner B, Corbett C. Recommended Immunological Assays to Screen for Ricin-Containing Samples. *Toxins*. 2015;7(12):4858.
64. Shyu R-H, Shyu H-F, Liu H-W, Tang S-S. Colloidal gold-based immunochromatographic assay for detection of ricin. *Toxicon*. 2002;40(3):255-8. doi:10.1016/S0041-0101(01)00193-3.
65. Klewitz T, Gessler F, Beer H, Pflanz K, Scheper T. Immunochromatographic assay for determination of botulinum neurotoxin type D. *Sensors and Actuators B: Chemical*. 2006;113(2):582-9. doi:<https://doi.org/10.1016/j.snb.2005.07.007>.
66. Liana DD, Raguse B, Gooding JJ, Chow E. Recent Advances in Paper-Based Sensors. *Sensors (Basel, Switzerland)*. 2012;12(9):11505-26. doi:10.3390/s120911505.
67. Sher M, Zhuang R, Demirci U, Asghar W. Paper-based analytical devices for clinical diagnosis: recent advances in the fabrication techniques and sensing mechanisms. Expert review of molecular diagnostics. 2017;17(4):351-66. doi:10.1080/14737159.2017.1285228.
68. Melikechi N, inventor Dover Photonics LLC, assignee. Preparation of fluid samples for laser induced breakdown spectroscopy and/or imaging analysis2018.
69. Noureddine Melikechi YM, inventor Delaware State University, assignee. Mono- and multi-element coded LIBS assays and methods2011.
70. Gondhalekar C, Biela E, Rajwa B, Bae E, Patsekin V, Sturgis J, Reynolds C, Doh I-J, Diwakar P, Stanker L, Zorba V, Mao X, Russo R, Robinson J. Detection of E. coli labeled with metal-conjugated antibodies using lateral-flow assay and laser-induced breakdown spectroscopy. *Analytical and Bioanalytical Chemistry*. 2020;412. doi:10.1007/s00216-019-02347-3.
71. Wu J, Liu Y, Cui Y, Zhao X, Dong D. A laser-induced breakdown spectroscopy-integrated lateral flow strip (LIBS-LFS) sensor for rapid detection of pathogen. *Biosensors and Bioelectronics*. 2019;142:111508. doi:<https://doi.org/10.1016/j.bios.2019.111508>.
72. Rehse SJ, Miziolek AW. Recent advances in the use of laser-induced breakdown spectroscopy (LIBS) as a rapid point-of-care pathogen diagnostic. 2012. p. 837106-7.

73. Bauer AJR, Buckley SG. Novel Applications of Laser-Induced Breakdown Spectroscopy. *Appl Spectrosc.* 2017;71(4):553-66. doi:10.1177/0003702817691527.
74. Taylor A, Barlow N, Day MP, Hill S, Patriarca M, White M. Atomic spectrometry update: review of advances in the analysis of clinical and biological materials, foods and beverages. *Journal of analytical atomic spectrometry.* 2017;32(3):432-76. doi:10.1039/c7ja90005h.
75. Markiewicz-Keszycka M, Cama-Moncunill X, Casado-Gavaldà MP, Dixit Y, Cama-Moncunill R, Cullen PJ, Sullivan C. Laser-induced breakdown spectroscopy (LIBS) for food analysis: A review. *Trends in Food Science & Technology.* 2017;65:80-93. doi:<https://doi.org/10.1016/j.tifs.2017.05.005>.
76. Hu H, Huang L, Liu M, Chen T, Yang P, Yao M. Nondestructive Determination of Cu Residue in Orange Peel by Laser Induced Breakdown Spectroscopy. *Plasma Science and Technology.* 2015;17(8):711.
77. Andersen M-BS, Frydenvang J, Henckel P, Rinnan Å. The potential of laser-induced breakdown spectroscopy for industrial at-line monitoring of calcium content in comminuted poultry meat. *Food Control.* 2016;64:226-33. doi:<https://doi.org/10.1016/j.foodcont.2016.01.001>.
78. Rehse SJ, Jeyasingham N, Diedrich J, Palchaudhuri S. A membrane basis for bacterial identification and discrimination using laser-induced breakdown spectroscopy. *Journal of Applied Physics.* 2009;105(10):102034. doi:10.1063/1.3116141.
79. Charfi B, Harith MA. Panoramic laser-induced breakdown spectrometry of water. *Spectrochimica Acta Part B: Atomic Spectroscopy.* 2002;57(7):1141-53. doi:[https://doi.org/10.1016/S0584-8547\(02\)00059-9](https://doi.org/10.1016/S0584-8547(02)00059-9).
80. Lal B, St-Onge L, Yu Yueh F, Singh J. LIBS Technique for Powder Materials. 2007.
81. Jantzi SC, Motto-Ros V, Trichard F, Markushin Y, Melikechi N, De Giacomo A. Sample treatment and preparation for laser-induced breakdown spectroscopy. *Spectrochimica Acta Part B: Atomic Spectroscopy.* 2016;115:52-63. doi:<https://doi.org/10.1016/j.sab.2015.11.002>.
82. Moncayo S, Rosales JD, Izquierdo-Hornillos R, Anzano J, Caceres JO. Classification of red wine based on its protected designation of origin (PDO) using Laser-induced Breakdown Spectroscopy (LIBS). *Talanta.* 2016;158(C):185-91. doi:10.1016/j.talanta.2016.05.059.
83. Choi D, Gong Y, Nam S-H, Han S-H, Yoo J, Lee Y. Laser-Induced Breakdown Spectroscopy (LIBS) Analysis of Calcium Ions Dissolved in Water Using Filter Paper Substrates: An Ideal Internal Standard for Precision Improvement. *Appl Spectrosc.* 2014;68(2):198-212. doi:10.1366/13-07163.
84. Abdel-Salam Z, Al Sharnoubi J, Harith MA. Qualitative evaluation of maternal milk and commercial infant formulas via LIBS. *Talanta.* 2013;115(C):422-6. doi:10.1016/j.talanta.2013.06.003.

85. Pasquini C, Cortez J, Silva LMC, Gonzaga FB. Laser Induced Breakdown Spectroscopy. *Journal of the Brazilian Chemical Society*. 2007;18:463-512.
86. Hunter AJR, Piper LG. Laser-Induced Breakdown Spectroscopy. Spark-induced breakdown spectroscopy: a description of an electrically generated LIBS-like process for elemental analysis of airborne particulates and solid samples. Cambridge, New York: Cambridge University Press; 2006.
87. Cremers DA, Radziemski LJ. Introduction. *Handbook of Laser-Induced Breakdown Spectroscopy*. John Wiley & Sons Ltd; 2013. p. 1-27.
88. Arantes de Carvalho GG, Moros J, Santos Jr D, Krug FJ, Laserna JJ. Direct determination of the nutrient profile in plant materials by femtosecond laser-induced breakdown spectroscopy. *Analytica Chimica Acta*. 2015;876:26-38. doi:<http://dx.doi.org/10.1016/j.aca.2015.03.018>.
89. Fornarini L, Spizzichino V, Colao F, Fantoni R, Lazic V. Influence of laser wavelength on LIBS diagnostics applied to the analysis of ancient bronzes. *Analytical and Bioanalytical Chemistry*. 2006;385(2):272-80. doi:10.1007/s00216-006-0300-1.
90. Gondal MA, Hussain T, Yamani ZH. Optimization of the LIBS Parameters for Detection of Trace Metals in Petroleum Products. *Energy Sources, Part A: Recovery, Utilization, and Environmental Effects*. 2008;30(5):441-51. doi:10.1080/15567030600826564.
91. Song K, Lee Y-I, Sneddon J. Applications of Laser-Induced Breakdown Spectrometry. *Applied Spectroscopy Reviews*. 1997;32(3):183-235. doi:10.1080/05704929708003314.
92. Barbieri Gonzaga F, Pasquini C. A compact and low cost laser induced breakdown spectroscopic system: Application for simultaneous determination of chromium and nickel in steel using multivariate calibration. *Spectrochimica Acta Part B: Atomic Spectroscopy*. 2012;69:20-4. doi:<http://dx.doi.org/10.1016/j.sab.2012.02.007>.
93. Cremers DA, Radziemski LJ. LIBS Apparatus Fundamentals. *Handbook of Laser-Induced Breakdown Spectroscopy*. John Wiley & Sons Ltd; 2013. p. 69-121.
94. Miziolek AW, Vincenzo Palleschi, Schechter I. *Laser Induced Breakdown Spectroscopy*. Cambridge University Press; 2006.
95. Hunter A, Wainner R, Piper L, Davis S, editors. Rapid field screening of soils for heavy metals with spark-induced breakdown spectroscopy (SIBS). *Laser Applications to Chemical and Environmental Analysis*; 2002 2002/02/07; Boulder, Colorado: Optical Society of America.
96. Cabalín LM, Laserna JJ. Experimental determination of laser induced breakdown thresholds of metals under nanosecond Q-switched laser operation. *Spectrochimica Acta Part B: Atomic Spectroscopy*. 1998;53(5):723-30. doi:[http://dx.doi.org/10.1016/S0584-8547\(98\)00107-4](http://dx.doi.org/10.1016/S0584-8547(98)00107-4).

97. Cristoforetti G, Legnaioli S, Palleschi V, Salvetti A, Tognoni E. Influence of ambient gas pressure on laser-induced breakdown spectroscopy technique in the parallel double-pulse configuration. *Spectrochimica Acta Part B: Atomic Spectroscopy*. 2004;59(12):1907-17. doi:<http://dx.doi.org/10.1016/j.sab.2004.09.003>.
98. Srungaram PK, Ayyalasomayajula KK, Yu-Yueh F, Singh JP. Comparison of laser induced breakdown spectroscopy and spark induced breakdown spectroscopy for determination of mercury in soils. *Spectrochimica Acta Part B: Atomic Spectroscopy*. 2013;87:108-13. doi:<http://dx.doi.org/10.1016/j.sab.2013.05.009>.
99. Margetic V, Pakulev A, Stockhaus A, Bolshov M, Niemax K, Hergenröder R. A comparison of nanosecond and femtosecond laser-induced plasma spectroscopy of brass samples. *Spectrochimica Acta Part B: Atomic Spectroscopy*. 2000;55(11):1771-85. doi:[http://dx.doi.org/10.1016/S0584-8547\(00\)00275-5](http://dx.doi.org/10.1016/S0584-8547(00)00275-5).
100. Wisbrun R, Schechter I, Niessner R, Schroeder H, Kompa KL. Detector for Trace Elemental Analysis of Solid Environmental Samples by Laser Plasma Spectroscopy. *Analytical Chemistry*. 1994;66(18):2964-75. doi:10.1021/ac00090a026.
101. Radziemski LJ, Cremers DA. *Laser-induced plasmas and applications*. 1989.
102. Freeman JR, Harilal SS, Diwakar PK, Verhoff B, Hassanein A. Comparison of optical emission from nanosecond and femtosecond laser produced plasma in atmosphere and vacuum conditions. *Spectrochimica Acta Part B: Atomic Spectroscopy*. 2013;87:43-50. doi:<http://dx.doi.org/10.1016/j.sab.2013.05.011>.
103. Anabitarte F, Cobo A, Lopez-Higuera JM. *Laser-Induced Breakdown Spectroscopy: Fundamentals, Applications, and Challenges*. ISRN Spectroscopy. 2012;2012:12. doi:10.5402/2012/285240.
104. Kashif Chaudhary SZHRaJA. *Laser-Induced Plasma and its Applications, Plasma Science and Technology - Progress in Physical States and Chemical Reactions. Laser-Induced Plasma and its Applications*. CC BY; 2016.
105. Cremers DA, Radziemski LJ. *Basics of the LIBS Plasma. Handbook of Laser-Induced Breakdown Spectroscopy*. John Wiley & Sons Ltd; 2013. p. 29-68.
106. Seely JF. Quantum Theory of Inverse Bremsstrahlung Absorption and Pair Production. In: Schwarz HJ, Hora H, editors. *Laser Interaction and Related Plasma Phenomena: Volume 3B*. Boston, MA: Springer US; 1974. p. 835-47.
107. Butler LRP, Laqua K, Strasheim A. Nomenclature, symbols, units and their usage in spectrochemical analysis—V radiation sources. *Spectrochimica Acta Part B: Atomic Spectroscopy*. 1986;41(5):507-44. doi:[http://dx.doi.org/10.1016/0584-8547\(86\)80190-2](http://dx.doi.org/10.1016/0584-8547(86)80190-2).

108. Lazic V, Barbini R, Colao F, Fantoni R, Palucci A. Self-absorption model in quantitative laser induced breakdown spectroscopy measurements on soils and sediments. *Spectrochimica Acta Part B: Atomic Spectroscopy*. 2001;56(6):807-20. doi:[http://dx.doi.org/10.1016/S0584-8547\(01\)00211-7](http://dx.doi.org/10.1016/S0584-8547(01)00211-7).
109. Cremers DA, Radziemski LJ. LIBS Analytical Figures of Merit and Calibration. *Handbook of Laser-Induced Breakdown Spectroscopy*. John Wiley & Sons Ltd; 2013. p. 123-50.
110. Loesel FH, Fischer JP, Götz MH, Horvath C, Juhasz T, Noack F, Suhm N, Bille JF. Non-thermal ablation of neural tissue with femtosecond laser pulses. *Applied Physics B*. 1998;66(1):121-8. doi:10.1007/s00340-003-1129-3.
111. von der Linde D, Sokolowski-Tinten K, Bialkowski J. Laser–solid interaction in the femtosecond time regime. *Applied Surface Science*. 1997;109–110:1-10. doi:[http://dx.doi.org/10.1016/S0169-4332\(96\)00611-3](http://dx.doi.org/10.1016/S0169-4332(96)00611-3).
112. Stoian R, Ashkenasi D, Rosenfeld A, Campbell EEB. Coulomb explosion in ultrashort pulsed laser ablation of Al₂O₃. *Physical Review B*. 2000;62(19):13167-73.
113. Chichkov BN, Momma C, Nolte S, von Alvensleben F, Tünnermann A. Femtosecond, picosecond and nanosecond laser ablation of solids. *Applied Physics A*. 1996;63(2):109-15. doi:10.1007/bf01567637.
114. Semerok A, Dutouquet C. Ultrashort double pulse laser ablation of metals. *Thin Solid Films*. 2004;453–454:501-5. doi:<http://dx.doi.org/10.1016/j.tsf.2003.11.115>.
115. Babushok VI, DeLucia Jr FC, Gottfried JL, Munson CA, Miziolek AW. Double pulse laser ablation and plasma: Laser induced breakdown spectroscopy signal enhancement. *Spectrochimica Acta Part B: Atomic Spectroscopy*. 2006;61(9):999-1014. doi:<http://dx.doi.org/10.1016/j.sab.2006.09.003>.
116. Baudelet M, Guyon L, Yu J, Wolf J-P, Amodeo T, Fréjafon E, Laloi P. Femtosecond time-resolved laser-induced breakdown spectroscopy for detection and identification of bacteria: A comparison to the nanosecond regime. *Journal of Applied Physics*. 2006;99(8):084701. doi:<http://dx.doi.org/10.1063/1.2187107>.
117. Rohwetter P, Yu J, Mejean G, Stelmazczyk K, Salmon E, Kasparian J, Wolf JP, Woste L. Remote LIBS with ultrashort pulses: characteristics in picosecond and femtosecond regimes. *Journal of analytical atomic spectrometry*. 2004;19(4):437-44. doi:10.1039/B316343A.
118. Le Droff B, Chaker M, Margot J, Sabsabi M, Barthélemy O, Johnston TW, Laville S, Vidal F. Influence of the Laser Pulse Duration on Spectrochemical Analysis of Solids by Laser-Induced Plasma Spectroscopy. *Appl Spectrosc*. 2004;58(1):122-9.
119. Kasem MA, Gonzalez JJ, Russo RE, Harith MA. Effect of the wavelength on laser induced breakdown spectrometric analysis of archaeological bone. *Spectrochimica Acta Part B: Atomic Spectroscopy*. 2014;101:26-31. doi:<http://dx.doi.org/10.1016/j.sab.2014.07.010>.

120. Barthélemy O, Margot J, Chaker M, Sabsabi M, Vidal F, Johnston TW, Laville S, Le Droff B. Influence of the laser parameters on the space and time characteristics of an aluminum laser-induced plasma. *Spectrochimica Acta Part B: Atomic Spectroscopy*. 2005;60(7–8):905-14. doi:<http://dx.doi.org/10.1016/j.sab.2005.07.001>.
121. Effenberger AJ, Scott JR. Effect of Atmospheric Conditions on LIBS Spectra. *Sensors (Basel, Switzerland)*. 2010;10(5):4907-25. doi:10.3390/s100504907.
122. Iida Y. Effects of atmosphere on laser vaporization and excitation processes of solid samples. *Spectrochimica Acta Part B: Atomic Spectroscopy*. 1990;45(12):1353-67. doi:[http://dx.doi.org/10.1016/0584-8547\(90\)80188-O](http://dx.doi.org/10.1016/0584-8547(90)80188-O).
123. Lee Y-I, Song K, Cha H-K, Lee J-M, Park M-C, Lee G-H, Sneddon J. Influence of Atmosphere and Irradiation Wavelength on Copper Plasma Emission Induced by Excimer and Q-switched Nd:YAG Laser Ablation. *Appl Spectrosc*. 1997;51(7):959-64.
124. Lal B, Zheng H, Yueh F-Y, Singh JP. Parametric study of pellets for elemental analysis with laser-induced breakdown spectroscopy. *Appl Opt*. 2004;43(13):2792-7. doi:10.1364/AO.43.002792.
125. Rosenwasser S, Asimellis G, Bromley B, Hazlett R, Martin J, Pearce T, Zigler A. Development of a method for automated quantitative analysis of ores using LIBS. *Spectrochimica Acta Part B: Atomic Spectroscopy*. 2001;56(6):707-14. doi:[http://dx.doi.org/10.1016/S0584-8547\(01\)00191-4](http://dx.doi.org/10.1016/S0584-8547(01)00191-4).
126. Tavassoli SH, Gragossian A. Effect of sample temperature on laser-induced breakdown spectroscopy. *Optics & Laser Technology*. 2009;41(4):481-5. doi:<http://dx.doi.org/10.1016/j.optlastec.2008.07.010>.
127. S. M. R. Darbani MG, A. E. Majd, M. Soltanolkotabi, H. Saghaififar. Temperature Effect on the Optical Emission Intensity in Laser Induced Breakdown Spectroscopy of Super Alloys. *Journal of European Optical Society - Rapid Publications*. 2014;9. doi:10.2971/jeos.2014.14058.
128. R. H. Scott AS. Laser induced plasmas for analytical spectroscopy. *Spectrochimica Acta Part B: Atomic Spectroscopy*. 1970;25(7). doi:10.1016/0584-8547(70)80038-6.
129. Bulatov V, Xu L, Schechter I. Spectroscopic imaging of laser-induced plasma. *Anal Chem*. 1996;68(17):2966-73. doi:10.1021/ac960277a.
130. Rai AK, Yueh FY, Singh JP, Rai DK. Chapter 11 - Laser-Induced Breakdown Spectroscopy of Solid and Molten Material. *Laser-Induced Breakdown Spectroscopy*. Amsterdam: Elsevier; 2007. p. 255-85.
131. Mao XL, Shannon MA, Fernandez AJ, Russo RE. Temperature and Emission Spatial Profiles of Laser-Induced Plasmas during Ablation Using Time-Integrated Emission Spectroscopy. *Appl Spectrosc*. 1995;49(7):1054-62.

132. Lee Y-I, Sawan SP, Thiem TL, Teng Y-Y, Sneddon J. Interaction of a Laser Beam with Metals. Part II: Space-Resolved Studies of Laser-Ablated Plasma Emission. *Appl Spectrosc.* 1992;46(3):436-41.
133. Aragon C, Aguilera JA. Two-Dimensional Spatial Distribution of the Time-Integrated Emission from Laser-Produced Plasmas in Air at Atmospheric Pressure. *Appl Spectrosc.* 1997;51(11):1632-8.
134. Kurniawan H, Jie Lie T, Kagawa K, On Tjia M. Laser-induced shock wave plasma spectrometry using a small chamber designed for in situ analysis. *Spectrochimica Acta Part B: Atomic Spectroscopy.* 2000;55(7):839-48. doi:[http://dx.doi.org/10.1016/S0584-8547\(00\)00155-5](http://dx.doi.org/10.1016/S0584-8547(00)00155-5).
135. Diwakar PK, Kulkarni P. Measurement of elemental concentration of aerosols using spark emission spectroscopy. *Journal of analytical atomic spectrometry.* 2012;27(7):1101-9. doi:10.1039/C2JA30025G.
136. Walters JP. The Formation and Growth of a Stabilized Spark Discharge. *Appl Spectrosc.* 1972;26(3):323-54.
137. Walters JP. Spark Discharge: Application to Multielement Spectrochemical Analysis. *Science.* 1977;198(4319):787-97.
138. Taefi N, Khalaji M, Tavassoli SH. Determination of elemental composition of cement powder by Spark Induced Breakdown Spectroscopy. *Cement and Concrete Research.* 2010;40(7):1114-9. doi:<http://dx.doi.org/10.1016/j.cemconres.2010.03.003>.
139. Body D, Chadwick BL. Simultaneous elemental analysis system using laser induced breakdown spectroscopy. *Review of Scientific Instruments.* 2001;72(3):1625-9. doi:<http://dx.doi.org/10.1063/1.1338486>.
140. Li K, Zhou W, Shen Q, Ren Z, Peng B. Laser ablation assisted spark induced breakdown spectroscopy on soil samples. *Journal of analytical atomic spectrometry.* 2010;25(9):1475-81. doi:10.1039/B922187E.
141. Gautier C, Fichet P, Menut D, Lacour J-L, L'Hermite D, Dubessy J. Quantification of the intensity enhancements for the double-pulse laser-induced breakdown spectroscopy in the orthogonal beam geometry. *Spectrochimica Acta Part B: Atomic Spectroscopy.* 2005;60(2):265-76. doi:<http://dx.doi.org/10.1016/j.sab.2005.01.006>.
142. Killinger DK, Allen SD, Waterbury RD, Stefano C, Dottery EL, editors. LIBS plasma enhancement for standoff detection applications 2008.
143. Weidman M, Baudelet M, Palanco S, Sigman M, Dagdigian PJ, Richardson M. Nd:YAG-CO₂ double-pulse laser induced breakdown spectroscopy of organic films. *Opt Express.* 2010;18(1):259-66. doi:10.1364/OE.18.000259.

144. Kwak J-h, Lenth C, Salb C, Ko E-J, Kim K-W, Park K. Quantitative analysis of arsenic in mine tailing soils using double pulse-laser induced breakdown spectroscopy. *Spectrochimica Acta Part B: Atomic Spectroscopy*. 2009;64(10):1105-10. doi:<http://dx.doi.org/10.1016/j.sab.2009.07.008>.
145. McDonald JT, Williams JC, Williams JC. Evaluation of the Time-Resolved Spark for the Determination of Sodium, Potassium, and Calcium in Microsamples. *Appl Spectrosc*. 1989;43(4):697-702.
146. Prasoon Diwakar PK. Effect of electrode characteristics and ambient gas on the sensitivity of aerosol measurement using spark emission spectroscopy. 2016. <https://www.scixconference.org/program/archive?p=1491&yearSelect=2012>.
147. Tognoni E, Cristoforetti G. Basic mechanisms of signal enhancement in ns double-pulse laser-induced breakdown spectroscopy in a gas environment. *Journal of analytical atomic spectrometry*. 2014;29(8):1318-38. doi:10.1039/C4JA00033A.
148. St-Onge L, Detalle V, Sabsabi M. Enhanced laser-induced breakdown spectroscopy using the combination of fourth-harmonic and fundamental Nd:YAG laser pulses. *Spectrochimica Acta Part B: Atomic Spectroscopy*. 2002;57(1):121-35. doi:[http://dx.doi.org/10.1016/S0584-8547\(01\)00358-5](http://dx.doi.org/10.1016/S0584-8547(01)00358-5).
149. Scaffidi J, Pender J, Pearman W, Goode SR, Colston BW, Carter JC, Angel SM. Dual-pulse laser-induced breakdown spectroscopy with combinations of femtosecond and nanosecond laser pulses. *Appl Opt*. 2003;42(30):6099-106. doi:10.1364/AO.42.006099.
150. Rai VN, Yueh F-Y, Singh JP. Study of laser-induced breakdown emission from liquid under double-pulse excitation. *Appl Opt*. 2003;42(12):2094-101. doi:10.1364/AO.42.002094.
151. Benedetti PA, Cristoforetti G, Legnaioli S, Palleschi V, Pardini L, Salvetti A, Tognoni E. Effect of laser pulse energies in laser induced breakdown spectroscopy in double-pulse configuration. *Spectrochimica Acta Part B: Atomic Spectroscopy*. 2005;60(11):1392-401. doi:<http://dx.doi.org/10.1016/j.sab.2005.08.007>.
152. Stratis DN, Eland KL, Angel SM. Dual-Pulse LIBS Using a Pre-ablation Spark for Enhanced Ablation and Emission. *Appl Spectrosc*. 2000;54(9):1270-4.
153. Uebbing J, Brust J, Sdorra W, Leis F, Niemax K. Reheating of a Laser-Produced Plasma by a Second Pulse Laser. *Appl Spectrosc*. 1991;45(9):1419-23.
154. Forsman AC, Banks PS, Perry MD, Campbell EM, Dodell AL, Armas MS. Double-pulse machining as a technique for the enhancement of material removal rates in laser machining of metals. *Journal of Applied Physics*. 2005;98(3):033302. doi:<http://dx.doi.org/10.1063/1.1996834>.

155. Belkov MV, Burakov VS, De Giacomo A, Kiris VV, Raikov SN, Tarasenko NV. Comparison of two laser-induced breakdown spectroscopy techniques for total carbon measurement in soils. *Spectrochimica Acta Part B: Atomic Spectroscopy*. 2009;64(9):899-904. doi:<http://dx.doi.org/10.1016/j.sab.2009.07.019>.
156. Zhou W, Li K, Shen Q, Chen Q, Long J. Optical emission enhancement using laser ablation combined with fast pulse discharge. *Opt Express*. 2010;18(3):2573-8. doi:10.1364/OE.18.002573.
157. Hou Z, Wang Z, Liu J, Ni W, Li Z. Combination of cylindrical confinement and spark discharge for signal improvement using laser induced breakdown spectroscopy. *Opt Express*. 2014;22(11):12909-14. doi:10.1364/OE.22.012909.
158. Lednev V, Pershin S, Bunkin A. Laser Beam Profile Influence on LIBS Analytical Capabilities: Single vs. Multimode Beam. *arXiv.org*. 2013.
159. Kramida A, Ralchenko Y, Reader J, Team NA. NIST Atomic Spectra Database (version 5.6.1). <http://physics.nist.gov/asd3>. Accessed 5/3/2017.
160. Martin M, Martin RC, Allman S, Brice D, Wymore A, Andre N. Quantification of rare earth elements using laser-induced breakdown spectroscopy. *Spectrochimica Acta Part B: Atomic Spectroscopy*. 2015;114(C):65-73. doi:10.1016/j.sab.2015.10.005.
161. Sciences GH. Helping you build a smarter diagnostic assay. 2013. <http://www.labxperts.eu/images/HerstellerPDFs/WhatmanSampleCollectionCards-S-Signed.pdf>.
162. SciAps. LIBS: Handheld Laser Induced Breakdown Spectroscopy (HH LIBS).
163. Instruments O, Andor. Resolution Calculator. <https://andor.oxinst.com/resolution-calculator>.
164. Yoon J, Lee J, Choi B, Lee D, Kim D, Kim D, Moon D-I, Lim M, Kim S, Choi S-J. Flammable carbon nanotube transistors on a nitrocellulose paper substrate for transient electronics. *Nano Research*. 2017;10(1):87-96. doi:10.1007/s12274-016-1268-6.
165. Millipore. Rapid Lateral Flow Test Strips. Considerations for Product Development.
166. Grayson K, de Silva CM, Hutchins N, Marusic I. Beam stability and warm-up effects of nd:yag lasers used in particle image velocimetry. *Measurement Science and Technology*. 2017;28(6):065301. doi:10.1088/1361-6501/aa6ad7.
167. Sciences GHL. Nitrocellulose backed membrane. <https://info.gelifesciences.com/Nitrocellulose-Membranes.html>.
168. Anabitarte F, Cobo A, Lopez-Higuera JM. Laser-Induced Breakdown Spectroscopy: Fundamentals, Applications, and Challenges. *ISRN Spectroscopy*. 2012. doi:10.5402/2012/285240.

169. RStudio. RStudio: Integrated Development Environment for R. Boston, MA: RStudio, Inc.
170. Alamelu D, Sarkar A, Aggarwal SK. Laser-induced breakdown spectroscopy for simultaneous determination of Sm, Eu and Gd in aqueous solution. *Talanta*. 2008;77(1):256-61. doi:10.1016/j.talanta.2008.06.021.
171. Ishizuka T. Laser emission spectrography of rare earth elements. *Analytical Chemistry*. 1973;45(3):538-41. doi:10.1021/ac60325a024.
172. Bhatt CR, Jain JC, Goueguel CL, McIntyre DL, Singh JP. Measurement of Eu and Yb in aqueous solutions by underwater laser induced breakdown spectroscopy. *Spectrochimica Acta Part B: Atomic Spectroscopy*. 2017;137(C):8-12. doi:10.1016/j.sab.2017.09.009.
173. Hartzler DA, Bhatt CR, Jain JC, McIntyre DL. Evaluating Laser-Induced Breakdown Spectroscopy Sensor Technology for Rapid Source Characterization of Rare Earth Elements. *Journal of Energy Resources Technology*. 2019;141(7). doi:10.1115/1.4042747.
174. Yang X, Hao Z, Shen M, Yi R, Li J, Yu H, Guo L, Li X, Zeng X, Lu Y. Simultaneous determination of La, Ce, Pr, and Nd elements in aqueous solution using surface-enhanced laser-induced breakdown spectroscopy. *Talanta*. 2017;163:127-31. doi:10.1016/j.talanta.2016.10.094.
175. Sabsabi M, Héon R, St-Onge L. Critical evaluation of gated CCD detectors for laser-induced breakdown spectroscopy analysis. *Spectrochimica Acta Part B: Atomic Spectroscopy*. 2005;60(7):1211-6. doi:<https://doi.org/10.1016/j.sab.2005.05.030>.
176. Camps-Valls G. Remote sensing image processing. San Rafael, California, Unites States: Morgan & Claypool; 2012.
177. Keshava N, Mustard JF. Spectral unmixing. *IEEE Signal Processing Magazine*. 2002;19(1):44-57. doi:10.1109/79.974727.
178. Amelio GF. Charge-coupled devices. *Scientific American*. 1974;230(2):22-31.
179. Zimmermann T, Rietdorf J, Pepperkok R. Spectral imaging and its applications in live cell microscopy. *FEBS Letters*. 2003;546(1):87-92. doi:10.1016/S0014-5793(03)00521-0.
180. Grégori G, Patsekin V, Rajwa B, Jones J, Ragheb K, Holdman C, Robinson JP. Hyperspectral cytometry at the single-cell level using a 32-channel photodetector. *Cytometry Part A*. 2012;81A(1):35-44. doi:10.1002/cyto.a.21120.
181. Doh I, Gondhalekar C, Patsekin V, Rajwa B, Hernandez K, Bae E, Robinson JP. A Portable Spark-Induced Breakdown Spectroscopic Instrument and its Analytical Performance. *Appl Spectrosc*. Accepted.
182. Corstjens PL, Li S, Zuiderwijk M, Kardos K, Abrams WR, Niedbala RS, Tanke HJ. Infrared up-converting phosphors for bioassays. *IEE proceedings Nanobiotechnology*. 2005;152(2):64-72. doi:10.1049/ip-nbt:20045014.

183. Vuojola J, Soukka T. Luminescent lanthanide reporters: new concepts for use in bioanalytical applications. *Methods and Applications in Fluorescence*. 2014;2(1):012001. doi:10.1088/2050-6120/2/1/012001.
184. Juntunen E, Myrskylainen T, Salminen T, Soukka T, Pettersson K. Performance of fluorescent europium(III) nanoparticles and colloidal gold reporters in lateral flow bioaffinity assay. *Anal Biochem*. 2012;428(1):31-8. doi:10.1016/j.ab.2012.06.005.
185. Aguilera JA, Aragón C, Madurga V, Manrique J. Study of matrix effects in laser induced breakdown spectroscopy on metallic samples using plasma characterization by emission spectroscopy. *Spectrochimica Acta Part B: Atomic Spectroscopy*. 2009;64(10):993-8. doi:<https://doi.org/10.1016/j.sab.2009.07.007>.
186. Sirven JB, Bousquet B, Canioni L, Sarger L. Laser-Induced Breakdown Spectroscopy of Composite Samples: Comparison of Advanced Chemometrics Methods. *Analytical Chemistry*. 2006;78(5):1462-9. doi:10.1021/ac051721p.
187. St John A, Price CP. Existing and Emerging Technologies for Point-of-Care Testing. *The Clinical biochemist Reviews*. 2014;35(3):155-67.
188. Novo D, Grégori G, Rajwa B. Generalized unmixing model for multispectral flow cytometry utilizing nonsquare compensation matrices. *Cytometry Part A*. 2013;83A(5):508-20. doi:10.1002/cyto.a.22272.
189. Carrell C, Kava A, Nguyen M, Menger R, Munshi Z, Call Z, Nussbaum M, Henry C. Beyond the lateral flow assay: A review of paper-based microfluidics. *Microelectronic Engineering*. 2019;206:45-54. doi:<https://doi.org/10.1016/j.mee.2018.12.002>.
190. Fluidigm. Maxpar Antibody Labeling Kit.
191. McGuire HM, Ashhurst TM. *Mass Cytometry Methods and Protocols*. 1st ed. 2019. ed. New York, NY : Springer New York : Imprint: Humana; 2019.
192. Janeway C. *Immunobiology 5 : the immune system in health and disease*. 5th ed. ed. Immunobiology five. New York: Garland Pub.; 2001.
193. Schneider CA, Rasband WS, Eliceiri KW. NIH Image to ImageJ: 25 years of image analysis. *Nat Methods*. 2012;9(7):671-5.
194. FSIS. 9CFR Part 304 Federal Register Rules and Regulations. In: *Agriculture*, editor.: Office of the Federal Register, National Archives and Records Administration; 1996. p. 38563-9037.
195. Laboratories B. *Microsphere Selection TechNote 201A*. 2008.
196. Hermanson GT. *Bioconjugate Techniques*. San Diego, UNITED STATES: Elsevier Science & Technology; 2013.

197. Nakajima N, Ikada Y. Mechanism of Amide Formation by Carbodiimide for Bioconjugation in Aqueous Media. *Bioconjugate Chemistry*. 1995;6(1):123-30. doi:10.1021/bc00031a015.
198. Gilles MA, Hudson AQ, Borders CL. Stability of water-soluble carbodiimides in aqueous solution. *Analytical Biochemistry*. 1990;184(2):244-8. doi:[https://doi.org/10.1016/0003-2697\(90\)90675-Y](https://doi.org/10.1016/0003-2697(90)90675-Y).
199. Antibody Labeling and Immobilization Sites. Thermo Fisher Scientific. <https://www.thermofisher.com/us/en/home/life-science/antibodies/antibodies-learning-center/antibodies-resource-library/antibody-methods/antibody-labeling-immobilization-sites.html>.
200. Adsorption to Microspheres Technote 204. Bangs Laboratories. 2013. <https://www.bangslabs.com/sites/default/files/imce/docs/TechNote%20204%20Web.pdf>. Accessed 10/9/18.
201. Adsorption Protocols Technote #13a. Bangs Laboratories. http://www.cyto.purdue.edu/cdroms/cyto4/7_spon/bangs/13a.pdf. Accessed 10/9/18.
202. Tarakanova YN, Dmitriev DA, Massino YS, Smirnova MB, Segal OL, Fartushnaya OV, Yakovleva DA, Kolyaskina GI, Lavrov VF, Dmitriev AD. Effect of conditions of monoclonal antibody adsorption on antigen-binding activity. *Applied Biochemistry and Microbiology*. 2012;48(5):506-12. doi:10.1134/s0003683812050122.
203. Kumar S, Aaron J, Sokolov K. Directional conjugation of antibodies to nanoparticles for synthesis of multiplexed optical contrast agents with both delivery and targeting moieties. *Nature Protocols*. 2008;3:314. doi:10.1038/nprot.2008.1.
204. Jazayeri MH, Amani H, Pourfatollah AA, Pazoki-Toroudi H, Sedighimoghaddam B. Various methods of gold nanoparticles (GNPs) conjugation to antibodies. *Sensing and Bio-Sensing Research*. 2016;9:17-22. doi:<https://doi.org/10.1016/j.sbsr.2016.04.002>.
205. Sánchez-Iglesias A, Grzelczak M, Altantzis T, Goris B, Pérez-Juste J, Bals S, Van Tendeloo G, Donaldson SH, Chmelka BF, Israelachvili JN, Liz-Marzán LM. Hydrophobic Interactions Modulate Self-Assembly of Nanoparticles. *ACS Nano*. 2012;6(12):11059-65. doi:10.1021/nn3047605.
206. Pensa E, Cortés E, Corthey G, Carro P, Vericat C, Fonticelli MH, Benítez G, Rubert AA, Salvarezza RC. The Chemistry of the Sulfur–Gold Interface: In Search of a Unified Model. *Accounts of Chemical Research*. 2012;45(8):1183-92. doi:10.1021/ar200260p.
207. Gao J, Huang X, Liu H, Zan F, Ren J. Colloidal Stability of Gold Nanoparticles Modified with Thiol Compounds: Bioconjugation and Application in Cancer Cell Imaging. *Langmuir*. 2012;28(9):4464-71. doi:10.1021/la204289k.

208. Yanagië H, Fujii Y, Sekiguchi M, Nariuchi H, Kobayashi T, Kanda K. A targeting model of boron neutron-capture therapy to hepatoma cellsin vivo with a boronated anti-(α -fetoprotein) monoclonal antibody. *Journal of Cancer Research and Clinical Oncology*. 1994;120(11):636-40. doi:10.1007/BF01245373.
209. McFarlane AS. Efficient Trace-labelling of Proteins with Iodine. *Nature*. 1958;182(4627):53-. doi:10.1038/182053a0.
210. Matea CT, Mocan T, Tabaran F, Pop T, Mosteanu O, Puia C, Iancu C, Mocan L. Quantum dots in imaging, drug delivery and sensor applications. *International journal of nanomedicine*. 2017;12:5421-31. doi:10.2147/ijn.s138624.
211. Yong K-T, Ding H, Roy I, Law W-C, Bergey EJ, Maitra A, Prasad PN. Imaging Pancreatic Cancer Using Bioconjugated InP Quantum Dots. *ACS Nano*. 2009;3(3):502-10. doi:10.1021/nn8008933.
212. Gondhalekar C, Rajwa B, Bae E, Patsekin V, Sturgis J, Kim H, Doh I-J, Diwakar P, Robinson JP. Multiplexed detection of lanthanides using laser-induced breakdown spectroscopy: a survey of data analysis techniques. *SPIE Proceedings*. 2019;11016:1101609--9. doi:10.1117/12.2521453.
213. Gondhalekar C. Alternative Approaches for Analysis of Complex Data Sets in Flow Cytometry. In: Robinson JP, Cossarizza A, editors. *Single Cell Analysis: Contemporary Research and Clinical Applications*. Singapore: Springer Singapore; 2017. p. 201-25.
214. Gondhalekar C, Rajwa B, Patsekin V, Ragheb K, Sturgis J, Robinson J. Alternatives to current flow cytometry data analysis for clinical and research studies. *Methods*. 2018;134-135. doi:10.1016/j.ymeth.2017.12.009.